



Heat Transfer in the Stator of Electrical Machines

Zur Erlangung des akademischen Grades eines Doktors der
technischen Wissenschaften ausgeführte Dissertation.

Eingereicht an der Fakultät für Elektrotechnik
der Technischen Universität Graz

durchgeführt von

Dipl.-Ing. Maximilian Schrittwieser

Institut für Grundlagen und Theorie der Elektrotechnik
der Technischen Universität Graz

Vorstand: Univ.Prof. Dipl.-Ing. Dr.techn. Oszkár Bíró

Betreuer: Univ.Prof. Dipl.-Ing. Dr.techn. Oszkár Bíró

Graz, im Dezember 2014

Preface

Working on this thesis the last three years in the Christian Doppler Laboratory for Multiphysical Simulation, Analysis and Design of Electrical Machines was a very interesting as well as challenging and enriching experience to me. At this point I would like to thank those people, without whose precious support, this work would not have been possible and successfully concluded.

First of all, I would like to express my deep and sincere gratitude to my research supervisor Univ.-Prof. Dr.techn. Oszkár Bíró. Thank you for your patient guidance, enthusiastic encouragement, constructive feedback and valuable time for discussion of scientific or other problems.

I am also deeply grateful for the support of the ANDRITZ Hydro GmbH. Special thanks are due, in particular, to Dr.mont. Ernst Farnleitner and Dr.mont. Gebhard Kastner for their advice and assistance throughout this work and for the productive working relationship.

Furthermore, I would like to thank the Christian Doppler Research Association for providing the productive working environment and the support of the work.

It is a pleasure to thank all my colleagues from the Christian Doppler Laboratory and the Institute of Fundamentals and Theory in Electrical Engineering at the Graz University of Technology. I am very grateful to your contributions, advice and detailed comments which have been of great value to me and turning the years in the laboratory into an unforgettable time.

Deepest gratitude goes to my wife for her patience, moral support and love in each situation during the last years and my daughter to give me the focus on the truly important things in life and cheering me up after a hard working day. I owe a debt of gratitude for all the hours stolen from them and their endurance is greatly appreciated.

Finally, I want to thank my parents, brother and friends for their indulgence and their encouragement which I appreciate very much.

Maximilian Schrittwieser

Statutory Declaration

I declare that I have authored this thesis independently, that I have not used other than the declared sources / resources and that I have explicitly marked all material which has been quoted either literally or by content from the used sources.

Eidesstattliche Erklärung

Ich erkläre an Eides statt, dass ich die vorliegende Arbeit selbständig verfasst, andere als die angegebenen Quellen / Hilfsmittel nicht benutzt und die den benutzten Quellen wörtliche und inhaltlich entnommene Stellen als solche kenntlich gemacht habe.

.....
Ort und Datum

.....
Unterschrift

Abstract

To guarantee the long-term availability of electrical machines and to meet the requirements for their growing efficiency, their design process has to be optimized. The arising losses depend on several parameters in different parts and to compute them in sufficient detail requires the cooperation of electrical and mechanical engineering. The focus of this work is the characterization of the convective heat transfer coefficient along the stator ventilation ducts of large synchronous machines used in hydro power plants. The computational fluid dynamics simulations carried out give detailed information about the cooling flow and thermal conditions. For the design process, these simulations are too time consuming, and the related coefficients have to be made available in a simpler way. Therefore, two different approaches have been used to characterize the convective heat transfer coefficients for the tooth and yoke region in the stator. One is a non-dimensional approach using a constrained non-linear optimization algorithm to fit the data obtained from the simulations by minimizing the least square error and the second one employs a neural network to realize the fitting. The used data sets include different machine designs, cooling schemes and operating conditions, so that a wide range of different machines is considered. It is shown that both methods are able to compute the convective wall heat transfer coefficient with sufficient accuracy for most engineering purposes. Comparisons resulting in good agreements have been made with a heat conduction model defining the convective wall heat transfer as a boundary condition on the walls, as well as with the well-established conjugate heat transfer method validated by measurements.

Kurzfassung

Um die langfristige Verfügbarkeit elektrischer Maschinen zu gewährleisten und die Voraussetzungen der Effizienzsteigerung zu gewährleisten, muß der Auslegungsprozess optimiert werden. Die Berechnung der auftretenden Verluste, abhängig von verschiedenen Parametern, in unterschiedlichen Teilen erfordert eine Kooperation von Elektrotechnik und Maschinenbau. Der Fokus dieser Arbeit beschäftigt sich mit der Bestimmung des konvektiven Wärmeüberganges entlang der Lüftungsschlitze des Stators von großen Synchronmaschinen eingesetzt in Wasserkraftwerken. Die ausgearbeiteten numerischen Strömungssimulationen geben detaillierte Informationen betreffend der Strömung des kühlenden Mediums wie auch thermische Zustände der Bauteile. Im Zuge des Designprozesses sind diese Simulationen zu zeit intensiv und die zusammenhängenden Koeffizienten müssen auf einen erleichterten Weg berechnet werden. Deswegen wurden zwei unterschiedliche Ansätze gewählt um den konvektiven Wärmeübergangskoeffizienten für den Zahn- und Jochbereich im Stator zu bestimmen. Zu Beginn wurde ein dimensionsloser Ansatz gewählt um mit einem nicht linearer Optimierungsalgorithmus mit definierten Nebenbedingungen die Daten, welche aus dem Simulationen bestimmt wurden, mit Hilfe der Methode der kleinsten Fehlerquadrate zu minimieren und weiters wurde ein neuronales Netzwerk verwendet. Die verwendeten Datensätze beinhalten eine Vielfalt an unterschiedlichen Maschinenvarianten bezüglich Geometrie, Kühlungskreisläufe und Betriebszustände, um somit einen großen Bereich der Approximation des konvektiven Wärmeübergangskoeffizienten zu gewährleisten. Es wurde aufgezeigt, dass beide Methoden den konvektiven Wärmeübergangskoeffizienten in ausreichender Genauigkeit für den Auslegungsprozess abbilden können. Im Weiteren wurde ein Wärmeleitungsmodell entwickelt um den konvektiven Wärmeübergangskoeffizienten als Randbedingungen an den Wänden zu definieren und einen Vergleich der Ergebnisse mit der etablierten „Conjugate Heat Transfer“ Methode zu bewerkstelligen, welche ebenfalls mit Messungen validiert wurde.

Contents

Preface	2
Statutory Declaration	3
Eidesstattliche Erklärung	3
Abstract	4
Kurzfassung	5
Contents	6
1 Introduction	9
1.1 Motivation	9
1.2 Review of literature	10
1.2.1 Heating and cooling of electrical machines	10
1.2.2 Thermal management and design of cooling scheme for electrical machines	11
1.3 Current practice	12
1.4 Aim and focus of the work	13
1.5 Scientific contributions	14
1.6 Outline of the work	15
1.7 Commercial software packages used	16
2 Fundamentals	17
2.1 Losses in electrical machines	17
2.1.1 Temperature rise during operation	17
2.1.2 Thermodynamic balance of energy	18
2.1.3 Heat sources	19
2.1.4 Cooling methods	20
2.2 Heat transfer	22
2.2.1 Heat transfer by conduction	22
2.2.2 Heat transfer by convection	24
2.2.3 Heat transfer by radiation	25
2.3 Fluid dynamics	26
2.3.1 Fluid and viscosity	27
2.3.2 Governing equations of fluid flow and heat transfer	27
2.3.3 Equation of thermodynamic state	32

2.3.4	Equations for viscous flow – the Navier-Stokes equations.....	32
2.3.5	Characteristic dimensionless numbers in fluid dynamics	33
2.3.6	Boundary layer	34
2.3.7	Turbulent flow	35
2.3.8	Reynolds Averaged Navier-Stokes (RANS) equations.....	36
2.3.9	Turbulent shear flow in wall proximity.....	38
2.4	Computational fluid dynamics	39
2.4.1	Discretization.....	39
2.4.2	Computation of turbulent flow	40
2.4.3	RANS models using eddy-viscosity turbulence models	41
2.4.4	Wall treatment	45
2.4.5	Mesh requirements	47
3	Enhancement of the state of the art design process for large hydro generators using numerical methods to simulate the fluid and thermal field	48
3.1	Overall model of a large hydro generator	48
3.1.1	Rotor-stator interaction.....	50
3.1.2	Numerical set-up	52
3.1.3	Evaluation of numerical parameters.....	53
3.1.4	Results of the computed flow field.....	55
3.1.5	Results of the computed thermal field.....	59
3.2	Single duct model.....	61
3.2.1	Geometry of the numerical models	61
3.2.2	Domain decomposition.....	62
3.2.3	Sensitivity study	63
3.2.4	Ventilation duct design study	64
4	Development of a conjugate heat transfer model to investigate the heat transfer along the stator ventilation ducts	69
4.1	Measurement of the stator laboratory model	69
4.1.1	Measurement set-up	70
4.1.2	Measuring physical parameters	71
4.2	CHT ventilation duct model.....	73
4.2.1	Geometry of the model.....	73
4.2.2	Numerical set-up	75
4.2.3	Material properties of the coolant	75
4.2.4	Material properties of the solids.....	76
4.2.5	Boundary conditions.....	76
4.3	Validation of the CHT model with measurements.....	76
4.3.1	Copper temperature	77
4.3.2	Iron temperature	79
4.3.3	Fluid temperature	79
4.4	Novel approach to compute the heat transfer for low Reynolds numbers	80
4.4.1	Validation of the IFM with measurements.....	81

5	Approximation of the convective wall heat transfer coefficient used for network methods in the design process	84
5.1	Non-dimensional approach	84
5.1.1	Selection of the data set.....	86
5.1.2	Non-dimensional variables defined.....	86
5.2	Constrained nonlinear optimization algorithm.....	87
5.2.1	Numerical approach	88
5.2.2	Accuracy of the developed formula	88
5.3	Neural network.....	93
5.3.1	Numerical approach	93
5.3.2	Boundary conditions.....	95
5.3.3	Architecture	95
5.3.4	Accuracy of the designed neural network	98
6	Improved heat conduction model to compute temperature distribution in the solid domains of the stator	102
6.1	Geometry of the model.....	102
6.2	Boundary conditions	104
6.2.1	Implementation of the heat convection	104
6.2.2	Definition of the electromagnetic losses	105
6.3	Validation of the HC model by comparison to the CHT model	105
6.3.1	Comparison of the computed temperatures in the solid domains	106
6.3.2	Comparison of the temperature distribution in the solid domains	109
7	Conclusion	112
8	References	115

1 Introduction

1.1 Motivation

Life without electrical machines is hardly conceivable today given their integration in our modern and technophile society in nearly every situation. Energy consumption by a constantly developing industry and by a public enjoying a rising standard of living is the main application of these machines. Efficiency and sustainability are two important keywords in the design process of modern companies to be globally competitive. Therefore, renewable energy supply, e.g. by wind power plants, hydro power plants, tidal power plants or geothermal power plants has become indispensable in the last decade. Higher efficiency can be achieved by customized machines tailored for the designed requirements.

An important aspect in covering the rising energy demand is the design process, with focus on the efficiency during the operation. The construction of such machines is a complex procedure involving several branches of engineering. The generation of the losses is an electromagnetic, thermal, mechanical and chemical process. Therefore the classification and knowledge of the behavior of the arising losses plays a decisive role in the design process. Large hydro generators transform mechanical energy in electricity in a power range from 10 MVA to 800 MVA. For this category of generators it is indispensable to ensure a continuous operation. The state of the art methods of design are based on networks, e.g. electromagnetic, fluid or thermal ones. The parameters in these networks are obtained by analytical approaches, measurements or numerical simulations. To optimize these parameters is an important topic in the research and development of electrical machines.

Numerical simulations have become an additional option in the design process of electrical machinery due to the fast development of computational resources in the last years. Regarding electromagnetic and mechanical design, finite element (FE) analysis is a state of the art tool. Especially two-dimensional (2-D) simulations are widely used, and three-dimensional (3-D) models will be state of the art in a few years. The situation is similar concerning the choice between steady state or transient simulations. The losses constituting the input quantities for the design of the cooling scheme can be determined using such methods.

Nowadays, the cooling of electrical machines is one of the most actual topics in the design process. The state of the art methods have been obtained from turbo machinery, e.g. fans or turbines. The possibility to compute the laminar or turbulent fluid flow has been the first step to understand different cooling schemes and visualize the problems in the circuit. Furthermore, a detailed optimization of different parts, especially in cases where measurements are not possible, has been made feasible. Furthermore, temperature peaks can be avoided and material can be saved, e.g. copper, iron and especially insulation, with the advantage of less weight and less energy consumption due to resources being saved. Computational fluid dynamics (CFD) is a commonly used numerical technique based on the finite volume (FV) method to solve 3-D transport equations in the fluid domain.

Furthermore, heat transfer is of special interest, particularly the convective heat transfer, which is inherently solved in CFD analysis, in contrast to FE methods where it has to be defined as a boundary condition on the walls. The conjugate heat transfer (CHT) method is capable of modeling the solid domains in addition to the fluid domain. It has the advantage of allowing the electromagnetic losses to be defined in the solid parts and solving the 3-D heat conduction first to be followed by the 3-D heat convection due to the cooling circuit. The anisotropy of the various material parameters has to be implemented, e.g. for thermal conductivity, dynamic viscosity and heat capacity to describe realistic fluid conditions. Including the solid domains in the CHT method has an additional advantage over CFD analysis when coupling with electromagnetic FE simulations is required. In summary, due to the rising complexity and demands concerning cooling, thermal computation in electrical machines is a topic of high interest.

1.2 Review of literature

The heat emission of electrical machines can be traced back to the arising losses. A detailed classification according to the origin of these losses can be found in [1] and [2]. The occurrence of the copper, eddy current, hysteresis and mechanical losses lead to a temperature rise in different parts [3]. On the one hand, there are parts heated up by the losses, like the copper bars, clamping plate, stator iron, rotor iron. On the other hand the heat transfer is responsible for a temperature rise in the distance bars, spacer, slot wedge and housing. The analytical computation of the arising losses and their transformation in heat has been discussed in detail in [4]. Several textbooks discuss the heat conduction, convection and radiation in detail, like [5] and [6].

1.2.1 Heating and cooling of electrical machines

The cooling design of electrical machines makes use of the heat transfer to transport the heat from the solids to a cooling medium. The heat is discharged at the walls between the solid and the fluid due to heat convection and heat conduction transports the energy in the solid domains. In addition to heat convection, heat radiation occurs at the walls where the cooling air is forced to stream by. The thermal conductivity is known for materials commonly used in manufacturing electrical machines. The radiation heat transfer coefficient is simply a function of the surface properties and can be reproduced accurately enough. The convective heat transfer coefficient is a parameter depending on the properties of the coolant as well as on the fluid flow characteristic and is quite hard to determine. There are several empirical formulas based on convection laws in simple geometrical cases which are readily available in undergraduate textbooks e.g. [7]-[10].

In the last decade, several investigations have been carried out concerning convective heat transfer in electrical machines, most of them for low powers of a few kVA with simple cooling strategies. A method to determine the convective heat transfer coefficient of totally enclosed fan cooled (TEFC) motors has been established in [11] based on temperature measurements at the end winding and end shield to describe the thermal behavior with thermal resistances. This method has been tested in other motor power classes and compared with other established analysis software in [12] and [13]. The convective wall heat transfer coefficient in the end region of TEFC motors strongly depends on the geometry and the operating speed and can be distributed over a wide range depending on the machine type as pointed out in [14]. In addition to treating other heat transfer problems at the end winding in electric machines, a summary of different correlations including different parts has been set up.

The heat transport and effects of the thermal conductivity of the rotor insulation on turbo generators have been analyzed in [15]. A ventilation analysis has been carried in [16] with focus on the thermal field in the stator assembly. Heat conduction has been focused on in [17]. Using the FE method, the eddy current losses and heat transfer characteristics of the stator winding have been investigated in [18]. The losses have been computed using an analytical approach as well as 2-D and 3-D FE analysis in addition to the solid temperatures and the resistance enhancement coefficient. The influence of eddy current loss on winding temperatures has also been demonstrated. Nowadays, 3-D FE models are state of the art to analyze the electromagnetic and thermal field in electrical machines, see e.g. [19] and [20]. In these works, the coupling between the electromagnetic and the thermal analysis is carried out to determine the temperatures in the stator assembly in addition to a design study having been performed. The main advantage of the FE method is that it allows the computation of the solid temperatures from the determined losses.

In case of large hydro generators, the heat transfer and the relation to the flow field have been under investigation in [21] with the focus on the volumetric flow distribution in the stator and the local heat transfer coefficient on the rotor winding sides and end surfaces. Measured wall heat transfer coefficient (WHTC) values have been compared to ones obtained by CFD in [22]. The link between the heat transfer coefficient and the flow field has been clearly demonstrated and the WHTC has been computed directly using CFD. The investigation in [23] describes the possibilities of this numerical method. Different parts of interest have been investigated and the results compared with those obtained by the established network method. The flow field and thermal field can be computed inherently and the electromagnetic losses have to be defined as thermal sources at the boundaries as shown in [24], a paper dealing with the set-up of a CFD model to solve the 3-D transport equations with the focus on the flow and thermal fields in the rotor and in the pole windings. For a detailed analysis with acceptable computation times, a simplified model has to be developed using a coupling between two different simulations, see [25]. The method to reduce the model as well as the definition of the boundary condition for the sub-domains is presented, in addition to the results of several parameters referring to the fluid and thermal fields. The interactions between the stator and the rotor and ways to reduce the generator model have been under investigation in [26].

1.2.2 Thermal management and design of cooling scheme for electrical machines

The machines investigated in this work are large synchronous machines with salient poles used in hydro power plants. The efficiency of such machines is higher than 98.5 % and the losses are in a range of about 2 MW, so their cooling is an important issue [27].

The copper, hysteresis, eddy current and mechanical losses arising during the generator operating lead to a temperature rise in the electrical machine. Appropriate standards have been defined for the allowable temperature limits in IEC 60034, [28]. In order to avoid overheating, the power losses have to be discharged by forced air cooling to ensure the operating characteristics [29]. In air cooled machines, special attention must be paid to the design of the cooling scheme focusing on the cooling air flow, because ventilation losses can get into the range of 20-40 % of the total power losses [30].

Therefore, an appropriate quantity of cooling air must be circulated through the machine to ensure the heat transport [31]. The required air pressure is generated by external fans, fans mounted on the shaft or by rotating structural parts. During the design process, special attention

has to be paid to the cooling of thermally critical parts of the machine, like stator core, stator winding, pole winding, pole shoe, clamping plate and end winding [32]-[36].

For designing the cooling of a generator, electromagnetic, thermal and air flow calculations are necessary. The commonly used network method has been established in the design process [32]. The flow paths through the machine are approximated, coupled and solved with parameters defined at the connecting nodes. Several parameters are needed to take account of accurate boundary conditions. Due to the large model size, FE methods and CFD are not economic to compute the whole machine at once. A coupling of these methods would be required for a complete thermal analysis of the machine. Nevertheless these methods are efficient for researches at specific parts to obtain coefficients to optimize the network method.

Therefore, the used parameters have to be estimated theoretically, by measurements or by numerical analysis. Numerical methods like FE techniques or CFD can be used to optimize the parameters in the applied networks. The relationship based on the mechanical and total energy balances make fundamental applications possible [38]. In that work, the CFD analysis of the rotor of a salient pole generator is presented showing that the formulation of the network parameters based on numerical methods is more exact and more comprehensive than applying usual experimental methods. A qualitative snapshot of the state of development is presented in [39]. An optimization of the ventilation concept of a traction machine by means of CFD is described in [40].

Many publications on the cooling of electrical machines have appeared in the last decade. An excellent summary of modern approaches for electro-thermal analyses using thermal and flow networks, FE method and CFD are described in [41].

Thermal analysis has long received less attention than electromagnetic design. However, in the last years, the topic has been taken up in several interesting papers. The combination of electromagnetic FE models and thermal networks has emerged as a possible procedure to predict temperatures in different machine types [42]-[44]. A 3-D FE simulation has been carried out for studying local rotor temperature rises for large synchronous machines [45]. In [46], a combination of CFD and thermal network has been used to model the machine. As mentioned above, special investigations are necessary to define or implement the convective heat transfer in an FE analysis or optimize the WHTC in thermal networks when designing the cooling of an electrical machine. Therefore, two different approaches have emerged to determine the convective heat transfer. One uses thermal resistances defined with the aid of temperatures gained by measurements [47], [11] and [14]. The other employs CFD calculations combined with measurements [48]-[50].

For the design process itself, CFD offers possibilities to obtain certain flow parameters to determine the convective heat transfer coefficient, see [51] and [52]. The improvement of the turbulence model [53] and wall treatment [54] are great opportunities to compute the convective WHTC in sufficient detail.

1.3 Current practice

Large hydro generators with salient poles are built as prototypes for special requirements defined by the relevant application. Most worldwide manufacturers have been producing such electrical machines over many decades and have a manifested history in the business. Their established methods for the development and design of machines have matured over decades, improved step-by-step by generations of engineers.

The principles of this traditional design are based on lumped-element circuit models. Especially in case of thermal calculations, thermal networks have been used since the beginning of the development of electrical machines. Nowadays, the network methods itself do not change very much, but improved computational techniques allow to accelerate the computations and enable solving more complex models involving thermal, air flow and electromagnetic analyses. Turbulent and compressible steady state and also transient problems can be solved presently in 2-D or even 3-D. The uncertain factors in these networks are their parameters calibrated with measurements on manufactured machines during decades of development. Therefore, this method works well as long as the designed machines are within established power classes, have similar geometries, operating conditions and familiar cooling methods. Furthermore, these techniques are cheap and extremely fast utilizing contemporary computer performance.

It is becoming ever more important for companies to be competitive in terms of material and manufacturing costs and, naturally, time. Therefore, novel concepts of electrical machines have to be invented, especially for the cooling, which has been somewhat neglected in the past decades. Nowadays, a more flexible approach is required for thermal analysis and especially for the calibration of thermal networks. The CFD method is one effective tool allowing to calibrate thermal and also fluid flow network models. The finite volume method is used thereby to solve the 3-D transport equations of the numerical model. On the one hand, the flow field is to be computed to determine mass flow rates, differences of specific or total pressure and related pressure loss coefficients and windage losses or rate of mechanical work transferred at rotating walls. On the other hand, the thermal field is solved inherently to calculate the solid and fluid temperatures and the related heat transfer to compute an average heat transfer coefficient. With the benefit of CFD, the parameters used in fluid and thermal networks can be updated and optimized.

Presently, the main purpose of CFD analysis for electrical machinery is the determination and formulation of correlations between cooling quantities. Such correlations, experimental or even numerical, are necessary to enable calculations of cooling parameters for designs with similar geometries. Indeed, even if CFD methods are available, simulations are currently conducted for selected representative machines or models only, due to the large geometrical variety of electrical machines. A complete CFD simulation for each design is practically impossible. Even if the geometry is invariant, the current state of the art in CFD with available hardware, does not yet allow the large cooling circuit or the entire machine to be modeled in its entirety by means of conjugate heat transfer. In this case conventional calculation methods are necessary to predict the overall performance of the cooling scheme.

1.4 Aim and focus of the work

The main objective of this thesis is to determine the convective wall heat transfer coefficient in the stator of large hydro generators with salient poles. Therefore, integrated in the standard design tool, a module has been developed to compute the WHTC for the tooth and yoke region, depending on geometric parameters, fluid properties and fluid conditions.

The first part of thesis deals with the development of a CFD model to investigate the fluid flow in the stator of a generator used in hydro power plants and compute the convective heat transfer of this machine. The complexity of such analysis is pointed out and also methods to reduce the computational effort for such simulations are introduced. Particularly, it is illustrated that the method can be very useful for the ventilation design of large hydro generators. Afterwards, a

reduced model has been investigated and several results have been compared with those obtained from the overall generator model.

In addition to the commonly used CFD analysis, a CHT model has been developed to compute the conductive and convective heat transfer in the stator. The solid bars are included and the temperature distribution is computed in the whole winding assembly and cooling fluid. The losses can be defined in the solid domains where they arise, and the anisotropic materials have been also included to model realistic conditions. This numerical solution has been validated with calorimetric temperature measurements for different winding assemblies and different mass flow rates.

The main focus has been to determine the convective WHTC by using a constrained non-linear optimization algorithm. Non-dimensional parameters have been used to describe the non-dimensional WHTC, the Nusselt number. Several CFD data have been correlated by using a least square technique. Additionally, a neural network has been designed, using similar non-dimensional parameters with the benefit of the possibility to include additional training parameters appearing in further designs.

Last but not least, a heat conduction model has been developed to test the determined WHTC as boundary condition parameters on the tooth and yoke wall. This model includes an energy balance equation to describe the heating up of the solid. The losses have been defined at the copper and iron using an analytical formula. The temperature distribution in the solid domains thus obtained has been validated with the conjugate heat transfer method.

1.5 Scientific contributions

This section is devoted to listing the scientific contributions of this work. The main findings have been summarized in the publications [55]-[64], but some unpublished results also are included.

- The state of the art method to compute the cooling in electrical machines has been compared with another approach for steady state simulations. The main focus is on the interaction between stator and rotor which can be handled with a Frozen Rotor or Mixing Plane interface in 3-D models to consider the rotor rotation. The difference of these overall models concerns the stator domain being considered as a pole section in the Frozen Rotor model and as a slot section in the Mixing Plane model. The Frozen Rotor method has been established for numerical computations of electrical machines in the last decades. The results show that the Mixing Plane model achieves the accuracy of the overall numerical model with 40% of the elements, a performance not attained by the Frozen Rotor model. Afterwards, a domain decomposition has been carried out to define the inlet condition on a single duct model. A slot section model and a pole section model including a single ventilation duct have been developed to prescribe the data from the Mixing Plane model as a boundary condition on the slot section model and the data from the Frozen Rotor model as a boundary condition on the pole section model. The advantages of these single duct models are the low number of elements and the fast computation time in contrast to the two different overall models, and still computing similarly accurate results along the ventilation duct. A sensitivity study has also been carried out for the determination of the wall heat transfer coefficient. It has been found that the heat transfer coefficient is mainly influenced by the mesh near the walls, as presented in the conference contribution [55]. Afterwards, this work has been extended and published as a journal paper in [56].

- A numerical model has been developed to compute the temperature distribution in the solid parts and also in the cooling fluid along the stator of large synchronous machines. The focus is on the conductive and convective heat transfer of different winding assemblies. The differences in the thermal treatment of the copper bars, stator iron and the fluid have been pointed out for each model. At the same time, all relevant effects have been validated with measurements for different volume flow rates. The results of these conjugate heat transfer models are in an excellent agreement with the calorimetric measurements and parts of this work have been first presented at a conference [57] and then published in [58].
- The time consuming numerical CFD and CHT computations are in the focus of the third contribution. A novel approach has been introduced to save elements in sub-ducts by introducing a surface thermal resistance in 3-D computations. As presented in chapter 2 describing the fundamentals, the main effect of heat transfer for low Reynolds numbers is the conductive heat transfer. This is confirmed by this work as well. The temperature distribution has been validated with measurements for different temperatures in the solid and fluid domain. The computation time can be reduced by more than 50 % compared to time consuming finite volume methods as presented in [59] and published in [60].
- The characterization of the convective wall heat transfer coefficient for the tooth and yoke region along the ventilation ducts has been presented first in [61]. A constrained non-linear optimization technique has been used to correlate the convective wall heat transfer coefficient to various design parameters based on the results of several CFD simulations. Afterwards, the heat flux can be obtained at the walls of a solid model defining the boundary condition under real operating conditions. This has allowed the development of a numerical 3-D heat conduction model consisting of the solid domains only with the fluid taken into account by boundary conditions defined at the walls. The simulations have been validated by comparison to the substantially more demanding CHT method. Parts of this work have been published in [62].
- A second method has been developed to determine the convective wall heat transfer coefficient in more detail by using an artificial neural network. The architecture of the network has been defined by cross validation to find the most efficient design for these applications. Several non-dimensional parameters define the input layer and the output layer has been chosen to characterize the Nusselt number. This neural network employs a Levenberg-Marquard modification of the Gauß Newton method to determine the Nusselt number in a least square error sense. The training data have been gained from several CFD computations, as also the test data. Last but not least, the computed wall heat transfer coefficient has been defined at the walls of a heat conduction model and the temperature distribution has been validated with the established CHT model as presented at [63]. This work is still in review process for a journal publication [64].

1.6 Outline of the work

A detailed literature review, including the state of the art methods to design the ventilation in rotating machines has been presented in chapter 1. This overview describes the availability of different methods, as well as examples of their application to electrical machines. Afterwards, the focus of the work has been established in addition to the presentation of the novel scientific contributions achieved during the three years of the PhD program. Last but not least, this outline of the work is included.

The second chapter deals with the fundamentals of the investigated topic, including losses in electrical machines, heat transfer, fluid dynamics and computational fluid dynamics. The different aspects of heat transfer are described in detail as well as the numerical background of the software used, including turbulence models, wall treatment and material modeling with special attention paid to the thermal managements of large synchronous machines.

Chapter 3 describes a detailed analysis using computational fluid dynamics for investigating the fluid flow and, additionally, the thermal field in large hydro generators. A method differing from the state of the art steady state simulation using a Frozen Rotor interface is presented by using a Mixing Plane interface with the benefit of less numerical effort. Furthermore, a novel technique has been applied to obtain the inlet data of the generator model and define these on two different single duct models. Hence, a detailed investigation concerning different designs of the stator duct is possible with a computation time of a few hours instead of weeks with the generator models. Finally, a sensitivity study has been also included in this chapter by using two different turbulence models and wall treatments to get information on the mesh dependence of the wall heat transfer coefficient.

For investigating the operating conditions more accurately, the conjugate heat transfer (CHT) method has been used in chapter 4. Therefore three 3-D numerical models have been created and simulated including five slot sections of the stator and three ventilation ducts. The main difference between these models is in the slot assembly with focus on the position of the insulated copper bars using a ripple spring, epoxy resin or simply air instead of a solid domain. Afterwards, the results have been validated with measurements of the investigated laboratory model. Additionally, a novel approach has been developed to eliminate the fluid domain from the problem region in case of creeping flows by introducing a surface thermal resistance. The method has been validated by comparison with the CHT solution and with measurements.

Chapter 5 deals with the approximation of the convective wall heat transfer coefficient. A constrained non-linear optimization algorithm has been used on the one hand. On the other hand, a neural network has been developed. The efficiency of both methods has been pointed out with their advantages and disadvantages detailed.

Thereupon, a novel heat conduction model has been developed in chapter 6. This model contains just the solid domains of a slot section of the stator. The heat convection has been defined on the wall boundaries by defining the approximated convective wall heat transfer coefficient and the fluid reference temperature has been obtained using the first law of thermodynamics. The validation has been made with the CHT method presented and validated in chapter 4.

The conclusions of the work are drawn in chapter 7.

1.7 Commercial software packages used

The software *CFX* from the software package *ANSYS v13.0* and *v14.5* has been used for the CFD analysis. The used meshes have been created with *ANSYS ICEM CFD v13.0*. Diagrams and other calculations have been accomplished with *MATLAB R 2012a*.

2 Fundamentals

2.1 Losses in electrical machines

2.1.1 Temperature rise during operation

Electrical machines are used to convert mechanical energy in electrical energy with an efficiency of more than 98%. Such a “from water to wire” system is explained in detail with the main parts shown in Fig. 1. A pump storage hydro power plant is presented where water is stored at a higher level and is transported through (2) the penstocks to (4) the turbine. The turbine extracts the potential, kinetic and pressure energy of the fluid flow. The mechanical energy is transported over a shaft from the turbine to the (5) generator. The generator converts this energy in electrical energy transported over (7) and (9) the switchgears, (8) the power transformer and (10) the transmission line to the end consumer.

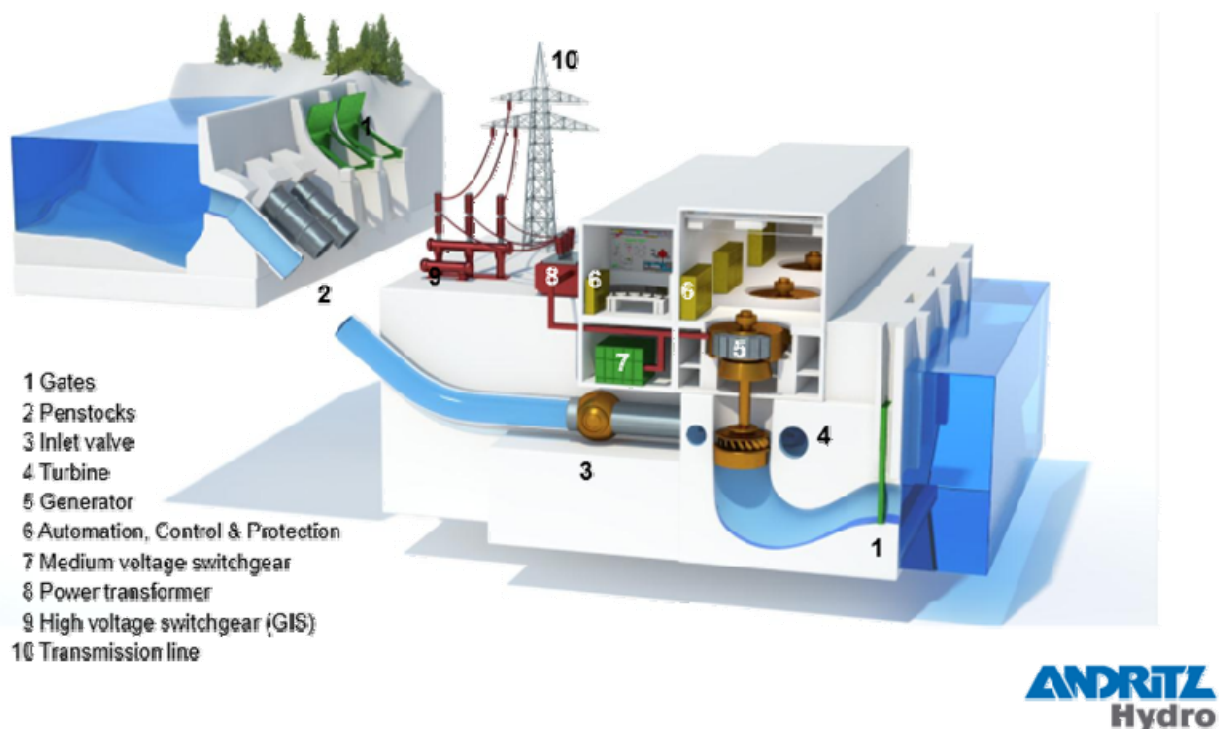


Fig. 1 Pump storage hydro power plant with included parts for electrical energy production [65]

The conversion of mechanical to electrical energy and vice versa within such an electrical device is always associated with losses. These arising power losses are heat losses and cause a temperature rise which has a harmful influence on the operating characteristics or induces component damage in the worst case. During the startup of the machine, all parts have uniform

temperature. The heating of different parts depends on the local loss density and the material properties. The high temperature gradients due to the differences in temperatures cause heat fluxes between the parts. Generally speaking the heat flow follows the negative temperature gradient through the different solid domains and finally reaches a cooling medium with the purpose to discharge the heat from the machine to the environment. During heat run tests, the temperatures and heat fluxes rise inside the electrical machine until the generated heat caused by the loss density in every part and the discharged heat are in equilibrium. Once the losses and discharged heat are balanced, no more heat is stored inside the machine and the temperatures of the parts remain at steady state values as long as the operating conditions remain constant.

The specification of the temperature difference between the coolant at the beginning of the cooling cycle and a particular location in the machine, also known as over-temperature, that of the reference coolant, as well as of the operating conditions for the measurement set-up can be found in [66]. The maximal arising over-temperature in an electrical machine is primarily limited by the thermal stability of the insulation material of the windings. Three methods of measuring the temperature of windings and other parts are the resistance (R), embedded temperature detector (EDT) and thermometer (Th) methods. The winding temperature is determined from the increase of the resistance of the winding by the resistance method. In case of the ETD method, the temperature is determined by means of temperature detectors built into the machine during construction at points inaccessible once the machine is manufactured. The thermometer method uses thermometers or thermocouples to determine the temperature at accessible surfaces of the completed machine. The maximal allowed over-temperatures for specific parts of the machine are known as over-temperature limits and are listed in the IEC 600341 standard, as shown in Table 1.

thermal class	130 (B)		155 (F)		180 (H)	
method for measurement	R	ETD	R	ETD	R	ETD
over-temperature limits in K	80	85	105	110	125	130

Table 1 Over temperature limits of the windings of a rotating electrical machine in a power class of more than 5000 kW, cooled by air [66]

2.1.2 Thermodynamic balance of energy

From the thermodynamic point of view, the energy balance equation can be described by the first law of thermodynamics for a closed system at a specific time instance as

$$dQ + dA_t = dE_o + dU. \quad (2.1)$$

The differential changes on the left hand side are those of the external energy transported over the system boundaries being the sum of the heat Q and of the technical work A_t and on the right hand side those of the energy stored in the system, the sum of the external energy E_o and of the internal energy U .

The changes of the externally supplied forms of energy, Q and A_t , are positive when energy is being added to the system and negative when taken away from it. During operation, the heat produced is usually taken away from the system and, therefore, its change is negative. Any other arising thermal energy Q_o which is transported to the system across the boundaries needs to be added positive. The work can be split into mechanical $A_{t,me}$ and electrical work $A_{t,el}$. Assuming the machine is operating as generator, the mechanical work is positive and the electrical work is negative.

The stored energy in the system comprises of the external energy E_o and internal energy U . Therefore, the external energy can be stored as potential energy $E_{o,pot}$, kinetic energy $E_{o,kin}$, electrical energy $E_{o,el}$ or magnetic energy $E_{o,mag}$.

The transported energy over the system boundaries is more relevant for the cooling process of an electrical machine than the stored energy. Hence, the first law of thermodynamics for an open system is more useful than (2.1) to describe the energy balance in more detail [67]:

$$dA_t + dQ_0 + \sum dm_i (h_i + e_{o,i}) = dE_o + dU . \quad (2.2)$$

The additional variables here are the specific enthalpy h_i , the specific energy $e_{o,i}$ and the mass m_i for the i^{th} transport across the system boundary. The energy balance can be expressed for steady state when the mass flow is constant and no storage occurs:

$$dA_t + dQ_0 + \sum dm_i (h_i + e_{o,i}) = 0 . \quad (2.3)$$

Considering a single coolant with only one transport in and out of the system, the steady state flow process covers all relevant specific variables for the cooling. Using the subscript 1 to denote the inlet and the 2 the outlet, the specific technical work a_t can be defined as follows:

$$a_t = h_2 - h_1 + e_{o,2} - e_{o,1} - q_0 . \quad (2.4)$$

All variables here are given as specific energy per unit mass. The enthalpy H includes the inner energy U and the energy stored in the fluid is expressed with the pressure p and the volume V :

$$H = U + pV \quad (2.5)$$

or, with the density ρ , for specific values per unit mass:

$$h = u + \frac{p}{\rho} . \quad (2.6)$$

2.1.3 Heat sources

Heat is produced by the various losses in a machine. The power provided to an electrical machine not converted from mechanical into electrical output power is transformed into heat Q . Generally speaking, the power losses P can be defined as the derivative with respect to time t of the heat Q :

$$P = \frac{dQ}{dt} . \quad (2.7)$$

The internal distribution of the losses depends on the type of the electrical machine. For a general overview, these losses are classified according to their physical origin as electrical losses, iron losses, mechanical losses and additional losses.

The ohmic losses are caused by the current I and the resistance R in the stator as well as the rotor winding and defined as

$$P_{co} = I^2 R . \quad (2.8)$$

Electric losses arise on the brushes, too, but there the voltage difference U_B is current dependent and the resistance is not linear:

$$P_B = U_B I . \quad (2.9)$$

The iron losses P_{ir} consist of hysteresis $P_{ir,hyst}$ and eddy current losses $P_{ir,eddy}$ and occur in the core in the rotor as well as in the stator due to alternating magnetization and depend on the frequency f linearly as $P_{ir,hyst} \sim f$. The eddy current losses depend on the square of the frequency as $P_{ir,eddy} \sim f^2$. All in all, the iron losses depend on the frequency f , the flux density B , an exponent β , the penetration depth δ and the material parameters k_{hyst} and k_{eddy} obtained from measurements or numerical simulations:

$$P_{ir} = P_{ir,hyst} + P_{ir,eddy} = k_{hyst} \cdot f \cdot B^\beta + k_{eddy} \cdot \delta^2 \cdot f^2 \cdot B^2. \quad (2.10)$$

Mechanical losses are divided into friction losses P_{fr} at the brushes and the bearing and windage losses P_w caused by ventilation. The windage losses are also known as dissipation losses and are much lower than the other losses. Dissipation is caused by internal friction and viscosity of the fluid and occurs when the kinetic energy of eddies gradually collapses into smaller eddies and finally turns into heat energy. Since dissipation losses are generated and included directly in the fluid, it is not necessary to transport these losses across the boundary.

The energy flow diagram in Fig. 2 shows the classification of losses in an electrical machine. The heat losses are stored in the material or removed with a coolant fluid using heat transfer methods to ensure acceptable operating conditions.

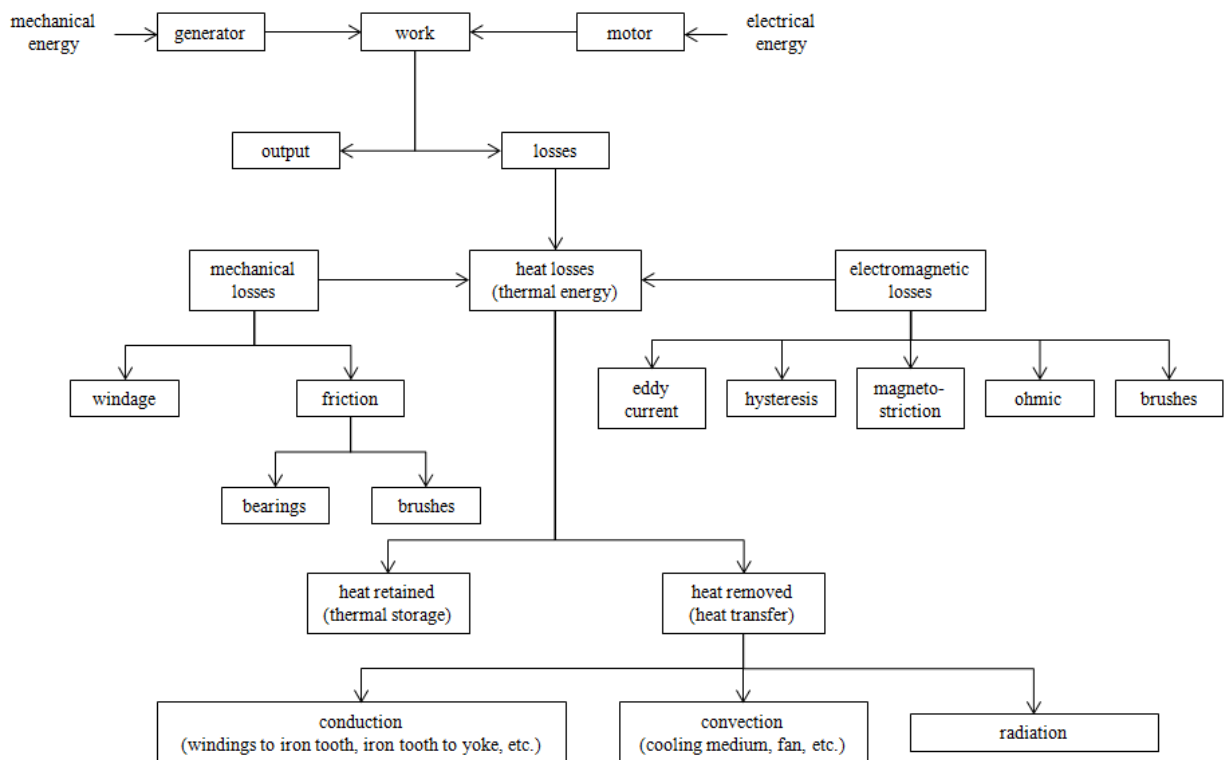


Fig. 2 Energy flow diagram in electrical machines [68]

2.1.4 Cooling methods

A rotating electrical machine is a non-homogenous heat exchanger with limitations in the temperature, tortuous conducting paths and thermal barriers. The arising heat losses have to be discharged to the environment either directly by a coolant or indirectly through a heat exchanger. Therefore, its thermal design involves electrical engineering, heat transfer, fluid dynamics and is connected to manufacture, measurements and specifications [68]. Furthermore, the over-

temperature in a machine can be controlled by a designed cooling method, the type of the medium to discharge the heat, the fluid flow conditions, the machine assembly as well as the materials between the heat source and the coolant. The categorization of the cooling methods can be divided into the design of the cooling circuits, the number of cooling circuits, the type of the cooling fluid and the conveying method of the coolant [68].

Different cooling methods are presented in Fig. 3 with regard to the standard of IEC 60034-6 [66]. If two cooling circuits are arranged in series, a distinction has to be made between a primary and secondary circuit with a primary and a secondary cooling fluid. The primary cycle discharges the heat directly from the different machine parts and the secondary cycle transports the heat from the primary cycle to the environment with a located heat exchanger. An open cooling circuit is characterized by a constantly renewed coolant taken from the immediate or close environment like ambient air or a water reservoir. In an alternative method, the coolant is circulated separated from the environment in what is called a closed circuit and the heat losses are transported from the primary to the secondary coolant in a heat exchanger. Machines without any cooling ducts or pipes for air inlet and outlet can only use the direct contact with the environment for surface cooling, a method known as free cooling circuit.

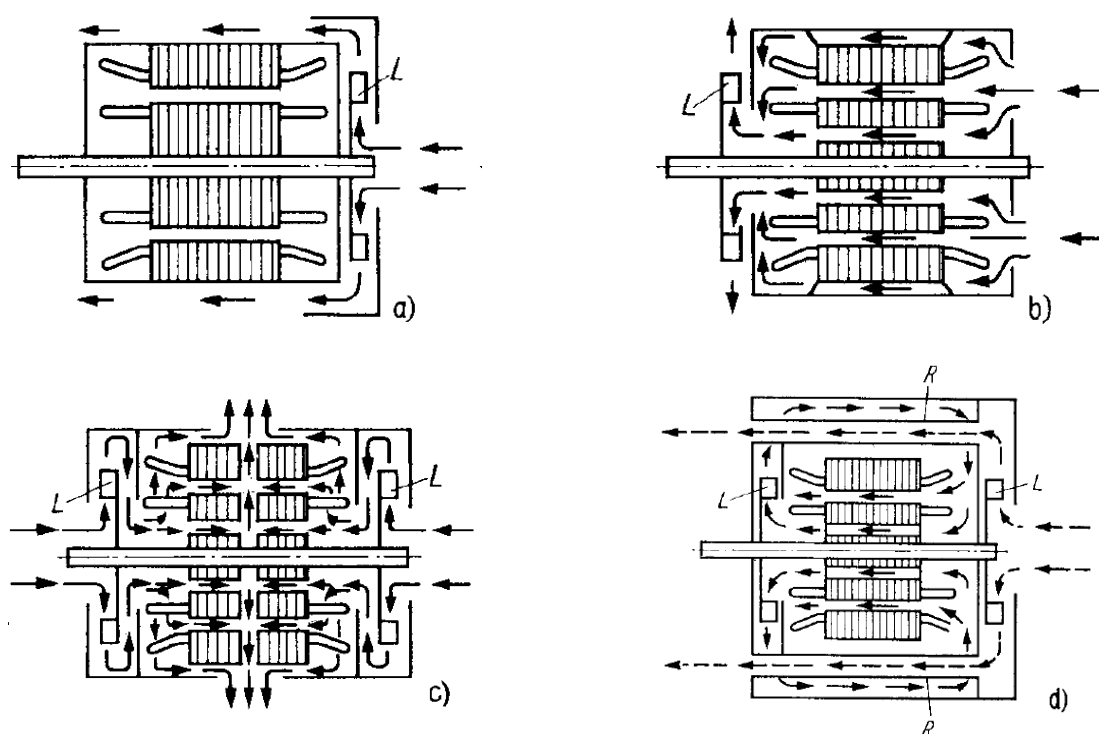


Fig. 3 Cooling circuits for small and medium size machines: (a) closed machines with surface cooling and outer radial fan (L) (cooling method IC 4A1A1), (b) machine with open cooling circuit including axial cooling ducts and a radial flow fan (L) (cooling method IC 0A1), (c) machine with open cooling circuit including axial and radial cooling ducts and two radial flow fans (L) (cooling method IC 0A1), (d) machine with a closed primary and an open secondary cooling circuit including radial cooling ducts with separated radial fans for each cycle (L) (cooling method IC 5A1A1) [1]

Regarding the cooling fluid, cooling methods can be classified as gas-cooled or liquid-cooled methods. In case of a gaseous coolant, the fan has the task to transport the medium through the electrical machine. These radial or axial fans can be mounted directly on the shaft (self-ventilation), or are driven by an external motor (external ventilation). Gaseous coolants are commonly used in small and medium size machines. The contamination of the transported gas by dust or moisture especially in large scale machines can be avoided by using a closed primary

circuit. Machines with hydrogen coolant are designed for high circumferential velocities in a closed and pressure resistant primary cycle. Beside the benefit of lower dissipation losses, the wall heat transfer coefficient in hydrogen cooled machines is about 50% higher than in air cooled machines and the operating conditions in a protective atmosphere reduces oxidation. Water is used as secondary coolant for a cooling method designed accordingly.

Liquids are usually transported with an external pump. Water, advantageous due to its high heat capacity, is used in directly cooled conductors where the coolant flows inside hollow conductors or in pipes beside.

Air is usually used as coolant in electrical machines due to limited space, weight and costs. Optimizing the cooling of such devices amounts to optimizing the air flow path through the machine driven by pressure. The ventilators providing the pressure can be conveniently designed for a specified single speed of rotor rotation and rotating direction. The ventilation design in case of changing operating conditions presents a problem, but this is not present in case of generators or motors with fixed operating conditions.

2.2 Heat transfer

The topic of heat transfer deals with the phenomena governing how energy is transported by various physical interactions between different systems. In the following chapter the main methods of the heat transfer will be described in detail. Therefore, the main attention will be paid to the question what is heat transfer and how can the energy be transported. The temperature gradient in or between different media is the driving force for the heat exchange. Heat transport is an energy transport caused by temperature gradient. Depending on the effect, there are three different means of heat transfer, namely conductive heat transfer, convective heat transfer and heat transfer by radiation.

2.2.1 Heat transfer by conduction

Heat conduction is an energy transport between neighboring molecules caused by the temperature gradient in the material. The energy is transported by conduction in solids impermeable to radiation. The heat conduction is overlapped by an energy transport due to the flowing movement (convection) and heat radiation in liquids or gases.

The energy transport in a conductive material can be described by the heat flux density vector \mathbf{q} as a function of the space variable \mathbf{x} and time t :

$$\mathbf{q} = \mathbf{q}(\mathbf{x}, t). \quad (2.11)$$

The direction of the heat flux is perpendicular to the isothermal lines, from higher to lower magnitude of temperature. The temperature gradient causes the heat flux in a conductive material and in addition to that the following proportionality between cause and effect can be drawn and the heat flux density can be described as [69]:

$$\mathbf{q} = -\lambda \text{grad}(T). \quad (2.12)$$

This equation is well known as the fundamental law of heat conduction discovered by Jean Baptiste Joseph Fourier. The negative sign considers the second law of thermodynamics: heat is transported in the direction of the temperature drop. The thermal conductivity λ is a material

property and is dependent on the temperature and pressure: $\lambda = \lambda(T, p)$. It is a scalar for isotropic materials, as for those listed in Table 2. The thermal conductivity depends on the molecular and atomic structure of the material. Due to the fundamental difference in the molecular distance in media in different phases, the relationship $\lambda_{solid} > \lambda_{liquid} > \lambda_{gas}$ holds.

material	λ in W / mK	material	λ in W / mK
silver	427	brickwork	0.5 ... 1.3
copper	399	water	0.598
aluminium 99.2%	209	air	0.0257
iron	81	CO ₂	0.0162

Table 2 Thermal conductivity of some materials at a temperature of 20 °C and a pressure of 100 kPa [70]

For materials, which consist of two or more different materials with different thermal conductivities arranged without spatial symmetry, anisotropy may occur when applying homogenization.

The sources of the heat flux density are constituted by the volume loss density p , so the heat conduction equation is:

$$\text{div}(\mathbf{q}) = -\text{div}(\lambda \text{grad}(T)) = p. \quad (2.13)$$

Definition of a thermal resistance

In the following, the definition of a thermal resistance will be explained on a simple example shown in Fig. 4. The heat flux density in x -direction can be computed as follows, by neglecting the heat flux in y - and z -direction:

$$q = -\lambda \frac{dT}{dx}, \quad (2.14)$$

$$q dx = -\lambda dT, \quad (2.15)$$

$$q \int_0^{\delta} dx = -\lambda \int_{T_1}^{T_2} dT, \quad (2.16)$$

$$q = \frac{\lambda}{\delta} (T_1 - T_2). \quad (2.17)$$

In writing (2.15), the one-dimensional form of (2.13) with zero right hand side has been used to imply that q is independent of x . This is justified by the fact that no volume loss density is present in the plate. Furthermore, the thermal conductivity is assumed to be independent of temperature. The limits of integration are shown in Fig. 4, the temperature at the left side ($x=0$) is T_1 and the temperature at the right face ($x=\delta$) is T_2 . Therefore, the heat flux for the flat plate with thickness δ , through a surface area A caused by a temperatures difference $T_1 - T_2$ can be computed as

$$Q = \frac{\lambda A}{\delta} (T_1 - T_2). \quad (2.18)$$

The quantity $\delta/\lambda A$ is a thermal resistance of the wall to the flow of heat by conduction:

$$R = \frac{\delta}{\lambda A}. \quad (2.19)$$

There is an analogy between heat flow systems and electric circuits, where the flow of electric current i is equal to the voltage (potential difference) $E_1 - E_2$ divided by the electrical resistance R_e . This analogy is a conventional tool, especially for visualizing more complex situations to be discussed in a later chapter.

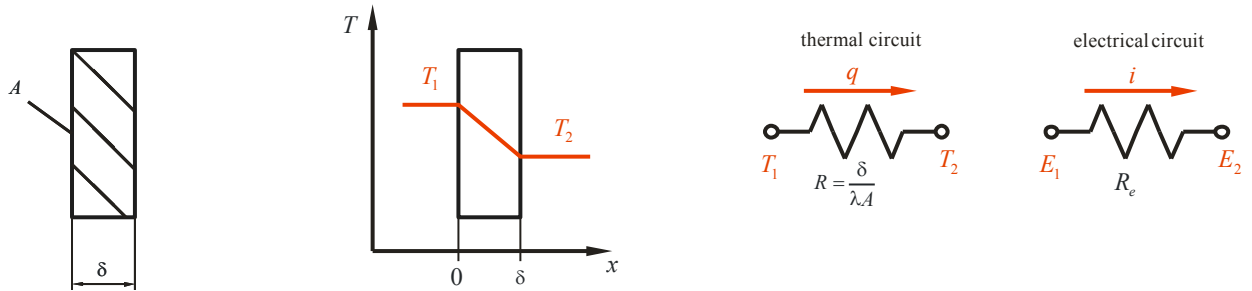


Fig. 4 Temperature distribution for steady state conduction through a plane wall and the analogy between thermal and electrical circuits [70]

2.2.2 Heat transfer by convection

Energy is not only transported by heat conduction in a fluid, but also by the macroscopic movement of the fluid itself. On the one hand, heat exchange by conduction occurs due to the temperature gradient and, on the other hand, the flow of enthalpy and kinetic energy results in energy transport as well. The superposition of heat conduction and energy transport due to the streaming fluid is called heat convection.

In many technical applications, the heat transfer between a cooling fluid and a solid wall is of interest. The efficiency of the convective heat transfer is influenced by the phenomena in a boundary layer, a model of which has been developed by Ludwig Prandtl [71]. The velocity profile changes from zero at the wall over a short distance in the boundary layer to the maximum value in the core flow as shown in Fig. 5. The heat transport from the solid material to the fluid starts with the conductive heat transport governed by Fourier's fundamental law at the boundary of the solid to the fluid. Hence, the convective heat transport depends on the value of the thermal conductivity λ of the fluid and the heat flux density q_w can be expressed directly at the wall as:

$$q_w = -\lambda \left(\frac{\partial T}{\partial y} \right)_{y=0}. \quad (2.20)$$

In the next step, the solution of the energy equation on the fluid side is needed, a quite difficult task. To simplify it, an analytical approach is used to compute the heat flux density as the product of the temperature difference between wall and fluid and a factor called wall heat transfer coefficient α . This is known as the Newtonian cooling law [72]:

$$q_w = \alpha (T_w - T_\infty). \quad (2.21)$$

For complex surfaces or turbulent flow conditions, α cannot be computed analytically and has to be found empirically or by numerical methods. It follows from (2.20) and (2.21) that

$$\alpha = -\lambda \frac{\left(\frac{\partial T}{\partial y}\right)_{y=0}}{T_w - T_\infty}. \quad (2.22)$$

The ratio λ/α hence depends on the slope of the temperature profile next to the surface and it characterizes the thickness of the thermal boundary layer $\delta_t \approx \lambda/\alpha$. The efficiency of the heat transfer is high if α is large and related to that δ_t is small.

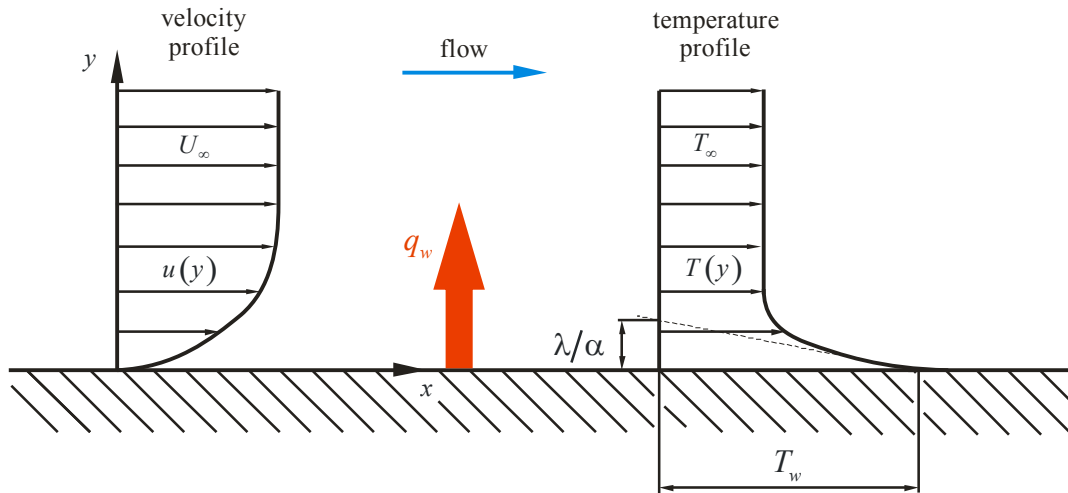


Fig. 5 Velocity and temperature profile for convection heat transfer from a heated plate with flow over its surface [70]

The wall heat transfer coefficient depends on the flow conditions and the physical properties of the fluid. It is mainly used as a mean value for a specific surface, if its value at a specific point is meant, the coefficient is denoted by α_x . Some examples for the magnitude of the wall heat transfer coefficient are shown in Table 3.

fluid	flow condition	α in W / m ² K
air	free convection	6 - 30
superheated steam or air	forced convection	30 - 300
oil	forced convection	60 - 1800
water	forced convection	300 - 18000
water	boiling	3000 - 60000
steam	condensing	6000 - 120000

Table 3 Magnitude of the convective heat transfer coefficients in typical cases [70]

2.2.3 Heat transfer by radiation

The quantity of energy leaving a surface as radiant heat depends on the absolute temperature and the nature of the surface. Each body emits energy carried by electromagnetic waves in and close to the infrared spectrum of light to the environment caused by the surface temperature, an effect called radiation. The emission caused by radiative heat transfer changes with the fourth power of the surface temperature T of the emitted body. The maximum heat flux density q_r on the surface of a body is given as

$$q_r = \sigma T^4. \quad (2.23)$$

This relationship is known as the Stefan Boltzman law, with the Stefan Boltzman constant given as $\sigma = 5.671 \cdot 10^{-8} \text{ W / m}^2 \text{ K}^4$ for ideally absorbed radiation. The material properties of the surface have to be considered by the inclusion of the emission coefficient ε for emitted radiation and the absorption coefficient a for absorbed radiation, respectively:

$$q_{r,em} = \varepsilon(T) \sigma T^4, \quad (2.24)$$

$$q_{r,ab} = a \sigma T^4. \quad (2.25)$$

In most technical applications, the processes of emission and absorption appear simultaneously and the total balance of exchanged power is of interest. For an emitting body with temperature T surrounded by an environment with temperature T_e , the resulting balance of power can be written with the surface area A as

$$Q = Q_{em} - Q_{ab} = A\sigma(\varepsilon T^4 - a T_e^4). \quad (2.26)$$

In most applications, the use of a gray body in a black environment is sufficient, when the absorption coefficient a can be assumed to be equal to the emission coefficient ε :

$$Q = Q_{em} - Q_{ab} = A\sigma\varepsilon(T^4 - T_e^4). \quad (2.27)$$

If the heated body is surrounded by a fluid, convective heat transfer occurs in addition to radiation and has to be considered in the overall heat flux density:

$$q = q_c + q_r = \alpha(T - T_\infty) + \varepsilon\sigma(T^4 - T_e^4) = (\alpha + \alpha_r)(T - T_e). \quad (2.28)$$

In many cases, the environmental temperature on the surface T_e and the temperature of the air T_∞ can be assumed to be equal. This leads to the expression of the heat transfer coefficient by radiation:

$$\alpha_r = \varepsilon\sigma \frac{T^4 - T_e^4}{T - T_e}. \quad (2.29)$$

The conclusion to be drawn from this equation is that the radiation heat flux depends on the fourth power of the temperature difference and has hence to be considered if the surface temperature is very high or the simultaneously arising convective heat transfer is very small, e.g. in case of buoyant convection [73].

2.3 Fluid dynamics

The convective heat transport is determined by the flow field and the fluid properties. The flow conditions can be described by the fundamental laws of fluid dynamics detailed in this section based on [74].

2.3.1 Fluid and viscosity

A fluid is considered as a continuum and its phase can be liquid (intermolecular interacting forces) or gaseous (no intermolecular interacting forces). This hypothesis including the resulting laws of continuum mechanics, are presented in [75].

Fluid mechanics deals with the behavior of fluids, i.e. media unlimitedly deformable under the influence of shear forces. The shear stress can be explained on the example shown in Fig. 6. The fluid flow is considered between two parallel flat plates at a constant distance h . The fluid adheres at the bottom plane with the effect that the velocity is 0 at $y=0$ and U at $y=h$. In between, the velocity distribution is linear and

$$u(y) = \frac{y}{h}U \quad (2.30)$$

holds.

Due to the constant force F , the plate moves with constant velocity U in the same direction and causes a shear stress τ in the fluid. If there is no other force acting on the fluid, the shear stress in the fluid is constant in every plane parallel to the plates from $y=0$ to h . Experiments on technically relevant fluids, e.g. air and water, have demonstrated that the shear stress and the velocity gradient are proportional and the Newtonian friction law for fluid friction is given by

$$\tau(y) = \mu \frac{du}{dy}. \quad (2.31)$$

The dynamic viscosity μ is a material parameter depending on the temperature. Equation (2.31) says that a fluid cannot sustain shear stress in rest, a condition defining the fluid as Newtonian.

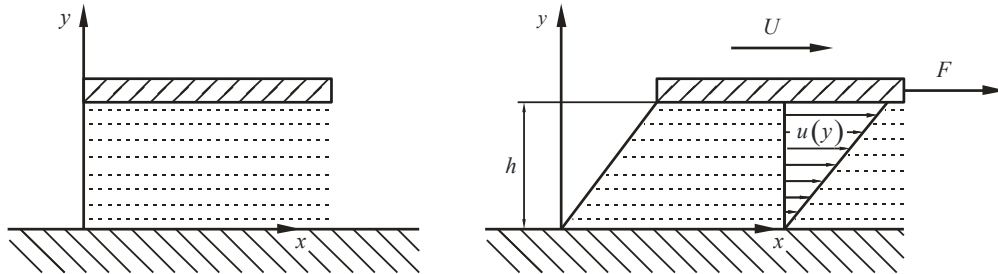


Fig. 6 Shear and related velocity distribution of a viscous fluid between two parallel flat plates [72]

2.3.2 Governing equations of fluid flow and heat transfer

The governing equations of fluid flow represent mathematical statements of the conservation laws of physics:

- The mass of a fluid is conserved
- The rate of change of momentum equals the sum of the forces on a fluid particle
- The rate of change of energy is equal to the sum of the rate of heat in addition to the rate of work done on a fluid particle

2.3.2.1 Conservation of mass

The mass flow rate across a face of a fluid element shown in Fig. 7 is given by the product of the density ρ , the area and the velocity component normal to the face. The rate of increase of mass inside the fluid element is equal to the net rate of flow of mass into the element across its face. This yields

$$\frac{\partial \rho}{\partial t} + \text{div}(\rho \mathbf{u}) = 0 \quad (2.32)$$

where \mathbf{u} is the velocity vector with components u , v and w . The unsteady, three-dimensional mass conservation or continuity equation at a point in a compressible fluid is defined by equation (2.32). The first term on the left hand side is the rate of change in time of the density and the second convective term describes the net flow of mass out of the element across its boundaries.

For an incompressible fluid, i.e. liquid, the density ρ is constant and the equation becomes

$$\text{div}(\mathbf{u}) = 0. \quad (2.33)$$

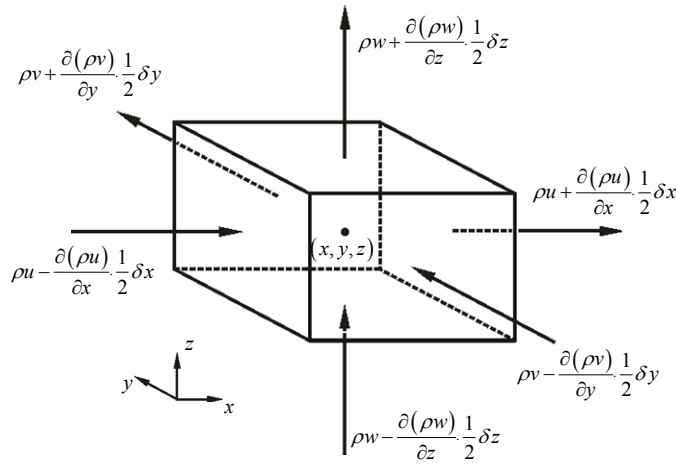


Fig. 7 Mass flows in and out of a fluid element [74]

2.3.2.2 Rates of change for a fluid particle and for a fluid element

The following momentum and energy conservation laws make statements about the changes in the properties of a fluid particle, a methodology called the Lagrangian approach. Each property of the particle is a function of time t and the position (x, y, z) . The value characterizing the property per unit mass is denoted by ϕ . The total derivative of ϕ with respect to time following a particle, called substantive derivative and written as $D\phi/Dt$, is

$$\frac{D\phi}{Dt} = \frac{\partial \phi}{\partial t} + \frac{\partial \phi}{\partial x} \frac{dx}{dt} + \frac{\partial \phi}{\partial y} \frac{dy}{dt} + \frac{\partial \phi}{\partial z} \frac{dz}{dt}. \quad (2.34)$$

Thereby, the fluid particle follows the flow, so $dx/dt = u$, $dy/dt = v$ and $dz/dt = w$. Hence the substantive derivative is given by

$$\frac{D\phi}{Dt} = \frac{\partial \phi}{\partial t} + u \frac{\partial \phi}{\partial x} + v \frac{\partial \phi}{\partial y} + w \frac{\partial \phi}{\partial z} = \frac{\partial \phi}{\partial t} + \mathbf{u} \cdot \text{grad} \phi. \quad (2.35)$$

Based on this Lagrangian approach, i.e. by tracking the motion and computing the rates of change of conserved properties ϕ for collections of fluid particles, it is possible to develop numerical models for fluid flow calculations. However, it is more common to develop equations for collections of fluid elements making up a region fixed in space, e.g. a duct region, a methodology called the Eulerian approach.

As in case of the mass conservation equation, the equations for rates of change per unit volume are of interest. The rate of change of a property ϕ per unit volume for a fluid particle is the product of $D\phi/Dt$ and the density ρ :

$$\rho \frac{D\phi}{Dt} = \rho \left(\frac{\partial \phi}{\partial t} + \mathbf{u} \cdot \text{grad} \phi \right). \quad (2.36)$$

The relationship between the substantive derivative of ϕ and rate of change of ϕ for a fluid element is developed below.

The generalization of the mass conservation for an arbitrary conserved property is

$$\frac{\partial(\rho\phi)}{\partial t} + \text{div}(\rho\phi\mathbf{u}) = 0. \quad (2.37)$$

This equation expresses the rate of change in time of ϕ per unit volume plus the net flow of ϕ out of the fluid element per unit volume. It is now rewritten to emphasize the relationship with the substantive derivative of ϕ :

$$\frac{\partial(\rho\phi)}{\partial t} + \text{div}(\rho\phi\mathbf{u}) = \rho \left[\frac{\partial \phi}{\partial t} + \mathbf{u} \cdot \text{grad} \phi \right] + \phi \left[\frac{\partial \rho}{\partial t} + \text{div}(\rho\mathbf{u}) \right] = \rho \frac{D\phi}{Dt} \quad (2.38)$$

This relationship states, that the rate of increase of ϕ of the fluid element and the net rate of flow of ϕ out of the fluid element equals the rate of increase of ϕ for a fluid particle.

The components of the momentum and energy equations with the relevant quantity replacing ϕ are given below:

$$\begin{array}{llll} x\text{-momentum:} & u & \rho \frac{Du}{Dt} & \frac{\partial(\rho u)}{\partial t} + \text{div}(\rho u \mathbf{u}) \end{array} \quad (2.39)$$

$$\begin{array}{llll} y\text{-momentum:} & v & \rho \frac{Dv}{Dt} & \frac{\partial(\rho v)}{\partial t} + \text{div}(\rho v \mathbf{u}) \end{array} \quad (2.40)$$

$$\begin{array}{llll} z\text{-momentum:} & w & \rho \frac{Dw}{Dt} & \frac{\partial(\rho w)}{\partial t} + \text{div}(\rho w \mathbf{u}) \end{array} \quad (2.41)$$

$$\begin{array}{llll} \text{energy:} & E & \rho \frac{DE}{Dt} & \frac{\partial(\rho E)}{\partial t} + \text{div}(\rho E \mathbf{u}) \end{array} \quad (2.42)$$

where E denotes the energy.

2.3.2.3 Conservation of momentum

Newton's second law states that the rate of change of momentum of a fluid particle equals the sum of the forces \mathbf{f}_i on the particle, i.e.

$$\rho \frac{D\mathbf{u}}{Dt} = \sum_i \mathbf{f}_i. \quad (2.43)$$

The rates of increase of the x -, y - and z -momentum per unit volume of a fluid particle are given by (2.39) - (2.41). The forces on fluid particles can be classified as surface forces and body forces. Centrifugal forces, Lorenz forces or the gravitational force are body forces $\mathbf{f}_i^B = \rho \mathbf{g}$, with the acceleration vector \mathbf{g} .

The pressure and viscous forces are surface forces \mathbf{f}_i^S and can be described by tensors. It is common practice to highlight the contributions due to the surface forces as separate terms in the momentum equation and to include the effects of body forces as source terms.

The stress σ_{xx} is perpendicular to the face of the control volume in the yz plane and the shear stresses τ_{yx} and τ_{zx} on the yx plane and zx planes. Therefore the stress tensor is defined as

$$\boldsymbol{\sigma} = \begin{pmatrix} \sigma_{xx} & \tau_{yx} & \tau_{zx} \\ \tau_{xy} & \sigma_{yy} & \tau_{zy} \\ \tau_{xz} & \tau_{yz} & \sigma_{zz} \end{pmatrix}. \quad (2.44)$$

If $\mathbf{u} = 0$, i.e. the fluid is at rest, then the shear stress is zero and the principle stress is equal to the hydrostatic pressure p , which can be separated from the principle stresses σ_{xx} , σ_{yy} and σ_{zz} in the stress tensor $\boldsymbol{\sigma}$ leaving the stress tensor $\boldsymbol{\tau}$:

$$\boldsymbol{\tau} = \boldsymbol{\sigma} - p\mathbf{I}_n = \begin{pmatrix} \sigma_{xx} & \tau_{yx} & \tau_{zx} \\ \tau_{xy} & \sigma_{yy} & \tau_{zy} \\ \tau_{xz} & \tau_{yz} & \sigma_{zz} \end{pmatrix} - \begin{pmatrix} p & 0 & 0 \\ 0 & p & 0 \\ 0 & 0 & p \end{pmatrix} = \begin{pmatrix} \tau_{xx} & \tau_{yx} & \tau_{zx} \\ \tau_{xy} & \tau_{yy} & \tau_{zy} \\ \tau_{xz} & \tau_{yz} & \tau_{zz} \end{pmatrix}, \quad (2.45)$$

with the identity tensor \mathbf{I}_n . Hence, the surface forces can be written as,

$$\mathbf{f}_i^S = \text{div}(\boldsymbol{\tau}). \quad (2.46)$$

The pressure p , a normal stress, and the components of the viscous stress τ define the state of stress in the fluid elements, as illustrated in Fig. 8a. In the suffix notation used, τ_{ij} indicates the stress acting in j -direction on a surface normal to the i -direction. Considering the x -components on right hand side only, the forces due to pressure and stress components are shown in the figure. The net force in x -direction is the sum of the force components acting in that direction on the fluid element.

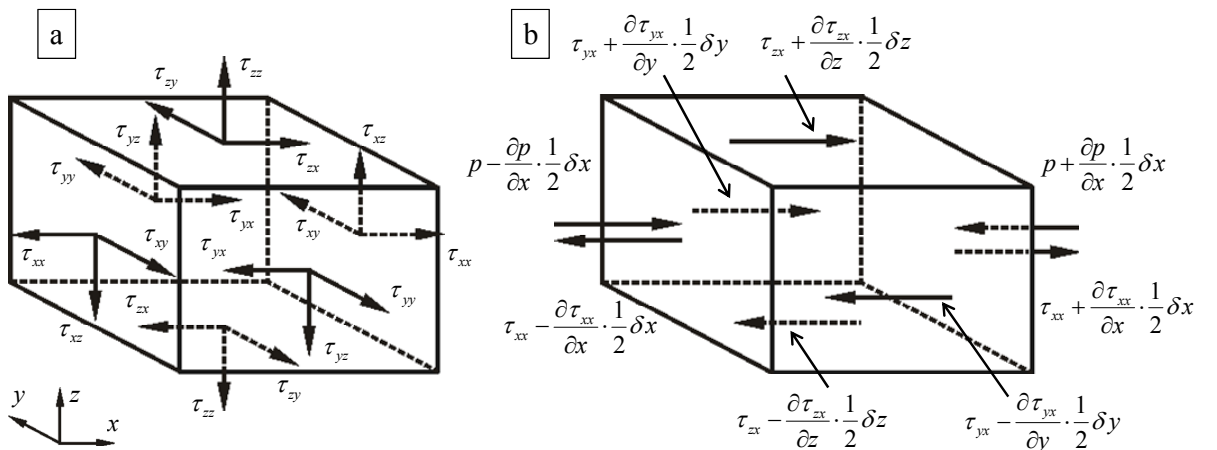


Fig. 8: (a) Stress components on faces of fluid element; (b) Stress components on the x -direction [74]

The total force per unit volume on the fluid due these surface stresses is equal to the sum of each surface pair divided by the volume $\delta x \delta y \delta z$:

$$\frac{\partial(-p + \tau_{xx})}{\partial x} + \frac{\partial \tau_{yx}}{\partial y} + \frac{\partial \tau_{zx}}{\partial z}. \quad (2.47)$$

Considering the body forces in further detail, their effect can be included by defining a source term S_{Mx} of x -momentum per unit volume and per unit time.

Thereupon, the x -component of the momentum equation is found by setting the rate of change of the x -momentum of the fluid particle equal to the total force on the element due to surface stresses plus the rate of increase of the x -momentum on surfaces:

$$\frac{\partial(\rho u)}{\partial t} + \text{div}(\rho u \mathbf{u}) = \frac{\partial(-p + \tau_{xx})}{\partial x} + \frac{\partial \tau_{yx}}{\partial y} + \frac{\partial \tau_{zx}}{\partial z} + f_x^B. \quad (2.48)$$

The same can be verified for the y -component of the momentum equation given by

$$\frac{\partial(\rho v)}{\partial t} + \text{div}(\rho v \mathbf{u}) = \frac{\partial \tau_{xy}}{\partial x} + \frac{\partial(-p + \tau_{yy})}{\partial y} + \frac{\partial \tau_{zx}}{\partial z} + f_y^B \quad (2.49)$$

and the z -component of the momentum equation by

$$\frac{\partial(\rho w)}{\partial t} + \text{div}(\rho w \mathbf{u}) = \frac{\partial \tau_{xz}}{\partial x} + \frac{\partial \tau_{yz}}{\partial y} + \frac{\partial(-p + \tau_{zz})}{\partial z} + f_z^B. \quad (2.50)$$

Using vector notation, the momentum conservation can be written as

$$\rho \frac{D\mathbf{u}}{Dt} = -\text{grad}(p) + \text{div}(\boldsymbol{\tau}) + \mathbf{f}^B. \quad (2.51)$$

2.3.2.4 Conservation of energy

The energy equation is derived from the first law of thermodynamics stating that energy cannot be created or destroyed, similar to mass conservation. The conservation of energy of the fluid particle is expressed by equating the rate of change of energy of the fluid particle to the sum of the net rate of work done on the fluid particle, the net rate of heat addition to the fluid and the rate of increase of energy due to sources. This can be expressed by the following equation:

$$\begin{aligned} \frac{\partial(\rho E)}{\partial t} + \text{div}(\rho E \mathbf{u}) &= \rho \mathbf{f}^B \cdot \mathbf{u} - \text{div}(p \mathbf{u}) \\ + \frac{\partial}{\partial x}(u \tau_{xx} + v \tau_{xx} + w \tau_{xz}) &+ \frac{\partial}{\partial y}(u \tau_{yx} + v \tau_{yx} + w \tau_{yz}) + \frac{\partial}{\partial z}(u \tau_{zx} + v \tau_{zx} + w \tau_{zz}) - \text{div}(\mathbf{q}) + \mathbf{Q}_q. \end{aligned} \quad (2.52)$$

The total energy E comprises the inner energy i and the kinetic energy including the Euclidean norm of the velocity vector $V = \|\mathbf{u}\|_2$ expressed as [76]:

$$E = i + \frac{V^2}{2}. \quad (2.53)$$

The kinetic and inner energy are included on the left hand side of equation (2.52). On the right hand side of this equation, the power of the body forces $\rho \mathbf{f}^B \mathbf{u}$, the surface forces

$-\text{div}(\rho \mathbf{u}) + \frac{\partial}{\partial x}(\dots) + \frac{\partial}{\partial y}(\dots) + \frac{\partial}{\partial z}(\dots)$, the transported heat energy over the system boundaries $\text{div}(\mathbf{q})$ and the inner energy source \mathbf{Q}_q appear.

2.3.3 Equation of thermodynamic state

The motion of a fluid in three dimensions is described by a system of five partial differential equations (2.48)-(2.52) as detailed above. Among the unknowns are four thermodynamic variables, namely density ρ , pressure p , inner energy i and temperature T .

The relationship between these thermodynamic variables can be obtained by the assumption of thermodynamic equilibrium [77]. The state of a substance can be described in thermodynamic equilibrium by means of just two state variables. Equations of state relate the other used variables to the two state variables. If ρ and T are used for the state variables the following state equations can be obtained for p and i :

$$p = p(\rho, T) \quad \text{and} \quad i = i(\rho, T). \quad (2.54)$$

The well-known state equation for an ideal gas expresses the pressure with the ideal gas constant R and the specific heat capacity at constant volume c_v :

$$p = \rho RT \quad \text{and} \quad i = c_v T. \quad (2.55)$$

Using the assumption of thermodynamic equilibrium, all but two thermodynamic state variables are eliminated. In case of compressible fluid flow, the state equations provide the link between the energy equation on the one hand and the mass conservation and momentum equations on the other. Furthermore, liquids and gases flowing at low speeds behave as incompressible fluids. Without density variations, there is no linkage between the conservation equations. Therefore, the flow field can be solved by considering the mass conservation and the momentum equations only. The energy equation has to be solved when investigating heat transfer problems.

2.3.4 Equations for viscous flow – the Navier-Stokes equations

A viscous flow includes different transport phenomena of friction, thermal conduction, and mass diffusion. The equations derived and discussed up to this point apply to a viscous flow, with the exception that mass diffusion is not included. Mass diffusion occurs, if there are concentration gradients of different chemical species in the flow. The governing equations contain as further unknowns the viscous stress components τ_{ij} . In three dimensional flows, the local rate of deformation is composed of the linear deformation rate and the volumetric deformation rate. However, the computation of the eleven scalar unknowns $\boldsymbol{\tau}$, p , ρ and \mathbf{u} with the mass conservation and the three momentum equations is not possible. Therefore, a connection between the shear stress components τ_{ij} and the flow field \mathbf{u} has to be defined.

In a Newtonian fluid, the viscous stresses are proportional to the rates of deformation. The three dimensional form of Newton's law of viscosity for compressible flows involves two constants of proportionality, the (first) viscosity μ , to relate stresses to linear deformations, and the second viscosity μ_2 , to relate stresses to the volumetric deformation [74]. Not much is known

about the second viscosity μ_2 , because its effect is small in practice. For gases, a good approximation can be obtained by taking the value $\mu_2 = -\frac{2}{3}\mu$, as shown in [74].

The nine viscous stress components, of which six are independent, can be obtained by introducing Stoke's law for frictional force:

$$\begin{aligned}\tau_{xx} &= \mu \left[2 \frac{\partial u}{\partial x} - \frac{2}{3} \operatorname{div}(\mathbf{u}) \right], & \tau_{xy} &= \tau_{yx} = \mu \left[\frac{\partial u}{\partial y} + \frac{\partial v}{\partial x} \right], \\ \tau_{yy} &= \mu \left[2 \frac{\partial v}{\partial y} - \frac{2}{3} \operatorname{div}(\mathbf{u}) \right], & \tau_{yz} &= \tau_{zy} = \mu \left[\frac{\partial v}{\partial z} + \frac{\partial w}{\partial y} \right], \\ \tau_{zz} &= \mu \left[2 \frac{\partial w}{\partial z} - \frac{2}{3} \operatorname{div}(\mathbf{u}) \right], & \tau_{zx} &= \tau_{xz} = \mu \left[\frac{\partial w}{\partial x} + \frac{\partial u}{\partial z} \right].\end{aligned}\quad (2.56)$$

Substitution of these shear stresses into (2.48), (2.49) and (2.50) yields the Navier-Stokes equations:

$$\frac{\partial(\rho u)}{\partial t} + \operatorname{div}(\rho u \mathbf{u}) = -\frac{\partial p}{\partial x} + \operatorname{div}[\mu \operatorname{grad}(u)] + f_x^B \quad (2.57)$$

$$\frac{\partial(\rho v)}{\partial t} + \operatorname{div}(\rho v \mathbf{u}) = -\frac{\partial p}{\partial y} + \operatorname{div}[\mu \operatorname{grad}(v)] + f_y^B \quad (2.58)$$

$$\frac{\partial(\rho w)}{\partial t} + \operatorname{div}(\rho w \mathbf{u}) = -\frac{\partial p}{\partial z} + \operatorname{div}[\mu \operatorname{grad}(w)] + f_z^B \quad (2.59)$$

Using these equations, an exact solution can be achieved for specific cases of laminar fluid flow.

If we use this Newtonian model for viscous stresses in the energy equations, we obtain

$$\frac{\partial(\rho i)}{\partial t} + \operatorname{div}(\rho i \mathbf{u}) = \rho \mathbf{f}^B \cdot \mathbf{u} - \operatorname{div}(p \mathbf{u}) + \Phi - \operatorname{div}(\mathbf{q}) + \mathbf{Q}_q. \quad (2.60)$$

The dissipation function Φ describes all arising effects due to viscous stresses in the internal energy and is extracted from the mechanical agency and converted into internal energy or heat:

$$\Phi = \mu \left\{ 2 \left[\left(\frac{\partial u}{\partial x} \right)^2 + \left(\frac{\partial v}{\partial y} \right)^2 + \left(\frac{\partial w}{\partial z} \right)^2 \right] + \left(\frac{\partial u}{\partial y} + \frac{\partial v}{\partial x} \right)^2 + \left(\frac{\partial u}{\partial z} + \frac{\partial w}{\partial x} \right)^2 + \left(\frac{\partial v}{\partial z} + \frac{\partial w}{\partial y} \right)^2 \right\}. \quad (2.61)$$

2.3.5 Characteristic dimensionless numbers in fluid dynamics

Experiments show that fluids with low viscosity and large characteristic length scales have similar flow conditions to fluids with high viscosity and small characteristics length scales.

This result is the basis for the introduction of various dimensionless numbers in fluid dynamics. One is the Reynolds number, which is proportional of the ratio of inertial forces to viscous forces [76]. The Reynolds number is defined by the fluid velocity u_∞ , the characteristic length L and the kinematic viscosity of the fluid ν :

$$Re = \frac{u_\infty L}{\nu} = \frac{u_\infty \rho L}{\mu}. \quad (2.62)$$

This variable is often used to indicate whether a flow is laminar or turbulent, e.g. in a pipe flow, a Reynolds number $Re < 2300$ indicates a laminar flow [79]. The relation between the flow and thermal fields is defined with the aid of the Prandtl number

$$Pr = \frac{\mu c_p}{\lambda} \quad (2.63)$$

where c_p denotes the specific heat capacity and λ the thermal conductivity.

The temperature field can be characterized with the Eckert number as

$$Ec = \frac{u_\infty^2}{c_p \Delta T} \quad (2.64)$$

e.g. for supersonic flows involving flow conditions with arising dissipation, where ΔT is the temperature difference between surface and environment. For fluid flows with low velocity and driven by the acceleration of gravity g as well as local change of density ρ , the Grashof number gains importance, characterized by the volumetric thermal expansion coefficient β :

$$Gr = \frac{g \beta L^3 \Delta T}{\nu^2}. \quad (2.65)$$

For heat transfer problems, the Nusselt number is relevant to characterize the ratio between heat flux density and the theoretical heat flux density by conduction [72]. The Nusselt number is defined with the thermal conductivity of the fluid λ as follows:

$$Nu = \frac{\alpha L}{\lambda}. \quad (2.66)$$

Investigating the temperature field inside a solid domain, the Biot number is useful. It is defined similarly to the Nusselt number by the heat transfer coefficient α , the characteristic length L and the thermal conductivity of the solid domain λ :

$$Bi = \frac{\alpha L}{\lambda}. \quad (2.67)$$

The ratio between compressive force (pressure) and inertial force is known as the Euler number, determined by pressure p , density ρ and fluid velocity u_∞ :

$$Eu = \frac{p}{\rho u_\infty^2}. \quad (2.68)$$

2.3.6 Boundary layer

In the following, a laminar steady state fluid flow is under consideration. As mentioned before, the non slip condition is valid at the boundary, i.e. the fluid velocity is zero for $y \rightarrow 0$ at the wall. Then, the velocity rises with the distance y to the surface until it reaches the value U_∞ . In outer regions, the flow condition is not influenced by the examined surface. The velocity boundary layer $\delta(x)$ is defined by the position where the velocity profile $u(y)$ reaches the value of the outer flow U_∞ . The velocity boundary layer is shown in Fig. 9, marked by a blue line.

The thermal boundary layer $\delta_t(x)$ is defined in a manner similar to the velocity boundary layer $\delta(x)$. The fluid temperature at the surface equals the surface temperature $T(y \rightarrow 0) = T_w$. As

shown in Fig. 9, the thermal boundary layer is marked by the red line for the condition $T_w > T_\infty$, the fluid temperature reaches the temperature of the outer flow T_∞ asymptotically.

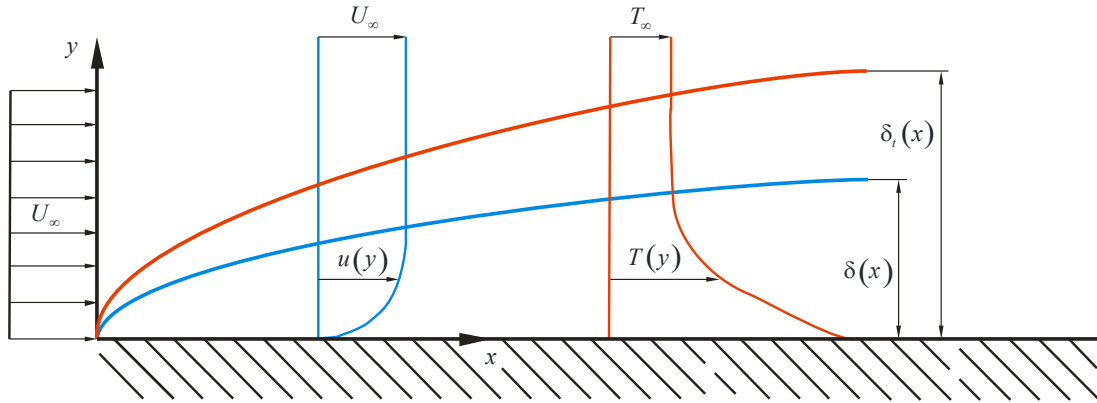


Fig. 9 Velocity and thermal boundary layer in a laminar steady state fluid flow [70]

The thermal and velocity boundary layers do not have the same thickness. The ratio of the thickness of the boundary layer is proportional to the square root of the Prandtl number [78]:

$$\frac{\delta}{\delta_t} \sim \sqrt{Pr} . \quad (2.69)$$

The mathematically and physically exact assumption for the boundary layer is the asymptotic approach of $u(y \rightarrow \infty) = U_\infty$. Since the exact boundary layer would not be finite when using this definition, a specified value of $0.99 \cdot U_\infty$ is conventionally selected as margin of the boundary layer [80].

2.3.7 Turbulent flow

The Navier-Stokes equations can be used to calculate the laminar flow under various conditions, but they fail when the fluid flow is turbulent. The motion becomes intrinsically unsteady even with constant imposed boundary conditions. The velocity and all other flow properties vary in a random and chaotic way and this characteristic regime is called turbulent flow. As shown in Fig. 10, the velocity \mathbf{u} can be split into a time averaged value $\bar{\mathbf{u}}$ and a fluctuating value \mathbf{u}' in the form $\mathbf{u} = \bar{\mathbf{u}} + \mathbf{u}'$. The behavior of the velocity u in the x direction can be described as follows:

$$u(x,t) = \bar{u}(x,t) + u'(x,t) . \quad (2.70)$$

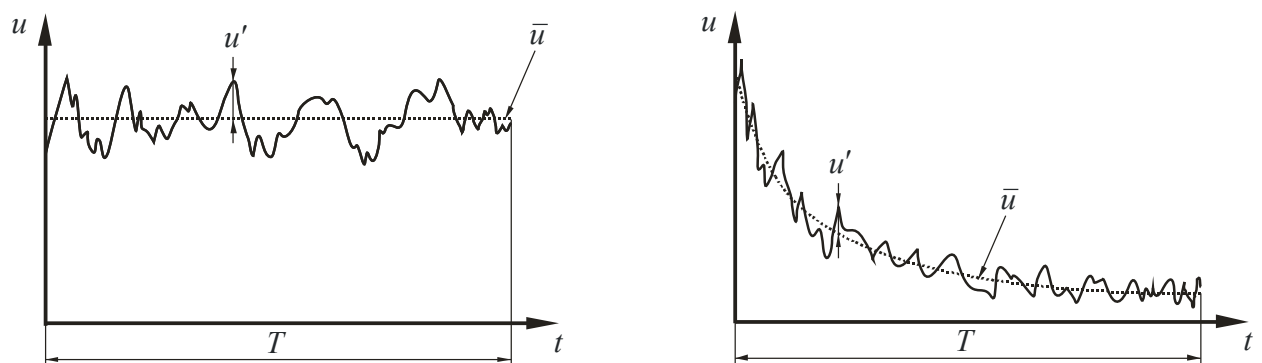


Fig. 10 Velocity measurement at a typical point in turbulent flow for steady state flow (left) and transient flow (right) [74]

In turbulent flow regimes, stochastically oscillating lateral and longitudinal movements relative to the mean flow of the particles require mechanical energy for permanent acceleration and deceleration. A transformation from kinetic into thermal energy is caused by the exchange of momentum and recurrent partial elastic deformation of fluid particles in the fluid, a phenomenon called dissipation. The isotropic dissipation rate is defined in [78] as

$$\varepsilon = \nu \left[\overline{\left(\frac{\partial u'}{\partial x}\right)^2} + \overline{\left(\frac{\partial v'}{\partial x}\right)^2} + \overline{\left(\frac{\partial w'}{\partial x}\right)^2} + \overline{\left(\frac{\partial u'}{\partial y}\right)^2} + \overline{\left(\frac{\partial v'}{\partial y}\right)^2} + \overline{\left(\frac{\partial w'}{\partial y}\right)^2} + \overline{\left(\frac{\partial u'}{\partial z}\right)^2} + \overline{\left(\frac{\partial v'}{\partial z}\right)^2} + \overline{\left(\frac{\partial w'}{\partial z}\right)^2} \right]. \quad (2.71)$$

The fluid has a higher shear stress and hence a higher viscosity in turbulence than under laminar flow conditions caused by the resulting additional flow resistance characterized by the turbulent wall shear stress τ_t , expressed for a fluid flow with the velocity u in x -direction as

$$\tau_t = \mu_t \frac{\partial u}{\partial y}. \quad (2.72)$$

The turbulent viscosity μ_t depends on the local flow conditions and is a parameter of momentum exchange. The eddy viscosity ν_t is used for numerical computations and is defined as

$$\nu_t = \frac{\mu_t}{\rho}. \quad (2.73)$$

The acceleration of fluid particles is a form of kinetic energy and is expressed by the turbulence kinetic energy k with the averaged velocity components for each Cartesian direction:

$$k = \frac{\overline{u'^2} + \overline{v'^2} + \overline{w'^2}}{2}. \quad (2.74)$$

For fluid boundary conditions, a frequently used expression is the turbulence intensity I_t :

$$I_t = \frac{u'}{u}. \quad (2.75)$$

2.3.8 Reynolds Averaged Navier-Stokes (RANS) equations

Next, the consequences of turbulent fluctuations for the mean flow equations are examined. To this end, the variables are replaced by time averaged and fluctuating ones and, assuming that the time average of each fluctuating variable is zero, the rules for calculating with averaged values are:

$$\overline{a+b} = \bar{a} + \bar{b}, \quad \overline{\bar{a}} = \bar{a}, \quad \overline{ab} = \bar{a}\bar{b}, \quad \overline{\frac{\partial a}{\partial s}} = \frac{\partial \bar{a}}{\partial s}. \quad (2.76)$$

Using these rules, the continuity and Reynolds Averaged Navier-Stokes equations can be expressed as follows:

$$\frac{\partial \rho}{\partial t} + \text{div}(\rho \bar{\mathbf{u}}) = 0, \quad (2.77)$$

$$\begin{aligned} \frac{\partial(\rho\bar{u})}{\partial t} + \text{div}(\rho\bar{u}\bar{\mathbf{u}}) = \\ -\frac{\partial\bar{p}}{\partial x} + \text{div}[\mu \text{grad}(\bar{u})] - \frac{\partial(\rho\bar{u}'^2)}{\partial x} - \frac{\partial(\rho\bar{u}'v')}{\partial y} - \frac{\partial(\rho\bar{u}'w')}{\partial z} + f_x^B, \end{aligned} \quad (2.78)$$

$$\begin{aligned} \frac{\partial(\rho\bar{v})}{\partial t} + \text{div}(\rho\bar{v}\bar{\mathbf{u}}) = \\ -\frac{\partial\bar{p}}{\partial y} + \text{div}[\mu \text{grad}(\bar{v})] - \frac{\partial(\rho\bar{u}'v')}{\partial x} - \frac{\partial(\rho\bar{v}'^2)}{\partial y} - \frac{\partial(\rho\bar{v}'w')}{\partial z} + f_y^B, \end{aligned} \quad (2.79)$$

$$\begin{aligned} \frac{\partial(\rho\bar{w})}{\partial t} + \text{div}(\rho\bar{w}\bar{\mathbf{u}}) = \\ -\frac{\partial\bar{p}}{\partial z} + \text{div}[\mu \text{grad}(\bar{w})] - \frac{\partial(\rho\bar{u}'w')}{\partial x} - \frac{\partial(\rho\bar{v}'w')}{\partial y} - \frac{\partial(\rho\bar{w}'^2)}{\partial z} + f_z^B. \end{aligned} \quad (2.80)$$

A detailed derivation of the RANS equations can be found in [80] and [82]. These equations represent the basis of most fluid dynamics simulation tools designed for engineering applications. An additional stress tensor is introduced on the right hand sides of the equations to consider the fluctuating flow conditions, also known as the Reynolds stress tensor, written with the suffix notation as

$$\bar{\tau}_{ij} = -\rho \overline{u'_i u'_j} = -\rho \begin{bmatrix} \overline{u'^2} & \overline{u'v'} & \overline{u'w'} \\ \overline{v'u'} & \overline{v'^2} & \overline{v'w'} \\ \overline{w'u'} & \overline{w'v'} & \overline{w'^2} \end{bmatrix}. \quad (2.81)$$

Similarly, extra turbulent transport terms arise when a transport equation is derived for an arbitrary scalar quantity, e.g. temperature. The time averaged transport equation for a scalar ϕ is

$$\begin{aligned} \frac{\partial(\rho\bar{\phi})}{\partial t} + \text{div}(\rho\bar{\phi}\bar{\mathbf{u}}) = \\ \text{div}[\Gamma_\phi \text{grad}(\bar{\phi})] - \phi' \frac{\partial(\rho\bar{u}'\phi')}{\partial x} - \phi' \frac{\partial(\rho\bar{v}'\phi')}{\partial y} - \phi' \frac{\partial(\rho\bar{w}'\phi')}{\partial z} + S_\phi \end{aligned} \quad (2.82)$$

with the diffusivity Γ_ϕ . The determination of the Reynolds stress tensor is computationally time consuming and is usually replaced by additional models in CFD simulations, [83] and [84].

2.3.9 Turbulent shear flow in wall proximity

In turbulent fluid flows along a solid surface, there is usually a substantial region of inertia dominated flow far away from the wall and a thin layer within which viscous effects are important. Close to the wall, the flow is influenced by viscous effects and does not depend on free stream parameters. The mean flow velocity depends on the distance y from the wall, the fluid density ρ and the viscosity μ , as well as the wall shear stress τ_{ij} . Therefore, the law of the wall can be written as:

$$u^+ = \frac{\bar{u}}{u_\tau} = f\left(\frac{\rho u_\tau y}{\mu}\right) = f(y^+). \quad (2.83)$$

The law includes the dimensionless velocity u^+ and the dimensionless wall distance y^+ . The last one is defined as $y^+ = y \frac{u_\tau}{\nu}$ and the appropriate velocity scale is the friction velocity

$$u_\tau = \sqrt{\frac{\tau_w}{\rho}}.$$

If the flow is stationary at the solid surface, turbulent eddying motions must stop very close to the wall, and the fluid behavior closest to the wall is dominated by viscous effects. This viscous sub layer is very thin ($0 \leq y^+ \leq 5$) and it can be assumed that the shear stress is approximately constant and equal to τ_w throughout the layer. This yields a linear relationship between velocity and wall distance and, hence, the fluid layer adjacent to the wall is also known as the linear sub-layer:

$$u^+ = y^+. \quad (2.84)$$

Further away from the wall, the velocity profile changes with a smooth transition between the viscous sub-layer and the logarithmic layer defined below. Neither the linear correlation, nor the logarithmic law of the wall is valid in this buffer layer ($5 \leq y^+ \leq 30$).

Beside these layers, an additional region ($30 \leq y^+ \leq 500$) exists where the viscous and turbulent effects are both important. The shear stress varies slowly with the distance from the wall and within this inner region it is assumed to be constant and equal to the wall shear stress. One further assumption regarding the length scale of turbulence allows to derive a logarithmic functional relationship between u^+ and y^+ [78]:

$$u^+ = \frac{1}{\kappa} \ln(y^+) + C. \quad (2.85)$$

The constant C and the von Karman's constant κ have been defined from measurements [74]. This region is named the logarithmic layer or log-law layer, see [80] and [70].

The different regions of the boundary layer are presented in Fig. 11 with the non-dimensional velocity plotted against the dimensionless wall distance. The different wall approximations are marked by the colored lines and the highest deviation can be seen to occur in the buffer layer.

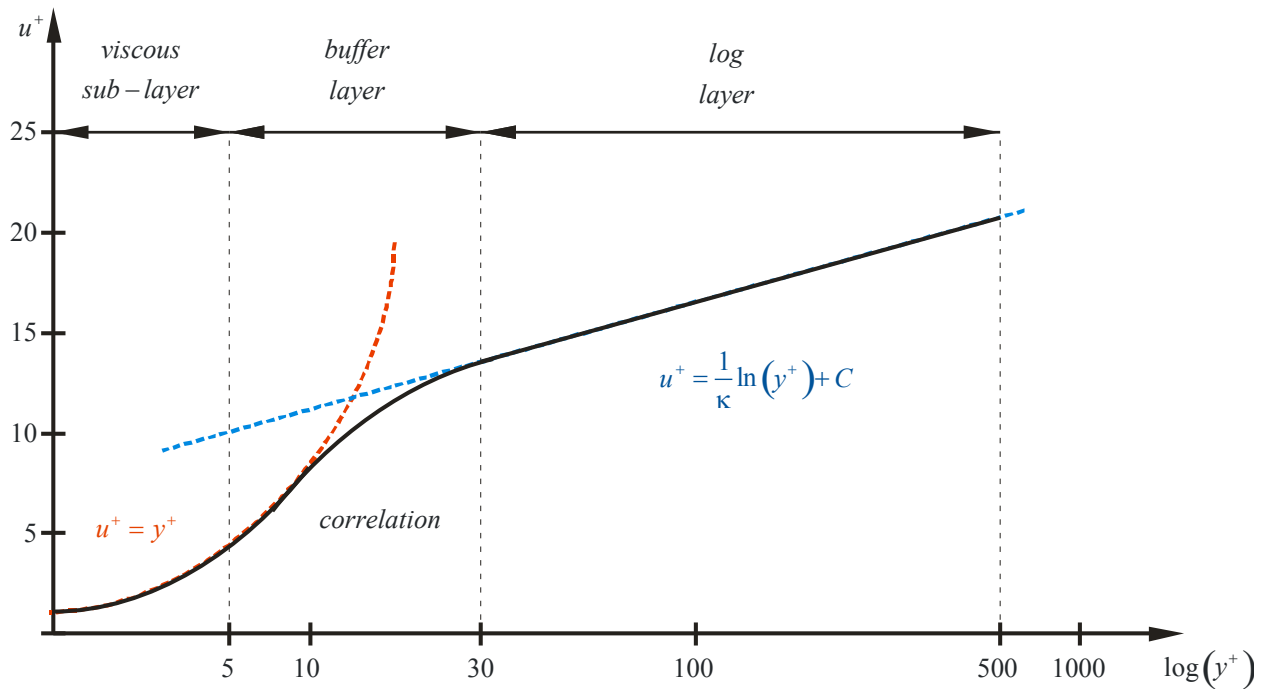


Fig. 11 Non dimensional velocity profile for a turbulent flow over a plate and identification of different regions within the turbulent boundary layer [85]

2.4 Computational fluid dynamics

The Navier-Stokes equations can be used for the analytical solution of simple problems under laminar flow conditions. However, the flow in technically relevant investigations is turbulent and involves complex geometries. Therefore, a numerical approach is required to compute the fluid dynamics and the related heat transfer. Computational fluid dynamics (CFD) are numerical calculations of fluid flow problems by dividing the investigated domain into small elements of finite size and simple geometry. The conservation equations can be applied to the single elements and solved by different methods using the discretization. Common methods for the numerical computation are the finite difference (FD) method, the finite element (FE) method and the finite volume method (FVM) [85]. The finite volume method has been established in CFD and has been used for the following investigations carried out with the program package ANSYS CFX.

2.4.1 Discretization

The discretization is the first step to solve the system of partial differential equations resulting from the turbulence model. The aim of this solution step is to transform this equation system into a system of algebraic equations for unknowns defined at discrete points in space and time. Therefore, the real fluid geometry is discretized by a numerical mesh in finite volumina to apply the FVM. After the discretization of the region, the transport equations have to be integrated over these cells. This will be shown for a general transport equation involving the transport quantity ϕ with the diffusion coefficient Γ_ϕ written as

$$\underbrace{\frac{\partial}{\partial t}(\rho\phi)}_{\text{transient term}} + \underbrace{\frac{\partial}{\partial x_i}(\rho u_i \phi)}_{\text{convection}} = \underbrace{\frac{\partial}{\partial x_i} \left(\Gamma_\phi \frac{\partial \phi}{\partial x_i} \right)}_{\text{diffusion}} + \underbrace{S_\phi}_{\text{source term}} \quad (2.86)$$

Gauss' integral theorem

$$\int_V \text{div}(\phi) dV = \int_A \mathbf{n} \phi dA \quad (2.87)$$

can be used to transform the volume integral into a surface integral to obtain the governing equations of the finite volume method:

$$\frac{d}{dt} \left(\int_V \rho \phi dV \right) + \int_A \mathbf{n} (\rho \mathbf{u} \phi) dA = \int_A \mathbf{n} (\Gamma_\phi \text{grad}(\phi)) dA + \int_V S_\phi dV \quad (2.88)$$

The volume integrals describe source terms and the surface integrals represent the flow through the volume boundaries. These integrals are approximated numerically to get the algebraic equations for a control volume. Details of the discretization implemented in the commercial software used can be found in [84].

2.4.2 Computation of turbulent flow

Turbulent flows occur in most technically relevant problems in industry. The characteristics of turbulent flow are a clearly transient behavior of the fluid in microscopic length scales and the chaotic fluctuation of the particles occurring in three spatial dimensions. A permanent charge of power is required of the fluid flow to maintain the movement of the fluid. The kinetic energy is also converted into irreversible heat energy, a phenomenon called dissipation. Turbulence can be regarded as a constant process of collapsing and emerging eddies in a wide band of length scale, which has to be taken into account for an accurate simulation of the fluid flow. Turbulence causes the appearance of eddies in the flow with a wide range of length and time scales that interact in a dynamically complex way.

A wide variety of different turbulence models are available today to append the equation system and compute the flow and thermal field of a specified problem. The right turbulence model has to be chosen from the available ones, depending on the defined problem and the resulting computational costs. Given the importance of avoiding or inducing turbulence in engineering applications, it is no surprise that a substantial amount of research effort has been dedicated to the development of numerical methods to capture the effects due to turbulence. The methods can be grouped into the following three categories [74]:

- **Direct numerical simulation (DNS)** computes the mean flow and all turbulent fluctuations. The unsteady Navier-Stokes equations are solved on spatial grids directly without any turbulence model, but a sufficient discretization of space and time is necessary. Therefore, a high computational effort and an enormous cost in terms of resources result for these simulations making them unsuitable for general applications in industry. However, they are commonly used in scientific research.
- **Large eddy simulation (LES)** is an intermediate form of turbulence simulation which tracks the behavior of larger eddies. The method involves a space filtering of the unsteady Navier-Stokes equations prior to the computations, which allows the larger eddies and eliminates the smaller ones. The effects on the resolved flow due to the smallest unresolved eddies are included by means of a sub-grid scale model. Unsteady

flow equations must be solved, so the demand on computing resources in terms of storage and amount of arithmetics is large, but this method can still be used for technically relevant problems with complex geometry.

- **Turbulence models for RANS equations** focus on the mean flow and the effects of turbulence on mean flow properties. The Navier-Stokes equations are time averaged including extra terms in the time averaged flow equations due to the interactions between various turbulent fluctuations. These extra terms are modeled with classical turbulence models using eddy-viscosity or Reynolds-stress models. The computational resources required for reasonably accurate flow computations are modest. Therefore, this approach has become the mainstay of engineering flow calculations over the last three decades.

2.4.3 RANS models using eddy-viscosity turbulence models

In order to be able to compute turbulent flows with the RANS equations, it is necessary to develop turbulence models to predict the Reynolds stresses and the scalar transport terms and close the system of the mean flow equations (2.77)-(2.80) and (2.82). Since it seems impossible to find an exact solution of this closure problem, the introduction of turbulence models is unavoidable. Commonly applied turbulence models use the eddy viscosity ν_t or turbulent viscosity μ_t for deriving the Reynolds stress tensor. It is assumed that the turbulent transport of mass, momentum and energy is controlled by the turbulent viscosity μ_t in the same way as laminar flow is controlled by the dynamic viscosity μ in the Navier-Stokes equations. Furthermore, turbulent stresses are found to increase as the mean rate of deformation increases. Boussinesq proposed that the Reynolds stresses might be proportional to the mean rates of deformation [74]. The Reynolds stress can be assumed to be

$$\bar{\tau}_{ij} = -\rho \overline{u'_i u'_j} = \mu_t \left(\frac{\partial \bar{u}'_i}{\partial x_j} + \frac{\partial \bar{u}'_j}{\partial x_i} \right) - \frac{2}{3} \rho \delta_{ij} k, \quad (2.89)$$

with the turbulent viscosity μ_t , and the turbulent pressure term involving the Kronecker symbol δ_{ij} and the kinetic energy k as defined in (2.74).

Turbulent transport of heat, mass and other scalar properties can be modeled similarly to the Reynolds flux. By analogy, the turbulent transport of a scalar ϕ is taken to be proportional to the gradient of the mean value of the transported quantity as follows:

$$-\rho \overline{u'_i \phi'} = \Gamma_t \frac{\partial \bar{\phi}}{\partial x_j}, \quad (2.90)$$

where Γ_t is the turbulent or eddy diffusivity. It can be assumed that the eddy diffusivity is fairly close to the turbulent viscosity defined by the Reynolds analogy. Therefore, a turbulent Prandtl/Schmid number $\sigma_t = \frac{\mu_t}{\Gamma_t}$ can be introduced [87].

The main aim of a turbulence model in a commonly used CFD code is to have a wide applicability, be accurate, simple and economical to run. The RANS turbulence models are classified on the basis of the number of additional transport equations needed to be solved along with the RANS flow equations.

A variety of RANS turbulence models are available today, each of them with advantages for specific application. Commonly used models are presented in Table 4 grouped by the used

method. The two equations eddy-viscosity turbulence models used in the thesis for investigating the fluid flow and the related heat transfer in electrical machines are discussed in more detail in the following sections.

type	no. of extra transport equations	name of developed turbulence model
eddy viscosity	zero	mixing length model
	one	Spalart-Allmaras model
	two	standard $k-\varepsilon$ model
	two	releasable $k-\varepsilon$ model
	two	re-normalisation group (RNG) $k-\varepsilon$ model
	two	standard $k-\omega$ model
	two	modified $k-\omega$ model
	two	baseline (BSL) zonal $k-\omega$ model
	two	shear stress transport (SST) zonal $k-\omega$ model
Reynolds stress	seven	Launder, Reece and Rodi (LRR) isotropization of production
	seven	Launder, Reece and Rodi quasi-isotropic (QI)
	seven	Special, Sarkar and Gatski (SSG)
	seven	SSG/LRR- ω
	seven	second moment closure (SMC- ω)
	seven	baseline (BSL)

Table 4 Commonly used turbulence models for different applications [74]

2.4.3.1 $k-\varepsilon$ turbulence model

The $k-\varepsilon$ turbulence model includes two additional transport equations to determine the turbulent viscosity μ_t . In the standard $k-\varepsilon$ turbulence model, developed by Launder and Spalding [88], one equation is for the turbulent kinetic energy k and another one for the turbulent dissipation ε , based on the relevant process causing changes to these variables. This turbulence model has been used in the last decades due its simple definition, its excellent performance for many industrially relevant flows and its high level of confidence due to its validation having been carried out for a wide range of problems.

The turbulent viscosity is defined with k and ε in this turbulence model:

$$\mu_t = C_\mu \rho \frac{k^2}{\varepsilon}. \quad (2.91)$$

The turbulent kinetic energy k and the turbulent dissipation ε are determined with the following transport equations [84]:

$$\frac{\partial(\rho k)}{\partial t} + \text{div}(\rho k \mathbf{u}) = \text{div} \left[\left(\mu + \frac{\mu_t}{\sigma_k} \right) \text{grad}(k) \right] + P_k + P_{kb} - \rho \varepsilon, \quad (2.92)$$

$$\frac{\partial(\rho \varepsilon)}{\partial t} + \text{div}(\rho \varepsilon \mathbf{u}) = \text{div} \left[\left(\mu + \frac{\mu_t}{\sigma_\varepsilon} \right) \text{grad}(\varepsilon) \right] + \frac{\varepsilon}{k} [C_{\varepsilon 1} (P_k + P_{\varepsilon b}) - C_{\varepsilon 2} \rho \varepsilon]. \quad (2.93)$$

If the approach of eddy viscosity is used for calculating the Reynolds stress tensor, the production rate of the turbulent kinetic energy P_k can be approximated as

$$P_k = \mu_t \text{grad}(\mathbf{u}) \cdot (\text{grad}(\mathbf{u}) + \text{grad}(\mathbf{u}^T)) - \frac{2}{3} \text{div}(\mathbf{u})(3\mu_t \text{div}(\mathbf{u}) + \rho k). \quad (2.94)$$

The influence of the forces caused by buoyancy is included with $P_{\varepsilon b}$ and P_{kb} in each equation:

$$P_{\varepsilon b} = C_3 \cdot \max(0, P_{kb}), \quad (2.95)$$

and, regarding P_{kb} , a differentiation has to be made for the ‘‘full buoyancy model’’ or the ‘‘Boussinesq buoyancy model’’ in the equation of the turbulent kinetic energy:

$$P_{kb,full} = -\frac{\mu_t}{\rho\sigma_{\rho,full}} g \cdot grad(\rho), \quad (2.96)$$

$$P_{kb,bous} = -\frac{\mu_t}{\rho\sigma_{\rho,bous}} \rho\beta g \cdot grad(T). \quad (2.97)$$

The constant values in the equations above are summarized in Table 5.

C_μ	σ_k	σ_ε	$C_{\varepsilon 1}$	$C_{\varepsilon 2}$	C_3	$\sigma_{\rho,full}$	$\sigma_{\rho,bous}$
0.09	1.0	1.3	1.44	1.92	1.0	0.9	1.0

Table 5 Constant values used in the standard k - ε turbulence model [89]

2.4.3.2 k - ω turbulence model

The k - ω turbulence model is well suited for flow calculations with focus on the inner flow field and has its validity for large Reynolds numbers. In zones near the wall, the k - ω turbulence model developed by Wilcox [90] yields more accurate results than other models. This turbulence model also solves two additional transport equations, one for the turbulent kinetic energy k and one for the turbulence frequency ω as follows [84]:

$$\frac{\partial(\rho k)}{\partial t} + div(\rho k \mathbf{u}) = div \left[\left(\mu + \frac{\mu_t}{\sigma_k} \right) grad(k) \right] + P_k + P_{kb} - C_k \rho k \omega, \quad (2.98)$$

$$\frac{\partial(\rho \omega)}{\partial t} + div(\rho \omega \mathbf{u}) = div \left[\left(\mu + \frac{\mu_t}{\sigma_\omega} \right) grad(\omega) \right] + C_{\omega 1} \frac{\omega}{k} P_k + P_{\omega b} - C_{\omega 2} \rho \omega^2. \quad (2.99)$$

The turbulent viscosity is defined as

$$\mu_t = \rho \frac{k}{\omega}. \quad (2.100)$$

The production rate of the turbulent kinetic energy P_k and P_{kb} are computed similarly as in the k - ε turbulence model. The additional force caused by buoyancy is computed as

$$P_{\omega b} = \frac{\omega}{k} \left((C_{\omega 1} + 1) C_3 \max(P_{kb}, 0) - P_{kb} \right). \quad (2.101)$$

The constant values in the equations above are included in Table 6.

σ_k	C_k	σ_ω	$C_{\omega 1}$	$C_{\omega 2}$	C_3
2.0	0.09	2.0	5/9	0.075	1.0

Table 6 Constant values used in the standard k - ω turbulence model [89]

Numerically, the k - ω turbulence model is very similar to the k - ε turbulence model. As pointed out, its strengths are in the computation of the viscose and logarithmic sub-layers of the

boundary layer close to the wall surface of the solid domain. It is still simple and numerically stable, but it is not able to simulate the behavior of the fluid flow in the free stream.

2.4.3.3 Shear stress transport (SST) turbulence model

The shear stress transport turbulence model, developed by Menter [91], combines the advantages of the k - ε turbulence model in the free stream and the advantages of the k - ω turbulence model in wall proximity. Hence, this turbulence model has acceptable computation times for the whole fluid domain, computes accurate results for different technical applications and is the most frequently used turbulence model in industry [92]. The activation of the right model depending on the wall distance is operated with a blending function F_1 .

The transport equations are defined as:

$$\frac{\partial(\rho k)}{\partial t} + \text{div}(\rho k \mathbf{u}) = \text{div} \left[\left(\mu + \frac{\mu_t}{\sigma_k} \right) \text{grad}(k) \right] + P_k + P_{kb} - \beta^* \rho k \omega, \quad (2.102)$$

$$\begin{aligned} \frac{\partial(\rho \omega)}{\partial t} + \text{div}(\rho \omega \mathbf{u}) = \\ \text{div} \left[\left(\mu + \frac{\mu_t}{\sigma_\omega} \right) \text{grad}(\omega) \right] + (1 - F_1) \frac{2\rho}{\sigma_{\omega 2} \omega} \text{grad}(k) \text{grad}(\omega) + \alpha^* \frac{\omega}{k} P_k + P_{\omega b} - \beta \rho \omega^2. \end{aligned} \quad (2.103)$$

The function F_1 has to switch between the value 0 in the free stream and the value 1 at the wall. It is hence defined as

$$F_1 = \tanh \left\{ \left\{ \min \left[\max \left(\frac{\sqrt{k}}{\beta^* \omega y}, \frac{500\nu}{y^2 \omega} \right); \frac{4\rho k}{CD_{kw} \sigma_{\omega 2} y^2} \right] \right\}^4 \right\}, \quad (2.104)$$

$$CD_{kw} = \max \left(2\rho \frac{1}{\sigma_{\omega 2} \omega} \text{grad}(k) \text{grad}(\omega); 10^{-10} \right). \quad (2.105)$$

Furthermore, the turbulent viscosity is defined with the blending function F_2 as follows:

$$\mu_t = \frac{\rho a_1 k}{\max(a_1 \omega, S F_2)}, \quad (2.106)$$

$$F_2 = \tanh \left\{ \left[\max \left(\frac{\sqrt{k}}{\beta^* \omega y}, \frac{500\nu}{y^2 \omega} \right) \right]^2 \right\}, \quad (2.107)$$

$$S = \sqrt{2S_{ij}S_{ij}} \quad \text{with} \quad S_{ij} = \frac{1}{2} \left(\frac{\partial v_i}{\partial x_j} + \frac{\partial v_j}{\partial x_i} \right). \quad (2.108)$$

A disadvantage of the k - ε and k - ω turbulence models is the continuous increase of the turbulent kinetic energy. Therefore, a production limiter prevents this effect in the SST turbulence model. The production rate of the turbulent kinetic energy P_k is limited as

$$P_k = \min(P_k, C_{\text{lim}} \rho \varepsilon). \quad (2.109)$$

All constants are computed by a blend from the corresponding constants of the k - ε and the k - ω model via $\alpha = \alpha_1 F + \alpha_2 (1 - F)$ etc. The constants for this model are:

β^*	α_1	β_1	σ_{k1}	$\sigma_{\omega 1}$	α_2	β_2	σ_{k2}	$\sigma_{\omega 2}$
0.09	5/9	3/40	0.85	0.5	0.44	0.0828	1.0	0.856

Table 7 Constant values used in the SST turbulence model [89]

2.4.4 Wall treatment

As mentioned before, the fluid flow can be divided into two different regions. On the one hand, the turbulent region with high Reynolds numbers and on the other hand regions with high molecular viscosity near the wall. The wall treatment to determine the position, location and size of separation is extremely important in fluid dynamic simulations [78]. The computation of the fluid flow near the walls requires a fine mesh here to discretize the boundary layer. The resulting computational time and effort may become impracticable and the resulting problems can be solved by different models for the wall treatments.

The standard wall functions implemented in ANSYS CFX are the scalable wall function for the k - ε turbulence model and the automatic wall treatment for the SST turbulence model. Wall functions are applied to ensure a simple computation of the boundary layer by using the logarithmic law of the wall. The function prescribes boundary conditions for different near wall regions with the benefit of avoiding time consuming iterations.

2.4.4.1 Scalable wall functions

This function uses the log-law and the first element near the wall has to be inside the log-law layer. This can be ensured easily for high Reynolds numbers, but not for low ones. This formulation becomes singular for $y^+ \rightarrow 0$.

Therefore, a limiter has been defined for the dimensionless wall distance by using a scalable wall function to ensure that the value of $y_{\text{lim}}^+ = 11.06$ is not exceeded. This value denotes the overlapping of the linear and logarithmic laws of the wall. The functions of the limiter and the log-law are defined as follows:

$$u^+ = \frac{1}{\kappa} \ln(\tilde{y}^+) + B, \quad (2.110)$$

$$\tilde{y}^+ = \max(y^+, y_{\text{lim}}^+). \quad (2.111)$$

This definition ensures that the value of \tilde{y}^+ is independent of the mesh resolution at the wall. Thus, the viscous sub-layer is moved into the wall, because the first element at the wall is assumed to be in the log-law layer. The disadvantage of the scalable wall function is that the thickness of the viscous sub-layer rises with smaller Reynolds numbers causing numerical errors due to neglecting the near wall effects in the buffer and linear zone.

2.4.4.2 Automatic near wall treatment

As pointed out before, wall functions are not always desirable, as they neglect the influence of the viscous sub-layer and this omission can have a significant effect on the solution.

Nevertheless, a robust and accurate viscous sub-layer formulation is desirable to solve the equations all over the surface. The automatic near wall treatment is based on the $k-\omega$ near wall formulation with the model shifting gradually between a viscous sub-layer formulation and wall functions, based on the grid density [93]. Therefore, a blending function depending on the dimensionless wall distance is defined, with the solution for ω in the linear and logarithmic near wall region, as follows:

$$\omega_{vis} = \frac{6\nu}{0.075y^2}, \quad \omega_{log} = \frac{1}{0.3} \frac{u_\tau}{y}. \quad (2.112)$$

After reformulation in terms of y^+ , and a smooth blending between the dissipation rates, one obtains

$$\omega_1(y^+) = \sqrt{\omega_{vis}^2(y^+) + \omega_{log}^2(y^+)}. \quad (2.113)$$

The velocity profile can be assumed to be described by a similar formulation:

$$u_\tau^{vis} = \frac{U_1}{y^+}, \quad u_\tau^{log} = \frac{U_1}{\frac{1}{\kappa} \ln(y^+) + C}, \quad u_\tau = \sqrt[4]{(u_\tau^{vis})^4 + (u_\tau^{log})^4}. \quad (2.114)$$

2.4.4.3 Solving the heat flux

For the treatment of the energy equation near the wall, an algebraic formulation is required to link the temperature and the heat flux. The formulation of Kader is used [94]:

$$T^+ = Pr y^+ e^{-\Gamma_w} + (2.12 \ln(1 + y^+) + \beta_{Pr}) e^{-1/\Gamma_w}, \quad (2.115)$$

with the functions

$$\beta(Pr) = (3.85 Pr^{1/3} - 1.3)^2 + 2.12 \ln(Pr); \quad \Gamma_w = \frac{0.01(Pr \cdot y^+)}{1 + 5 Pr \cdot y^+}, \quad (2.116)$$

and the definition of the non-dimensional temperature

$$T^+ = \frac{T_w - T}{T_\tau}, \quad T_\tau = \frac{q_w}{\rho c_p u_\tau}. \quad (2.117)$$

The wall heat flux can be defined with the wall temperature T_w , the fluid temperature T_∞ and the temperature profile T^+ :

$$q_w = \frac{\rho c_p u_\tau^+}{T^+} (T_w - T_\infty). \quad (2.118)$$

This formulation is valid through the entire y^+ range of the viscous sub-layer and the logarithmic profile. For the current formulation, \tilde{y}^+ defined in (2.111) has to be used in order to be consistent with the momentum equations.

For scalable wall functions, the temperature profile follows the logarithmic law similar to the velocity profile:

$$T^+ = 2.12 \ln(y^+) + \beta, \quad (2.119)$$

$$\beta = (3.85Pr^{1/3} - 1.3)^2 + 2.12 \ln(Pr). \quad (2.120)$$

2.4.5 Mesh requirements

The computational grid is the fundamental characteristic of any given numerical simulation. It defines a discrete representation of the geometric region of the investigated problem. The mesh subdivides the solution region into a finite number of cells (or elements). The mesh generator ANSYS ICEM CFD has been used to produce a mesh for the defined problems by using hexahedral elements. The appropriate default properties of orthogonality, expansion rate and aspect ratio are described in [95].

Depending on the complexity of the geometry and the solution of the heat flux [93], the approximation of near wall effects in CFD simulations fits best to measured data involving values for the dimensionless wall distance $y^+ \approx 1$ for a resolved boundary layer or $y^+ \approx 30$ for a log-law layer. It is widely accepted that the most unsuited value is given by $y^+ = 11.06$ where the highest error is computed. For a proper resolution of the boundary layer not less than 10 hexahedral layers are required. Using the Reynolds number Re , the characteristic length L and y^+ , the height of the first element at the wall can be calculated [96]:

$$y_0 = L y^+ \sqrt{74} Re^{-13/14}. \quad (2.121)$$

Using these requirements, accurate solutions can be achieved still saving computational time, costs and resources.

3 Enhancement of the state of the art design process for large hydro generators using numerical methods to simulate the fluid and thermal field

Simulating the heat transfer in the stator ventilation ducts is a time consuming process due to the high numerical effort caused by the large number of elements resulting in long computation time. The fluid conditions at the stator ventilation duct inlet depend on the preceding parts, like end winding, clamping plate and rotor. These parts have a great influence on the temperature distribution in the cooling fluid, mass flow distribution and also on the efficiency of the related heat transfer triggered by the cooling scheme.

Additionally, the turbulence model and the wall treatment influence the numerical results. The model investigated includes rotating and stationary parts. Therefore, a choice has to be made between a transient or steady state simulation, with different implementations of the rotor movement. The aim of this chapter is to compare two different Multiple Frame of Reference methods for steady state simulations, the commonly used Frozen Rotor method and the Mixing Plane method. These numerical simulations have been made with a coarse mesh at the walls to alleviate the high numerical effort of the computation of the fluid and thermal field in a large hydro generator. A detailed simulation of the stator duct has then been carried out with a fine mesh on single duct models to determine the convective heat transfer. The inlet boundary conditions have been obtained from the overall models utilizing the Frozen Rotor or Mixing Plane method, by using a domain decomposition technique. An interface has been defined in the overall model at the middle of the air gap between rotor and stator. Having analyzed the numerical model, it is possible to evaluate different variables on this surface. Thus it is possible to prescribe specified variables on a ventilation duct model for further investigations. The reduction of the overall model to a single duct model allows a detailed and efficient analysis of the fluid flow and related heat transfer along the ventilation ducts with the required quality of the mesh.

Parts of this chapter have been taken from the work presented in [55] and published in more detail in [56].

3.1 Overall model of a large hydro generator

Computational fluid dynamics in large hydro generators has attained an important role in the design process during the last century to obtain different parameters concerning the flow and thermal field in such an electric device. The main parts of such numerical models are the fluid domains in the space between the solid parts. The solids parts are taken into account by a wall

boundary conditions on the temperature or heat flux in commonly used CFD models. The flow paths are divided into sub-domains by control surfaces where the different variables are evaluated. As mentioned before, the dimensions of hydro generators are large and the number of the necessary finite volumes to discretize the problem is quite high. Therefore, it makes sense to define boundary conditions to save elements and hence to arrive at lower computational costs. These boundary conditions are dictated by the operating conditions and the cooling scheme.

In most cases the fan is positioned on the top and bottom of the shaft or, in case of an externally mounted fan, on the housing, so the cooling circuit is symmetric with respect to a plane perpendicular to the machine axis. Therefore, a symmetry condition along this plane in the middle of the machine can be defined and, hence, 50% of the elements can be saved. Furthermore, the pole pair number divides the machine into circumferential sections with similar inflow conditions for each. Using a rotational periodic boundary conditions for a pole section allows simulating a smaller model depending on the number of salient poles included. This reduced model and the related numerical set-up yields identical results as the simulation of the whole machine would produce.

An example of such a reduced model is shown in Fig. 12 with the parts of an external ventilation circuit included. The ventilation system of this generator transports the air from (a) the inlet through the machine to (j) the outlet. The fan is designed to be axial or radial and serves to produce a high air flow and determined pressure at the inlet to ensure the circulation of the coolant in the machine. Afterwards, the fluid streams through (c) the end winding to the pole gap between (e) the pole, located at (f) the rotor. Further on, the air is transported over (g) the air gap and along (h) the ventilation ducts to (j) the outlet. The heat exchanger is positioned behind the outlet and cools down the warm air to establish the required inlet temperature of the circuit. For the investigation of the fluid and thermal field along the ventilation ducts, it is important to know the prevailing conditions in the air gap, i.e. one has to focus on the heat exchange influenced by preceding parts, like (c) the end winding and (e) pole winding. Therefore, it is not possible to disregard these parts and they are included in the overall models of the generator to determine the air gap conditions for further investigations.

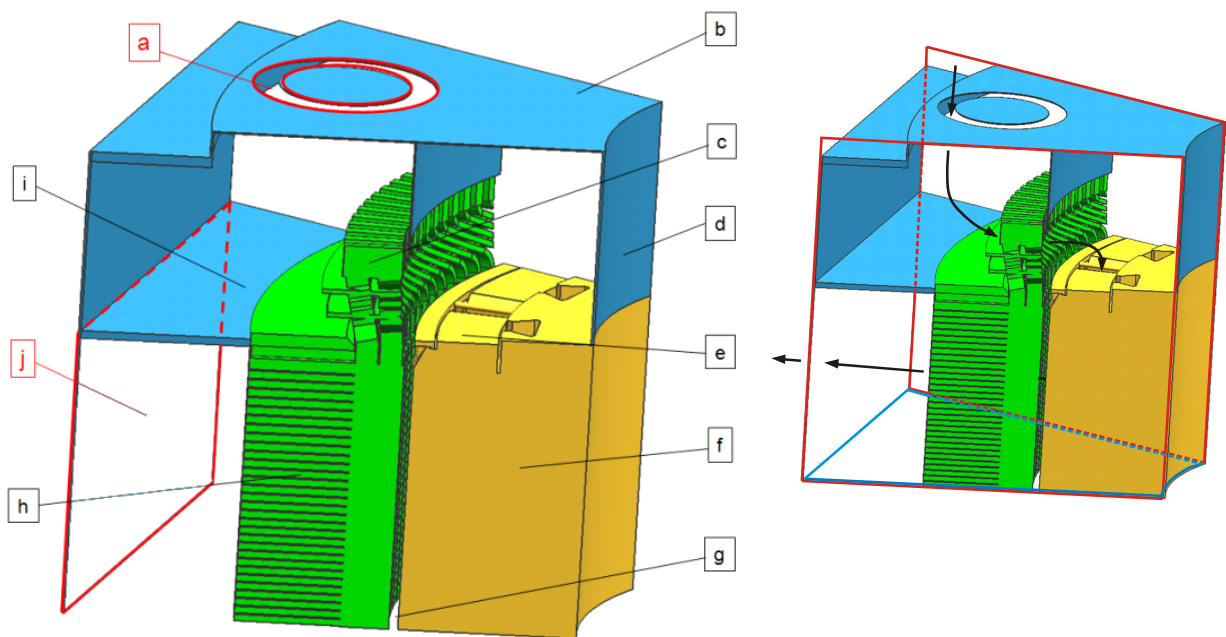


Fig. 12. On the left: overall model including one pole section of the investigated hydro generator showing the (a) inlet, (b) bearing support, (c) end winding, (d) shaft, (e) pole with pole winding, (f) rotor, (g) air-gap, (h) stator with stator ducts, (i) web plate, (j) outlet. On the right: fluid path (black) through the machine showing the axially symmetric (blue) and periodic (red) boundary conditions

3.1.1 Rotor-stator interaction

The rotor-stator interaction has also to be taken into account in a suitable way. Transient calculations are not economic due to the high computational burden and the long computing time. Steady state simulations are preferred for many engineering applications because they have a shorter simulation time, a simplified post processing and, in many cases, only time averaged values are of interests.

In case of transient simulations, the rotor rotation is taken into account, i.e. the relative position of the components changes in each time step. Hence, two or more components in different frames of reference are solved and the geometry is updated at every time step. This method solves correct physics, takes account of reverse flow and of the close coupling of the components, but the computational efforts are very high, a large amount of data has to be stored for the post processing and, in order to start from a good initial guess, a steady state solution has to be carried out in advance. A transient calculation of such an electrical device is, therefore, not economic for industrial applications.

A steady state analysis neglects the transient terms in the flow equations and uses a steady state approximation. For this analysis type, a Frozen Rotor (FR) or a Mixing Plane (MP) model can be chosen for the information transfer between the Multiple Frames of Reference (MFR). Each interface model connects the outlet of the rotating domain for upstream with the inlet of the stationary domain for downstream and thus simulates the rotor rotation. The rotating region is provided with an extra source term to account for the movement, including the centrifugal and Coriolis forces.

The FR method assigns the flow parameters locally from the rotating to the stationary system. This method is recognized as an established approach for simulating the cooling flow in an electrical machine, as summarized in [41]. In addition, a validation of this interface model has been carried out by the industrial partner ANDRITZ Hydro GmbH using a 1-D network method including the flow and thermal fields with the global mass flow and energy balances verified, as well as by means of measurements over the last decades. The latter have included measurements of the mass flow, of temperature and of fluid pressure at different locations and also temperature measurements in the solid domains.

The MP method averages the flow parameters in circumferential direction on the upstream side (outlet: rotating domain) and commits those averaged values to the downstream side (inlet: stationary domain). This method has already been widely used in CFD investigations focusing on the aerodynamic performance of turbines or compressors as well [97] and [98]. Generally spoken, all MFR methods simulate the rotor rotation for each component in a local frame of reference and each control volume is contained only in one reference frame in ANSYS CFX.

The difference between these two overall models is illustrated in Fig. 13. The rotor-stator interface (RSI) is positioned in the middle of the air gap, separating (a) the rotor and (b) the stator domains. The main difference between the compared numerical models is in the modeling of the stator. It is evident that the MP model has fewer elements than the FR model. In fact, for the overall model shown in Fig. 12, the 16.360 million elements of the FR model can be reduced to 9.702 million elements in the MP model, which means a reduction by 40%. The reduction of the stator in the MP model is made possible by the change of pitch caused by the circumferential averaging on the rotor-stator interface. The figure shows the modelled pole section in the rotor domain for the FR as well as for the MP model. The advantage of the MP interface is an averaged flow in the circumferential direction, allowing to reduce the stator to a slot section instead of a pole section containing 13 slot sections. However, some flow structures are missing due to the circumferential averaging procedure of the stage interface. Furthermore, a faster

computation time of about 66 hours with 8 cores can be achieved for the MP model as opposed to 89 hours with 36 cores for the FR model.

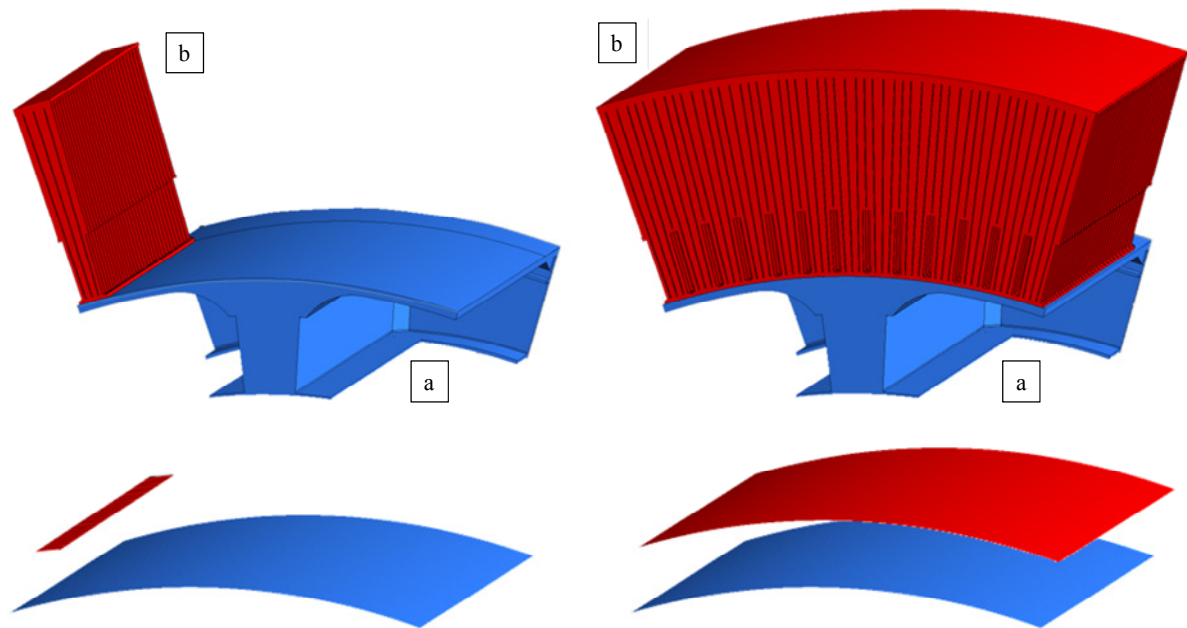


Fig. 13 Fluid domains of (a) the rotor and (b) stator for the MP model on the left hand side and for the FR model on the right hand side

The MP method defines bands in axial (z -) direction (see Fig. 14) both on the outlet of (a) the rotor surface and on the inlet of (b) the stator surface. These bands are a few millimeters long in the z -direction and are indicated by colors in Fig. 14. On the outlet of the upstream surface, all fluxes are averaged in the azimuthal (Θ) direction on each band. These averaged values of the fluxes calculated on the upstream side on the rotor outlet are transmitted to the downstream side on the stator inlet. Generally speaking, the fluid flow in the stator domain is a circumferentially averaged flow for a specific pitch. Therefore, the relative position of the two domains to each other is not included in MP simulations [84]. The advantage of this interface model is the computational efficiency, the possibility for a large pitch change and the coupled sets of equations, which makes this model very useful in practice.

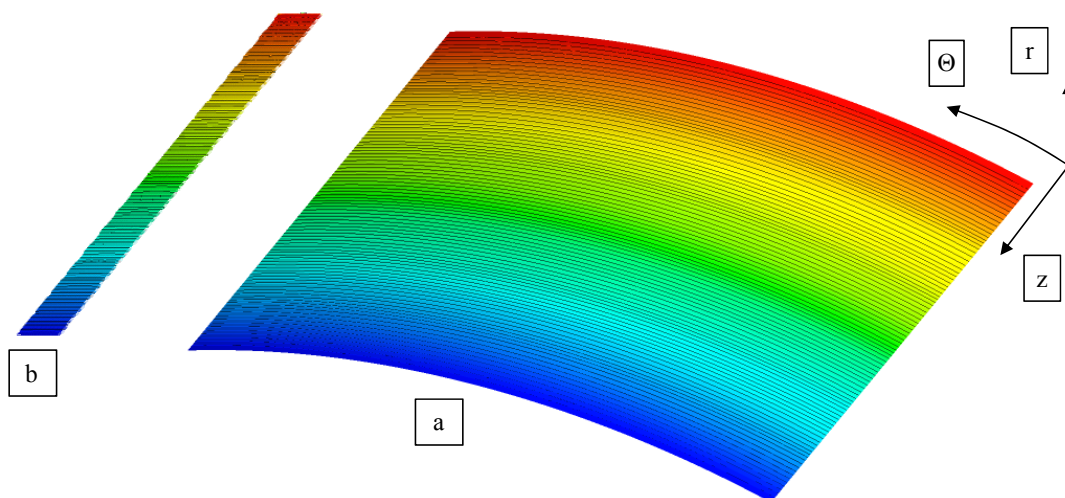


Fig. 14 Rotor-stator interface of the MP model including the generated bands on (a) the upstream rotor interface and (b) the downstream stator interface

The FR model captures the relative position of the stator and rotor domain and takes account of local interactions, e.g. reverse flows and hot spots along the pole section of each stator duct. There is no reduction from the pole section to a slot section like in the MP model, so the RSI coincides on the two components in this model. In contrast to MP, no circumferential averaging is necessary, only a frame change from the rotating to the stationary domain [84] has to be carried out.

3.1.2 Numerical set-up

3.1.2.1 Turbulence model

The standard k - ε model is used in many cases for RANS simulations of turbulent flow conditions because of its robustness, economy and reasonable accuracy for a wide range of flows. However, the model performs poorly with non-equilibrium boundary layers, because it tends to predict the onset of separations too late and to under-predict the amount of separation. This has a strong influence on different effects, such as heat transfer and multi-phase phenomena. The Shear Stress Transport (SST) model has been chosen for simulating the fluid flow and the heat transfer in the numerical models presented in this work to investigate the fluid and the related thermal field for large hydro generators. This turbulence model uses the advantages of the turbulence/frequency based k - ω model at the wall and the k - ε model in the bulk flow, as explained in chapter 2.4.3.3.

An important issue in turbulence modeling is the numerical treatment in near wall regions. The wall shear stress and heat transfer predictions have been determined by the near wall formulation. For SST, the wall boundary treatment exploits the simple and robust near wall formulation of the k - ω turbulence model and switches automatically from a low Reynolds number formulation to a wall function treatment based on grid density. Therefore, the optimal performance of the turbulence model is ensured for any given grid.

3.1.2.2 Fluid properties

State of the art numerical models mostly assume constant solid and fluid properties. In this work, air is taken to be a compressible coolant fluid with constant properties with a specific heat capacity of $c_p = 1004.4 J/kgK$, dynamic viscosity $\mu = 1.831 \cdot 10^{-5} Pa \cdot s$ and thermal conductivity of $\mu = 2.61 \cdot 10^{-5} W/mK$. The ideal gas equation has been used to compute the density of the fluid with the molecular mass n , the absolute pressure p_{abs} and the universal gas constant R_0 as follows:

$$\rho = \frac{n \cdot p_{abs}}{R_0 \cdot T}. \quad (3.1)$$

3.1.2.3 Boundary conditions

The radiators for cooling down the air circulated between the outlet and the inlet of the fan as well as the fan itself have not been modeled. Therefore, boundary conditions have been defined following the outlet of the fan (inlet parameters) and preceding the inlet of the radiators (outlet parameters). In case of a reverse flow at the outlet region, it is important to define conditions for the incoming fluid flow. To facilitate a comparison, the two models have similar boundary conditions at the model air inlet, outlet and heated walls, as shown in Table 8.

fluid condition		thermal condition	
volume flow rate	3 m ³ /s	winding	115 °C
fluid inlet temperature	40 °C	pole winding	82 °C
reference pressure	101325 Pa	stator core tooth	92 °C
rotational speed	600 min ⁻¹	stator core yoke	85 °C

Table 8 Boundary conditions of the overall models for a specified type of large hydro generator

3.1.3 Evaluation of numerical parameters

The stator core of a large hydro generator consists of laminated iron sheets marked (a) in Fig. 15. The ventilation duct is generated by distance bars positioned on further sheets indicated by (b). Thus the coolant can stream from the inner diameter along the rectangular channels to the outer diameter and ensures the heat transfer in the stator core and the winding assembly.

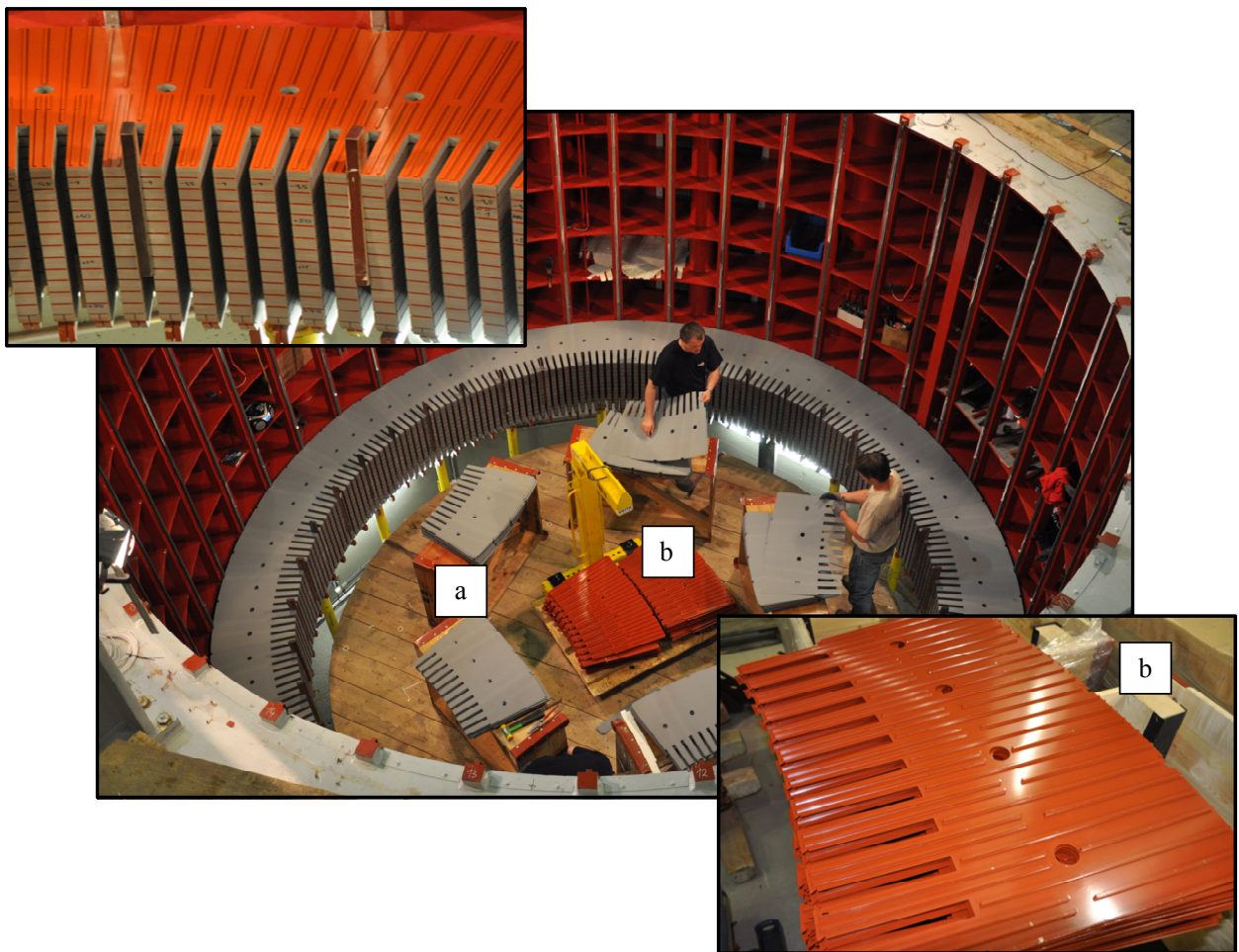


Fig. 15 Generation of the ventilation ducts in the stator of a large hydro generator with (a) laminated iron sheets and (b) steel lamination with included distance bars

The determination of the cooling flow and the resulting heat exchange in electrical machines needs several parameters to be computed and obtained on different surfaces. Therefore, a distinction has to be made between control surfaces to investigate the flow field and wall surfaces to determine the heat flux from the solid to the fluid domain.

The flow control surfaces selected are shown in Fig. 16. Note that the ventilation duct is divided into four sub-channels which have been evaluated separately and the mass flow averaged parameter for a quantity ϕ is defined as follows:

$$\phi_{fluid,surface} = \frac{\sum_{i=1}^n m_{area,i} \cdot \phi_{area,i}}{\sum_{i=1}^n m_{area,i}}. \quad (3.2)$$

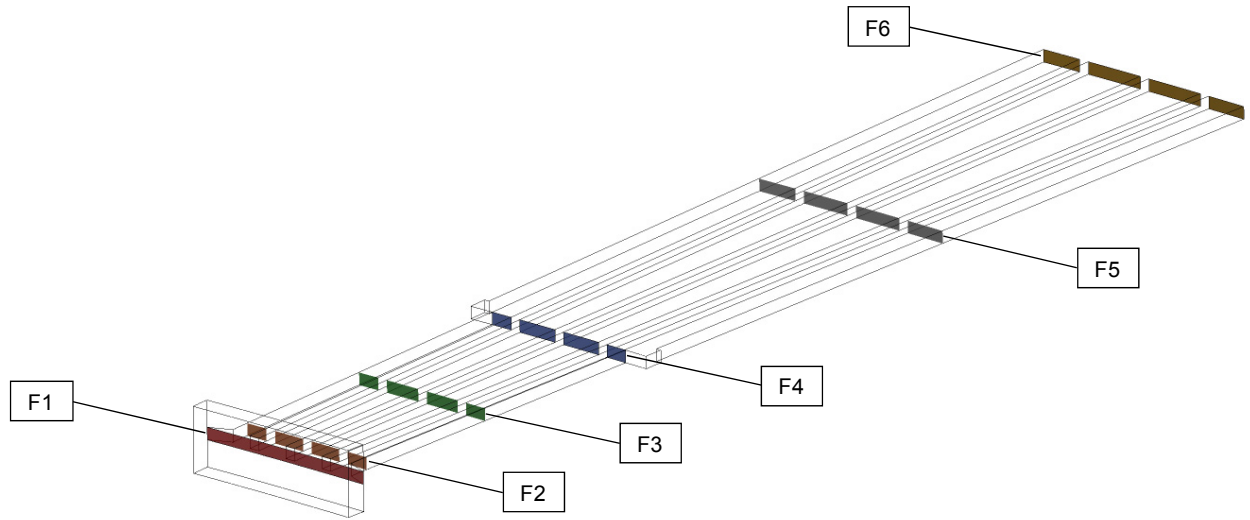


Fig. 16 Fluid control surfaces along the stator ventilation ducts shown for one slot section

The parameters computed at the walls have been determined as area averaged values:

$$\phi_{wall,surface} = \frac{\sum_{i=1}^n A_{area,i} \cdot \phi_{area,i}}{\sum_{i=1}^n A_{area,i}}. \quad (3.3)$$

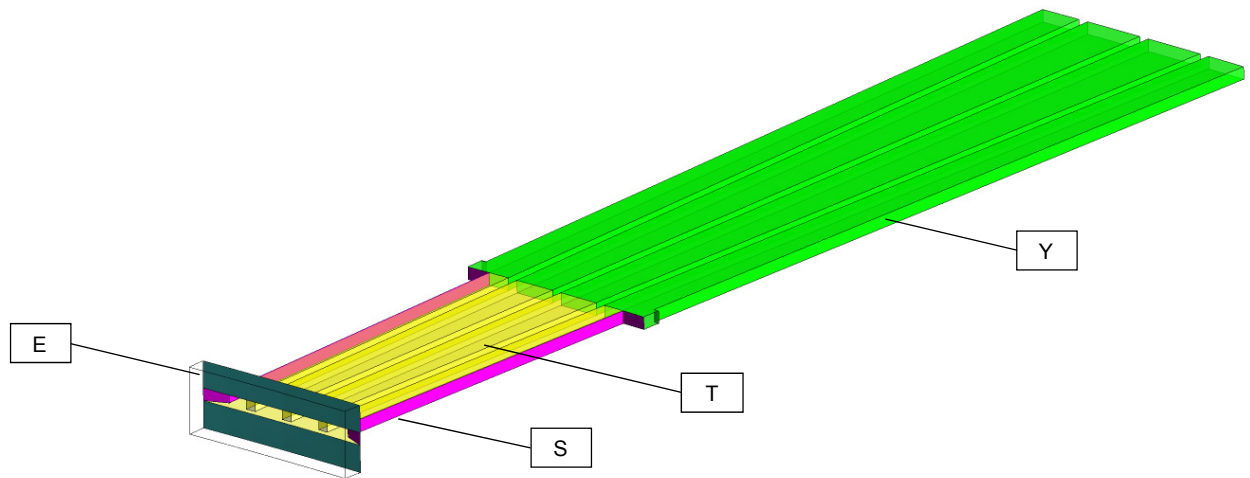


Fig. 17 Wall surfaces along the stator ventilation ducts presented for one slot section

Fig. 17 shows the different walls: (E) the stator core at the inner diameter, (S) the slot area where the winding assembly is positioned, (T) the tooth area and (Y) the yoke area. The legends

and parameters are suppressed in the following figures due to proprietary reasons. Therefore, the calculated values have been normalized by the value of the same parameter calculated on the 20th duct of the Frozen Rotor model, i.e.

$$\phi_{norm,i} = \frac{\phi_i}{\phi_{FR,20}}. \quad (3.4)$$

3.1.4 Results of the computed flow field

3.1.4.1 Mass flow rate

The principal criterion to ensure a proper comparison of the relevant CFD flow variables is the mass flow rate distribution caused by the inlet conditions at the ventilation ducts concerning the velocity vector \mathbf{u} , the temperature T , the kinetic turbulent energy k and the turbulent eddy dissipation ε . The mass flow rate consists of the circumferential, axial and radial velocity (u , v and w) and the fluid density ρ . The mass flow distribution obtained by the two multiple frames of reference models are presented in Fig. 18. The deviation is less than 4.6% over the 29 ventilation ducts in the stator. The increase of the mass flow is caused by the symmetric boundary condition defined in the axial middle of the machine following the 29th duct.

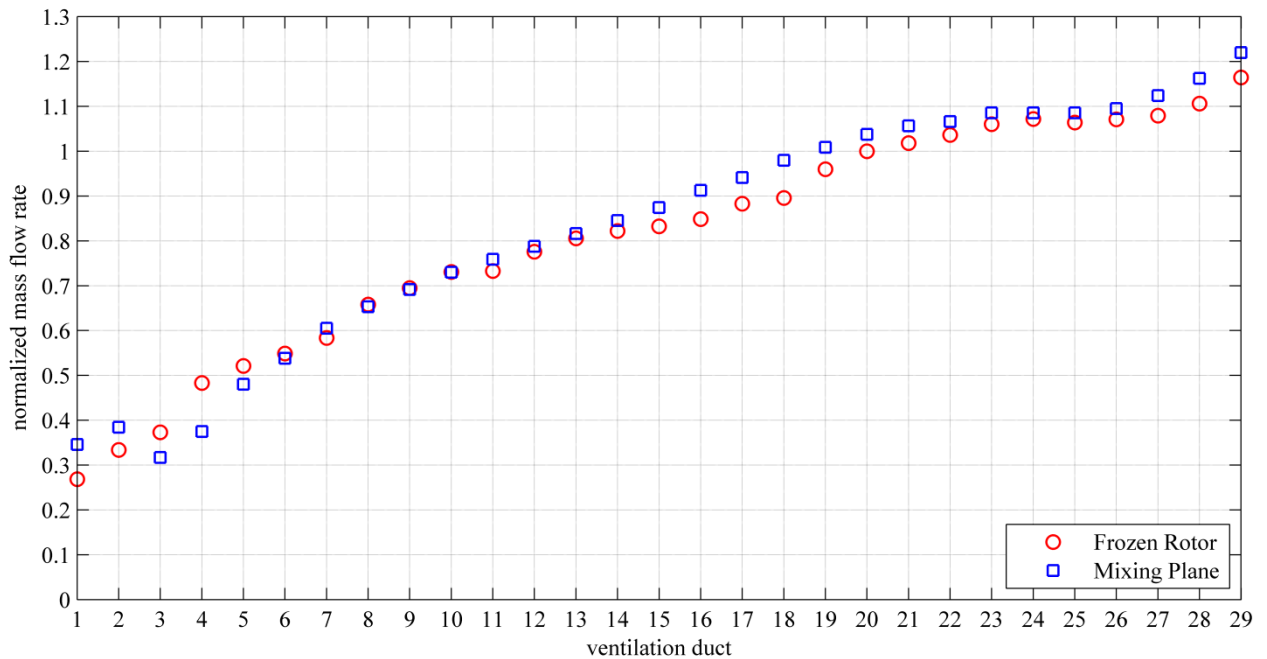


Fig. 18 Normalized mass flow rate distribution over the ventilation ducts in the stator for the Frozen Rotor and the Mixing Plane model

For understanding the dynamics of the cooling flow, the zones of recirculation (blue) are shown in Fig. 19 for a single ventilation duct positioned on the top of the electrical machine, (denoted as the first ventilation duct), and in Fig. 20 for a ventilation duct in the middle, near the symmetry plane. It is evident that the variation from the top to the middle cooling duct flow is associated with the variation of the mass flow rate. The higher mass flow rate in the middle of the generator produces less flow separation than the flow located at the top. The highest recirculation zones are also located in the tooth region and the lowest in the yoke region. The FR method retains the relative position of the rotating to the stationary frame and captures local interactions like reverse flows.

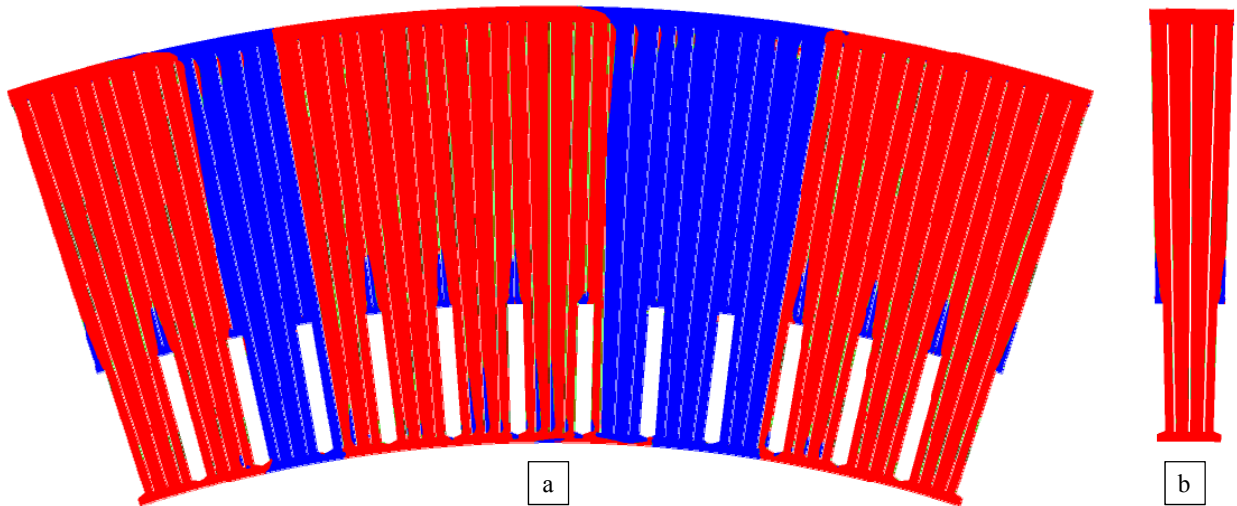


Fig. 19 Recirculation zones for (a) the FR and (b) the MP model in the ventilation ducts computed at the first ventilation duct, positioned on the top of the large hydro generator

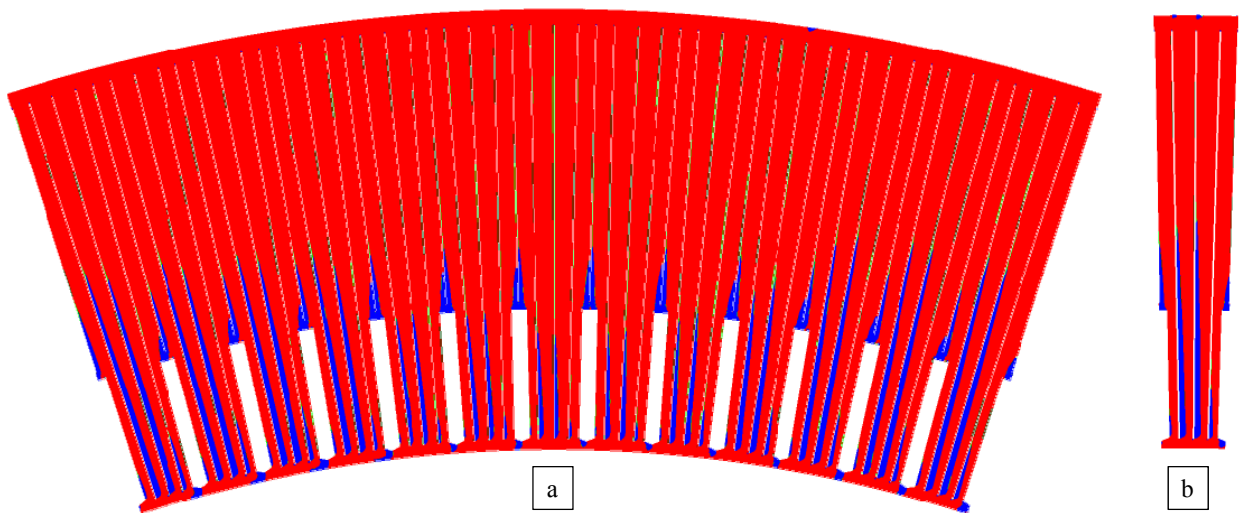


Fig. 20 Recirculation zones for (a) the FR and (b) the MP model in the ventilation ducts computed at the 29th ventilation duct, positioned on the middle of the large hydro generator

3.1.4.2 Velocity distribution

The main difference between the two MFR models is due to the circumferential averaging at the rotor-stator interface. Therefore, the circumferential velocity has an important role and an analogy concerning up- and downstream interface must be given in the middle of the air gap between the rotor and the stator. The normalized velocity distribution of the circumferential velocity component is plotted in Fig. 21, with an averaged difference of 10.5% between the two methods, a value higher than in the mass flow rate.

The design of the slot wedge at the stator inlet has a significant effect on the flow separations and the related pressure losses as well as the heat transfer along the ventilation ducts. The flow characteristic is shown for the 20th duct including the velocity of the stationary frame for the FR and MP models in Fig. 22. The Mixing Plane model leads to results which correspond to a slot averaged velocity distribution of the Frozen Rotor model. The flow characteristic is the same in both models concerning the local flow separations at the duct inlet, at the channel extension, and the resulting recirculation zones both in the tooth and in the yoke region.

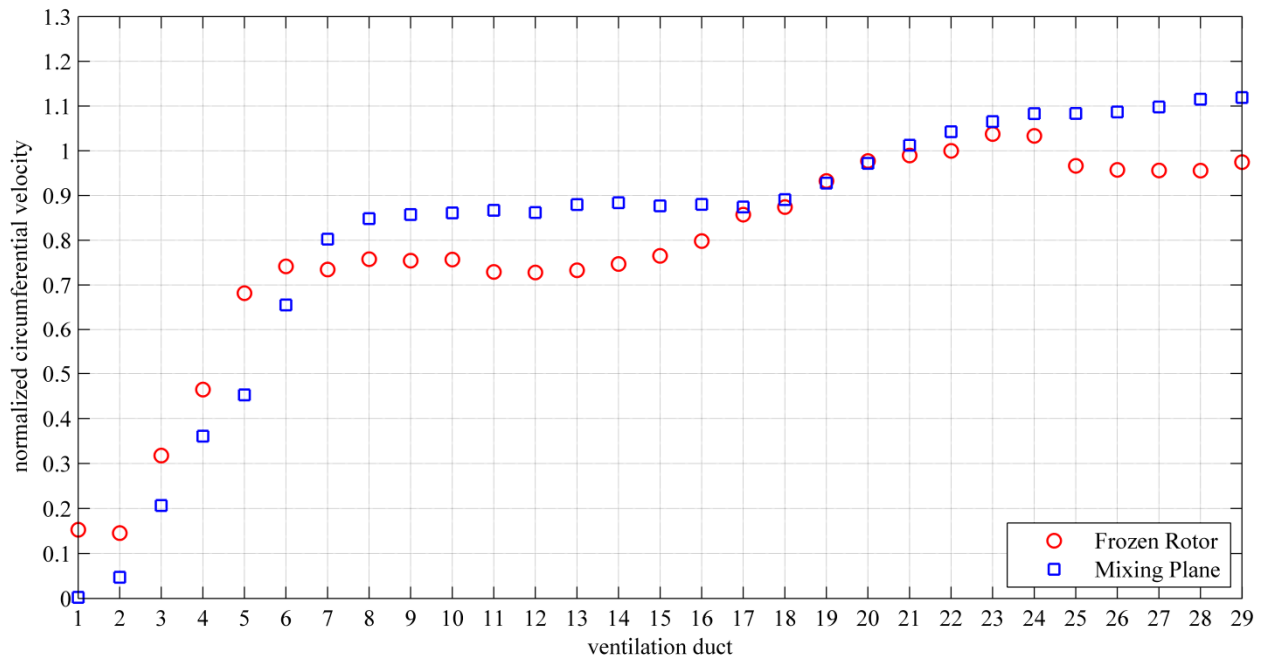


Fig. 21 Normalized circumferential velocity over the ventilation ducts in the stator for the Frozen Rotor and the Mixing Plane model

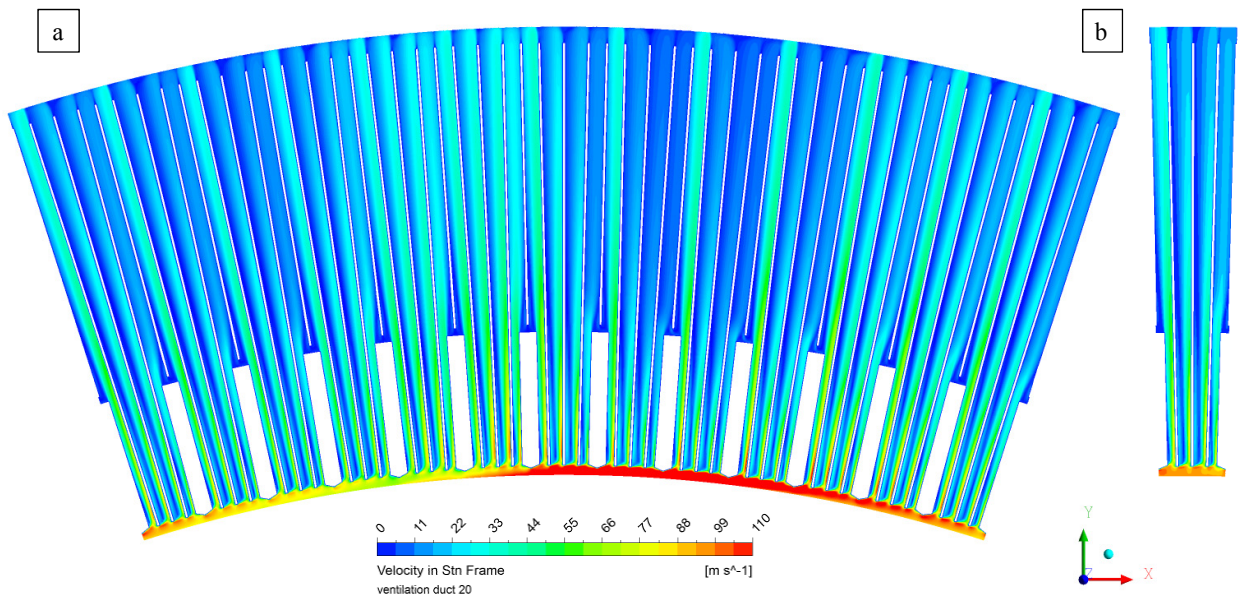


Fig. 22 Velocity of stationary frame plotted for (a) the Frozen Rotor and (b) Mixing Plane model

The magnitude of the circumferential velocity close to the inlet region is about 100 meters per second and is dominant compared to the radial velocity. In Fig. 23, the flow field at the tooth and yoke region of the 20th ventilation duct is shown for the MP model. The fluid cannot follow the contour of the wedge and the distance bars (indicated by circles), leading to reverse flows near these areas (shown by the arrows). The reverse flows are different in the sub-ducts A, B, C and D. A further effect is the completely different flow at the admissions of the various slot areas. The slot area at duct A is charged with a very high mass flow rate compared with the slot area located at duct B. The reverse flow is also different for each sub-duct; channels C and D have an increased reverse flow that stops even in the yoke region, in contrast to channels A and B where it is located in the tooth region. The channel extension causes further reverse flows at the inlet of the yoke region for channels A and B.

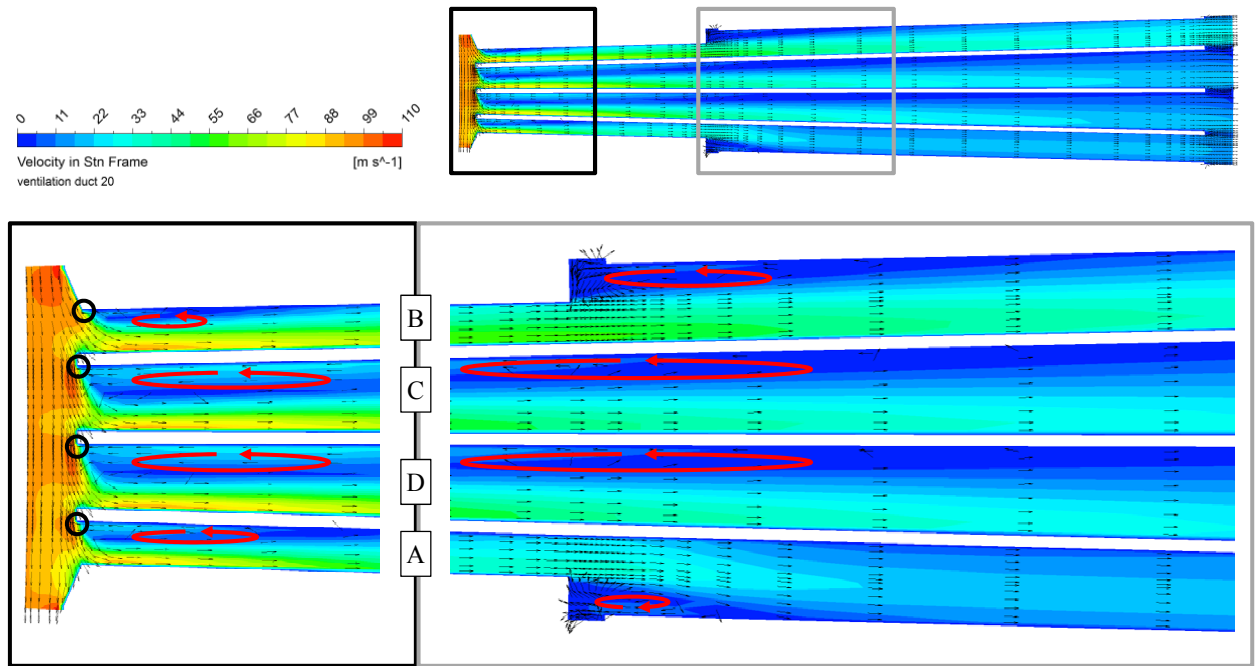


Fig. 23 Velocity and included velocity vector of stationary frame of the MP model computed at the 20th duct for the tooth and yoke region

The velocities in circumferential and radial direction match in the different models (see Fig. 24). The rapid decay of the circumferential velocity from the control area F2 up to control area F3 is due to the return of the fluid at the beginning of the sub-ducts A, B, C and D. The velocity vector changes along the stator duct. The circumferential velocity decreases to zero, even in the middle of the tooth region F3, and hence a high pressure loss results. Due to the complexity of the arrangement, the energy transport cannot be calculated analytically. The computed circumferential velocity of the FR model at F1 has been chosen as basis to normalize the numerical results.

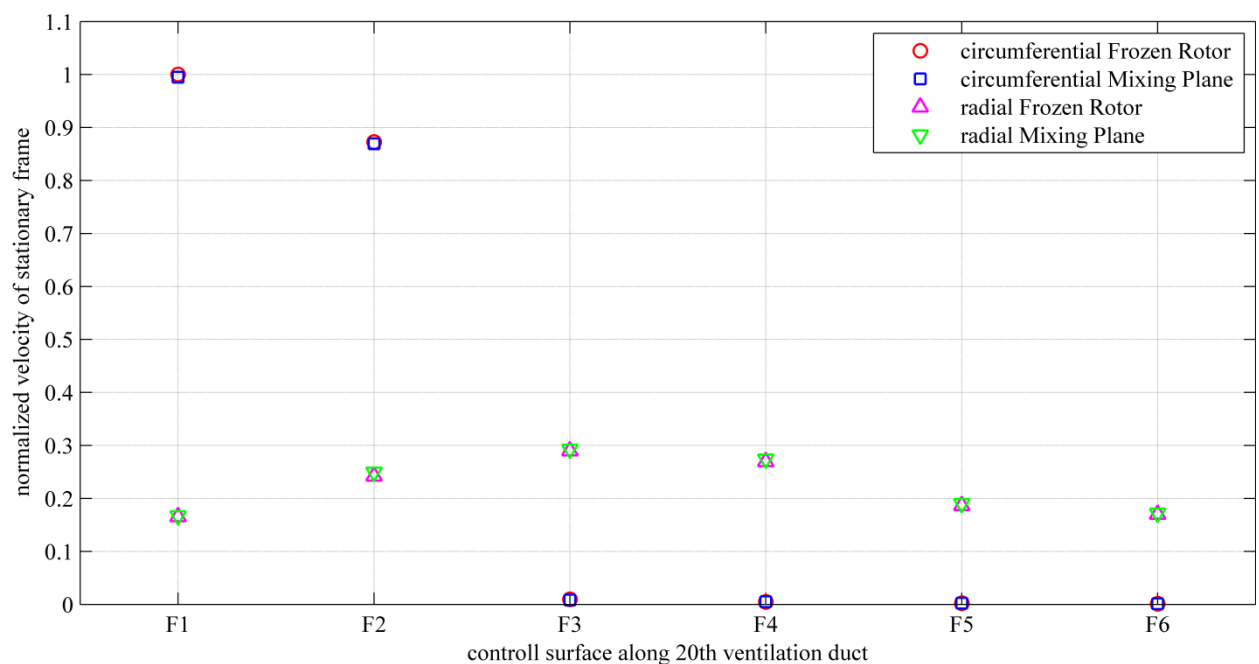


Fig. 24 Normalized circumferential and radial velocity along the 20th ventilation duct of the FR and MP model computed at the fluid control surfaces (F1-F6)

3.1.4.3 Total pressure losses

Concerning the losses and efficiency of the electrical machine, the pressure gradient along the flow path is important for the design of the fan and the cooling scheme. The localization of the pressure losses is obtained from the use of CFD and special measures are necessary to optimize the efficiency, e.g. employing different designs at the stator duct inlet, or different cross sections and lengths of the rectangular channels.

The total pressure losses have been computed for the stator ventilation ducts and are shown in Fig. 25 normalized by the total loss along the 29th duct of the Mixing Plane model. The total losses include the losses of the tooth and yoke region for both MFR models. The deviation of the averaged total pressure is about 0.7%. The main total losses occur in the tooth region caused by the rotor rotation and the arising flow separations in the rectangular sub-ducts. The losses computed at the yoke region are caused by the extension of the sub-ducts, causing additional reverse flows.

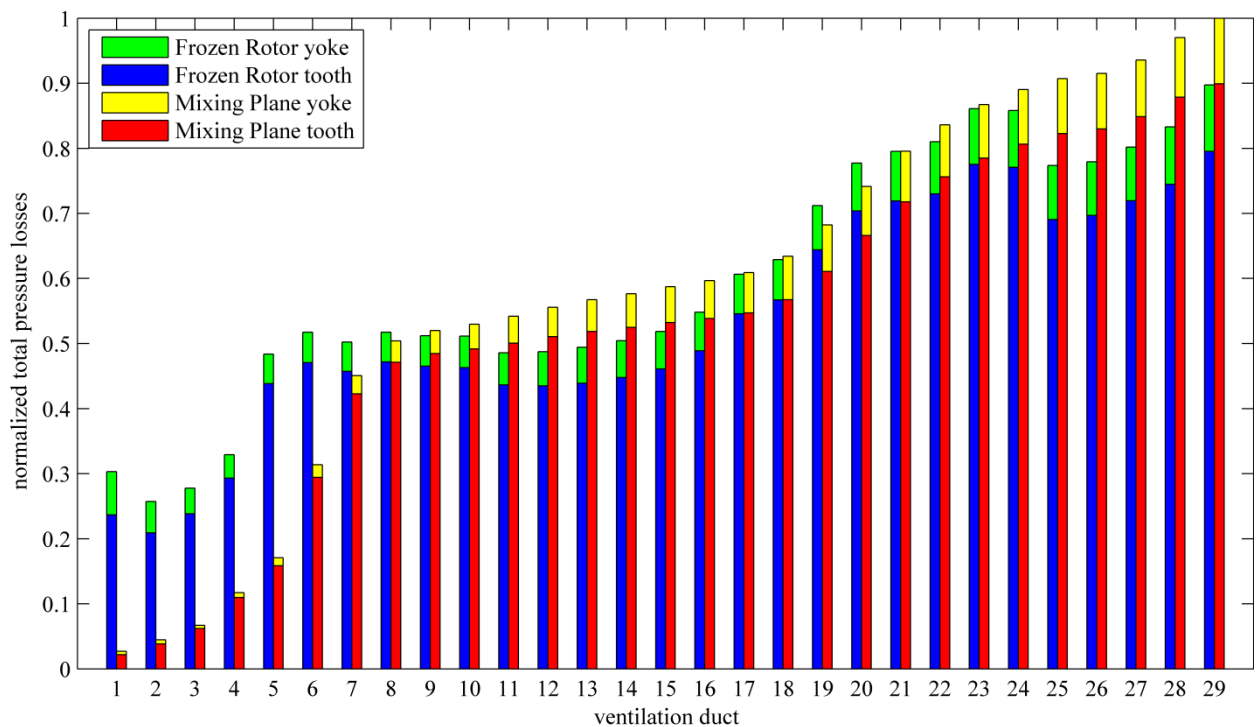


Fig. 25 Normalized total pressure losses for FR and MP model computed at tooth and yoke region

3.1.5 Results of the computed thermal field

3.1.5.1 Temperature distribution

The distribution of the fluid temperature is also an important parameter for computing the convective wall heat transfer coefficient. The heat transfer surfaces shown in Fig. 17 have to be impinged with the coolant to discharge the heat from the solid domains. The temperature of the circulated air has to be in a range between 30°C and 80° to ensure the heat transfer. The normalized temperatures have been evaluated on the stator ventilation ducts F1 and on the outlet F6 for both MFR models, as presented in Fig. 26. The deviations are 7.3% at F1 and about 1.8% at F6.

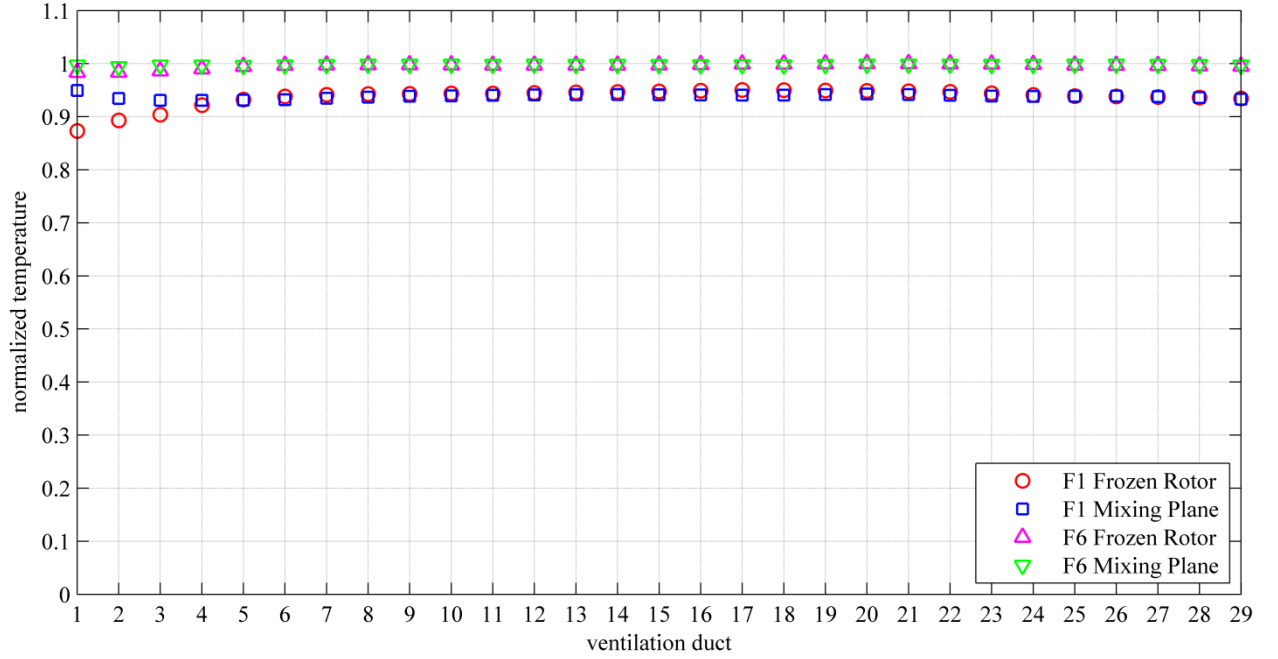


Fig. 26 Normalized temperature distribution at the fluid control surface F1 and F6 for the FR and MP model

3.1.5.2 Wall heat transfer coefficient

A further important goal of this investigation is to gain information about the magnitude of the wall heat transfer coefficient along the ventilation ducts. Therefore, the WHTC has been computed at the slot, tooth and yoke surface, see Fig. 17. The definition of the convective WHTC α is

$$\alpha = \frac{q_{wall}}{T_{wall} - T_{ref,fluid}}, \quad (3.5)$$

with the heat flux at the evaluated wall surface q_{wall} , the temperature at the wall surface T_w and the fluid reference temperature $T_{ref,fluid}$. The used reference temperature is a mean value of the mass flow averaged temperatures at the inlet surface and the outlet surface along each evaluation wall, see Fig. 16. E.g. for the tooth region, with the temperatures $T_{fluid,F1}$ at the inlet and $T_{fluid,F4}$ at the outlet, and for the yoke region, with the temperatures $T_{fluid,F4}$ at the inlet and $T_{fluid,F6}$ at the outlet:

$$T_{ref,fluid(tooth)} = \frac{T_{fluid,F4} + T_{fluid,F1}}{2}, \quad (3.6)$$

$$T_{ref,fluid(yoke)} = \frac{T_{fluid,F6} + T_{fluid,F4}}{2}. \quad (3.7)$$

A comparison has been made between this definition and the commonly used logarithmic mean temperature difference [99], and the deviation has turned out to be less than 1 K.

The different WHTCs have been computed for the MP and FR models and evaluated as area averaged values for the slot, tooth and yoke surface, see Fig. 27. Each value has been normalized by the computed WHTC at the 20th duct at the tooth region of the FR model. The averaged difference is less than 10% between the two MFR models.

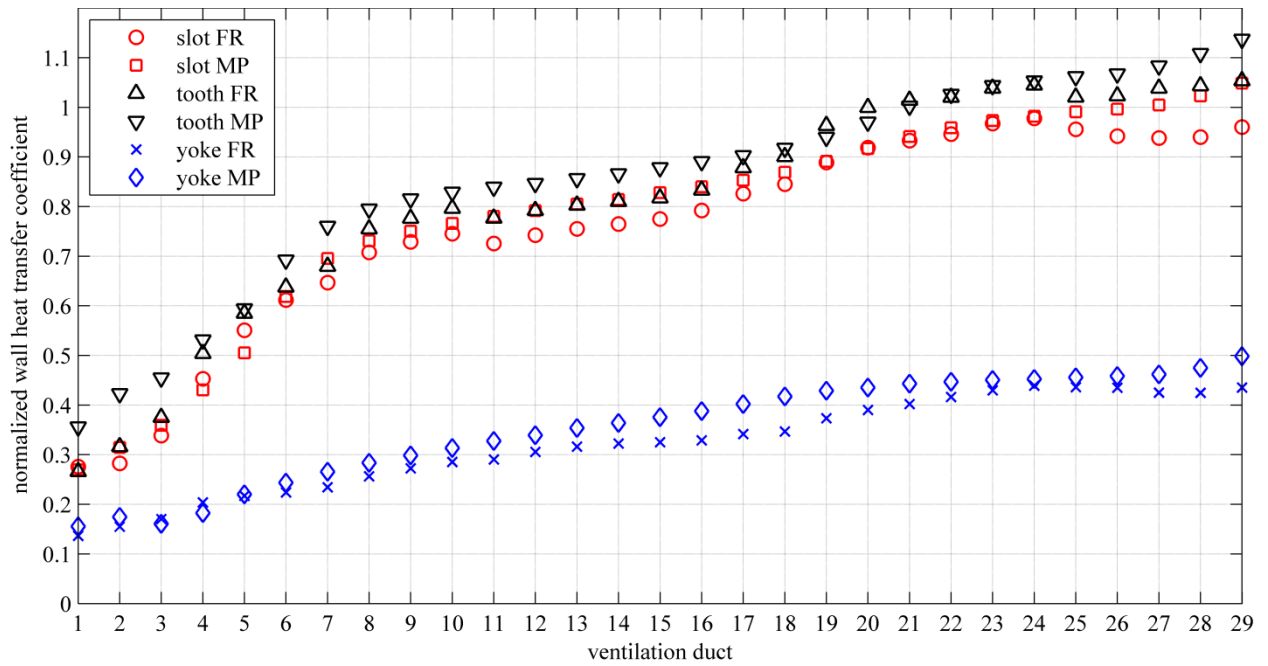


Fig. 27 Normalized wall heat transfer coefficient computed for slot, tooth and yoke region for FR and MP model

3.2 Single duct model

The investigations concerning the different implementation of the rotor rotation with the Frozen Rotor and Mixing Plane models show a low deviation of less than 11% for the evaluated parameters. This means, that it is possible to save 40% of the elements in the stator without overly compromising the accuracy of the results.

With focus on the heat transfer, further investigations have been made concerning the numerical modeling and computation of large hydro generator models. Using computational facilities available today, the value of $y^+ \approx 1$ for the dimensionless wall distance recommended in section 2.4.5 cannot be realized by CFD computations in the stator ventilation ducts, since this would lead to unbearably high numerical costs and time. The distribution of the wall heat transfer coefficient depending on the dimensionless wall distance is therefore examined in this section in more detail using single duct models. The models are similar to the MP and FR models in the stator with the main difference of including a single ventilation duct only.

3.2.1 Geometry of the numerical models

Two single duct models have been created from the overall models, called the pole section model (PSM) and the slot section model (SSM), respectively, as shown in Fig. 28. The PSM includes 13 slot sections while the SSM extends over one only.

Another important issue is to get information about the heat transfer coefficient at the slot area in dependence on the different flow conditions of the channels A and B. Therefore, the slot areas have been split into three sections. The wall heat transfer coefficient has been calculated on two slot surfaces called slot leading side located in channel A and slot trailing side located in channel B.

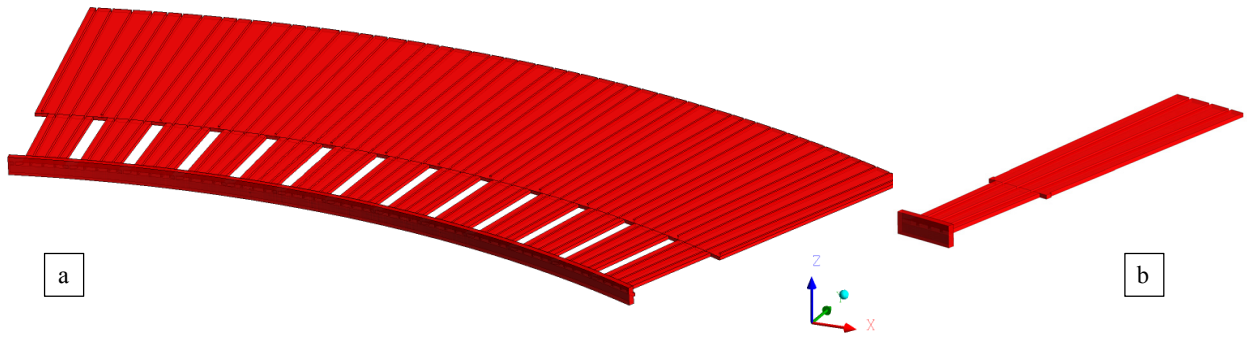


Fig. 28 Single duct models, (a) PSM and (b) SSM

3.2.2 Domain decomposition

The inlet conditions are created by profiles gained from the Frozen Rotor and the Mixing Plane overall models of the large hydro generator investigated. The inlet parameters are the velocity vector \mathbf{u} , the temperature T , the turbulent kinetic energy k and the kinetic dissipation ε . The velocity vector includes the information on the circumferential, radial and axial velocity components. These parameters have been determined at the stator side of the rotor-stator interface and are impressed at the surfaces F1 of the stator duct inlet areas at the section models, see Fig. 16. The inlet parameters obtained from each element surface of the MFR models are defined on the corresponding element surfaces of the single duct models. The inlet area is in the middle of the air gap between the rotor and the stator. Generally speaking, the inlet conditions have been obtained from the global domain of the MFR models and defined at the local domains of the single duct model.

The specified inlet boundary conditions have been computed with the MFR models at the RSI. Afterwards, the single duct model of the investigated ventilation duct can be positioned at the same location along the z -axis as shown in Fig. 29, leading to the same inlet conditions in both models. As a consequence, different investigations concerning mesh refinement, new geometric designs or other specified boundary conditions along the ventilation ducts can be carried out using smaller models.

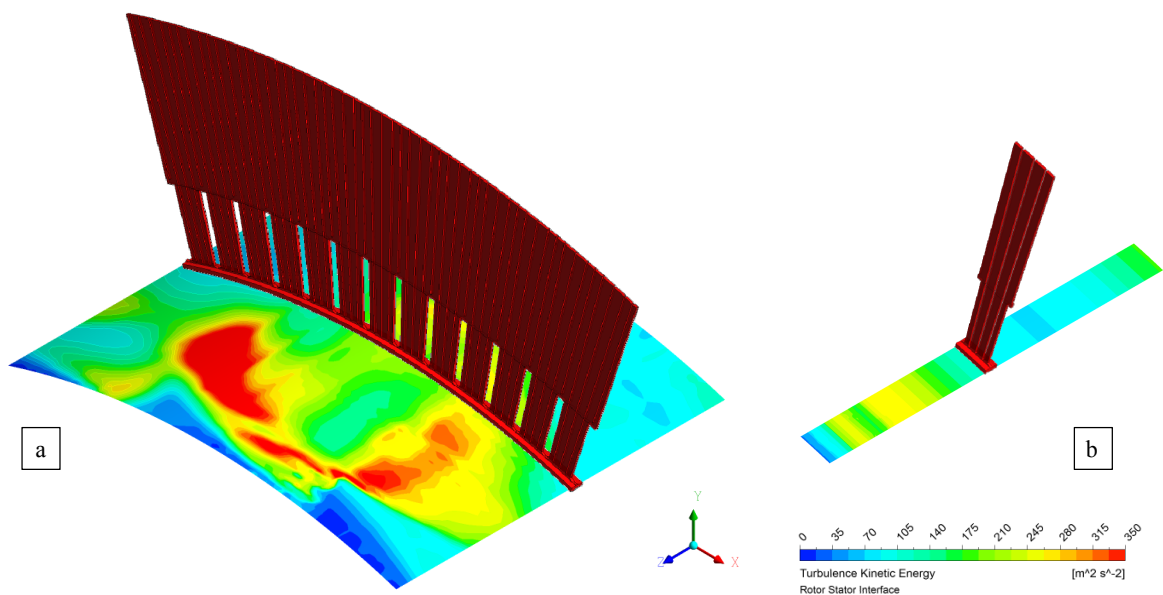


Fig. 29 Boundary condition transfer at the RSI from the overall MFR models to (a) the PSM and (b) the SSM

3.2.3 Sensitivity study

The goal of the sensitivity study is to obtain information on the computed WHTC depending on mesh refinement. As pointed out in [93], the required dimensionless wall distance $y^+ \leq 1$ is not feasible in the overall MFR models. Therefore, the deviation of the numerical results for meshes of different density is used to obtain information on the computational error concerning the heat transfer.

The following quality and sensitivity study has also been made to confirm the advantages of the SST turbulence model. Therefore, both the SST and the $k-\varepsilon$ turbulence models have been used and the mesh close to the wall has been refined in order to calculate the wall heat transfer coefficient on the tooth, yoke and the slot wall sides in dependence on the dimensionless wall distance. Additionally, the differences in the wall treatment of the used turbulence models can also be investigated.

The different element sizes for the PSM and the SSM resulting from the mesh refinement are presented in Table 9. The different meshes of the single duct models consist of hexahedral elements similar to those used in the MFR models and the numerical set-up has also been defined identically.

mesh nr.	number of elements		dimensionless wall distance			
	PSM	SSM	PSM tooth	PSM yoke	SSM tooth	SSM yoke
1	1.381.040	104.910	1,3	1,7	1,4	1,7
2	1.037.996	78.842	5,7	3,3	5,9	3,3
3	751.528	57.062	12,2	6,9	12,2	6,8
4	517.796	39.282	24,5	13,5	26,6	14,0
5	332.960	25.214	55,3	26,7	56,0	28,1
6	193.180	14.570	113,2	50,9	115,0	54,3
7	94.926	7.062	228,3	101,3	225,5	104,2

Table 9 Properties of the different models for investigating the effect of mesh refinement in the PSM and the SSM

The normalized convective wall heat transfer coefficient at the 20th ventilation duct has been plotted against the dimensionless wall distance for the pole and slot section models, evaluated at the tooth region in Fig. 30 and at the yoke region in Fig. 31. The WHTC has been normalized by the value obtained using the finest mesh of the PSM computed with the SST turbulence model with automatic wall treatment.

The main difference seen in the two figures is that the SST turbulence mode is substantially influenced by the mesh refinement. This is due to the automatic wall treatment as described in chapter 2.4.4. The $k-\varepsilon$ turbulence model computes almost the same value of the WHTC for all meshes. This is the result of the scalable wall function being used. The numerical solution of the SSM is similar to that of the PSM both for the tooth and for the yoke region.

The results computed with the SST turbulence model within the log-law layer, $30 \leq y^+ \leq 500$ seems to be constant and the highest deviation is in the buffer layer, $5 \leq y^+ \leq 30$, due to the blending of different wall treatment functions.

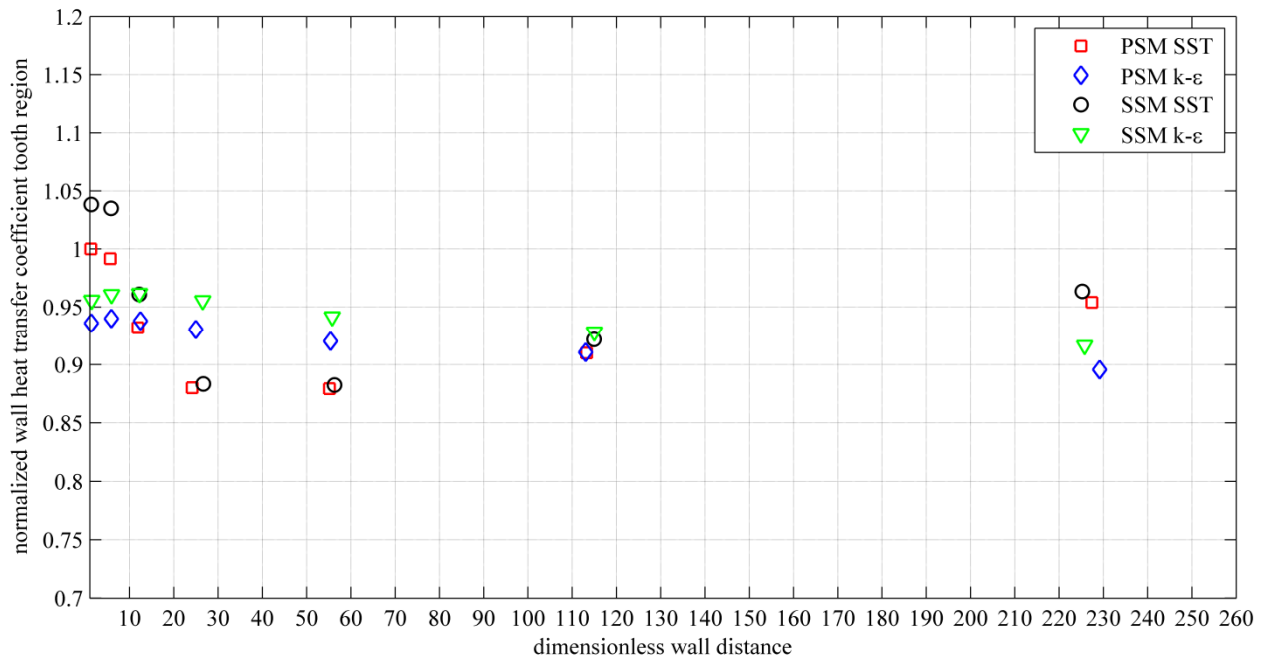


Fig. 30 Normalized wall heat transfer coefficient plotted over the dimensionless wall distance computed at the tooth region of the PSM and SSM at the 20th ventilation duct for the SST and k-ε turbulence model

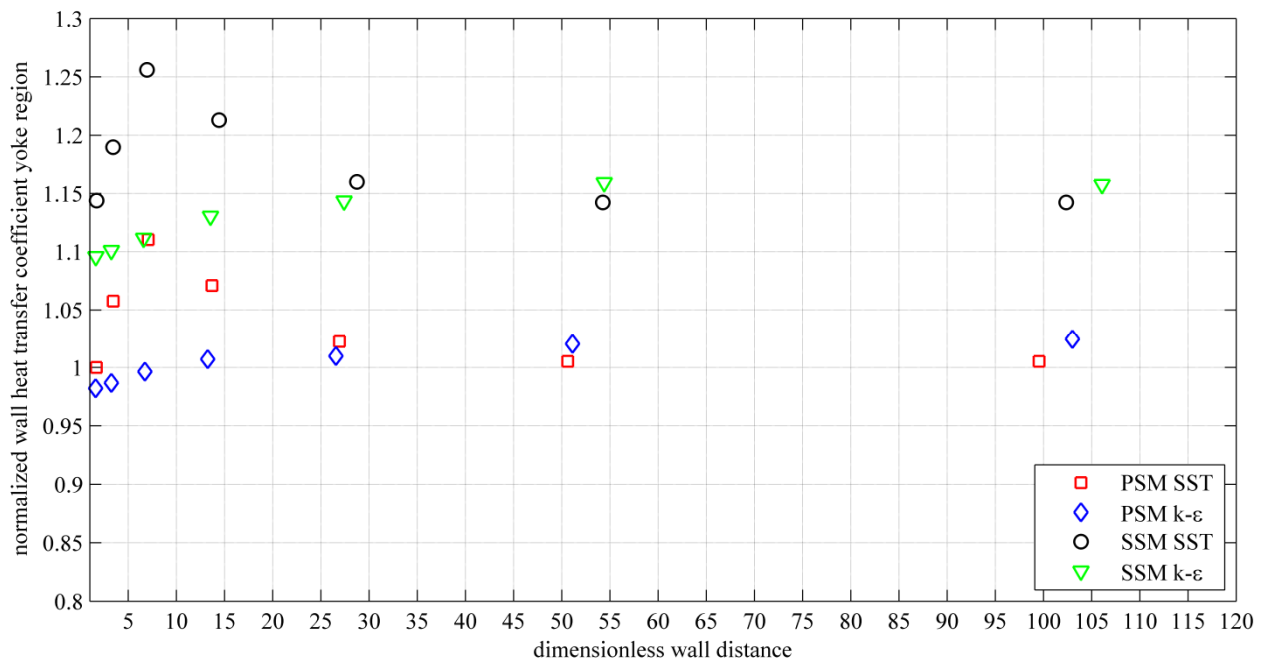


Fig. 31 Normalized wall heat transfer coefficient plotted over the dimensionless wall distance computed at the yoke region of the PSM and SSM at the 20th ventilation duct for the SST and k-ε turbulence model

3.2.4 Ventilation duct design study

A further advantage of the single duct models is that different designs of the ventilation duct with focus on the heat transfer can be analyzed in a few hours. This feature is utilized in the following to investigate various exemplary ventilation duct designs.

Seven different designs of the stator ventilation ducts have been prepared to be studied by numerical simulations in order to evaluate their fluid and thermal parameters, see Fig. 32. The

variants V1 and V3 include three rectangular channels in contrast to the other variations. The arising pressure losses in the tooth region can be minimized by the suitable design of the slot wedge and the distance bars at the stator duct inlet. Therefore, three different slot wedge designs have been investigated: the one implemented in the standard design (V1 and V3), a flattened longer wedge (V2, V4 and V5), a one sided wedge (V6), as well as a one sided wedge over the whole slot (V7). The commonly used design of the distance bars is used in V1-V5 and a new design featuring a screwed bar in the inlet is implemented in V6 and V7. To investigate the possibility to lower the production costs, the material of the distance bars is reduced in V3-V7 and the number of channels in the yoke region is reduced from four to three in V5-V7.

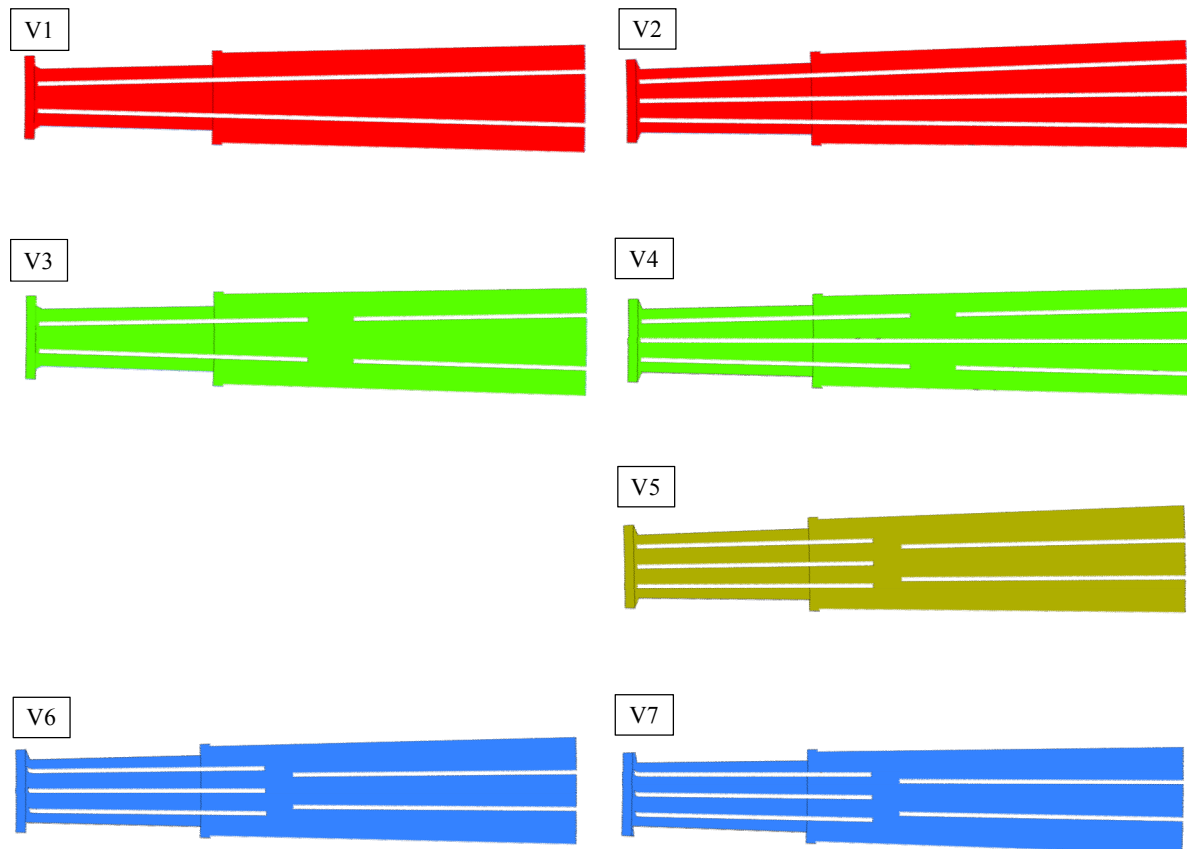


Fig. 32 Variations of ventilation duct design

3.2.4.1 Results and evaluation

The distribution of the mass flow rate is decisive for further parameters like the pressure losses and heat transfer coefficient. Therefore, this distribution has been determined at the fluid control surface F2 located at the tooth region as shown in Fig. 33, and at F5 located in the yoke region as plotted in Fig. 34. The channels A, B, C and D are defined as shown in Fig. 23.

The benefit of four channels (V2 and V4-V7) contrary to three channels (V1 and V3) is the more uniform distribution of the mass flow rate. This results in similar heat transfer along the walls defining the boundary of the channels. The slot wedge design at the inlet implies different flow rates for the channels A and B, as seen when comparing the variation V1 with V2 or V3 with V4. The difference between V5, V6 and V7 is caused by the difference in the distance bars at the stator inlet; the slot wedge design has a limited effect on the mass flow distribution. The

screwed distance bars result in higher mass flow rates nearly the same for all channels in V6. In case of V7, the rates in channels A and B near the slot as well as for channels C and D are similar.

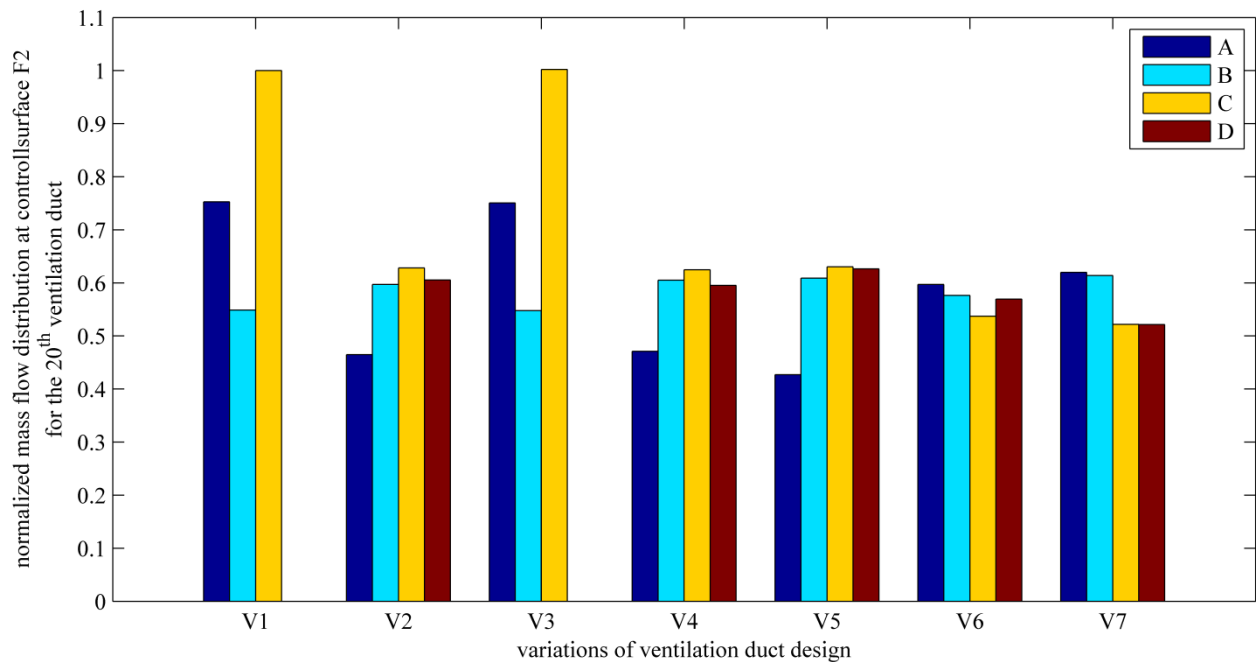


Fig. 33 Distribution of the mass flow rate in the tooth region for the investigated ventilation duct designs

The interruption of the distance bar in radial direction has no influence on the mass flow distribution in the tooth region as seen in Fig. 33. The difference in the yoke region is also not significant, as it is clear in Fig. 34 for V1 and V3 as well as V2 and V4. The change from four to three channels in the yoke results in higher mass flow rates with the same characteristics as computed for the tooth region.

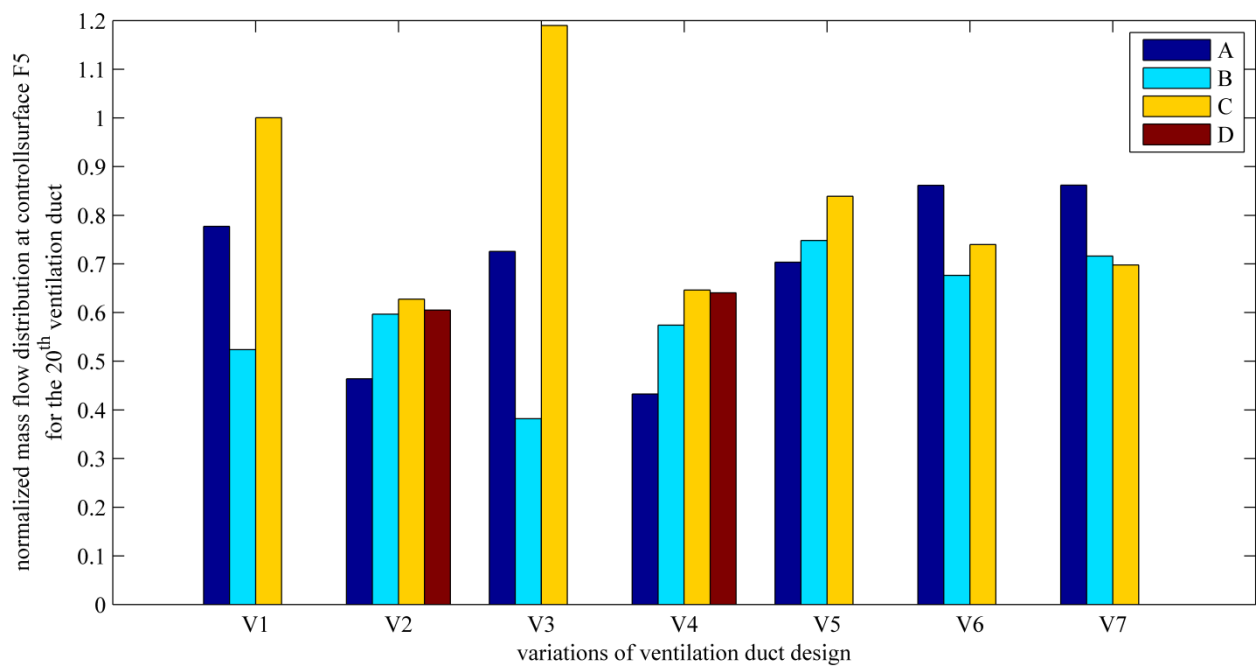


Fig. 34 Distribution of the mass flow rate in the yoke region for the investigated ventilation duct designs

Fig. 35 presents the total pressure losses for the tooth and yoke regions of the various models. The highest total losses arise in V1 and V3 due to the sub-optimal slot wedge design and the three channels in the cross section. The lowest losses are computed for V6 and V7 mainly thanks to the screwed bar at the inlet of the duct.

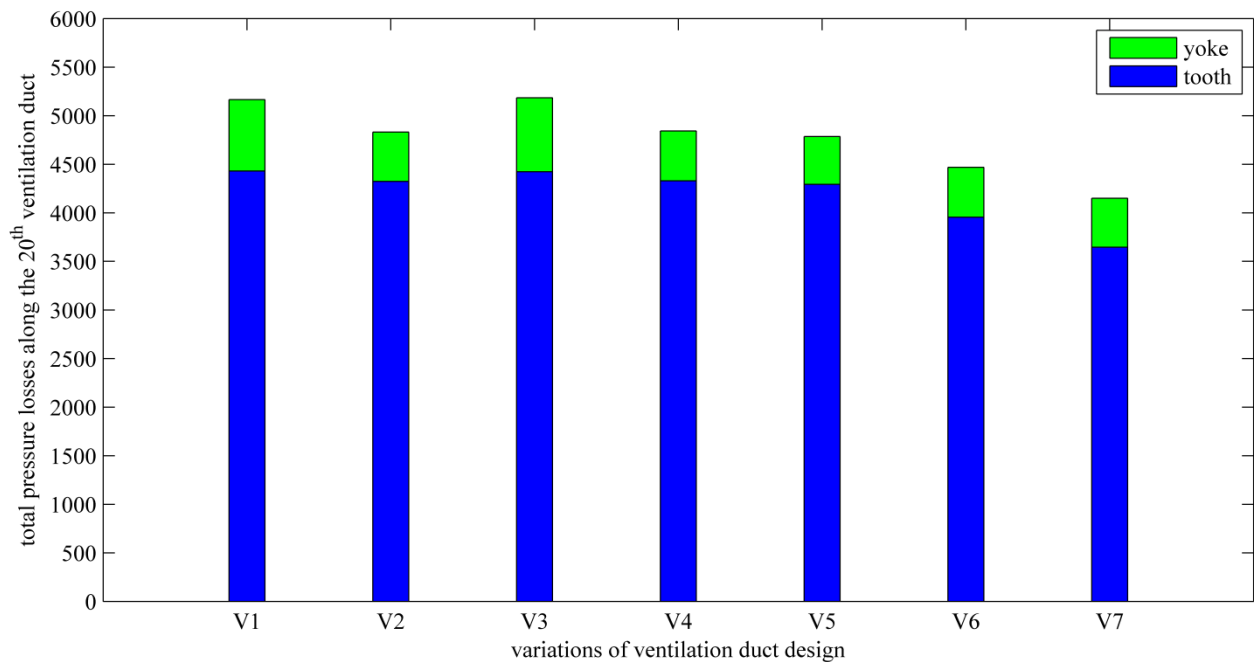


Fig. 35 Total pressure losses along tooth and yoke region for the investigated ventilation duct designs

For further investigations, the slot surface has been split into three separated surfaces as plotted in Fig. 36. S_A is along channel A and, similarly, S_B along channel B, S_Y is at the slot ground. The tooth (T) and yoke surface (Y) are the same as before.

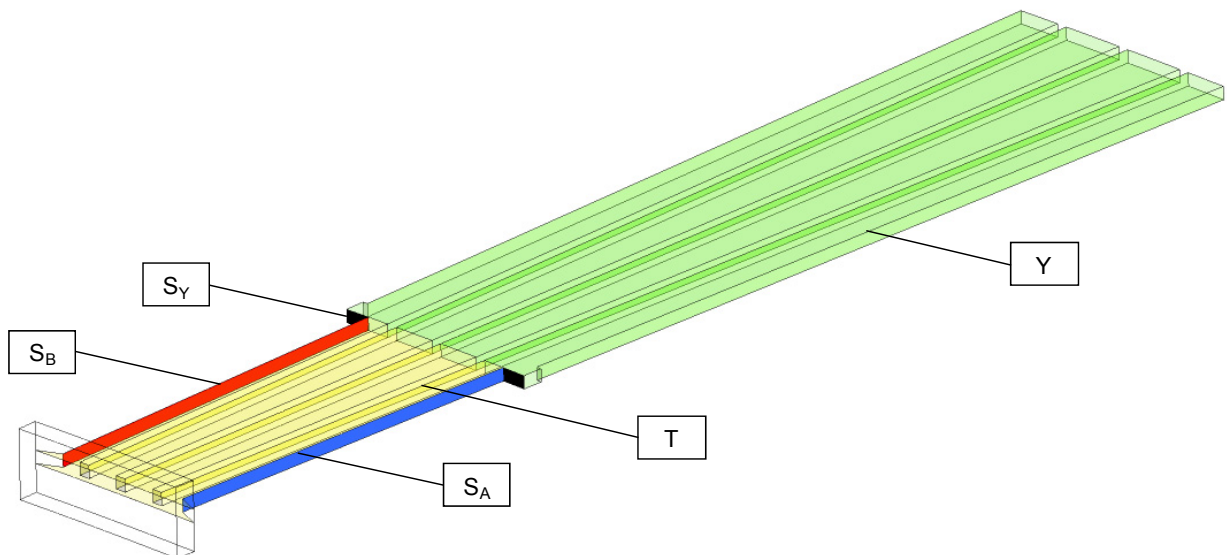


Fig. 36 Investigated surfaces to compute the heat transfer coefficient at (S_A , S_B and S_Y) the slot surfaces, at (T) the tooth surface and at (Y) the yoke surface

As easily seen in Fig. 37, the wall heat transfer coefficient is lower for the slot wedge design in V1 and V3 especially at the surface S_B . For the yoke region, the conclusion can be drawn that the reduction from four to three channels results in higher heat transfer coefficient, as seen in the

values obtained for V5-V7. The difference in the WHTC between S_A and S_B is about 60% for V1 and V3 and about 40-50% for the other models.

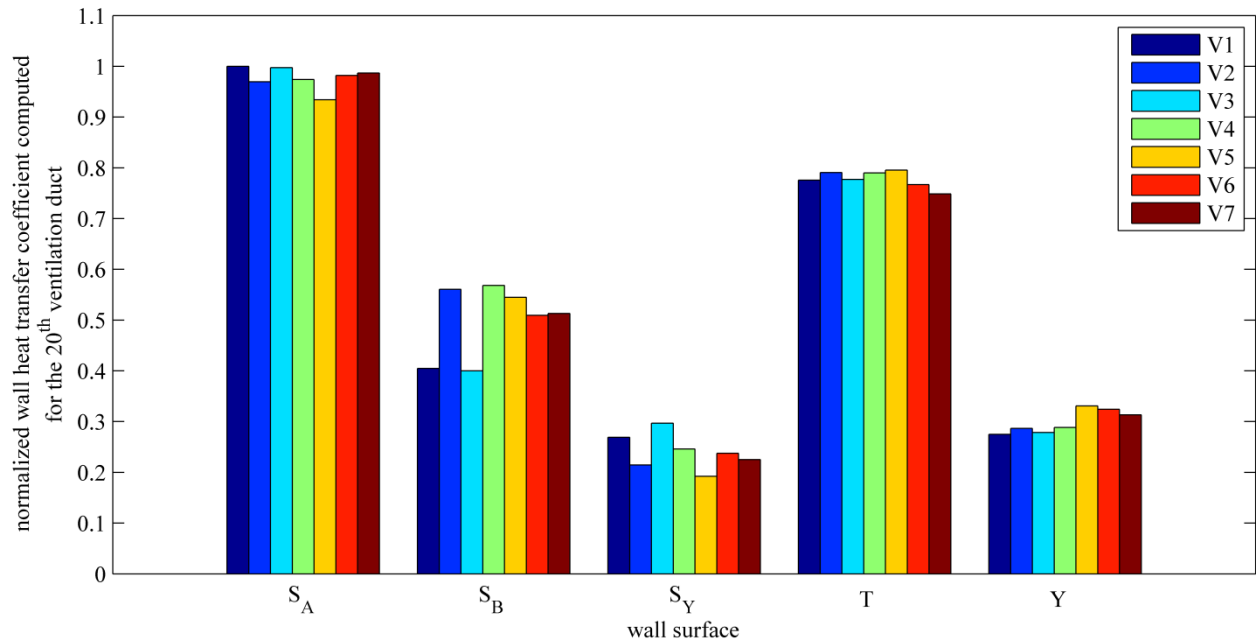


Fig. 37 Computed wall heat transfer coefficient at (S_A , S_B and S_Y) the slot surfaces, at (T) the tooth surface and at (Y) the yoke surface for the investigated ventilation duct designs

In conclusion, V1 and V3 have consistently worse results for each investigated parameter than the other variations do. The two decisive factors are the number of rectangular channels and the slot wedge design. Furthermore, the reduction by one channel in the yoke region has more advantages as illustrated by the results for models V5-V7. The screwed bars at the stator inlet in V6 and V7 have their main benefit in evoking lower pressure losses. The material reduction of the bars in the yoke region is not detrimental for the flow or thermal field but has a high benefit in lowering the costs of the electrical machine.

4 Development of a conjugate heat transfer model to investigate the heat transfer along the stator ventilation ducts

The purpose of this chapter is to develop a numerical method based on computational fluid dynamics to simulate the heat transfer inside electrical machines. The conjugate heat transfer (CHT) method used takes both heat convection and heat conduction into account to determine the temperature rise in the stator duct models of large hydro generators. This method has the benefit of investigating the heat transfer both in the fluid and the solid domains. The CHT method is an application of CFD with the energy equations solved in the solid domains. Hence, it allows defining the arising losses as thermal sources in the solid domains. Such copper and iron losses can be obtained by electromagnetic calculations. This approach simulates the physical situation more accurately than prescribing a constant value of the heat flux or the temperature at the walls as it is usual in common CFD simulations. Another advantage of CHT over other approaches is that it considers the actual wall heat transfer coefficient.

Three different test cases are studied with different slot section components. The numerical models are validated by comparison to measurement data for a range of mass flow rates. A combination of numerical simulations and measurements is presented. The measured data for the air mass flow and the heat losses are used as boundary conditions for the determination of the temperature distribution in the solid and fluid domains. The data obtained by the numerical computation are compared with measurement data for different mass flow rates of the cooling fluid. The quality of the computed values depending on the different mass flow rates shows a good agreement with the measured data. The temperature distribution in the solid domains depending on different material properties is also obtained in this investigation. This validation has been presented at the conference [57] and published in [58].

Furthermore, a detailed analysis of the fluid flow in small air gaps is carried out using an approach based on a surface thermal resistance neglecting the convective heat transfer. This interface method (IFM) is compared with the CHT simulation and the calorimetric measurements. These findings have been presented at the conference [59] and accepted for publication in [60].

4.1 Measurement of the stator laboratory model

A simplified model of a stator section has been under experimental investigation at the industrial partner ANDRITZ Hydro GmbH [100]. The main objective of the measurements has been to find and compare the thermal characteristics of different winding assemblies.

The conventional design of fixing the winding assembly in the slot uses epoxy resin. The disadvantage of this material is that the cross section of the rectangular cooling channels can be

reduced by the leaking of the epoxy resin during the positioning of the windings in the slot. A fixation of the winding assembly in the slot can also be achieved by introducing a ripple spring on one side along the winding. Furthermore, a design without epoxy resin or ripple spring is also possible to fix the winding in radial position by using a slot wedge, which leads to an air gap between stator iron and the winding assembly. Each method has advantages and disadvantages, especially in the temperature distribution in the solid domains which will be investigated in this section.

4.1.1 Measurement set-up

The laboratory model and the cooling scheme are shown in detail in Fig. 38. The cooling fluid, air, streams from the inlet through the measuring nozzle (a) to the temperature probe (b) and from there through rectangular channels of wood (c) into the stator duct model (d). Upon heat exchange, the warm air streams through wooden ducts to an outlet channel, which includes resistance thermo elements (f). The outer surface of the model has been insulated (e) to reduce the secondary heat flux.

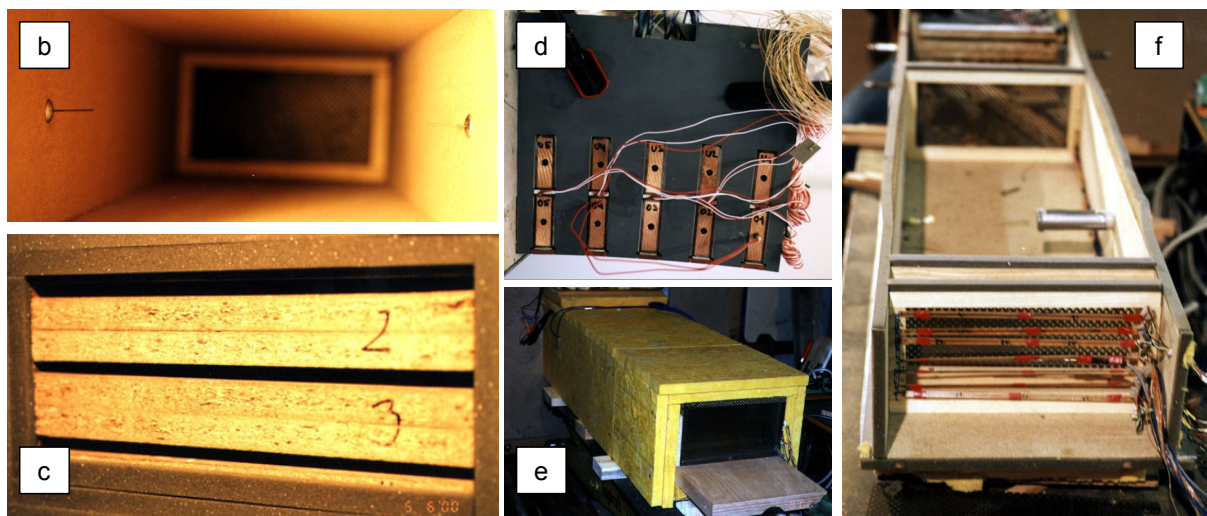
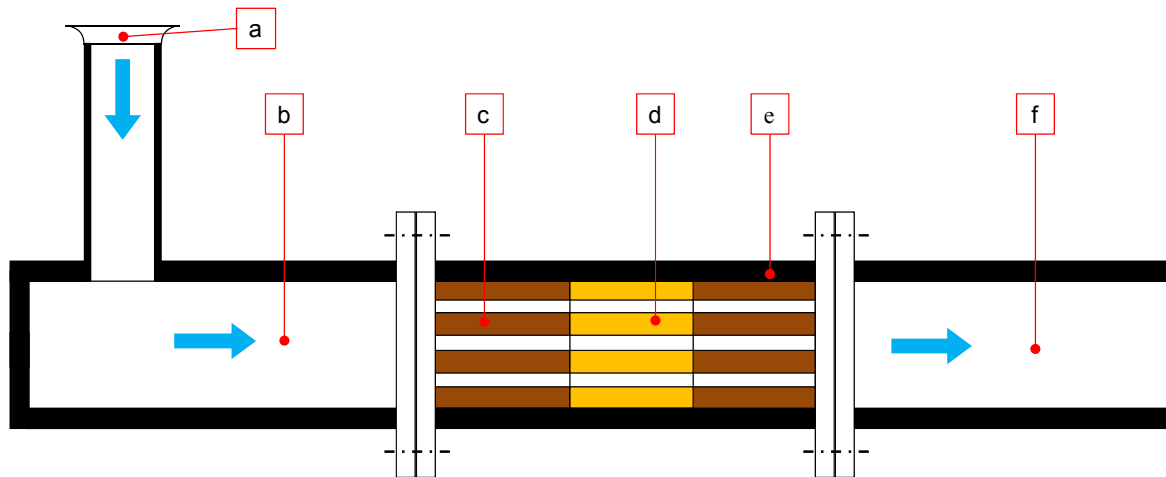


Fig. 38 Calorimetric measurement and experimental set-up of the stator laboratory model; (a) measuring nozzle, (b) Pt-100 temperature probe, (c) wooden channels, (d) stator duct model, (e) insulation of the model and (f) resistance thermo elements

4.1.2 Measuring physical parameters

The measuring nozzle defines the volume flow rate V_{in} immediately in front of the model inlet [100]. The fluid temperature T and density ρ have been measured at the inlet and outlet of the stator duct model. These calorimetric measurement data allow calculating the heat flux in steady state. The energy exchange occurs in the stator duct model. Therefore, it is important to calculate both the solid temperature and the fluid temperature in the ducts. Fig. 39 shows the positions of the temperature probes in the iron domain. The stator model consists of a section including five slots in circumferential direction and three ventilation ducts with distance bars between the laminated iron sheets in axial direction. The temperature has been measured in two stator cores, (a) and (b). To accomplish this, 15 Pt-100 resistance thermometers [101] with a 20 mm probe length have been positioned at each stator core.

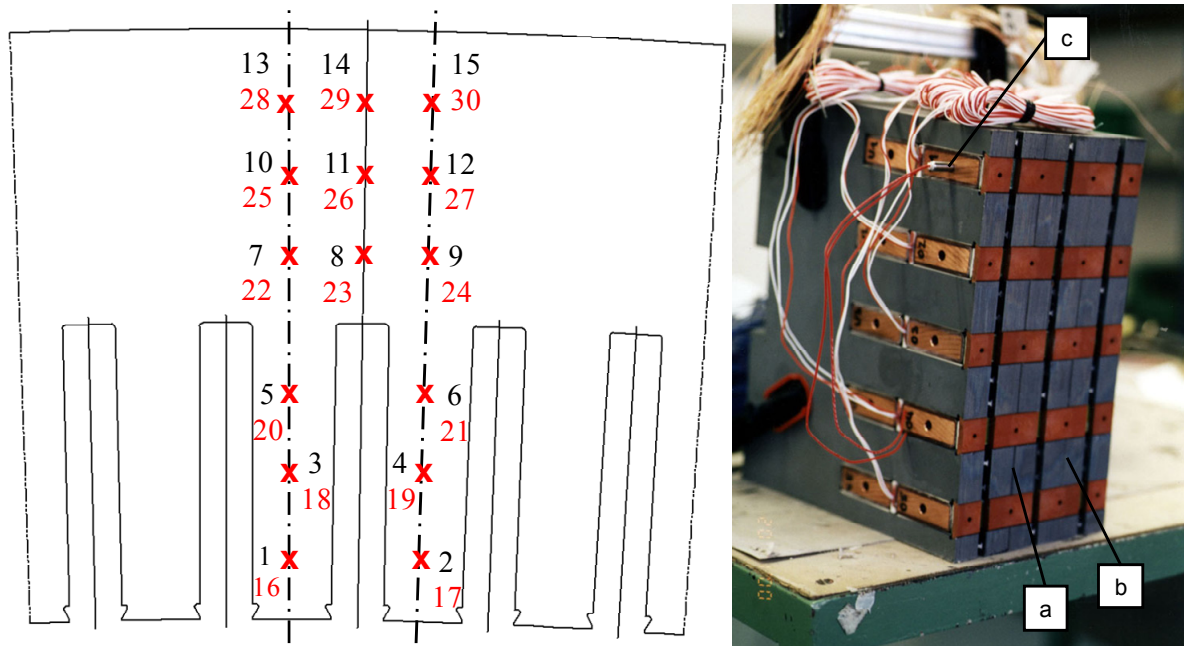


Fig. 39 Positions of measurement probes in the iron; (a) 1st stator core, (b) 2nd stator core and (c) heating rod

The heat sources have been simulated by heating rods positioned in a hole in the middle of the winding bars made of solid copper, see Fig. 40. The length of the rod has been 100 mm, with a diameter of 6 mm and a constant heat output. The upper and lower bars have been heated up to reach steady state. The heat output has been constant during the whole experiment. Thereupon, the temperatures have been measured in each copper bar with two NiCrNi thermocouples 60 mm in length [100]. The temperature in the spacer has been measured by a Pt-100.

The temperature characteristics of the different stator models have been measured for five different operating conditions mainly differing in the volume flow rate. The computed temperature differences in the fluid, copper and iron domain have been normalized by the fluid inlet temperature. The inlet conditions of the volume flow rate and the measured temperature differences for each model under investigation are presented in Table 10. The temperatures are averaged values of the measured temperatures of the solid domains, like T_{copper} and T_{iron} . The fluid temperatures are the measured values at the inlet T_{in} and outlet T_{out} . The different operating conditions have been obtained by varying the volume flow rate V_{in} and the density ρ_{in} at the inlet.

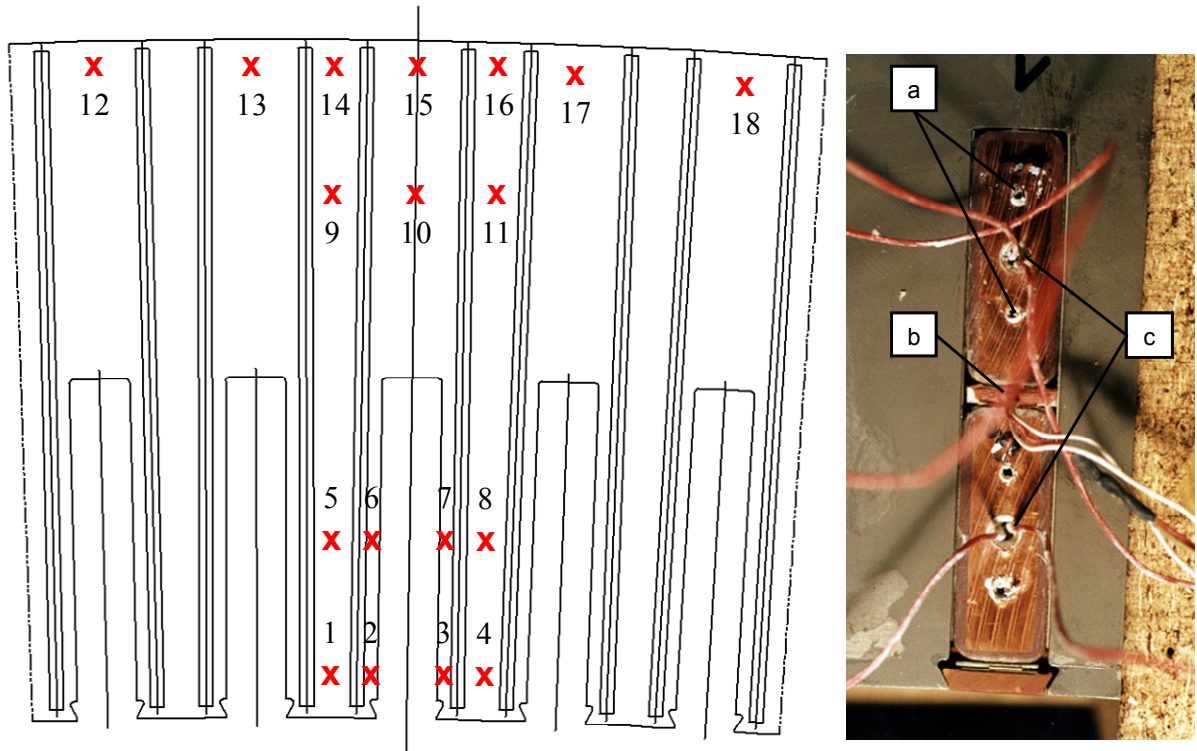


Fig. 40 Positions of temperature measurement devices for the cooling fluid; solid temperature positions for measuring (a) copper temperature and (b) spacer temperature; position of (c) the heating rod

	V_{in} m ³ /s	ρ_{in} kg/m ³	$\frac{T_{out} - T_{in}}{T_{in}}$	$\frac{T_{copper} - T_{in}}{T_{in}}$	$\frac{T_{iron} - T_{in}}{T_{in}}$
model A	0.080	1.130	0.12	1.39	0.27
	0.060	1.129	0.16	1.60	0.36
	0.040	1.138	0.26	1.99	0.55
	0.025	1.134	0.41	2.35	0.81
	0.015	1.133	0.68	2.96	1.30
model B	0.079	1.155	0.15	1.80	0.48
	0.061	1.154	0.21	2.04	0.60
	0.041	1.152	0.31	2.40	0.83
	0.025	1.154	0.51	2.94	1.22
	0.015	1.152	0.81	3.55	1.80
model C	0.078	1.155	0.15	1.80	0.51
	0.060	1.149	0.20	2.03	0.64
	0.041	1.147	0.31	2.34	0.85
	0.025	1.149	0.51	2.84	1.23
	0.015	1.151	0.81	3.39	1.77

Table 10 Calorimetric measurement results

4.2 CHT ventilation duct model

In order to study the measurement results in detail, a comparison with numerical results was carried out, where it was useful to apply the CHT method, because it takes both convection and conduction into account. Therefore, the numerical heat transfer model could be made more realistic, especially regarding the temperature rise in the solid domains caused by losses.

4.2.1 Geometry of the model

The measurement set-up has been simulated, meshed and analyzed using the commercial software. The whole numerical model is shown in Fig. 41. The cooling scheme is the same as during the measurements, i.e. the wooden channels have also been modeled. Adiabatic walls have been assumed at the top and the bottom of the numerical model in z -direction. In addition, a periodic boundary condition has been defined at the surfaces normal to the x -direction. The goal of this is to reduce the section to be analyzed (less number of nodes together with smaller elements) with the advantage of lower computational costs.

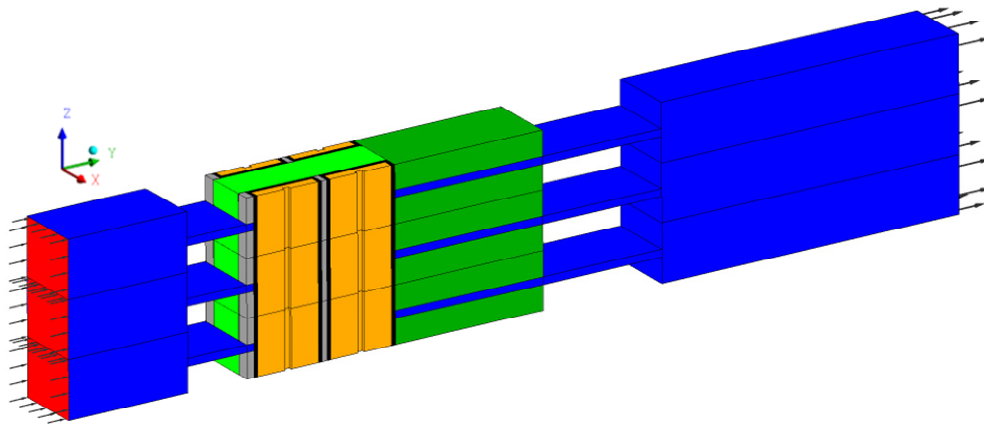


Fig. 41 Numerical CHT stator laboratory model

Fig. 42 shows the numerical stator model in detail. For the calculation, one slot section has been investigated. This is made possible by the inlet conditions being the same for each slot section in the measurement. The winding assemblies have been exactly modeled as in the measurement set-up, i.e. copper bars (d) and (e) with insulation (f), spacer (g) between the winding bars and, for positioning in radial direction, the slot wedge (h). The iron (b) and (c) is located at the top and bottom of the fluid (a).

The difference in the models is in the contact between insulation and iron resulting in various types of the winding assembly, as indicated in Fig. 43. Model A has an air gap (blue) between insulation and iron teeth. This air gap has a constant width of 0.25 mm along the insulated copper bars. The cooling fluid can stream in axial direction from one duct to another thanks to the air gap.

A ripple spring (red) with a constant width of 0.5 mm is positioned on one side between the iron teeth and the insulation instead of the air gap in model B. This ripple spring has a corrugation along the diagonal direction of the y - z plane which has to be smoothed along the surface. This is achieved by a thermal resistance at the contact interface causing an asymmetric energy transport and higher thermal fluxes at the side without a ripple spring.

Finally, model C is similar to model A, with the difference that epoxy resin (white) is also present. In this case the air can stream in axial direction through the air gap (blue), like in model A.

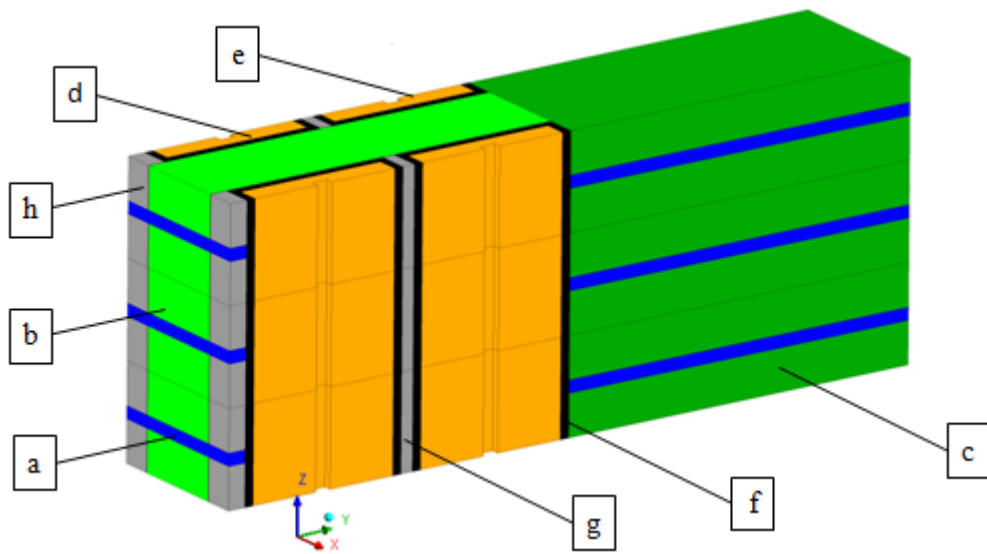


Fig. 42 Numerical CHT stator laboratory model consisting of (a) the fluid in the stator duct, (b) iron teeth, (c) iron yoke, (d) top copper bar, (e) bottom copper bar, (f) insulation, (g) spacer between bars and (h) slot wedge

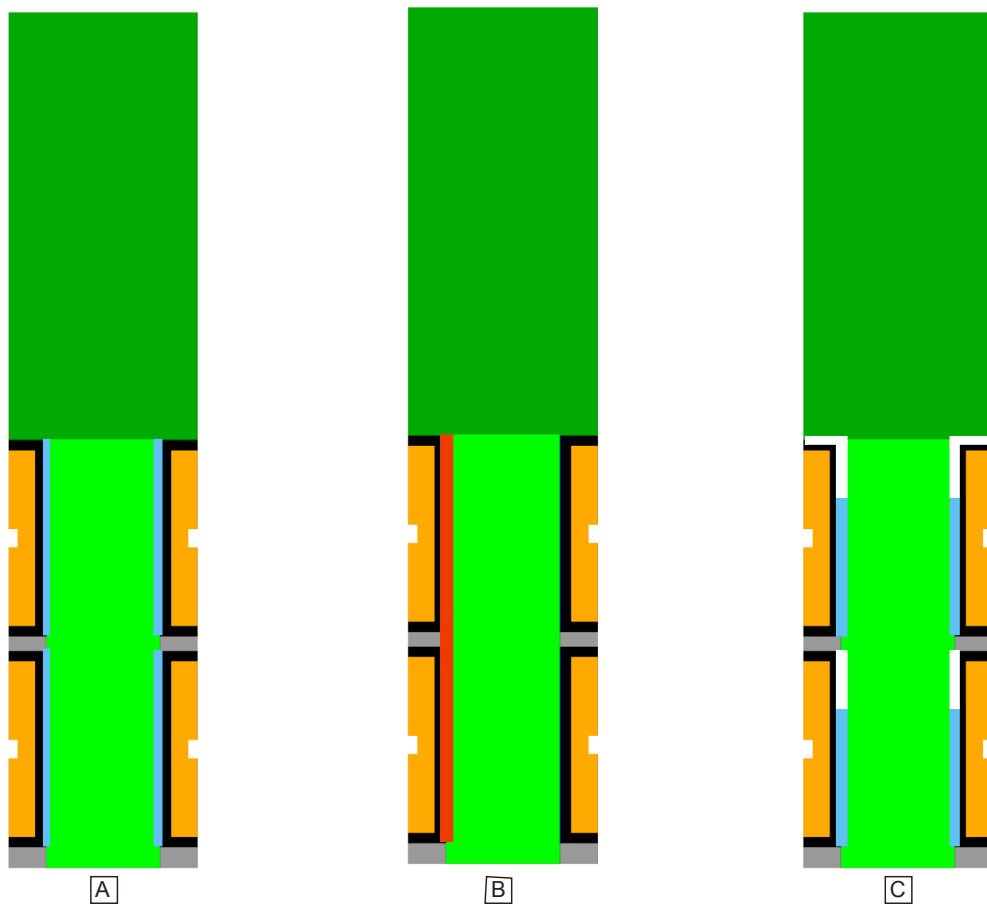


Fig. 43 Investigated models with different winding assemblies; (blue) air, (red) ripple spring and (white) epoxy resin

4.2.2 Numerical set-up

The SST turbulence model with automatic wall treatment has been used for a detailed simulation of the fluid flow and the heat transfer in the different fluid and solid domains. The thin air gap in model A and model C has been modeled with an extremely fine mesh to reach the value $y^+ \approx 1$ for the dimensionless grid parameter in order to obtain accurate results and to be able to decide whether heat convection has to be taken into account or heat conduction is the driving force at low Reynolds numbers.

4.2.3 Material properties of the coolant

The commonly used material properties of air defined as an ideal gas have been adopted to implement the temperature dependence of the streaming fluid. The material parameters as listed in [99] have been adjusted by a Gauss Newton method. The heat capacity c_p is expressed by the zero pressure polynomial [89] as

$$\frac{c_p}{R_s} = a_1 + a_2T + a_3T^2 + a_4T^3 + a_5T^4, \quad (4.1)$$

with the gas constant for air $R_s = 287.12 \text{ J/kgK}$, the temperature T and the additional coefficients

$$\begin{aligned} a_1 &= 3.57, & a_2 &= -4.3 \cdot 10^{-4} \text{ K}^{-1}, \\ a_3 &= -4.2 \cdot 10^{-8} \text{ K}^{-2}, & a_4 &= 3.1 \cdot 10^{-9} \text{ K}^{-3}, \\ a_5 &= -2.4 \cdot 10^{-12} \text{ K}^{-4}. \end{aligned}$$

The values for the dynamic viscosity μ are approximated by the Sutherland formula

$$\frac{\mu}{\mu_{ref}} = \frac{T_{ref} + S_\mu}{T + S_\mu} \cdot \left(\frac{T}{T_{ref}} \right)^{n_\mu}, \quad (4.2)$$

similarly the thermal conductivity λ :

$$\frac{\lambda}{\lambda_{ref}} = \frac{T_{ref} + S_\lambda}{T + S_\lambda} \cdot \left(\frac{T}{T_{ref}} \right)^{n_\lambda}. \quad (4.3)$$

In these formulas, S_μ and S_λ stand for the Sutherland constant and n_μ and n_λ for the appropriate exponents. For the reference viscosity and reference conductivity, the following values have been chosen from a material property table [99] at the reference temperature $T_0=325 \text{ K}$ which is close to the mean operating temperature of the cooling fluid:

$$\begin{aligned} S_\mu &= 77.80 \text{ K}, & \mu_0 &= 1.97 \cdot 10^{-5} \text{ Pa s}, & n_\mu &= 1.57, \\ S_\lambda &= 60.71 \text{ K}, & \lambda_0 &= 2.82 \cdot 10^{-3} \text{ W/mK}, & n_\lambda &= 1.66. \end{aligned}$$

The material properties are accurately approximated in the temperature range from about 260 K to 670 K with this approach. It is not recommended to use these parameters outside this range of temperature [99].

The approximation of the temperature dependent parameters is plotted in Fig. 44 with the blue line and the reference points marked by the red circles.

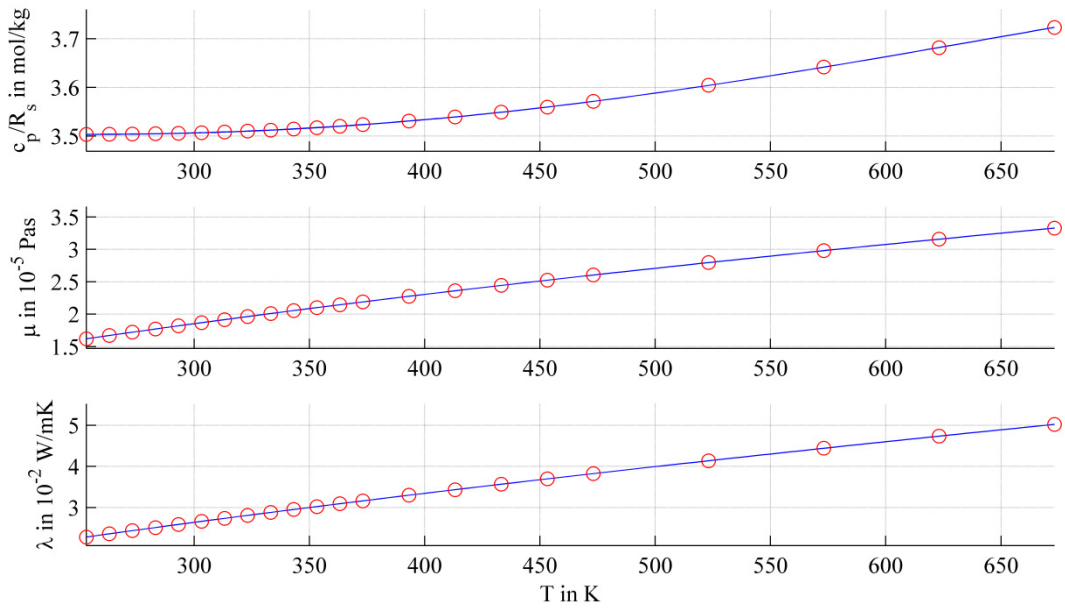


Fig. 44 Material properties of air at a pressure of 1 bar as obtained from [99] (red circle) and by the approximation used (blue line)

4.2.4 Material properties of the solids

The CHT method solves the transport equations in the solid domains, too. The most important material parameter in this equation is the thermal conductivity λ , which has great influence on heat conduction and has to be known accurately. This parameter has been assumed to be isotropic for the copper, insulation, spacer, slot wedge, ripple spring, distance bar and epoxy resin and to be anisotropic for the iron.

4.2.5 Boundary conditions

The mass flow rate and the inlet temperature have been defined as measured, see Table 10. The pressure at the outlet has been taken to equal the ambient pressure. The heat output from the heating element has been prescribed along a length of 100 mm in the middle of the copper bars with a constant value obtained from the measurement.

4.3 Validation of the CHT model with measurements

The following figures show a comparison of the CHT solution data (red line) with the measurement data (blue line) for three temperature differences. The temperature values have been normalized in the following figures by the fluid temperature measured at the inlet.

The comparison shows a good agreement of the numerical solution with measurements for each stator duct model. The averaged deviations are less than 1.5% for the copper temperature, less than 8% for the iron temperature and less than 3.5% for the fluid temperature. Based on these results, the conclusion can be drawn that the best agreement for these simplified numerical models is obtained for model C and the worst for model A within a range of less than 10%. Both sets of results indicate minimal relative benefits of model C in contrast to the other designs.

4.3.1 Copper temperature

The temperature difference in Fig. 45 is calculated with an average value of the copper temperature in the top and bottom bar and the fluid temperature at the inlet. The deviation occurs in the copper, because the inlet temperature has been defined from the measurements for the CFD calculation and is, therefore, exactly the same as in the measurement.

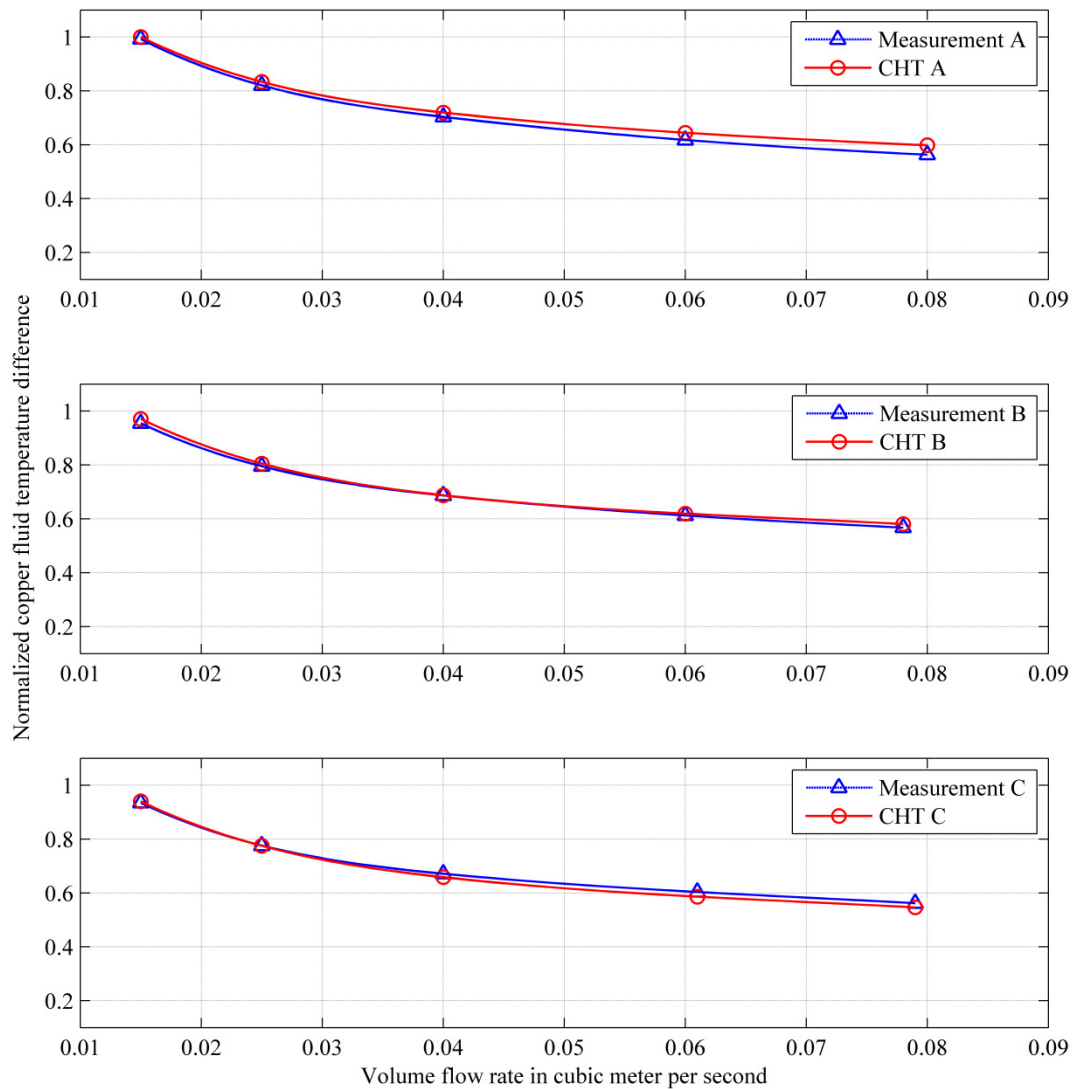


Fig. 45 Normalized temperature difference between copper and fluid inlet for the model A, model B and model C, obtained by measurements and CHT simulation

The average deviation is 1.98% for model A, 0.95% for model B and 1.06% for model C. The diagram shows that the differences between the models become smaller with a higher flow rate in the measurements, a behavior not reflected in the calculation. The difference of the results at the highest flow rate is 3.54% for model A, 1.34 % for model B, and 1.57 % for model C.

The distribution of the temperature is plotted in Fig. 46 for the stator duct models A, B and C for a volume flow rate of 0.015 m³/s. The surface shown is at the middle of the first stator core and the temperature is plotted in the whole solid domain. The highest copper temperatures are found in model A, caused by the low thermal conductivity of the used fluid in the air gap between the iron and the insulation. This effect has an influence on the heat conduction. The low

mass flow rate is also a disadvantage for the convective heat transfer. The result of these two effects is that the heat could not be absorbed by the cooling flow and the solid domains are heated up.

The asymmetric temperature in model B is also recognizable in the iron; the temperature in the iron is higher on the opposite side of the ripple spring (bottom side) caused by the higher heat flux. The heat flux is mainly transported by convection. The thermal conductivity on the side of the ripple spring is lower due to the air pockets resulting from the corrugation of the ripple spring.

The epoxy resin in model C ensures a lower temperature in the insulation than along the air gap (see details in Fig. 46 C). This has a positive effect on the properties of the insulation during aging.

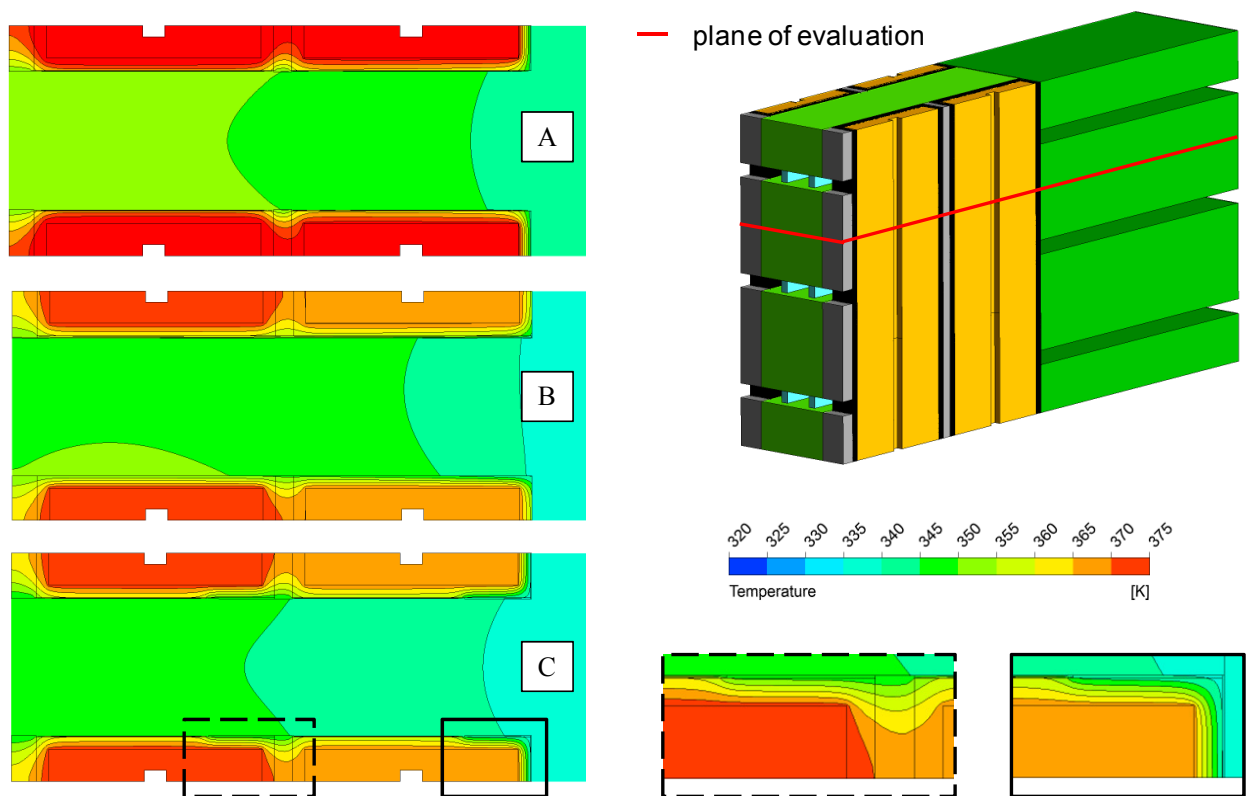


Fig. 46 Temperature plot through the middle of the stator core at the plane marked by red including the solid domains for model A, B and C at a volume flow rate of $0.015 \text{ m}^3/\text{s}$

4.3.2 Iron temperature

The iron temperature has been calculated as an average value of all measuring points (Fig. 39). The difference to the fluid inlet temperature has been plotted as before. The average deviation is 13.20 % for model A, 6.04 % for model B and 3.52 % for model C. Note that model A has the highest deviation for the iron temperature, see Fig. 47. The deviation for each winding assembly decreases with at higher volume flow rates.

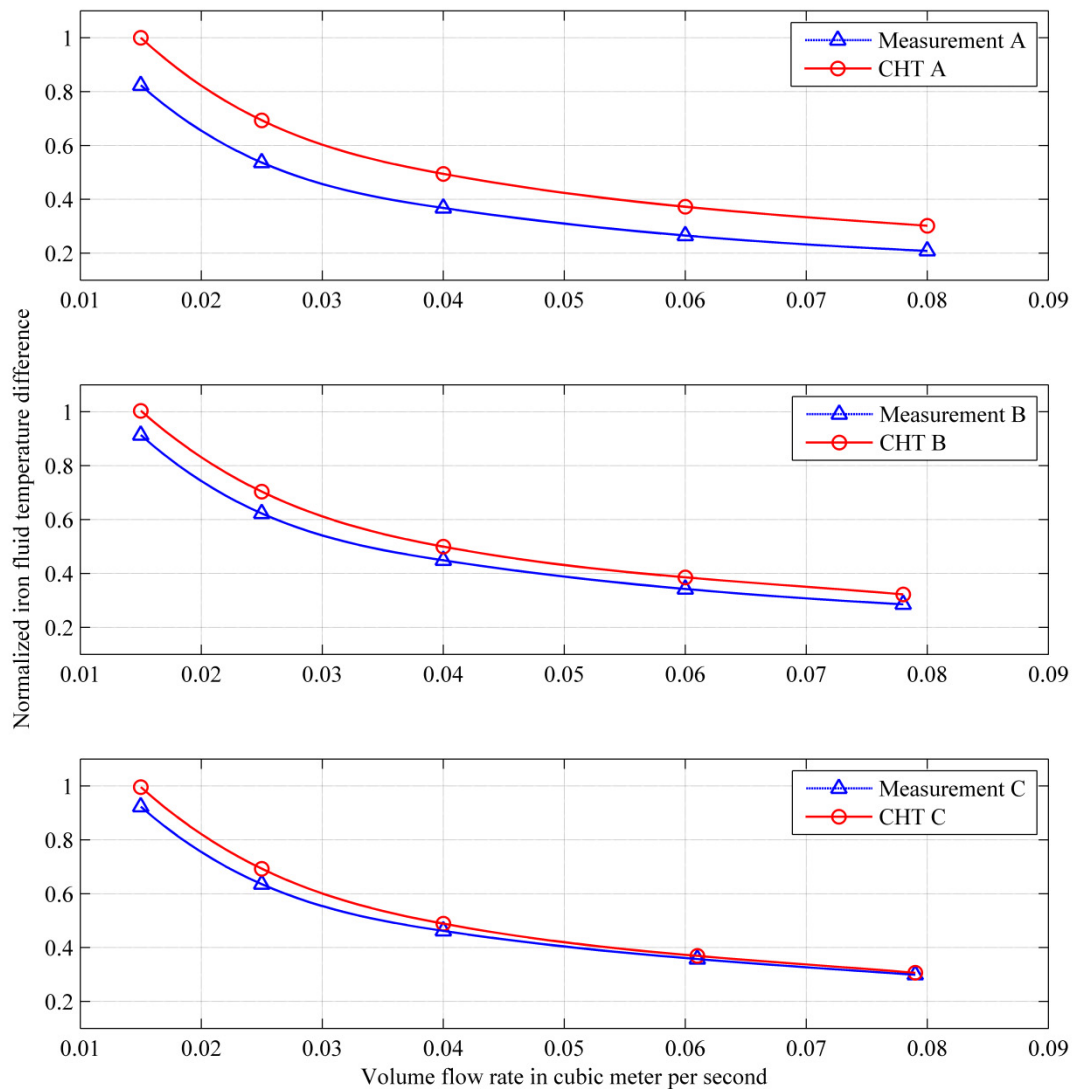


Fig. 47 Normalized temperature difference between iron and fluid inlet for the model A, model B and model C, obtained by measurements and CHT simulation

4.3.3 Fluid temperature

The fluid temperature rise is shown in Fig. 48. The temperature difference has been calculated with the inlet and outlet temperature of the air. The difference decreases with the volume flow rate. The average value of the difference is 0.97 % for model A, 1.09 % for model B and 0.99 % for model C. The highest deviation at the lowest flow rate is about 2.84 % for model A, 3.47 % for model B and 3.10 % for model C.

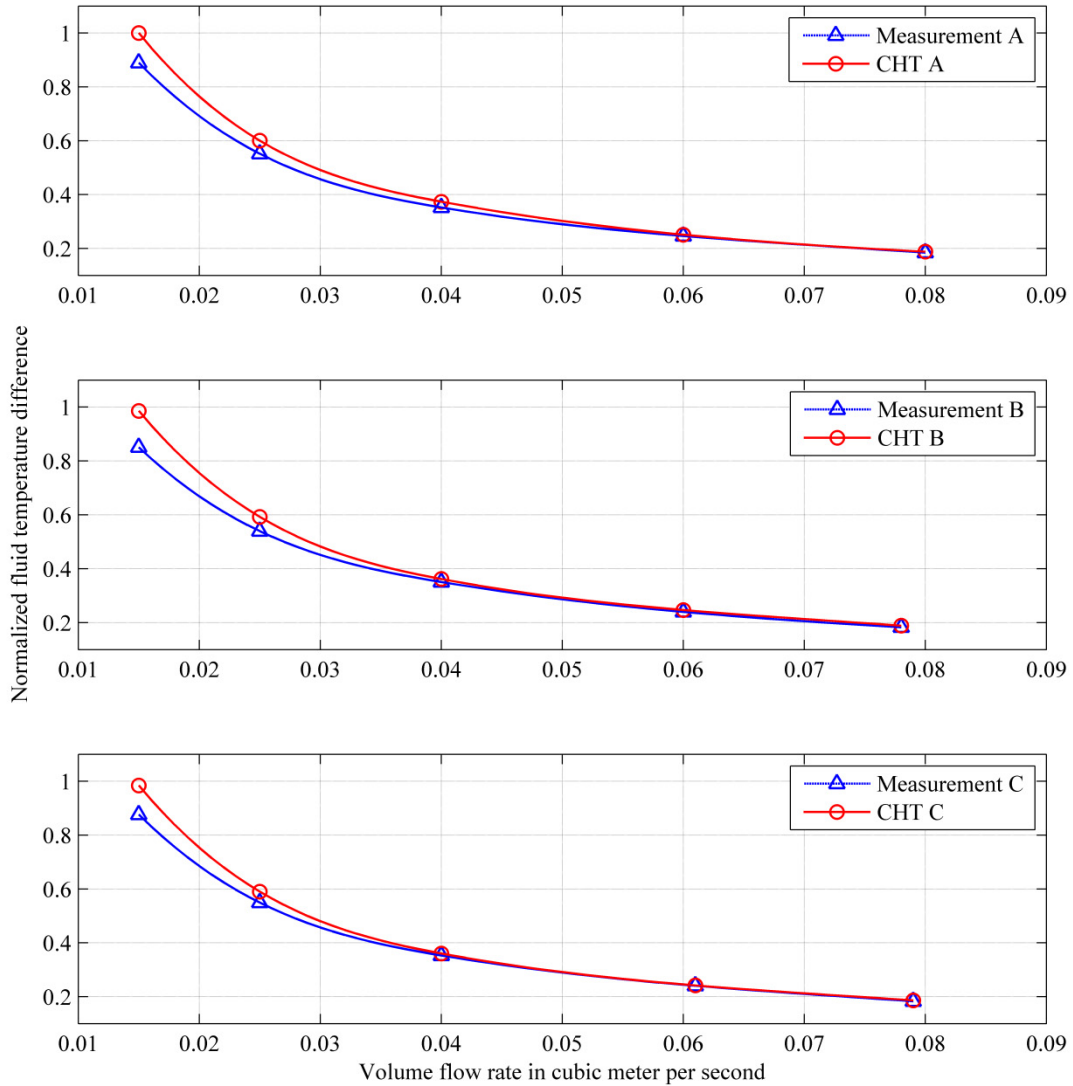


Fig. 48 Normalized temperature difference between fluid inlet and outlet for the model A, model B and model C, obtained by measurements and CHT simulation

4.4 Novel approach to compute the heat transfer for low Reynolds numbers

In the following, the air gap defined as 0.25 mm in model A as well as in model C is focused on for further study concerning the fluid flow in this axial gap between the insulation of the winding bars and the stator iron. This gap may cause a fluid flow from one duct to another and the resulting effects on the cooling are investigated. The Reynolds number in this area is in the laminar zone [78] and this can cause problems to the numerical solution [74] due to the turbulence model used [102]. A fine mesh with a dimensionless wall distance of $y^+ \leq 1$ must also be generated in the air-gap as presented in [57] and [58] for the CHT model based on the finite volume method (FVM), which increases the numerical effort. This requirement has been satisfied in the whole fluid domain for the investigated numerical models.

Another option to compute accurate results concerning the temperature distribution in the fluid and solid domains in contrast to the presented laboratory model is to omit the air gap and define

a thermal resistance R (in Kelvin per Watt) on the interface between the insulation and stator iron:

$$R = \frac{d}{\lambda \cdot A}, \quad (4.4)$$

where d (in meters) is the path length of the air gap, A (in square meters) is the path area and λ (in Watt per meter and Kelvin) is the thermal conductivity of the material, which is dependent on the computed temperature. This interface replaces the air gap in model A and the consequence is that only the heat conduction has to be solved there. This method has also been used for model C, with two different thermal resistances defined for the air and for the epoxy resin. This technique is called interface method (IFM) in the following. Obviously, it also includes finite volumes in the radial air gap. The thermal dependence of the material concerning the air plays a crucial role for this simulation, which has been defined for the surface thermal resistance.

4.4.1 Validation of the IFM with measurements

The following figures show a comparison of the results obtained by the FVM and the IFM, concerning the modeling of the axial air gap. The numerical results for each method and for each model have been validated with the measurement data. Each computed temperature characteristic can be compared to these both for the solid and for the fluid domain. The temperature difference has been normalized in each figure by the measured temperature at model A obtained at the lowest volume flow rate of $0.015 \text{ m}^3/\text{s}$.

In Fig. 49 the difference between the averaged copper temperature in the top and bottom bars and the fluid inlet temperature has been calculated. The averaged deviation for the numerical results of the FVM and the IFM compared to measurement data is about 1-2% and in the same range for model A and model C.

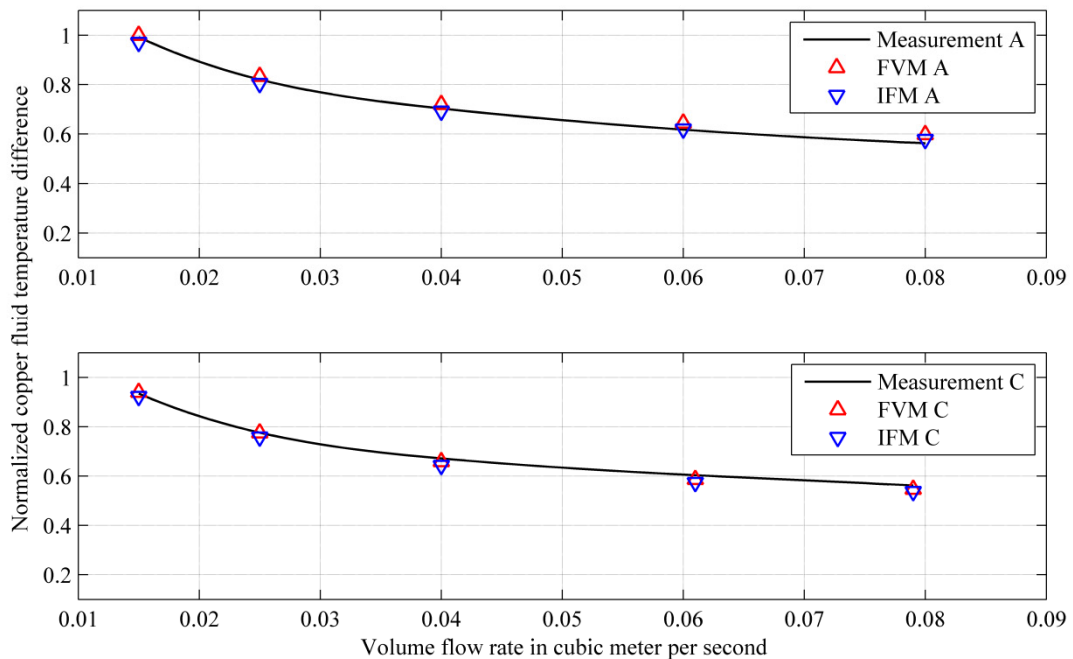


Fig. 49 Normalized temperature difference between copper and fluid inlet for the model A and model C, obtained by numerical simulation with CHT (FVM and IFM) and measurements

The difference between the averaged iron temperature of each stator core and the fluid inlet temperature is plotted against the volume flow rate in Fig. 50. The deviation for model A is about 13% and for model C about 4% and it is the same for each numerical method.

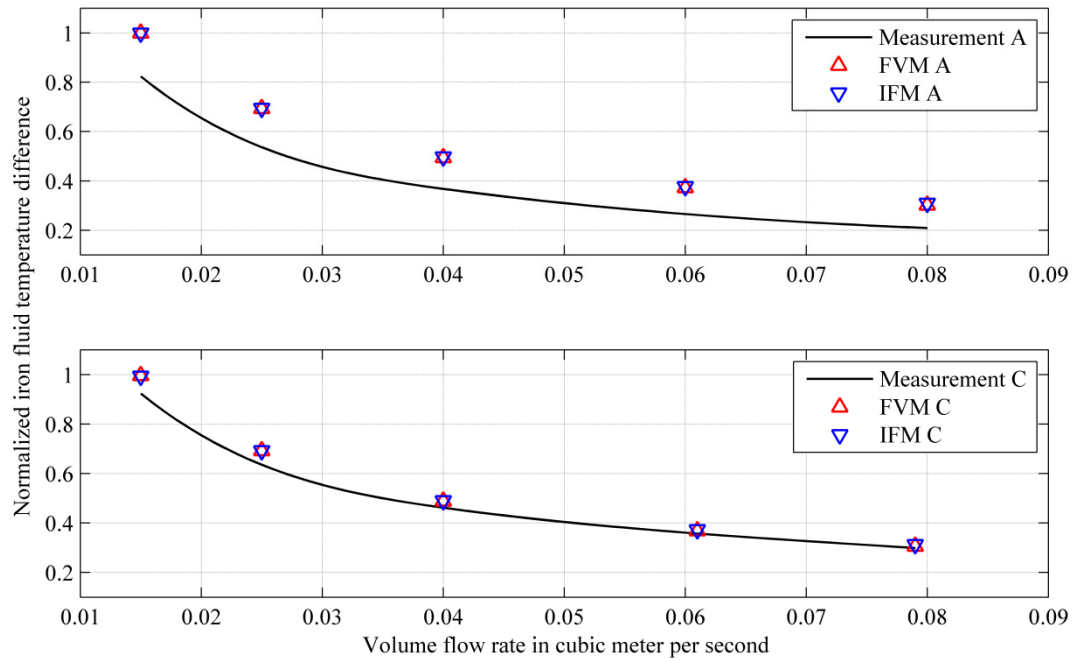


Fig. 50 Normalized temperature difference between iron and fluid inlet for the model A and model C, obtained by numerical simulation with CHT (FVM and IFM) and measurements

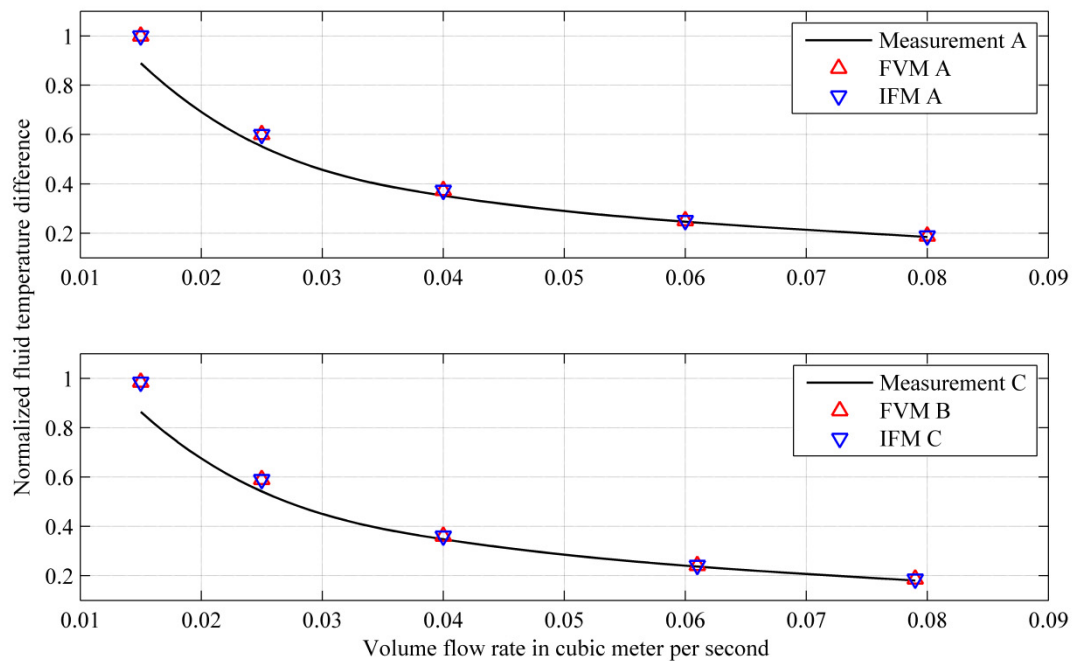


Fig. 51 Normalized temperature difference between fluid outlet and fluid inlet for the model A and model C, obtained by numerical simulation with CHT (FVM and IFM) and measurements

The heating up for the cooling air is shown in Fig. 51 with the deviations of about 4% for model A and 1% for model C both for the FVM and for the IFM. The decrease of the deviation with the increase of the flow rate can be explained by steady state being reached faster for a higher flow rate.

In summary, the evaluated results show that the error is the same for both numerical methods. This observation is valid for the computed temperatures in the solid domain and also in the heating up of the cooling fluid. The conclusion can be drawn that heat convection can be neglected for creeping flows in the air gap and, therefore, heat conduction is the main effect for the heat transfer at low Reynolds numbers. Hence, the modeling of the air gap between iron and insulation can be avoided and, thus, elements can be saved. In fact, the solution time is less than half when employing a thermal resistance instead of modeling the gap, with practically same results.

5 Approximation of the convective wall heat transfer coefficient used for network methods in the design process

As discussed in chapter 1, the network method is established as a state of the art tool in the design process of electrical machines. The various physical phenomena are represented in the electrical, air flow and thermal networks and these networks are connected with each other. The network characteristics are based on analytical formulas developed over years of manufacturing experience and are as accurate as the coefficients occurring in those formulas. These coefficients can be determined by numerical methods to improve their accuracy.

The convective WHTC is one of the most important parameters in thermal networks. In order to identify it, CFD has been used to generate a huge data set corresponding to various operational conditions and geometrical dimensions to approximate the Nusselt number (2.66) yielding the convective WHTC. The data set includes the WHTC corresponding to a wide range of different large hydro generators built by ANDRITZ Hydro GmbH in the last decades. The coefficients in the data set have been validated by comparing them with results obtained by analytical formulas and measurements. Afterwards, a non-dimensional approach has been used to define a formula to approximate the dependence of the WHTC on fluid flow, geometry and thermal variables. The parameters and exponents used in the formula have been computed with a least square method. As an alternative, a neural network has been designed to yield the WHTC for any specified input. Both methods will be explained in detail in this chapter, with their advantages and disadvantages pointed out.

Parts of this chapter have been presented at two conferences, [61] and [63]. One has been published in [62] and the other one is still in review process for publication [64].

5.1 Non-dimensional approach

A non-dimensional approach is commonly used to describe physical phenomena, e.g. characterizing the convective heat transfer on surfaces or pressure losses along a specified region. The main advantage of this method is that the solution found is also useable for similar problems and can be applied to a variety of machine sizes and operating conditions.

As shown for a pipe or duct flow, e.g. in [70], there is a correlation between the Nusselt number and the Reynolds number known as Dittus-Boelter equation which can be written as

$$Nu = 0.023 \cdot Re^{4/5} \cdot Pr^n \quad (5.1)$$

where $n=0.4$ for heating and $n=0.3$ for cooling. This formula is valid, if supersonic effects are neglected. Based on this equation, further formulas have been obtained to approximate the

Nusselt number and to compute the convective WHTC using similar empirical formulas, including the hydraulic diameter d_h defined by the cross section A and the perimeter U , as well as the length of the channel L as described in the heat atlas (HA) [99]:

$$Nu_{HA} = 0.0214 \cdot (Re^{0.8} - 100) \cdot Pr^{0.4} \cdot \left[1 + \left(\frac{d_h}{L} \right)^{2/3} \right], \quad (5.2)$$

$$d_h = \frac{4 \cdot A}{U}. \quad (5.3)$$

Similar formulas are known to have been developed to determine the heat convection in heat exchangers including directional flow phenomena, a situation not relevant in electrical machines. Therefore, these formulations are not feasible in technical applications concerning large hydro generators, as illustrated in Fig. 52. The approximation defined in (5.2) (blue line in the figure) yields a poor representation of the values evaluated by CFD. An additional curve is plotted in red, using the formula

$$Nu_{corr} = a \cdot Nu_{HA} + b, \quad (5.4)$$

where the factor a and the offset b has been determined with a fitting tool using a least mean square technique as implemented in Matlab [103]. The 29 points obtained by CFD characterize the ventilation ducts of a large hydro generator for a specific design. For the development of a global approximation of the Nusselt number to compute the convective wall heat transfer coefficient, the factors a and b have to be expressed by non-dimensional variables to take account of different inlet conditions in view of the wide range of different designs concerning operating conditions, cooling schemes and geometrical variations.

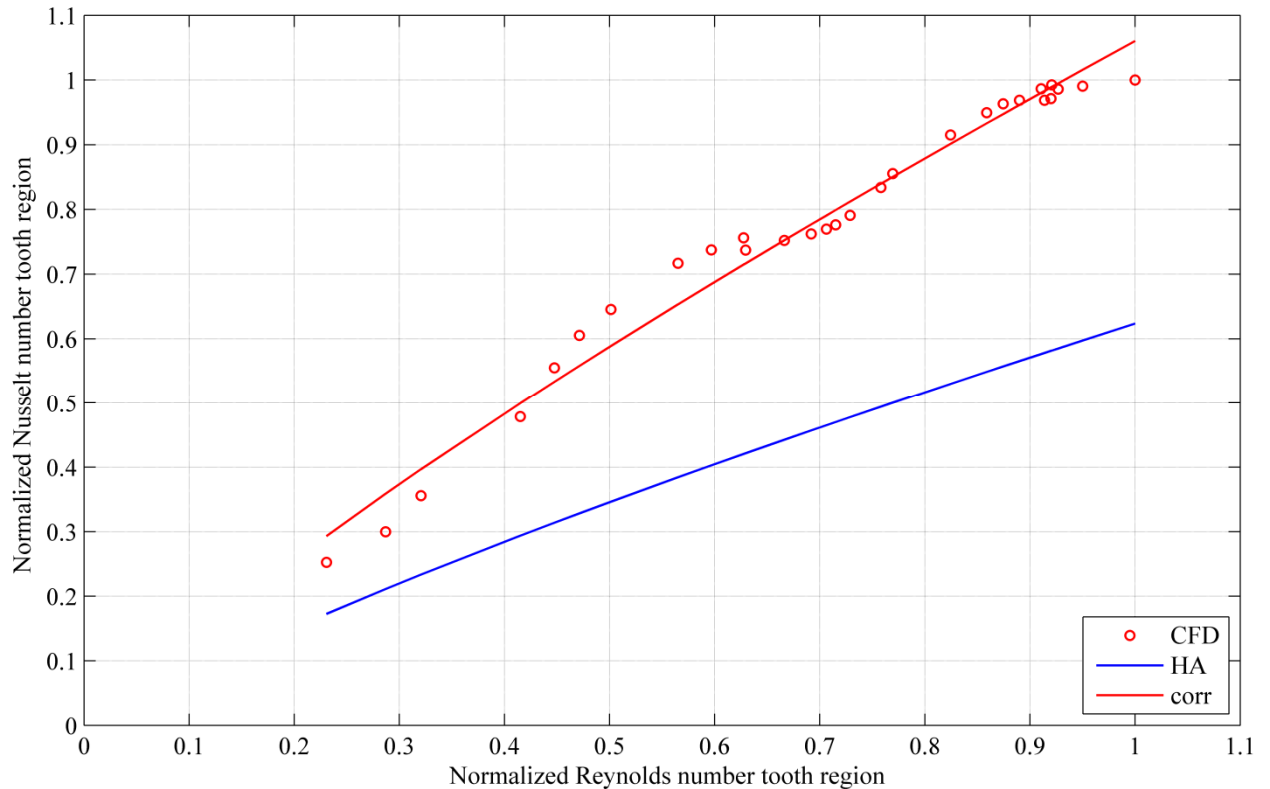


Fig. 52 Approximation results of the normalized Nusselt number plotted against the Reynolds number for different approaches including the Nusselt number obtained by CFD, the formula (5.2) of the heat atlas (HA) and the further correlation (corr) defined in (5.4) do determine the Nusselt number

5.1.1 Selection of the data set

The above results imply that further variables have to be defined to represent this particular application in sufficient detail and to achieve accurate results. All in all, 2547 configurations of the ventilation ducts have been defined, simulated and evaluated following the numerical computation of the 117 different CFD models with stator domains including the evaluated ventilation ducts in order to obtain non-dimensional variables to be able to define the WHTC in sufficient detail. The models simulated by CFD differ in three points.

The main difference is in the operating condition with focus on the operating speed. The data contain large hydro generators with a rotational speed in the range from 187.5 rpm up to 1000 rpm.

Furthermore, the cooling scheme plays a crucial role and the numerical models have been set up to include self and external ventilation as well as axial and radial fans. Additionally, different volume flow rates of the air of the fan as well as flow path with different admission points are presumed.

Last but not least, a wide range of different geometrical dimensions are included in the models, especially in the ventilation duct design but also in the design of parts preceding the stator in the thermal flow, e.g. pole and end winding, which influence the fluid flow in the rectangular cooling ducts positioned in the stator.

5.1.2 Non-dimensional variables defined

The non-dimensional variables defined for the investigation include flow characteristics, geometric variables and thermal variables. Additionally, the ventilation duct has been split into the tooth and yoke regions, and the Nusselt number has been computed locally for each region. This is explained by the different characteristics concerning flow and thermal field as well as geometrical design as mentioned in chapter 3.1.3.

Concerning the flow characteristics, four variables are included to describe the Nusselt number. First of all, the two Reynolds numbers are defined as follows:

$$Re_T = \frac{\rho_{F3} \cdot w_{F3} \cdot d_{h,F3}}{\mu_{F3}}, \quad (5.5)$$

$$Re_Y = \frac{\rho_{F5} \cdot w_{F5} \cdot d_{h,F5}}{\mu_{F5}}. \quad (5.6)$$

The index T denotes the tooth region where the mass flow averaged parameters have been determined at the surface $F3$ and Y stands for the yoke region with the evaluation of the mass flow averaged parameters in surface $F5$, see Fig. 16. The two Reynolds numbers are defined with the aid of the density ρ , the radial velocity w , the hydraulic diameter d_h and the dynamic viscosity μ evaluated for each region.

Additionally a Reynolds number Re_\ominus characterizing the flow field at the inlet of the ventilation duct has been defined. The parameters have been evaluated at the surface $F1$ (Fig. 16) with the difference in the circumferential velocity v_u and the height of the air gap L_\ominus between rotor and stator:

$$Re_\ominus = \frac{\rho_{F1} \cdot v_{u,F1} \cdot L_\ominus}{\mu_{F1}}. \quad (5.7)$$

Furthermore two different velocity ratios are included to define the arising physical effects in the different regions and over the axial length in more detail. The ratio for the tooth and yoke regions is denoted by X_1 and it includes the circumferential velocity $v_{u,F1}$ evaluated at the fluid control surface F1 and the rotational velocity at the poles u_{pole} . The latter is defined with the outer diameter of the rotor d_{pole} and the rotational speed n .

The second velocity ratio has been defined for the tooth region and denoted by $X_{2,T}$ as well as for the yoke region denoted by $X_{2,Y}$. They include the radial velocities w_{F3} and w_{F5} as well as the circumferential velocity $v_{u,F1}$.

Concerning relevant geometric designs two variables have been selected, concerning the design of the rectangular channels ($Y_{1,T}$ and $Y_{1,Y}$) and to include different designs of the slot wedge (Y_2).

The hydraulic diameter $d_{h,F3}$ and the length of the tooth L_{F3} are used to define $Y_{1,T}$ for the tooth region, and similarly for the yoke region evaluated at the surface F5.

The parameter Y_2 concerning the slot wedge design includes one and double sided wedge designs as well as a missing slot wedge.

The Prandtl number Pr has also been included and defined separately for the tooth and yoke regions:

$$Pr_T = \frac{\mu_{F3} \cdot c_{p,F3}}{\lambda_{F3}}, \quad (5.8)$$

$$Pr_Y = \frac{\mu_{F5} \cdot c_{p,F5}}{\lambda_{F5}}. \quad (5.9)$$

Last but not least, the second thermal variable is the Nusselt number, which is the target parameter computed and for which the least mean square error is to be minimized:

$$Nu_T = \frac{\alpha_{F3} \cdot d_{h,F3}}{\lambda_{F3}}, \quad (5.10)$$

$$Nu_Y = \frac{\alpha_{F5} \cdot d_{h,F5}}{\lambda_{F5}}. \quad (5.11)$$

In the following sections, two different numerical approaches will be presented which yield a formula or a network to approximate the Nusselt number in an acceptable range by using a least mean square technique with the target being the Nusselt number computed with CFD. The WHTC α can then be computed from the Nusselt number Nu using the hydraulic diameter d_h and the thermal conductivity λ .

5.2 Constrained nonlinear optimization algorithm

For the characterization of the WHTC, the following non dimensional parameters have been defined: the velocity ratios X_1 , $X_{2,T}$ and $X_{2,Y}$, the geometry parameters $Y_{1,T}$ and $Y_{1,Y}$, the Prandtl numbers Pr_T (5.8) and Pr_Y (5.9), the Reynolds numbers Re_T (5.5) and Re_Y (5.6) and also a further Reynolds number Re_ϕ (5.7). These parameters are used to develop a formula to yield the Nusselt number Nu as follows:

$$Nu = C_1 \cdot Re^{0.8} \cdot Pr^{0.4} \cdot Y_1^{2/3} + C_2, \quad (5.12)$$

$$C_1 = a_0 + a_1 \cdot X_1^{\varepsilon_1} + a_2 \cdot X_2^{\varepsilon_2} + a_3 \cdot Re_{\Theta}^{\varepsilon_3}, \quad (5.13)$$

$$C_2 = b_0 + b_1 \cdot X_1^{\kappa_1} + b_2 \cdot X_2^{\kappa_2} + b_3 \cdot Re_{\Theta}^{\kappa_3}. \quad (5.14)$$

A constrained nonlinear optimization technique has been used to determine the factors a_i and b_i as well as the exponents ε_i and κ_i in (5.13) and (5.14).

The slot wedge geometry has a substantial influence on the fluid flow and on the related heat transfer through the ventilation duct. Therefore, the non-dimensional parameter Y_2 has also been introduced to characterize the slot wedge type. The optimization has been carried out separately for each slot wedge type and for each region (tooth and yoke), so that the factors and exponents depend on Y_2 . As described in sub-section 5.1.1, the data set used includes different machine designs, cooling schemes and operating points to cover a wide range of the Nusselt number values and to ensure an accurate regression analysis.

5.2.1 Numerical approach

The appropriate specification of the initial values and of the bounds of the feasible ranges for the factors and exponents is important in developing suitable techniques. Hence, an interior point algorithm has been used attempting to find a constrained minimum of a scalar function of several variables starting at an initial estimate. The main goal of the algorithm is to find the solution of a minimum problem specified as

$$\min_x f(x) \text{ for } \begin{cases} c(x) \leq 0 \\ ceq(x) = 0 \\ A \cdot x \leq b \\ Aeq \cdot x = beq \\ lb \leq 0 \leq ub \end{cases}, \quad (5.15)$$

b and beq are vectors, A and Aeq are matrices, $c(x)$ and $ceq(x)$ are vector functions and $f(x)$ is a scalar function [103].

5.2.2 Accuracy of the developed formula

Having determined the factors and exponents, the Nusselt number for a specific operating point can be calculated. The accuracy of the developed formula can be characterized by the relative error for the tooth and yoke region defined as follows:

$$e_{relative,i} = \frac{Nu_{CFD,i} - Nu_{PF,i}}{Nu_{CFD,i}} \quad (5.16)$$

where i stands for T or Y .

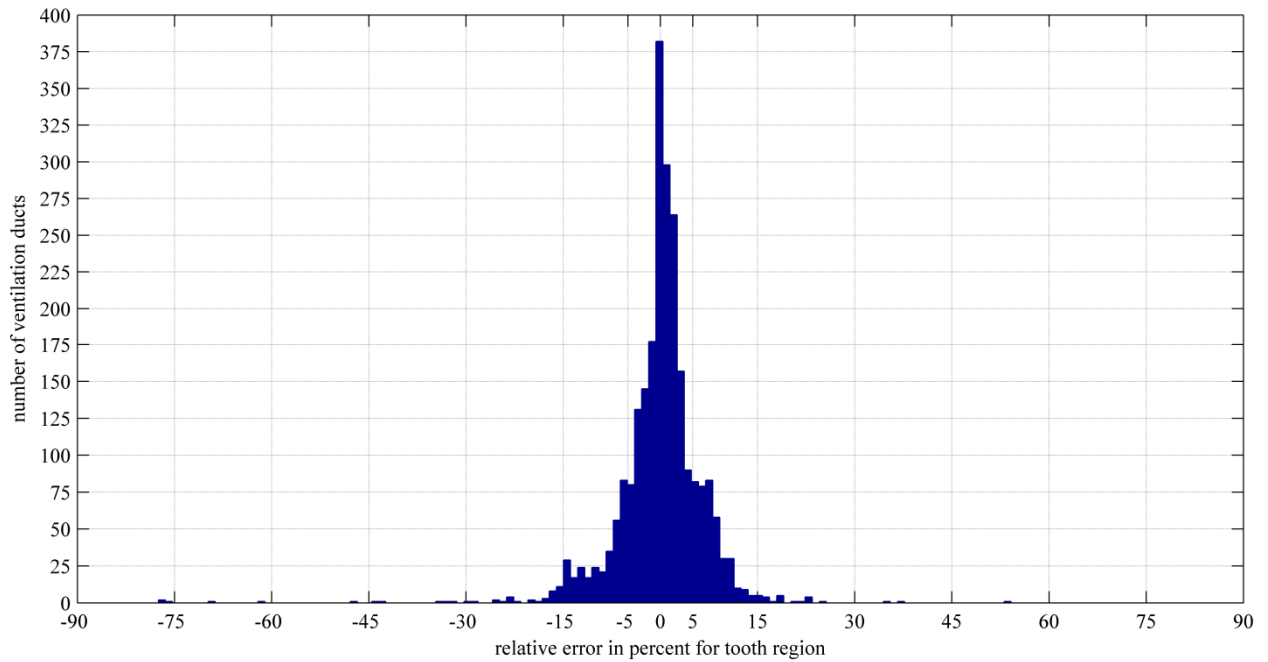


Fig. 53 Histogram of the computed relative error obtained for the data set evaluated for the tooth region

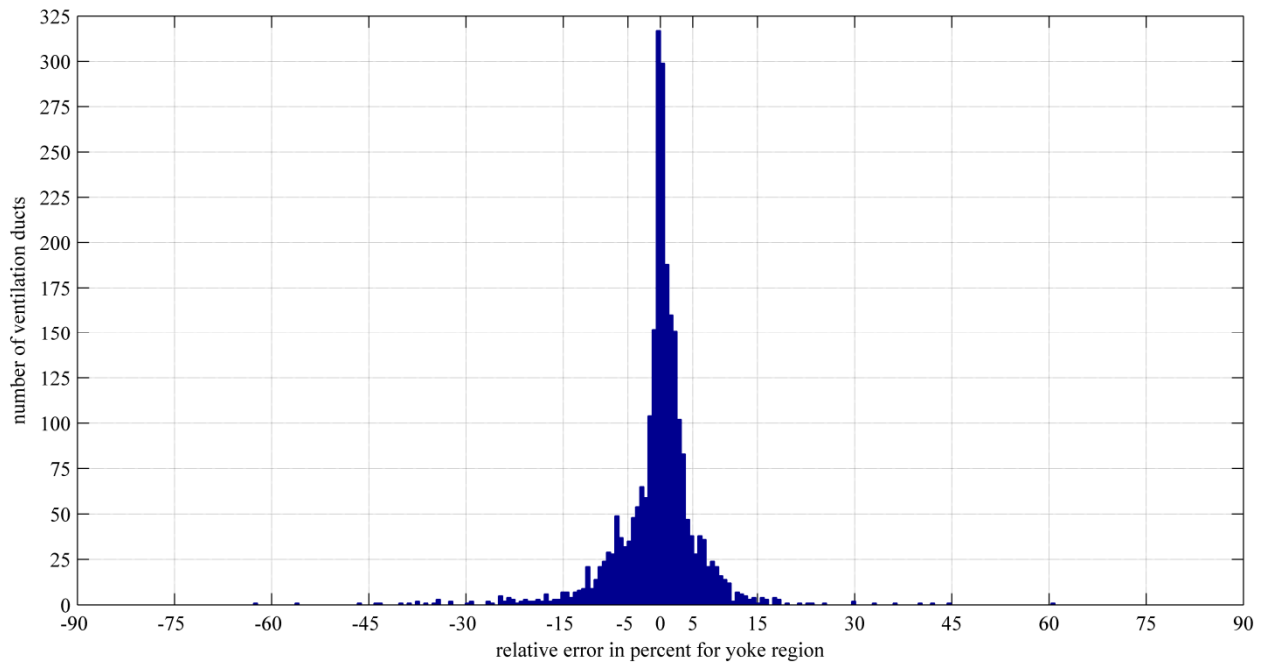


Fig. 54 Histogram of the computed relative error obtained for the data set evaluated for the yoke region

The distribution of the relative error over the data set is shown with the aid of histograms for the tooth in Fig. 53, and for the yoke region in Fig. 54.

Compared to the values of the Nusselt number computed by CFD, the average relative error of the approximation obtained is below 10% for both regions. The range of the relative error being below 10% includes 2261 Nusselt numbers for the tooth region and 2322 for the yoke region out of the 2547 computed values (see sub-section 5.1.1).

Fig. 55, Fig. 56, Fig. 57 and Fig. 58 compare the Nu values computed by CFD with those obtained by the power function approximation for the tooth and yoke regions. The results have been evaluated for all the machine designs included and displayed separately for eight different

operating conditions (m_1, \dots, m_8). For the operating condition denoted by m_1 , the power function approximation (5.12) was not able to yield acceptable values, therefore, this data set has been not considered in the determination of the constants in the formula.

In the diagrams, the Nusselt number has been normalized by its highest computed value in the tooth region. If $Nu_{CFD} = Nu_{PF}$ held, the points would be on the dotted 45°-line and a bound of 10% is shown by the solid black lines.

A regression value of 0.99201 has been computed for the tooth, and 0.99196 for the yoke region. The regression value measures the correlation between the Nusselt numbers approximated with the power function and those evaluated with CFD. The closer the regression value gets to 1, the better the approximated function describes the CFD results.

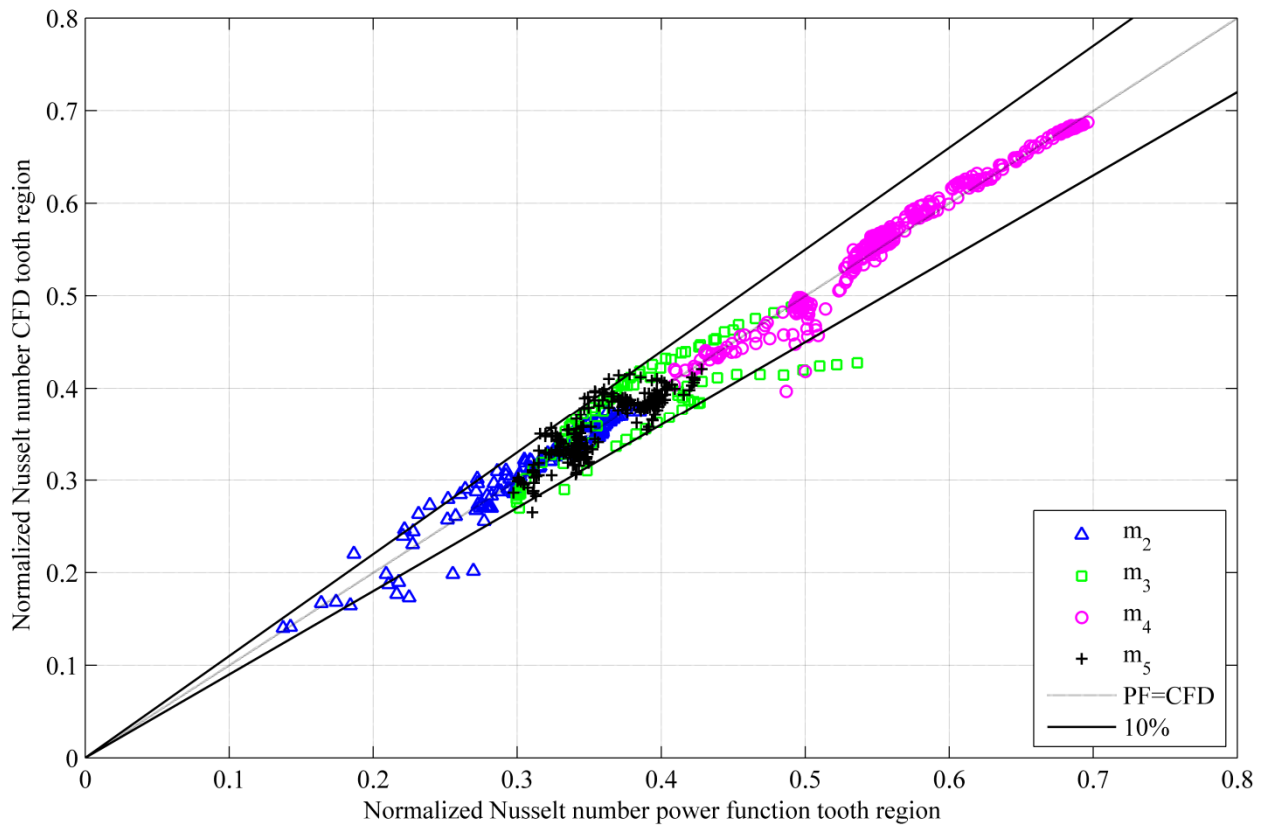


Fig. 55 Normalized Nusselt number computed by CFD versus normalized Nusselt number approximated with a power function for different machine designs for tooth region

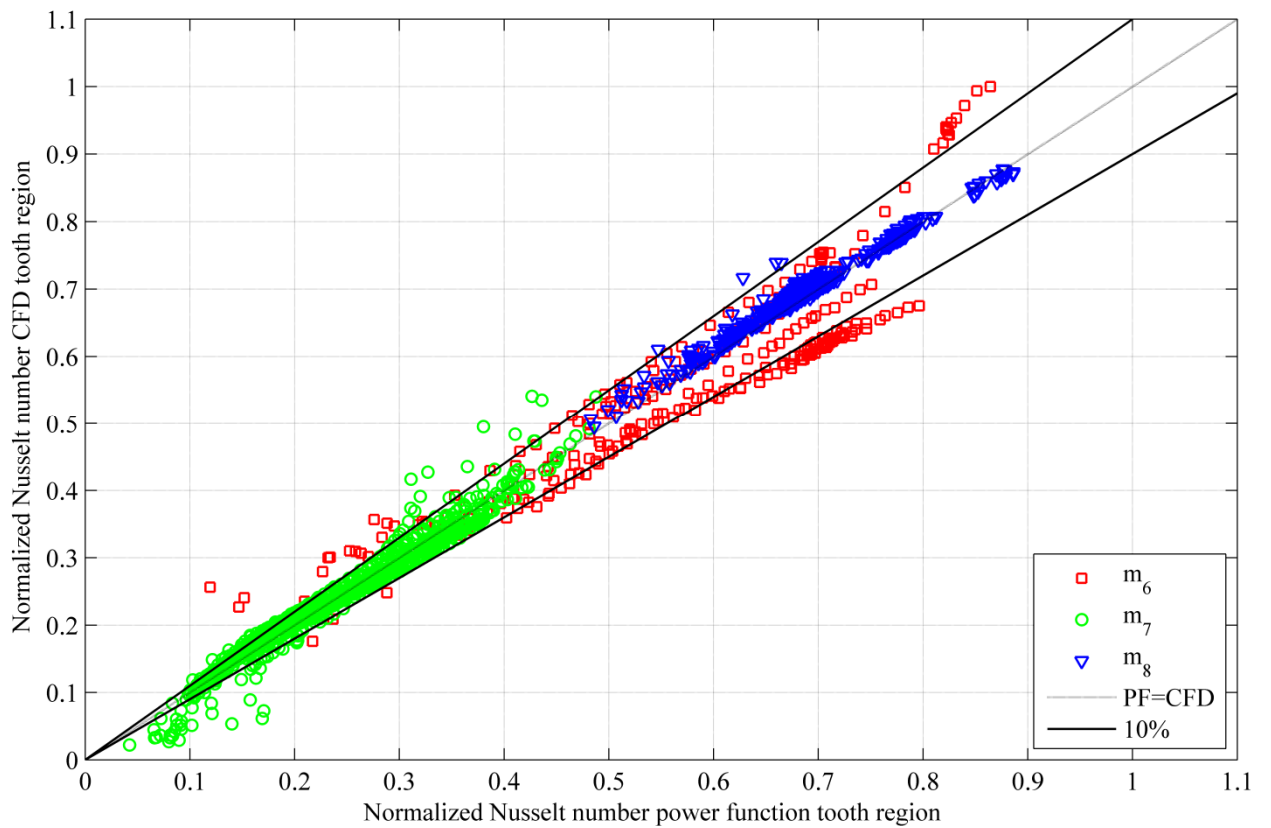


Fig. 56 Normalized Nusselt number computed by CFD versus normalized Nusselt number approximated with a power function for different machine designs for tooth region

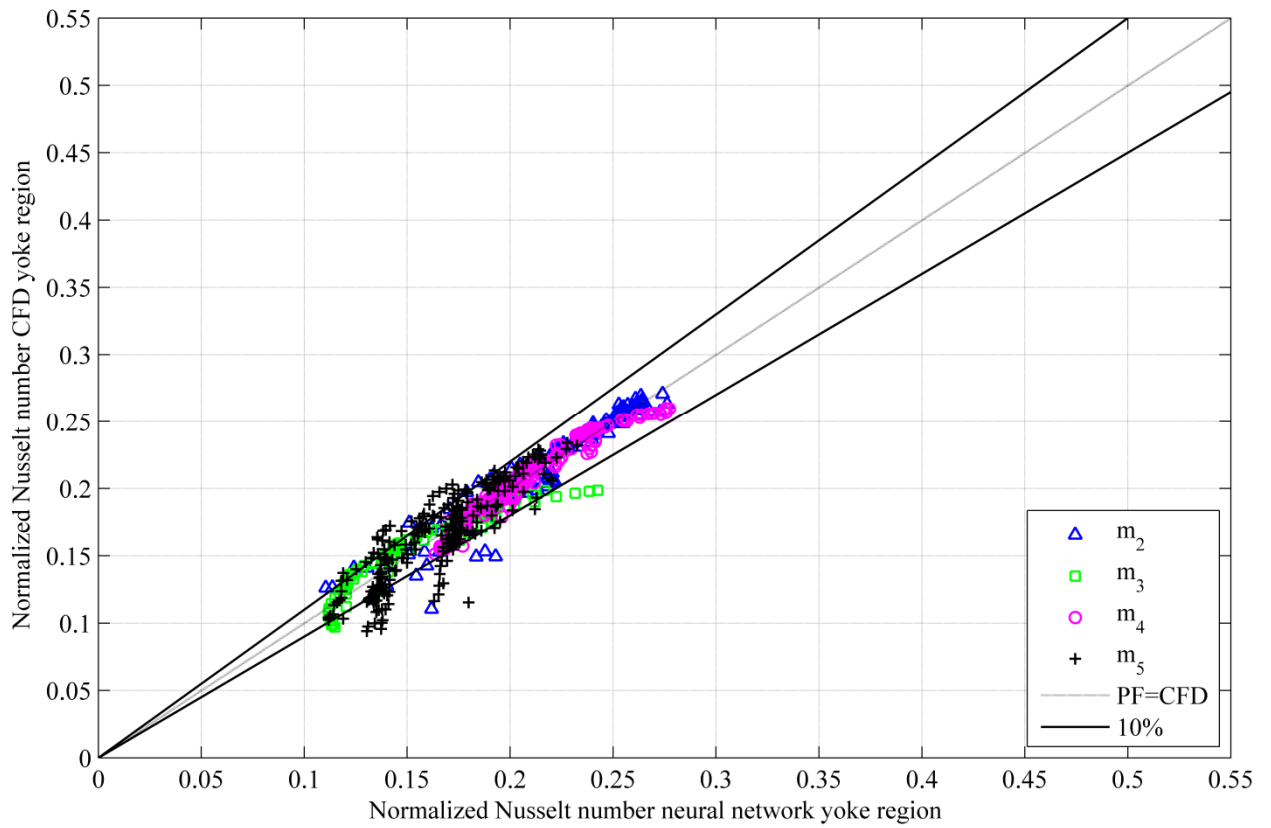


Fig. 57 Normalized Nusselt number computed by CFD versus normalized Nusselt number approximated with a power function for different machine designs for yoke region

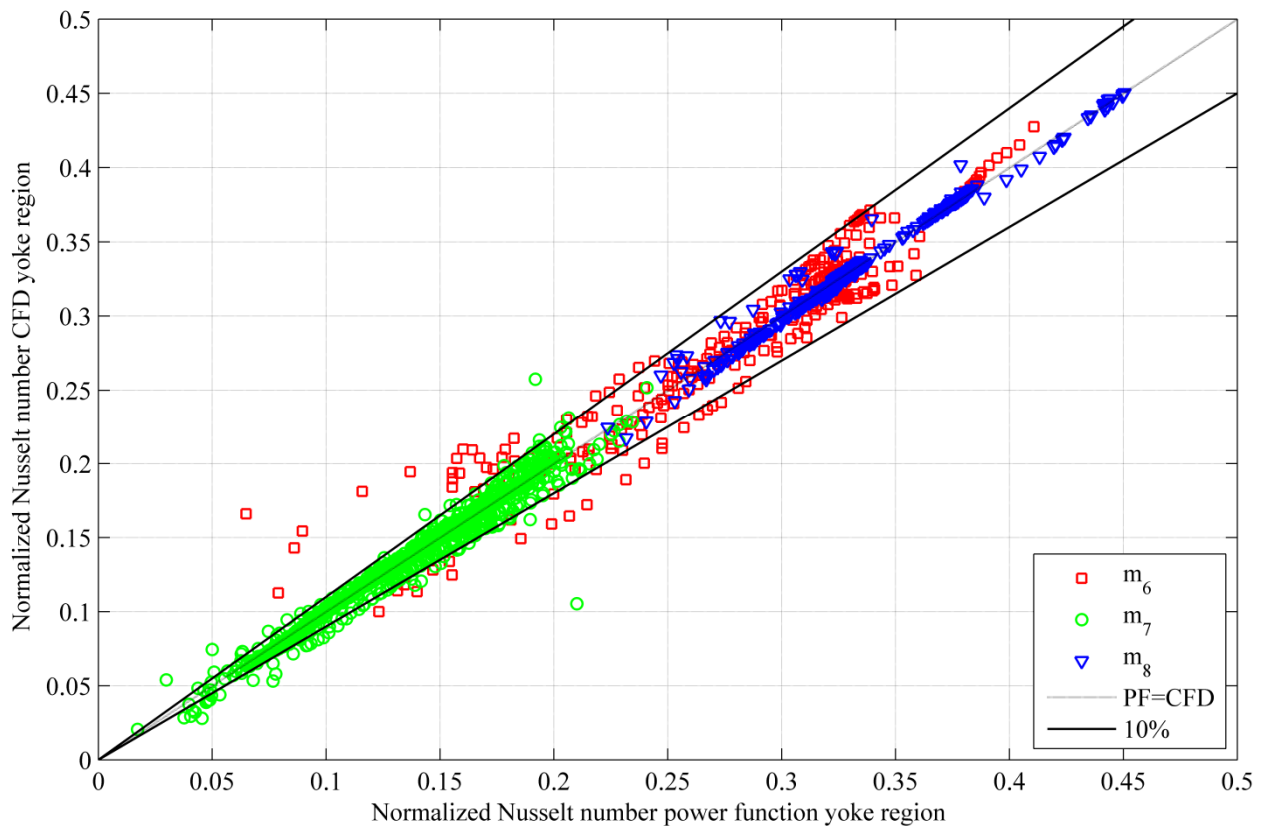


Fig. 58 Normalized Nusselt number computed by CFD versus normalized Nusselt number approximated with a power function for different machine designs for yoke region

5.3 Neural network

For turbulent flows, it is not possible to calculate the convective WHTC analytically, and an alternative approach is required. The accuracy of the numerical approach presented in the previous section is not sufficient. Therefore, a further method has been used to develop a tool able to compute the Nusselt number more accurately by employing more parameters than the technique presented in section 5.2. The parameters are the input variables of a neural network to compute the Nusselt number in an acceptable range using appropriate weight matrices and bias vectors. The proper architecture of such a weighted neural network (multi-layer perceptron) is developed in this section for the defined problem and the unknown weight matrices and bias vectors are determined. The main advantage of neural networks is their flexible nonlinear modeling capability. Indeed, it is not necessary to specify a particular model in advance, the model is adaptively formed based on the features of the input data included. This approach is suitable to treat empirical data sets with no theoretical guidance available to suggest an appropriate process governing the generation of data. This enables the computation of the convective WHTC for various operating points with sufficient accuracy even for future design variations.

5.3.1 Numerical approach

Neural networks are computational models inspired by the operation of the central nervous system. These systems are capable of machine learning and pattern recognition and are widely used in computer science and related fields [104]. Typically, neural networks are trained so that a particular input leads to a specific target output. The network is adjusted based on a comparison of the output and the target, until the network output matches the target. Neural networks can be described with an input layer \mathbf{x} , the weight matrix \mathbf{w} , the hidden layer or the activation function \mathbf{h} , the bias layer \mathbf{b} and the defined targets \mathbf{t} , which should match the computed output of the network.

The net input to unit i in layer $k+1$ is

$$a_{(i)}^{(k+1)} = \sum_{j=1}^k w_{(i,j)}^{(k+1)} \cdot a_{(j)}^{(k)} + b_{(i)}^{(k+1)}, \quad (5.17)$$

and its output, with the relevant transfer function f , will be

$$h_{(i)}^{(k+1)} = f^{(k+1)} \left(a_{(i)}^{(k+1)} \right). \quad (5.18)$$

For an m -layer network, the system equations in matrix form are given by

$$\mathbf{h}^{(0)} = \mathbf{x}, \quad (5.19)$$

$$\mathbf{h}^{(k+1)} = \mathbf{f}^{(k+1)} \left(\mathbf{w}^{(k+1)} \cdot \mathbf{h}^{(k)} + \mathbf{b}^{(k+1)} \right), \quad (5.20)$$

$$k = 0, 1, \dots, m-1 \quad (5.21)$$

where k denotes the number of the hidden layer.

The task of the network is to learn associations between a specified set of input-output pairs $\{(\mathbf{x}_{(1)}, \mathbf{t}_{(1)}), (\mathbf{x}_{(2)}, \mathbf{t}_{(2)}), \dots, (\mathbf{x}_{(q)}, \mathbf{t}_{(q)})\}$. The feed forward network propagates the data through the architecture to the output layer. The forward propagation has the purpose of computing the activations and outputs of all possible gates by sending information through the network.

Afterwards, the computed deviation (error) between the computed output layer \mathbf{y} and the target \mathbf{t} has to be back-propagated [105]. The disadvantage of the error back-propagation (EBP) algorithm is the weak convergence as elaborated in [106]. As an alternative, the Levenberg-Marquard (LM) algorithm was originally developed to serve as an intermediate optimization algorithm between the Gauß-Newton (GN) method and gradient descent (GD) algorithm, and to address the limitations of each technique, as published in [107] and [108]. The GN method has excellent convergence properties, but if the initial values are not selected properly, it may diverge. The GD algorithm is limited by slow convergence, but exhibits excellent behavior in the vicinity of a minimum point and is not affected by the choice of the initial values. According to the GN method, the update rule for the increment of weights $\Delta\mathbf{w}$ of the neural network is

$$\Delta\mathbf{w} = -\left[\nabla^2\mathbf{E}_{(\mathbf{w})}\right]^{-1} \cdot \nabla\mathbf{E}_{(\mathbf{w})}, \quad (5.22)$$

where $\nabla^2\mathbf{E}_{(\mathbf{w})}$ represents the Hessian matrix and $\nabla\mathbf{E}_{(\mathbf{w})}$ is the matrix of the gradient tensor:

$$\nabla^2\mathbf{E}_{(\mathbf{w})} = \begin{bmatrix} \frac{\partial^2 e_{1(w)}}{\partial w_1 \partial w_1} & \frac{\partial^2 e_{1(w)}}{\partial w_1 \partial w_2} & \cdots & \frac{\partial^2 e_{1(w)}}{\partial w_1 \partial w_n} \\ \frac{\partial^2 e_{2(w)}}{\partial w_2 \partial w_1} & \frac{\partial^2 e_{2(w)}}{\partial w_2 \partial w_2} & \cdots & \frac{\partial^2 e_{2(w)}}{\partial w_2 \partial w_n} \\ \vdots & \vdots & \ddots & \vdots \\ \frac{\partial^2 e_{N(w)}}{\partial w_n \partial w_1} & \frac{\partial^2 e_{N(w)}}{\partial w_n \partial w_2} & \cdots & \frac{\partial^2 e_{N(w)}}{\partial w_n \partial w_n} \end{bmatrix}. \quad (5.23)$$

If we assume that $\mathbf{E}_{(\mathbf{w})}$ is a sum of squares function of the error vector $\mathbf{e}_{(\mathbf{w})}$:

$$\mathbf{E}_{(\mathbf{w})} = \sum_{i=1}^N \mathbf{e}_{(w)}^2, \quad (5.24)$$

$$\mathbf{e}_{(w)} = \mathbf{t}_{(w)} - \mathbf{y}_{(w)}, \quad (5.25)$$

then it can be shown that

$$\nabla\mathbf{E}_{(\mathbf{w})} = \mathbf{J}_{(w)}^T \mathbf{e}_{(w)}, \quad (5.26)$$

$$\nabla^2\mathbf{E}_{(\mathbf{w})} = \mathbf{J}_{(w)}^T \cdot \mathbf{J}_{(w)} + \mathbf{S}_{(w)}, \quad (5.27)$$

where $\mathbf{J}_{(w)}$ is the Jacobian matrix

$$\mathbf{J}_{(w)} = \begin{bmatrix} \frac{\partial e_{1(w)}}{\partial w_1} & \frac{\partial e_{1(w)}}{\partial w_2} & \cdots & \frac{\partial e_{1(w)}}{\partial w_n} \\ \frac{\partial e_{2(w)}}{\partial w_1} & \frac{\partial e_{2(w)}}{\partial w_2} & \cdots & \frac{\partial e_{2(w)}}{\partial w_n} \\ \vdots & \vdots & \ddots & \vdots \\ \frac{\partial e_{N(w)}}{\partial w_1} & \frac{\partial e_{N(w)}}{\partial w_2} & \cdots & \frac{\partial e_{N(w)}}{\partial w_n} \end{bmatrix}, \quad (5.28)$$

and

$$\mathbf{S}_{(w)} = \sum_{i=1}^N \mathbf{e}_{(w)} \cdot \nabla^2 \mathbf{e}_{(w)}. \quad (5.29)$$

For the GN method, it is assumed that $\mathbf{S}_{(w)} \approx 0$, and the update (5.22) becomes:

$$\Delta \mathbf{w} = - \left[\mathbf{J}_{(w)}^T \cdot \mathbf{J}_{(w)} \right]^{-1} \cdot \mathbf{J}_{(w)}^T \mathbf{e}_{(w)}. \quad (5.30)$$

The Levenberg-Marquardt modification to the GN method is

$$\Delta \mathbf{w} = - \left[\mathbf{J}_{(w)}^T \cdot \mathbf{J}_{(w)} + \lambda \mathbf{I} \right]^{-1} \cdot \mathbf{J}_{(w)}^T \mathbf{e}_{(w)}. \quad (5.31)$$

If λ is large, the above expression approximates GD with a learning rate of $1/\lambda$, while for a small λ , the algorithm approximates the GN method. By adaptively adjusting the parameter λ , the LM algorithm can switch between its two extremes - the gradient descent and Gauß-Newton method - and combine the advantages of both. The LM algorithm has the benefit of converging even for start values far away from the final minimum, a fact indicating its robustness.

The initialization of the layer's weights and biases has been achieved with a layer initialization function called Nguyen-Widrow initialization algorithm [109]. The initial weights and bias values are chosen by the algorithm in order to distribute the active region of each neuron in the layer approximately evenly across the layer's input space [110].

5.3.2 Boundary conditions

The data obtained by CFD-analysis have to be split into training, validation and test data sets. The learning algorithm computes the weight and bias vectors with the training data set and the network is adjusted according to its error. Afterwards, the validation set is used for a fine adjustment and to halt training when generalization stops improving. The test data have no effect on training and provide an independent measure of network performance during and after training. The data set of 2547 investigated ventilation duct has been split into 70% training data, 15% validation and 15% testing data.

The input layer \mathbf{x} has been defined by means of the Reynolds number Re and the Prandtl number Pr . Additionally, further input variables introduced in section 5.2 have been included, namely the velocity ratios (X_1, X_2), geometrical parameters concerning duct and wedge geometry (Y_1, Y_2) and the rotational Reynolds number Re_{\odot} :

$$\mathbf{x} = [Re, Pr, X_1, X_2, Y_1, Y_2, Re_{\odot}]^T. \quad (5.32)$$

The target \mathbf{t} has been defined as the computed Nusselt number Nu given by CFD simulations:

$$\mathbf{t} = [Nu_{CFD}]^T. \quad (5.33)$$

5.3.3 Architecture

Unfortunately, finding the ideal design of the architecture is not straightforward. On the one hand, there should be enough neurons to capture the functional behavior between input and output. On the other hand, over-fitting should be avoided in any case. Over-fitting arises, if the

neural network approximates the original data very well, but the approximation fails with new data. Over-fitting generally occurs when a model is excessively complex, having too many neurons in the hidden layer relative to the number of parameters in the input layers. Therefore, a cross validation has been carried out to get information about the efficiency of the current network. In the present work, an m -fold cross validation has been selected. The data set has been split into five cases including 510 different randomly chosen examples, as shown in Fig. 59. Afterwards, the weights, bias layers, activations and outputs of the possible gates have been trained (using 70% of the data) and validated (including 15% of the data) by using four of the data set groups. In the following, the omitted data set is used for testing by computing the mean square error (MSE) of the remaining 15% of the data. The MSE is the mean value of the squared differences between the target t_i and the output of the neural network y_i over all 2547 examples in the analyzed data set:

$$MSE = \frac{\sum (t_{(i)} - y_{(i)})^2}{2547}. \quad (5.34)$$

After this, the testing data set has been changed and this step starts again and ends if each of the five parts of data sets has been used for testing. The MSE characterizes the accuracy and effectiveness of the designed network. This has to be carried out for each design and, hence, the appropriate choice of the right architecture and of the used input parameters can be made. The non-dimensional input parameters with negligible influence on the output can be identified based on the weight vector in the first hidden layer.

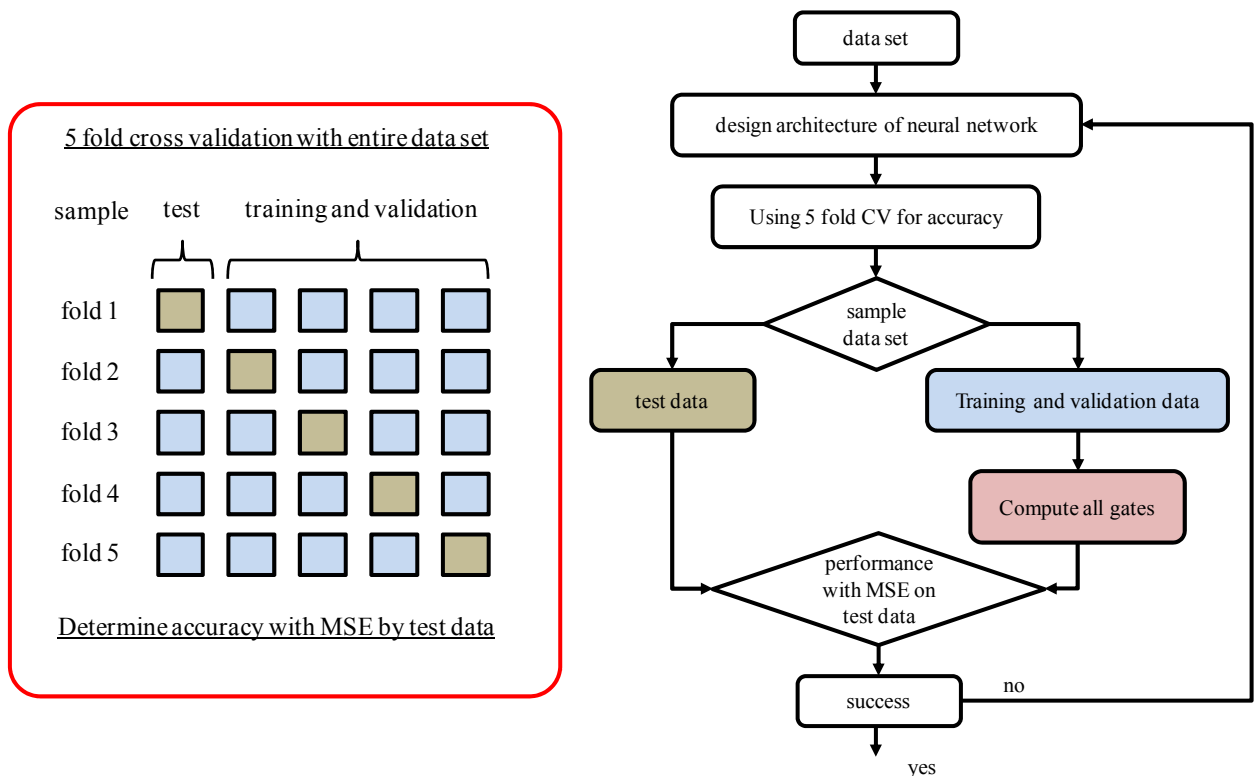


Fig. 59 Flow diagram to evaluate the accuracy of the design neural network using a cross validation (CV)

Afterwards, the architecture with the best mean error result has to be trained, validated and tested with the entire data set by splitting the data in training data (70%), validation data (15%) and testing data (15%) as mentioned before. Fig. 60 shows the designed architecture of the neural network. The hidden neurons include the transfer function f . In the designed network, a hyperbolic tangent sigmoid transfer function $f^{(1)}$ has been used in the first layer and a linear

transfer function $f^{(2)}$ in the second layer to compute the output with the defined input to arrive at the least error between output and target:

$$f^{(1)} = \tanh\left(a_{(i)}^{(1)}\right) = \frac{2}{1 + e^{-2a_{(i)}^{(1)}}} - 1, \quad (5.35)$$

$$f^{(2)} = a_{(i)}^{(2)}. \quad (5.36)$$

The designed neural network has been trained and validated to approximate the Nusselt number in an acceptable range by using a least mean square technique for a data range including each designed and built large hydro generator of ANDRITZ Hydro in the last decades. This numerical approach can be used to compute further Nusselt numbers by any input generated with a network method. Including additional machine designs can be easily carried out by further training. It is worth noting that the approximation works well for the given range of the inlet and outlet parameters shown in Table 11 and it is not recommended to use the same parameters outside this range of the non-dimensional variables.

tooth	min. value	max. value	yoke	min. value	max. value
Re _T	264	21052	Re _Y	171	16511
Re _Θ	30614	423096	Re _Θ	30614	423096
X ₁	0.0019	1.9284	X ₁	0.0019	1.9284
X _{2,T}	0.0246	304	X _{2,Y}	0.0371	463
Y _{1,T}	0.0302	0.0906	Y _{1,Y}	0.0129	0.0520
Y ₂	0	2	Y ₂	0	2
Pr _T	0.7046	0.7615	Pr _Y	0.7046	0.7615
Nu _T	24	77	Nu _Y	11	37

Table 11 Ranges of the used non dimensional parameters presented for tooth and yoke region

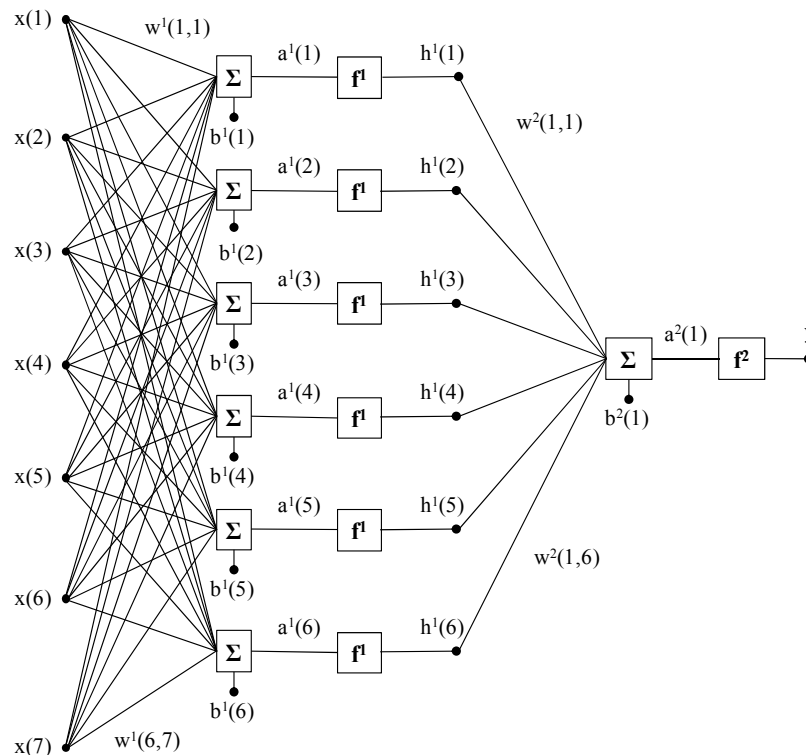


Fig. 60 Architecture of the two layer feed forward network used

5.3.4 Accuracy of the designed neural network

In knowledge of the weight matrices and bias vectors defined after the training and validation of the neural network, the Nusselt number of a specific operating point can be calculated. The efficiency of the designed neural network can be characterized by the relative error for the tooth and yoke regions defined as follows:

$$e_{relative,i} = \frac{Nu_{CFD,i} - Nu_{NN,i}}{Nu_{CFD,i}}. \quad (5.37)$$

The representation of the relative error and its distribution over the data are shown with the aid of histograms for the tooth in Fig. 61, and for the yoke region in Fig. 62.

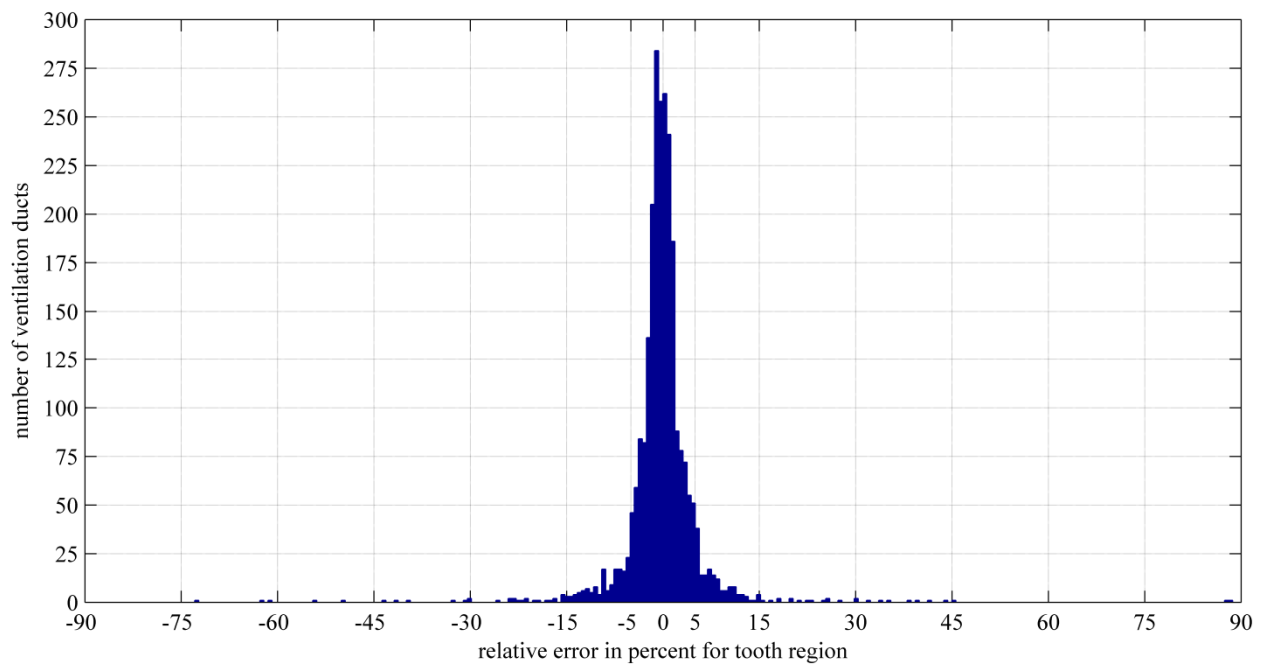


Fig. 61 Histogram of the computed relative error obtained for the data set evaluated for the tooth region

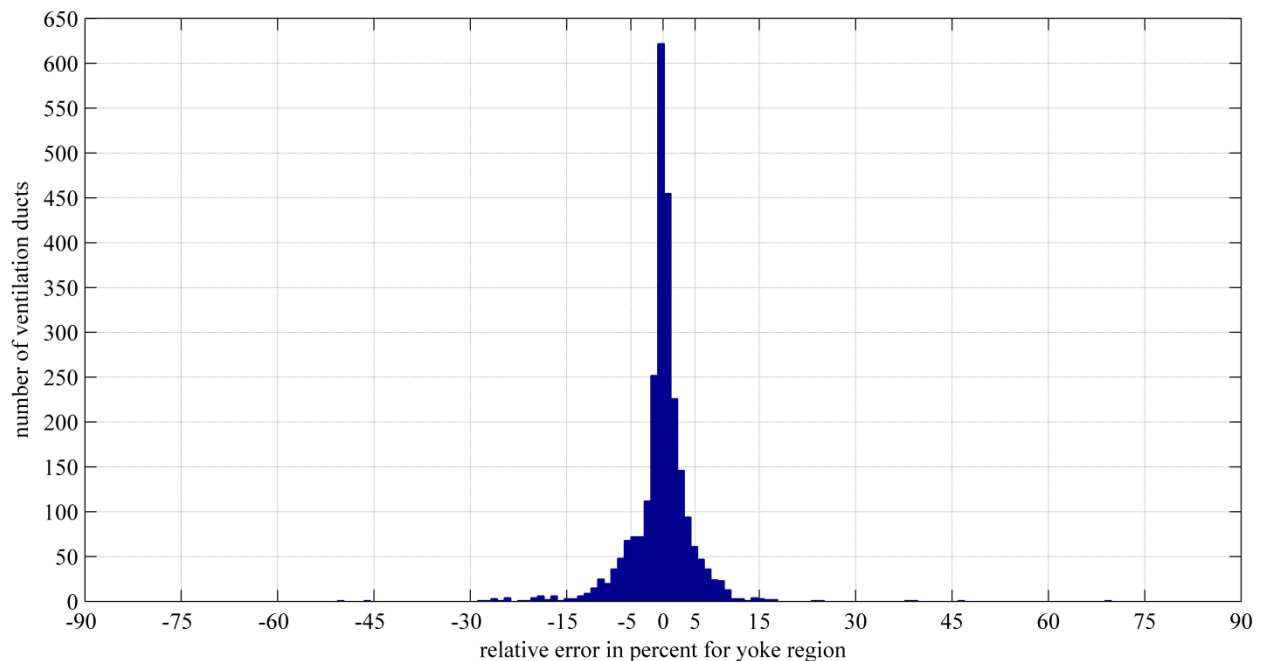


Fig. 62 Histogram of the computed relative error obtained for the data set evaluated for the yoke region

Compared to the values of the Nusselt number computed by CFD, the average relative error of the approximation obtained is below 5% for both regions. The bound of the relative error of 5% includes 2178 Nusselt numbers for the tooth region and 2089 for the yoke region, again out 2547 examples. As few as 132 Nusselt numbers evaluated at the tooth and 106 at the yoke have a higher error than 10%.

Fig. 63, Fig. 64, Fig. 65 and Fig. 66 compare the Nu values computed by CFD with those obtained from the neural network for the tooth and yoke regions. The results have been evaluated for all machine designs included and displayed separately for the eight different operating conditions ($m_1, m_2, \dots, \text{and } m_8$). Contrary to the power function approximation introduced in section 5.2, none of the operating conditions presented any problem for the neural network.

In the diagrams, the Nusselt number has been normalized by its highest computed value in the tooth region. If $Nu_{CFD} = Nu_{NN}$ held, the points would be on the dotted 45°-line and a bound of 5% is shown by the solid black lines.

A regression value of 0.997 has been computed for the tooth, and 0.995 for the yoke region, which are better than the regression values obtained with the power function approximation.

By means of neural networks it is possible to approximately calculate the average WHTC in the tooth and yoke regions of ventilation ducts of large air cooled synchronous machines. The definition of dimensionless parameters as inlet-outlet pairs of the neural network has the benefit of scalability depending on specific characteristic design parameters. Due to its relatively low computational effort, this approach is suitable for the thermal design of rotating electrical machines. In the procedure outlined for obtaining correlations of the convective WHTC of ventilation ducts with geometrical data as well as operational conditions, the CFD method was used for the determination of the inlet-outlet parameters for the neural network. A high accuracy of the neural network method has been achieved within a narrow range of 5% for the relative error and regression values to denote a correlation of 0.996 compared to values computed by CFD for the investigated machine designs.

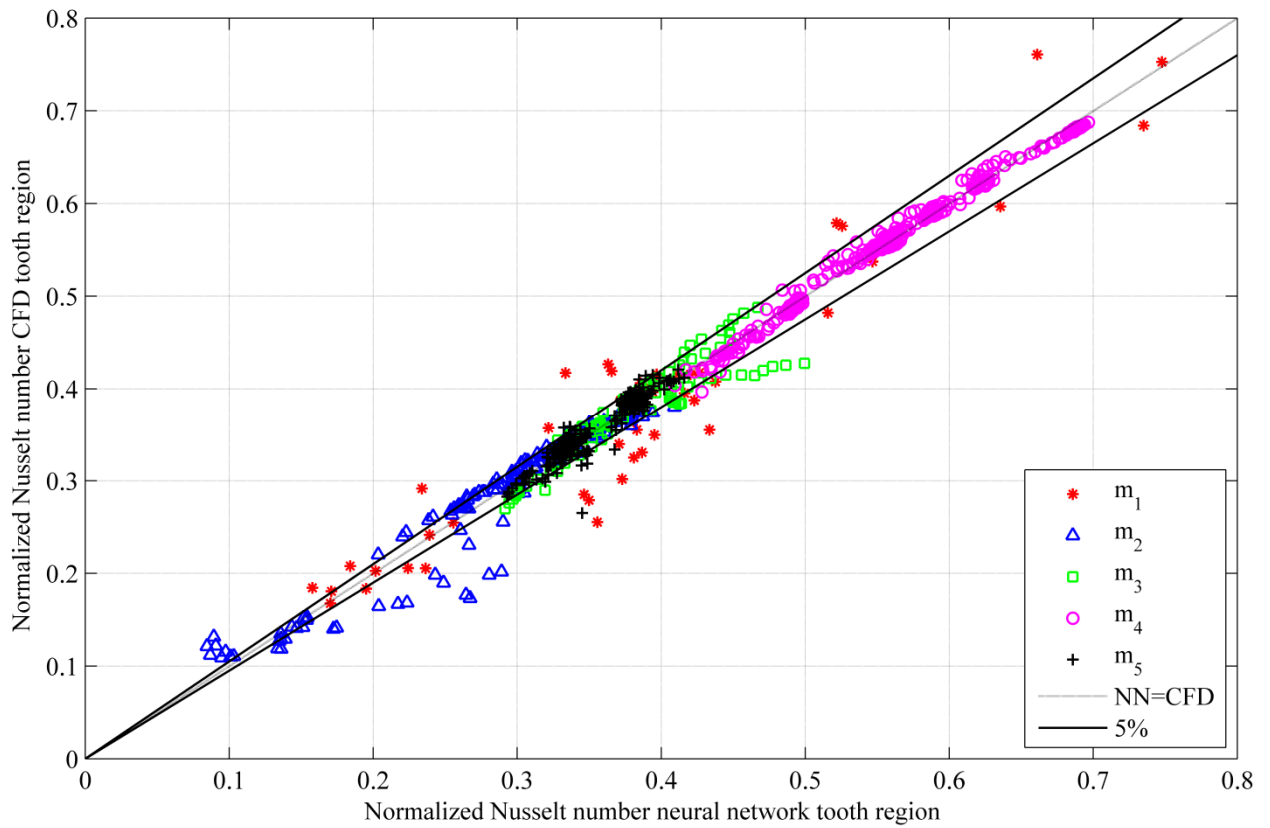


Fig. 63 Normalized Nusselt number computed by CFD versus normalized Nusselt number approximated with the neural network for different machine designs for tooth region

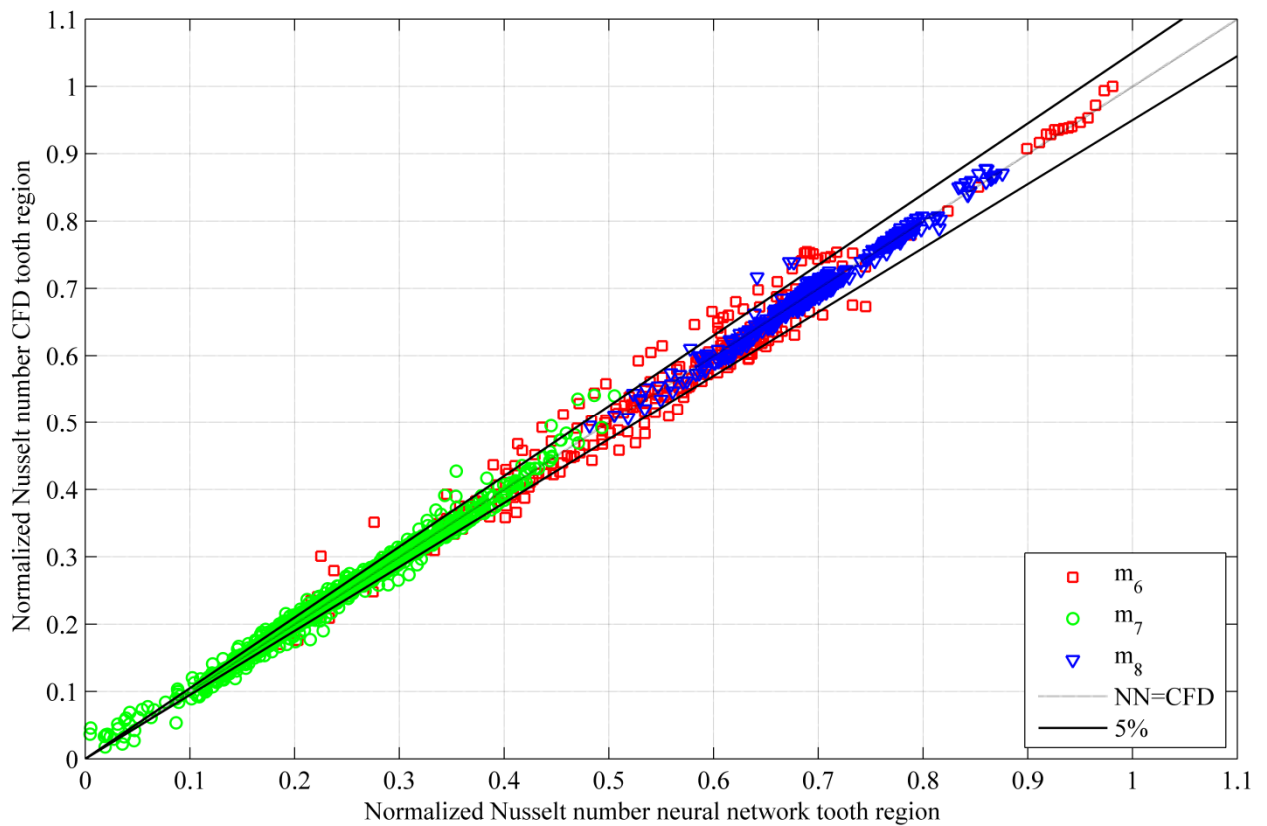


Fig. 64 Normalized Nusselt number computed by CFD versus normalized Nusselt number approximated with the neural network for different machine designs for the tooth region

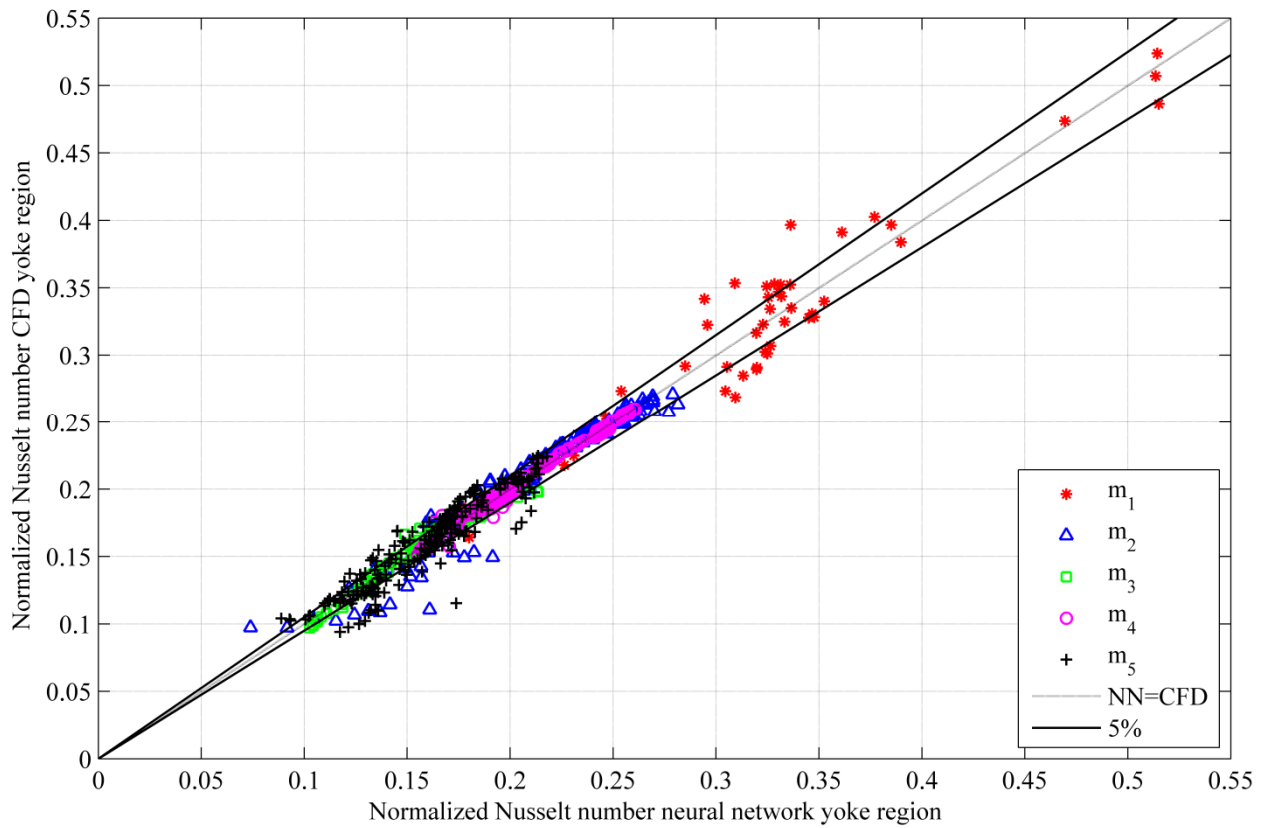


Fig. 65 Normalized Nusselt number computed by CFD versus normalized Nusselt number approximated with the neural network for different machine designs for the yoke region

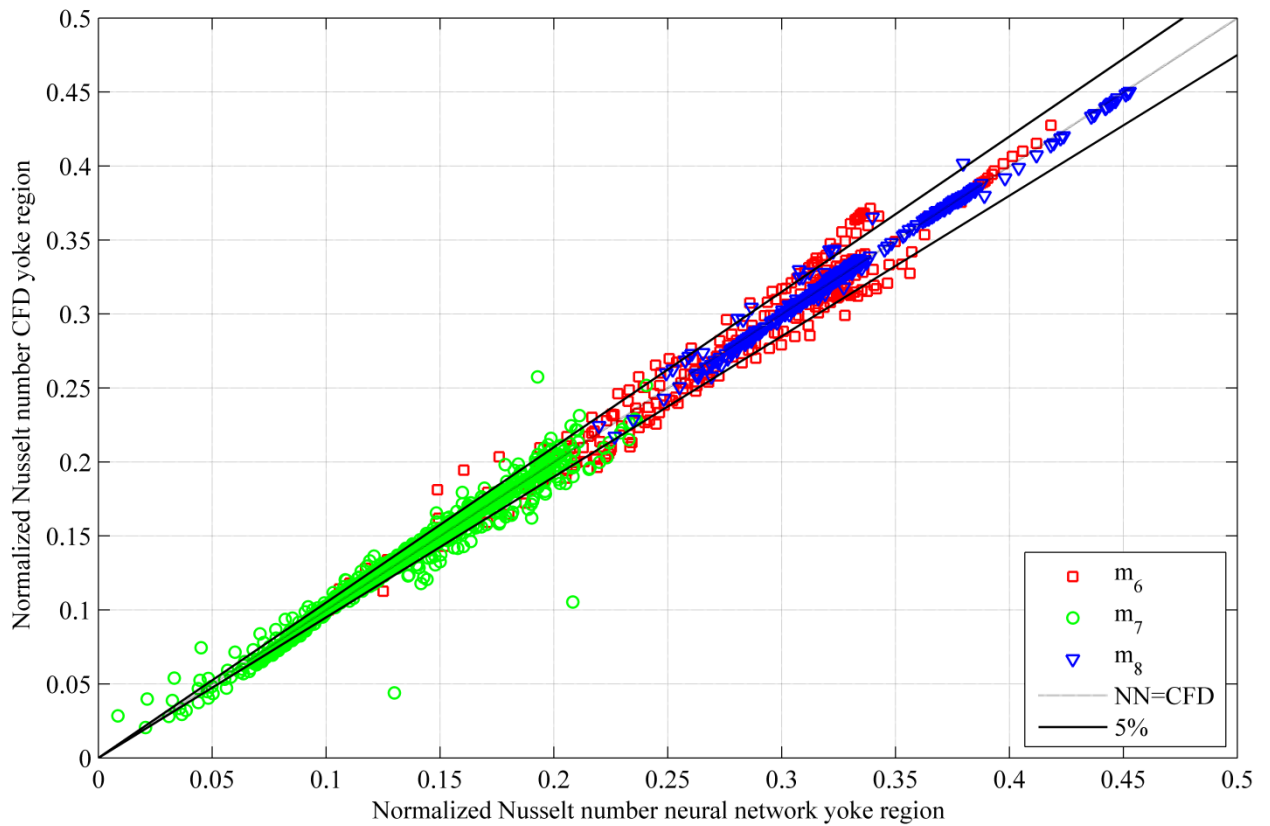


Fig. 66 Normalized Nusselt number computed by CFD versus normalized Nusselt number approximated with the neural network for different machine designs for the yoke region

6 Improved heat conduction model to compute temperature distribution in the solid domains of the stator

Having approximated the convective wall heat transfer coefficient by means of a constrained non-linear optimization algorithm or of a neural network, the heat convection can be defined as a boundary condition in a numerical model of heat conduction in the solid domains. The fluid reference temperature required in the boundary condition can be computed using an additional energy balance equation stating that the energy used to heat up of the coolant is equal to the heat evacuated from the solid domains due to the power losses. As a result, a novel slot section model of the ventilation duct can be generated. This has been analyzed, evaluated and validated against the well-established conjugate heat transfer method. The numerical model developed contains the solid domains of the stator of a large hydro generator including one slot section. The possibility of disregarding the fluid domain has large benefits in reducing the necessary numerical effort. The power losses can be defined in copper bars as well as in the stator iron. The analysis of the model allows the computation of the temperature field in the investigated parts which, in turn, can be compared with temperatures computed by the CHT model presented in chapter 4. The time consuming computations of the CHT simulation can be substituted by simply analyzing heat conduction (HC) in a model of the solid domains. The thermal field can be typically obtained in a few minutes in contrast to several hours needed by the CHT method.

Parts of the following chapter have been presented at two conferences [61] and [63]. Thereupon, some results were published in [62] and others are still in peer review for a further journal publication [64].

6.1 Geometry of the model

An axial half of a slot section model is presented in Fig. 67. The rectangular channels of a ventilation duct are built up by (b) space blocks inserted in the (a) stator iron. The stator winding consists of the (c) bottom and the (d) top bars, including the copper strands coated with insulation, the (e) filler and the (f) slot wedge. The thermal conductivity of the solid media is a parameter with great influence on the results of the heat conduction and has to be defined as accurately as possible. It has been assumed to be isotropic for the insulation, filler, slot wedge, space blocks and anisotropic for the copper bars and iron core. This set up takes account of the lamination of the iron sheets and also the Röbel- transposition in the copper bars.

The losses are defined for the (c) bottom and (d) top bar, directly in the copper as well as in the (a) stator with a distinction between the tooth and yoke iron regions. Afterwards, the heat transfer has been defined at the surface of the tooth and yoke regions by implementing the heat convection as a boundary condition. The energy equation has then to be solved to determine the

temperature distribution in the solid domains by the computing the heat conduction using (2.13). The losses in this equation are defined in section 6.2.2. The main benefit of this model is the accurate determination of the temperature in the solid domains and the low computational costs involved.

The CHT model employed includes the fluid additionally to the solid domains, as indicated in Fig. 68. The resulting numerical costs are high in comparison to the HC approach, since the SST turbulence technique needs the determination of the RANS models and, in addition, the automatic wall treatment has to be employed to solve the fluid flow and the related heat transfer. The anisotropic fluid properties concerning the thermal conductivity, dynamic viscosity and specified heat capacity are inherent in this numerical approach, too.

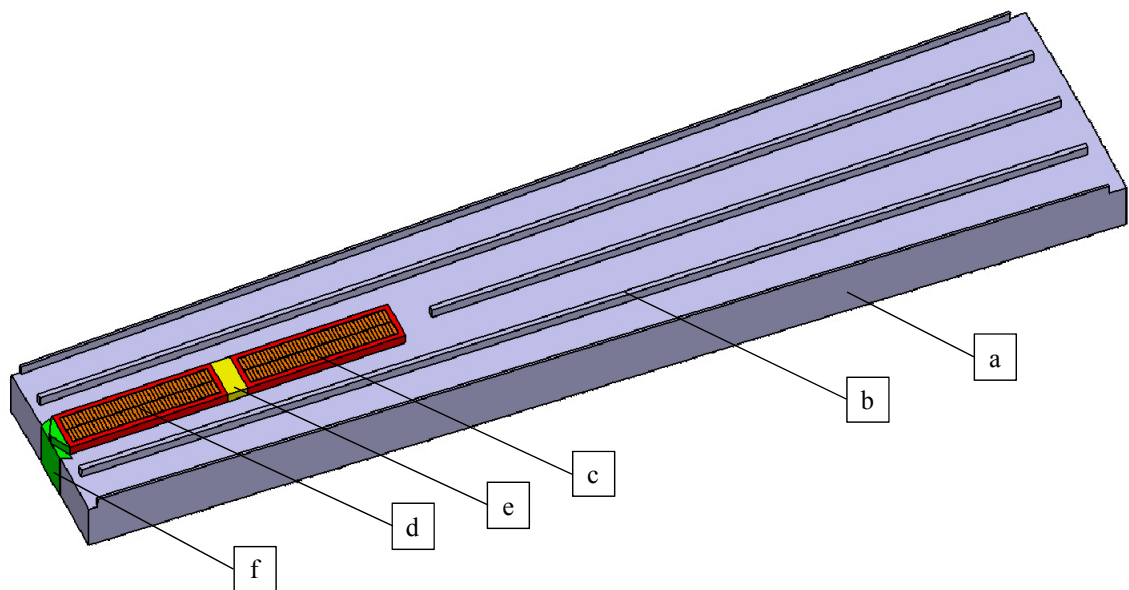


Fig. 67 Novel heat conduction model including the solid domains (a) stator iron, (b) distance bar, (c) bottom bar, (d) top bar, (e) filler and (f) slot wedge

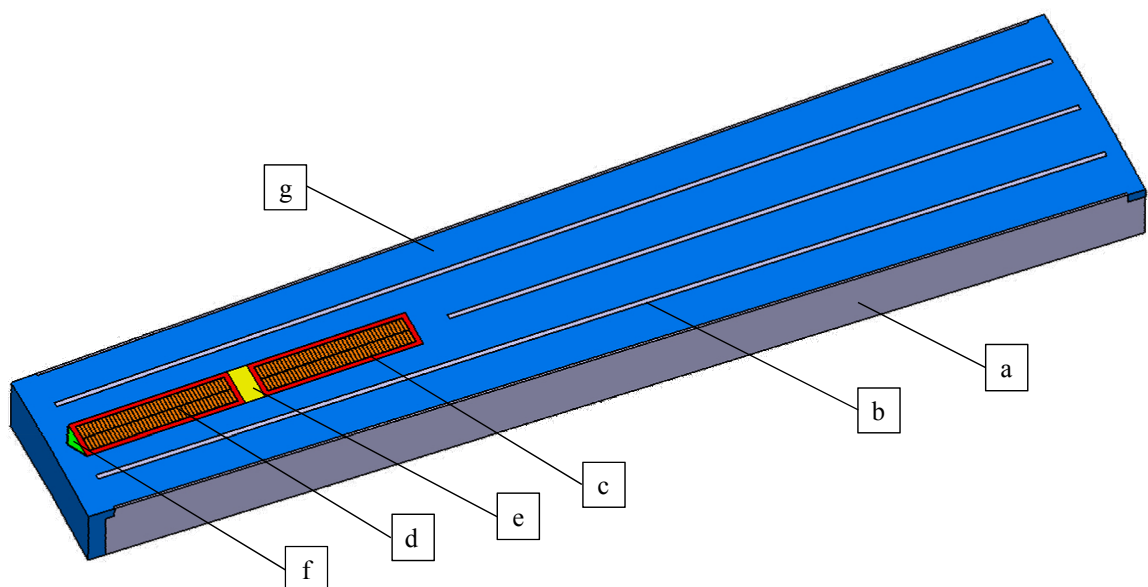


Fig. 68 Conjugate heat transfer model including the solid domains (a) stator iron, (b) distance bar, (c) bottom bar, (d) top bar, (e) filler, (f) slot wedge and (g) the fluid

6.2 Boundary conditions

6.2.1 Implementation of the heat convection

The time consuming computation of the heat convection represented by the wall heat transfer coefficient having been determined enables the introduction of a boundary condition on the surfaces of the tooth and yoke involving the WHTC α obtained by the power function approximation or from the neural network. Furthermore, the fluid reference temperature $T_{fluid,ref}$ is also needed to determine the convective heat flux q_{conv} at the surface in addition to the surface averaged wall temperature T_w to be solved. Indeed, the following equation is valid:

$$q_{conv} = \alpha \cdot (T_{wall} - T_{fluid,ref}), \quad (6.1)$$

$$T_{fluid,ref} = \frac{T_{fluid,inlet} + T_{fluid,outlet}}{2}. \quad (6.2)$$

The fluid reference temperature is the average of the defined inlet and unknown outlet temperatures. In (6.1), the fluid reference temperature is still an unknown, to be determined.

Therefore, an energy balance equation has been set up using the first law of thermodynamics stating that the heat responsible for heating up the fluid flow is equal to the heat transported over the surface from the solid to the fluid. The transported heat over the wall surface Q_{wall} can be defined with the convective wall heat transfer coefficient α , the temperature difference between wall temperature T_{wall} and fluid reference temperature $T_{fluid,ref}$ and the surface area A_{wall} . The heating up of the fluid can be expressed with the energy difference computed between the outlet enthalpy $H_{fluid,outlet}$ and the inlet enthalpy of the fluid flow $H_{fluid,inlet}$. The enthalpy is computed with the mass flow rate of the fluid \dot{m}_{fluid} , the specific heat capacity c_p and the temperature, $T_{fluid,outlet}$ for the enthalpy evaluated at the outlet and $T_{fluid,inlet}$ evaluated at the inlet. This can be expressed by the following equations:

$$Q_{wall} = H_{fluid,outlet} - H_{fluid,inlet}, \quad (6.3)$$

$$\alpha \cdot (T_{wall} - T_{fluid,ref}) \cdot A_{wall} = \dot{m}_{fluid} \cdot c_p \cdot (T_{fluid,outlet} - T_{fluid,inlet}). \quad (6.4)$$

By using (6.2), the fluid reference temperature can be expressed and the unknown outlet temperature of the fluid $T_{fluid,outlet}$ can be expressed as follows:

$$T_{fluid,outlet} = \frac{\alpha \cdot T_{wall} \cdot A_{wall} + \left(\dot{m}_{fluid} \cdot c_p - \frac{1}{2} \cdot \alpha \cdot A_{wall} \right) \cdot T_{fluid,inlet}}{\dot{m}_{fluid} \cdot c_p + \frac{1}{2} \cdot \alpha \cdot A_{wall}}. \quad (6.5)$$

Hence, the fluid reference temperature is defined and the numerical model can be analyzed. The domain has been split into the tooth and yoke regions to facilitate testing the two approximations of the WHTC determined by the neural network and the power function approach. The mass flow rate and the temperature at the inlet are obtained from CFD or the network method to ensure that the equation system can be solved to determine the thermal field in the solid domains in the HC model.

6.2.2 Definition of the electromagnetic losses

The power losses in the solid domains represent real operating conditions. Therefore they have been defined as thermal sources in the copper bars p_{copper} and in the stator iron p_{iron} as:

$$p_{copper} = \frac{J^2}{\sigma}, \quad (6.6)$$

$$p_{iron} = p_{hyst} + p_{eddy} = k_{hyst} \cdot f \cdot B^\beta + k_{eddy} \cdot \delta^2 \cdot f^2 \cdot B^2, \quad (6.7)$$

where J stands for the current density, σ for the conductivity, f for the frequency, B for the flux density, β is a suitable exponent, δ denotes the penetration depth and k_{hyst} and k_{eddy} are numerical parameters obtained from measurements and characterizing the material.

6.3 Validation of the HC model by comparison to the CHT model

The validation has been carried out for different inlet conditions for all ventilation ducts of a large hydro generator. These inlet conditions have been obtained from the overall model analyzed by CFD. The same inlet conditions have been defined in the HC model as well as in the CHT model investigating each of the 29 ventilation ducts. The approximated convective wall heat transfer coefficients are shown for each numerical approach in Fig. 69, normalized by the highest WHTC arising in the CHT solution.

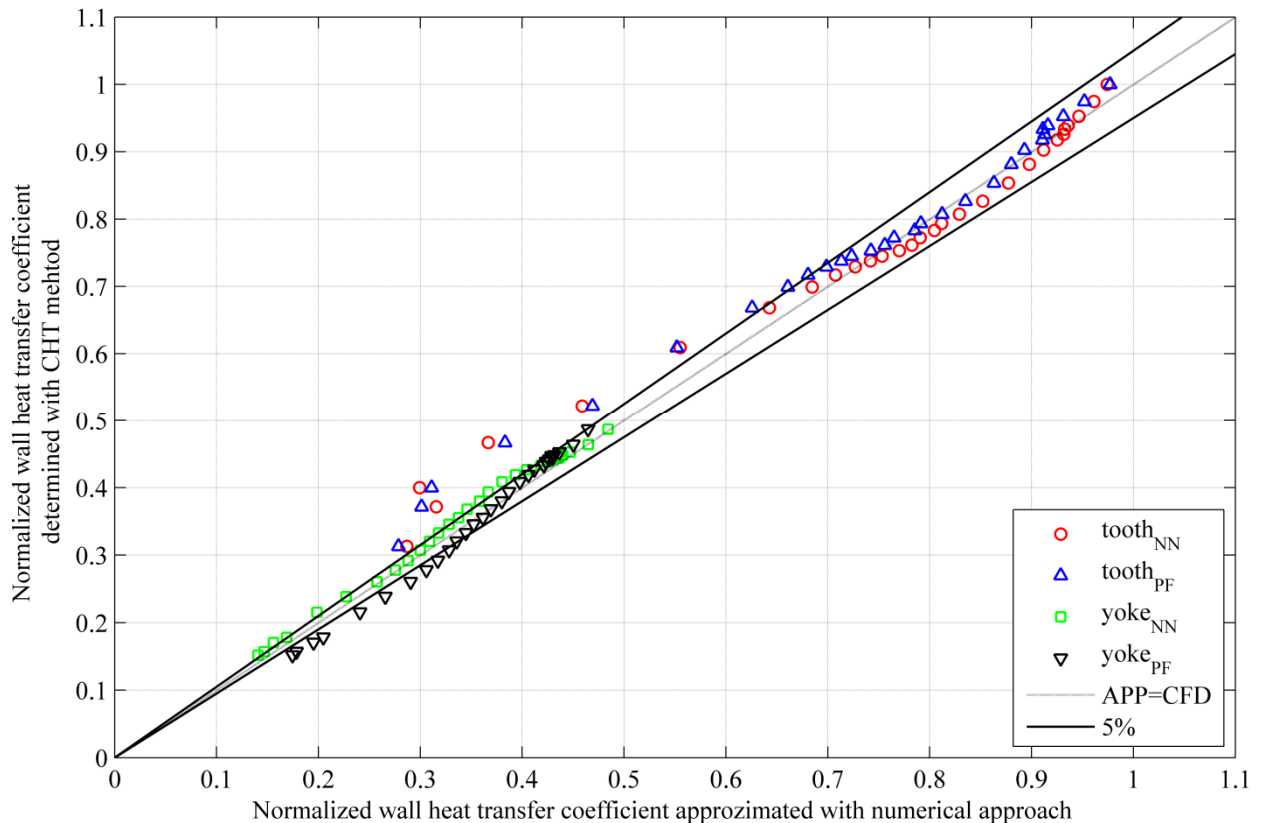


Fig. 69 Normalized wall heat transfer coefficient obtained by CHT versus normalized wall heat transfer coefficient approximated with neural network (NN) and power function (PF) for 29 different ventilation ducts

The solid black lines define the deviation with an error of 5% and a deviation of 0% is marked with the dotted black line of 45°. The index NN denotes the WHTC obtained from the neural network and PF the WHTC computed by the power function.

6.3.1 Comparison of the computed temperatures in the solid domains

The solid temperatures of the top bar, bottom bar, spacer, iron tooth and iron yoke have been evaluated both from the CHT and the HC models. The computed temperatures of the HC model have been obtained by using the WHTC approximated by constrained non-linear optimization in Fig. 70 and Fig. 71, and by the neural network in Fig. 72 and Fig. 73. For each numerical approach, the temperature of the CHT model has been plotted against the temperature of the HC model. Both the volume averaged temperature and the maximal arising temperature have been evaluated in the different solid domains. The normalized steady state temperatures and normalized temperature distributions have been expressed in centigrades.

The temperature deviation is in a range of 5%, marked by the solid black lines for both cases. The relative error has been computed with the following formula for each ventilation duct:

$$e_{relative,solid} = \frac{T_{CHT,solid} - T_{HC,solid}}{T_{CHT,solid}}. \quad (6.8)$$

Thereupon, the averaged error for the volume as well as the maximal volume temperature have been computed for the investigated 29 ventilation ducts.

Table 12 summarizes the computed averaged error (6.8) for all 29 ventilation ducts evaluated for each solid domain with the WHTC obtained both by power function approximation and by the neural network.

part	WHTC obtained from power function		WHTC obtained from neural network	
	averaged temperature	maximal temperature	averaged temperature	maximal temperature
top bar	2,96%	3,31%	2,85%	3,19%
spacer	0,54%	1,19%	0,48%	1,08%
bottom bar	1,11%	0,89%	1,13%	0,96%
iron tooth	1,44%	0,96%	1,39%	0,83%
iron yoke	0,83%	0,43%	0,55%	0,27%

Table 12 Averaged relative errors in the investigated ventilation ducts computed for averaged and maximal volume temperatures and for both numerical approaches

It has been found that the temperature deviations between the HC model and CHT model are relatively small (about 3%) implying that the HC model, together with approximations of WHTC and the fluid reference temperature, is generally applicable for calculating stator temperatures. Both approximations of the convective WHTC obtained by neural network and constrained non linear optimization compute the same accurate temperature field in the solid domains. The HC model takes benefit of shorter calculation times, which are about 15 minutes for the HC model contrary to 12 hours for the CHT model. The omitted fluid domain makes the time consuming meshing process of the boundary layer unnecessary and hence decreases the computation time considerably in comparison to CFD/CHT investigations.

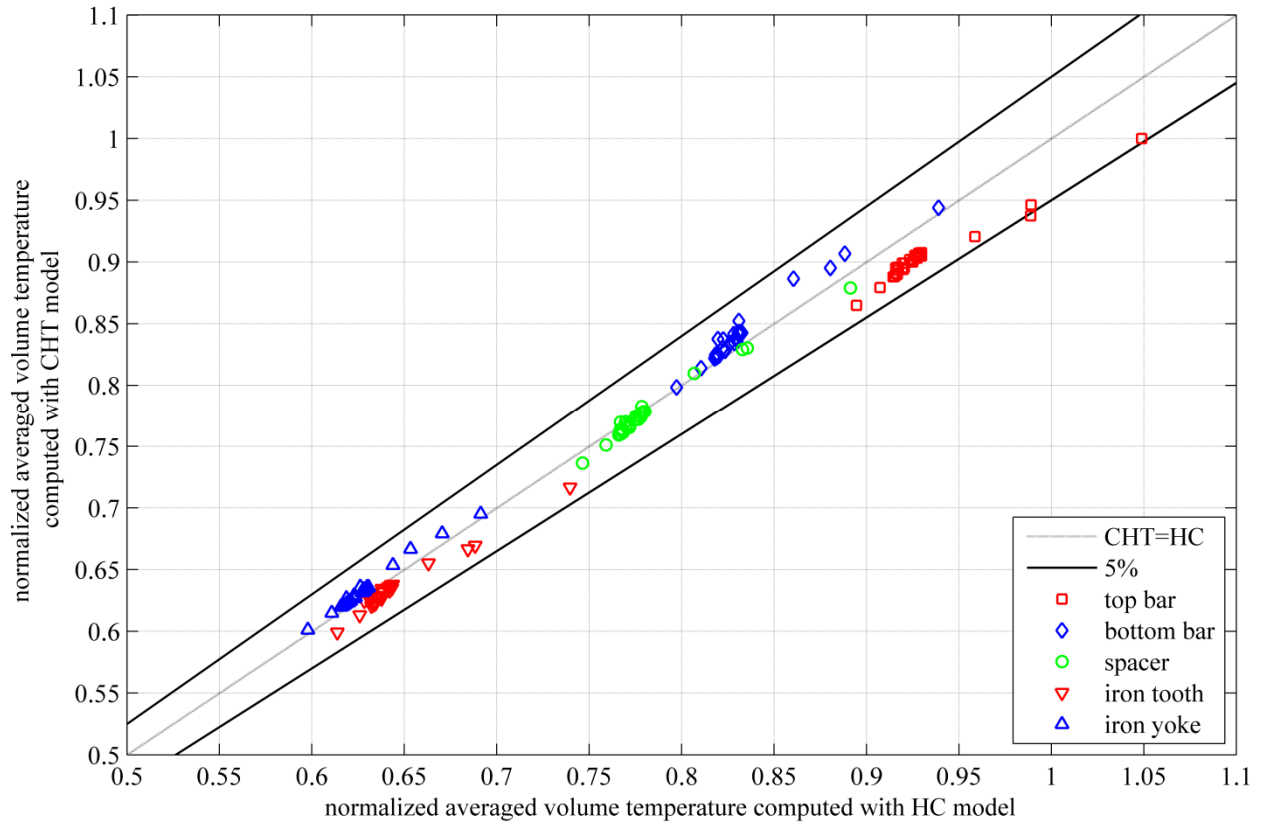


Fig. 70 Normalized averaged volume temperature of the various components for the CHT model and the HC model with the defined convective wall heat transfer coefficient approximated with the power function

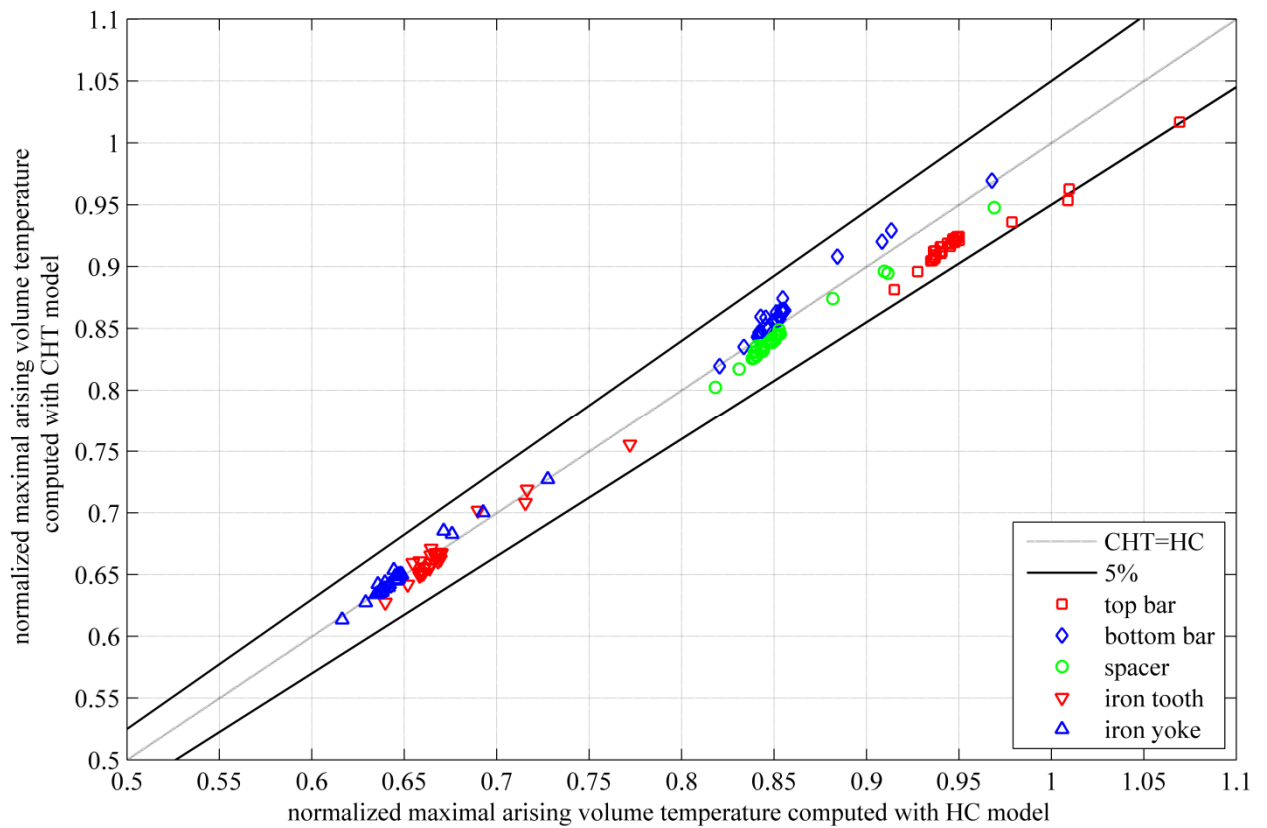


Fig. 71 Normalized maximal arising volume temperature of the various components for the CHT model and the HC model with the defined convective wall heat transfer coefficient approximated with the power function

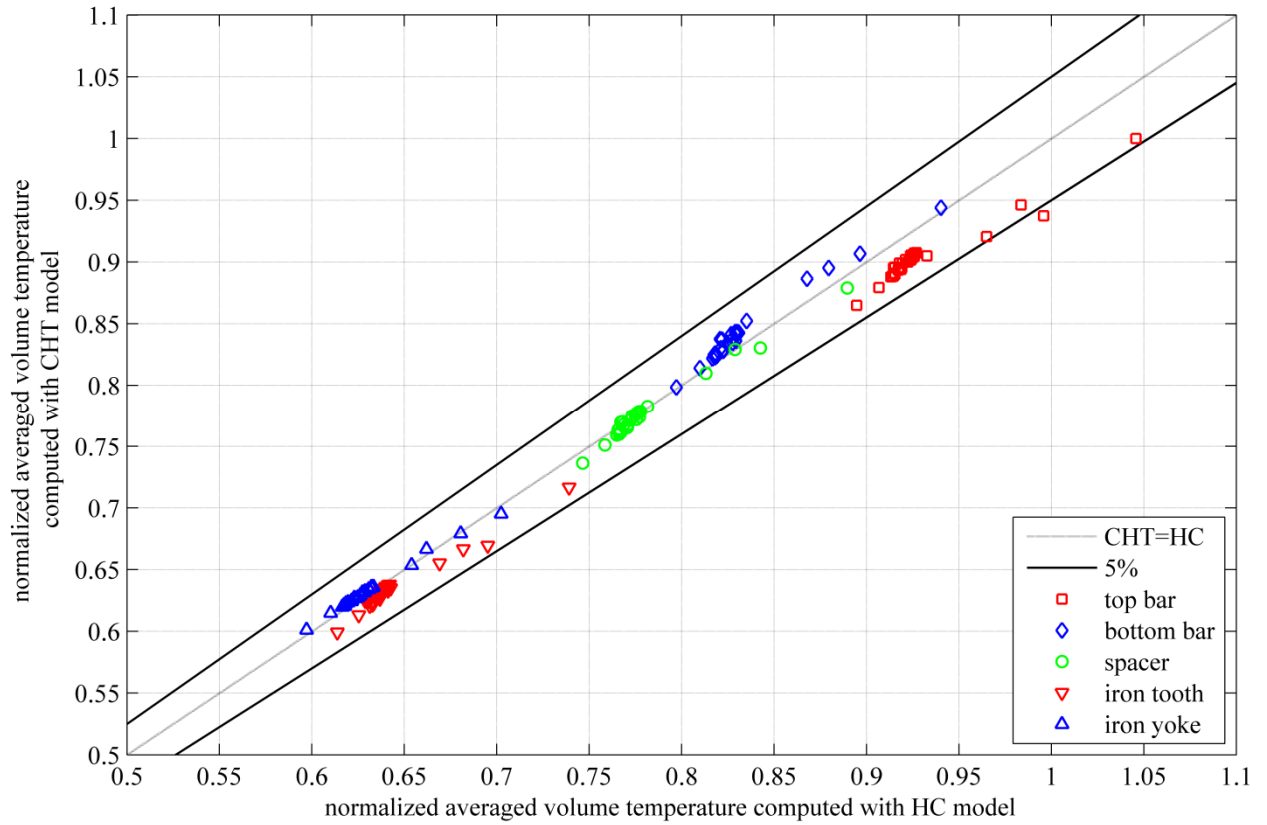


Fig. 72 Normalized averaged volume temperature of the various components for the CHT model and the HC model with the defined convective wall heat transfer coefficient approximated with the neural network

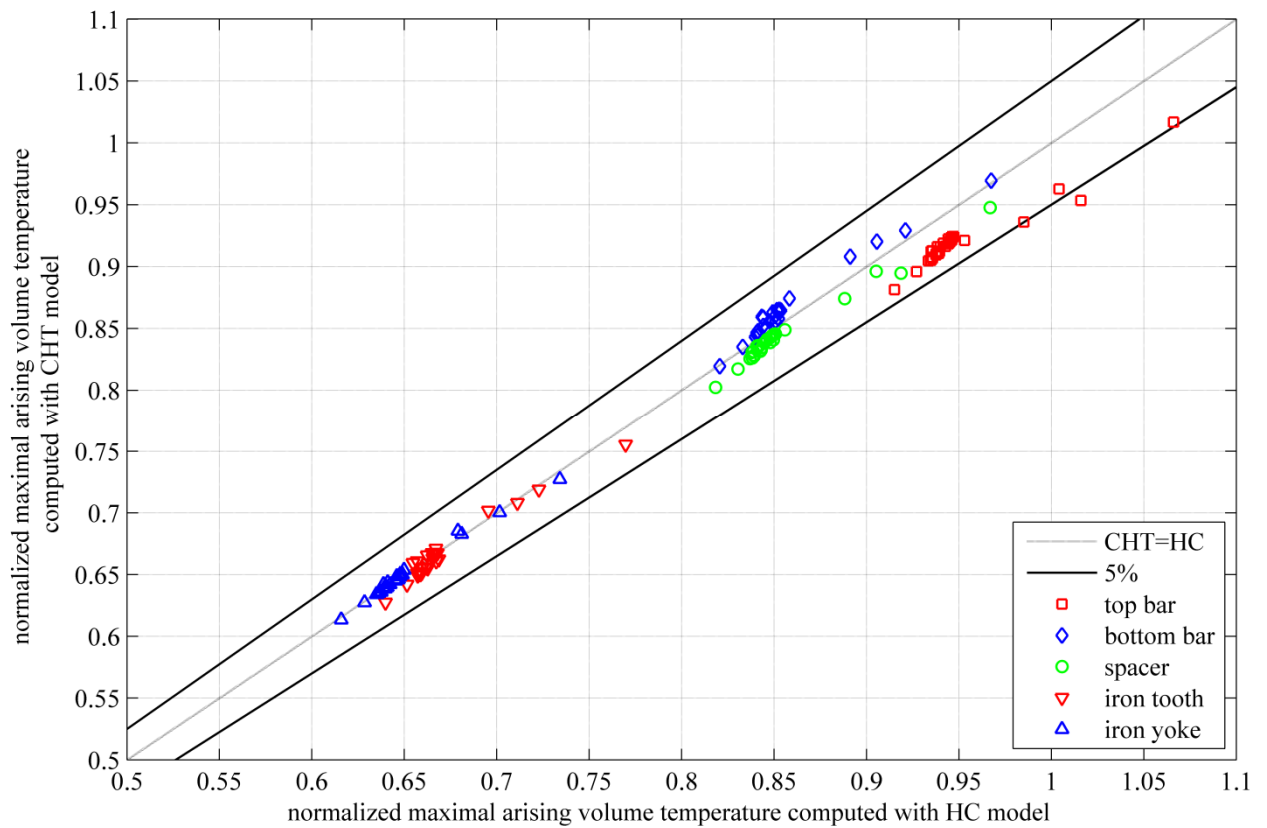


Fig. 73 Normalized maximal arising volume temperature of the various components for the CHT model and the HC model with the defined convective wall heat transfer coefficient approximated with the neural network

6.3.2 Comparison of the temperature distribution in the solid domains

The temperature distribution in radial direction computed as an averaged axial value over the (a) slot plane and over the (b) iron plane shown in Fig. 74 is investigated to characterize the heat transport. The normalized temperature distribution on both planes is shown in Fig. 75 and Fig. 77 averaged over the slot wedge, the insulated top bar, the filler, the insulated bottom bar and through the yoke iron evaluated on the slot plane for the boundary conditions obtained with the power function approximation and the neural network. In addition, the distributions in Fig. 76 and Fig. 78 show the normalized temperatures in the iron averaged over the tooth and yoke regions evaluated in the iron plane.

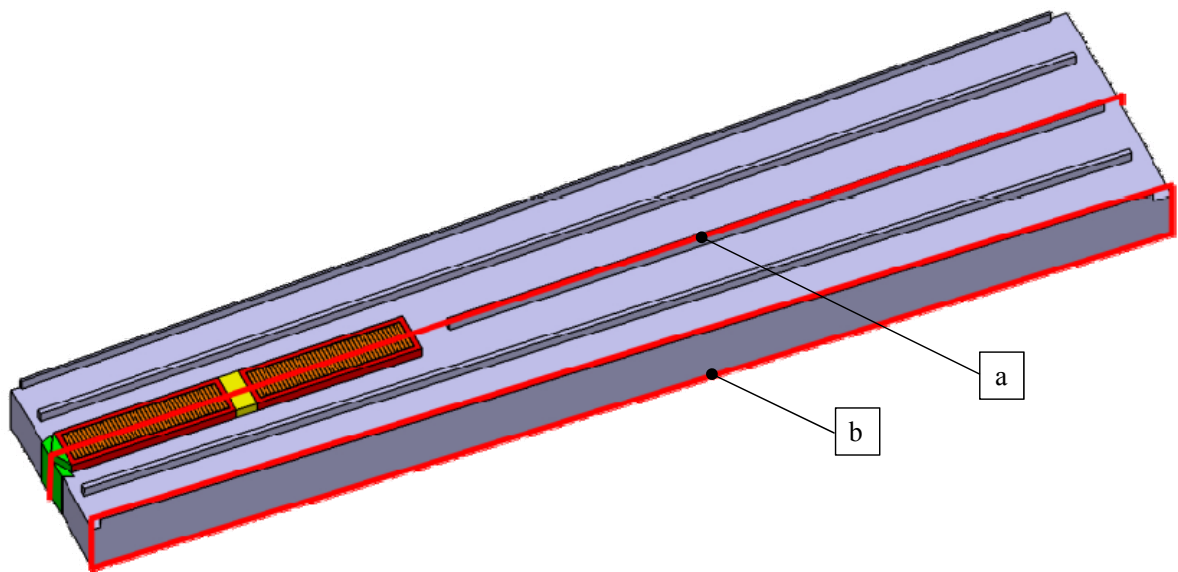


Fig. 74 HC model with (a) slot plane and (b) iron plane to evaluate the temperature distribution in radial direction along the ventilation duct

The deviation between the CHT model and the HC model is presented in the figures by using the WHTC approximated by constrained non-linear optimization in Fig. 75 and Fig. 76, and by the neural network in Fig. 77 and Fig. 78 evaluated for the 20th duct as an example. The deviations in the other 29 ducts have the same magnitude as in the duct presented. The higher deviation in the tooth region is caused by the inlet condition which neglects the turbulent effects given by the rotor rotation and by the wall heat transfer coefficient being defined as a constant value. This effect is also included in the yoke region, but the deviation is less than in the tooth due to less reverse flows occurring. Nevertheless, the temperature deviation is below 3%, a low value for the temperature ranges involved. The averaged error computed at the slot plane is about 0.9% and 1.2% at the iron plane evaluated for the HC model with the WHTC obtained by power function approximation and it is 0.87% at the slot plane and 1.11% at the iron plane evaluated for the HC model with the WHTC obtained by the neural network. The error for the neural network is 1.53% in the tooth and 0.47% in yoke over the slot plane and 1.21% in the tooth iron and 0.49% in the yoke iron evaluated at the iron plane. With the power function approximation, the error at the slot plane is 1.58% in the tooth and 0.48% in the yoke region and on the iron plane it is 1.27% at the tooth and 0.50% at the yoke region. The compared results indicate a relatively small deviation as presented in chapter 6.3.1, so that this model achieves an accurate evaluation of the temperature distribution on the specified slot and iron planes.

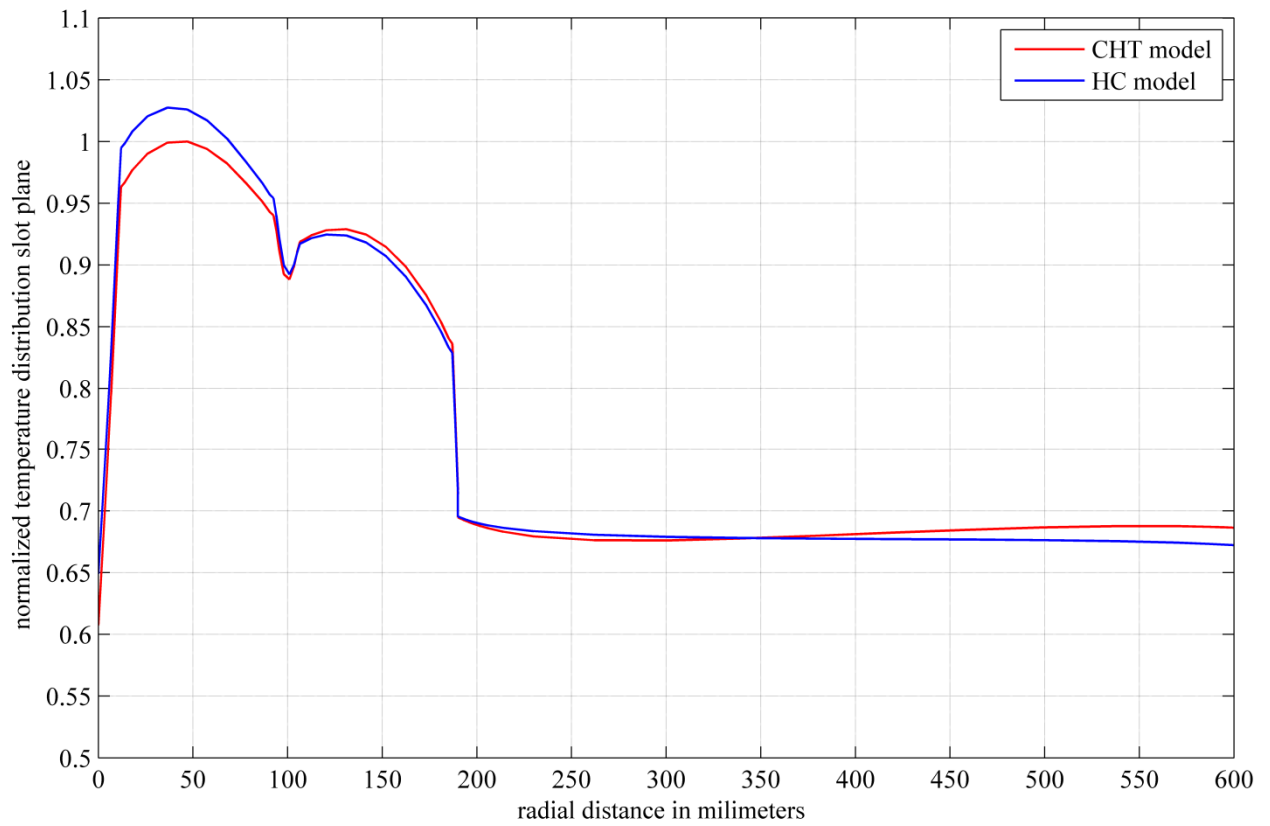


Fig. 75 Normalized temperature distribution in the mean slot plane computed for the 20th ventilation duct of the CHT model and the HC model with the approximated WHTC obtained by the power function approximation

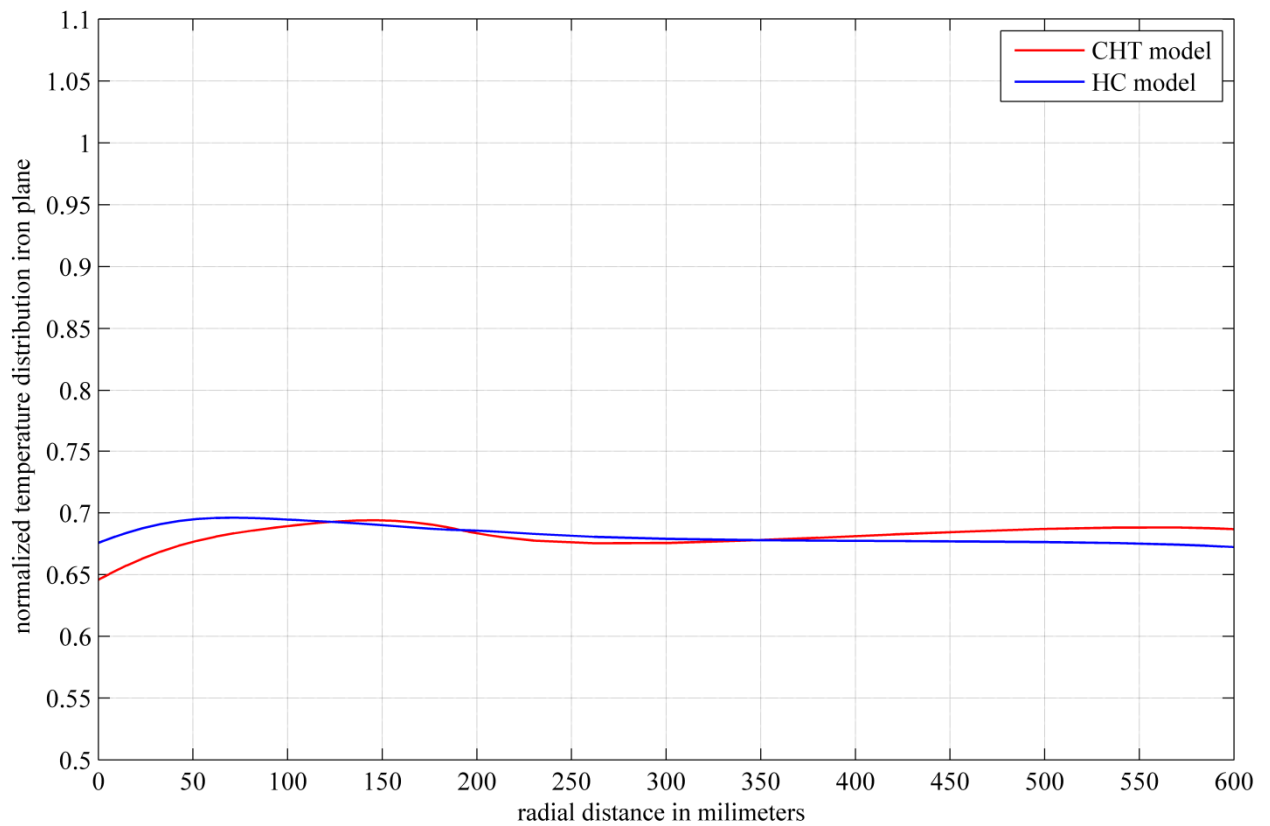


Fig. 76 Normalized temperature distribution in the mean iron plane computed for the 20th ventilation duct of the CHT model and the HC model with the approximated WHTC obtained by the power function approximation

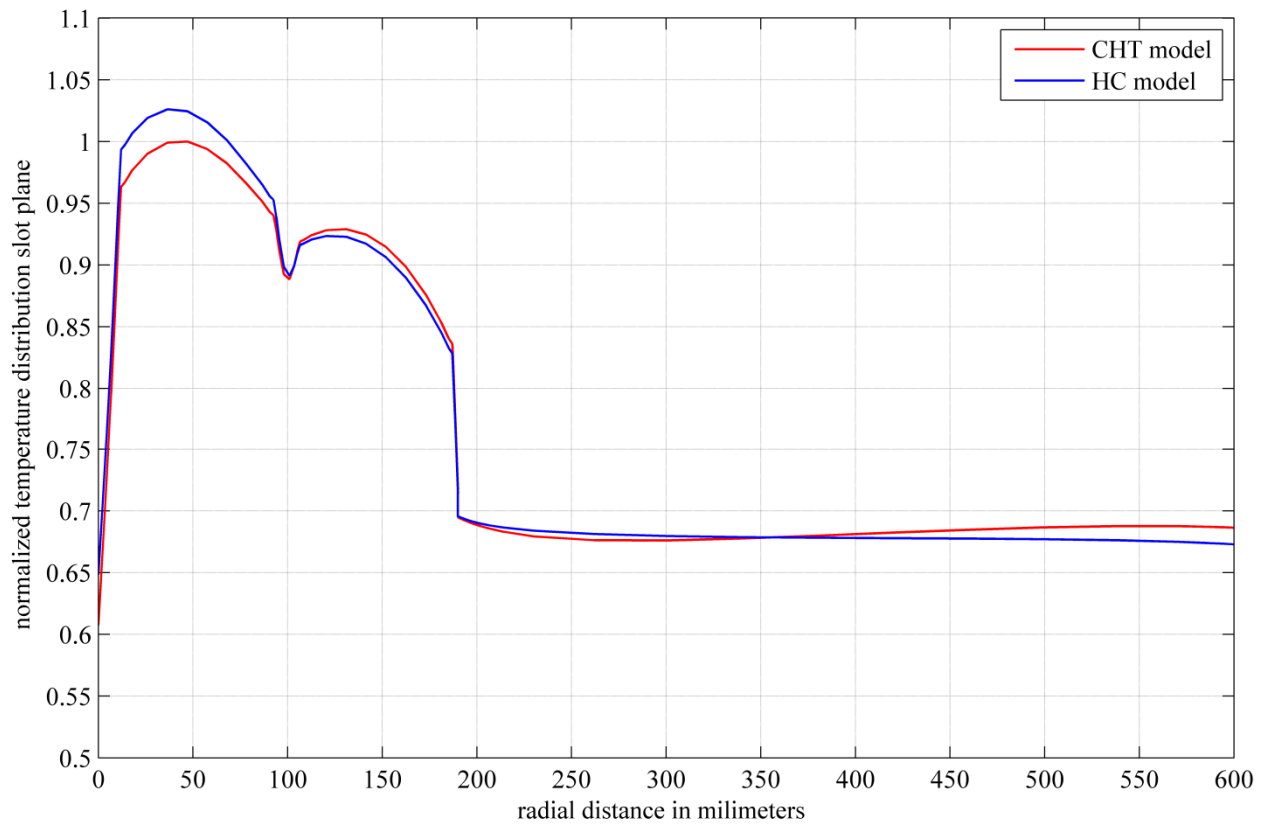


Fig. 77 Normalized temperature distribution in the mean slot plane computed for the 20th ventilation duct of the CHT model and the HC model with the approximated WHTC obtained by the neural network

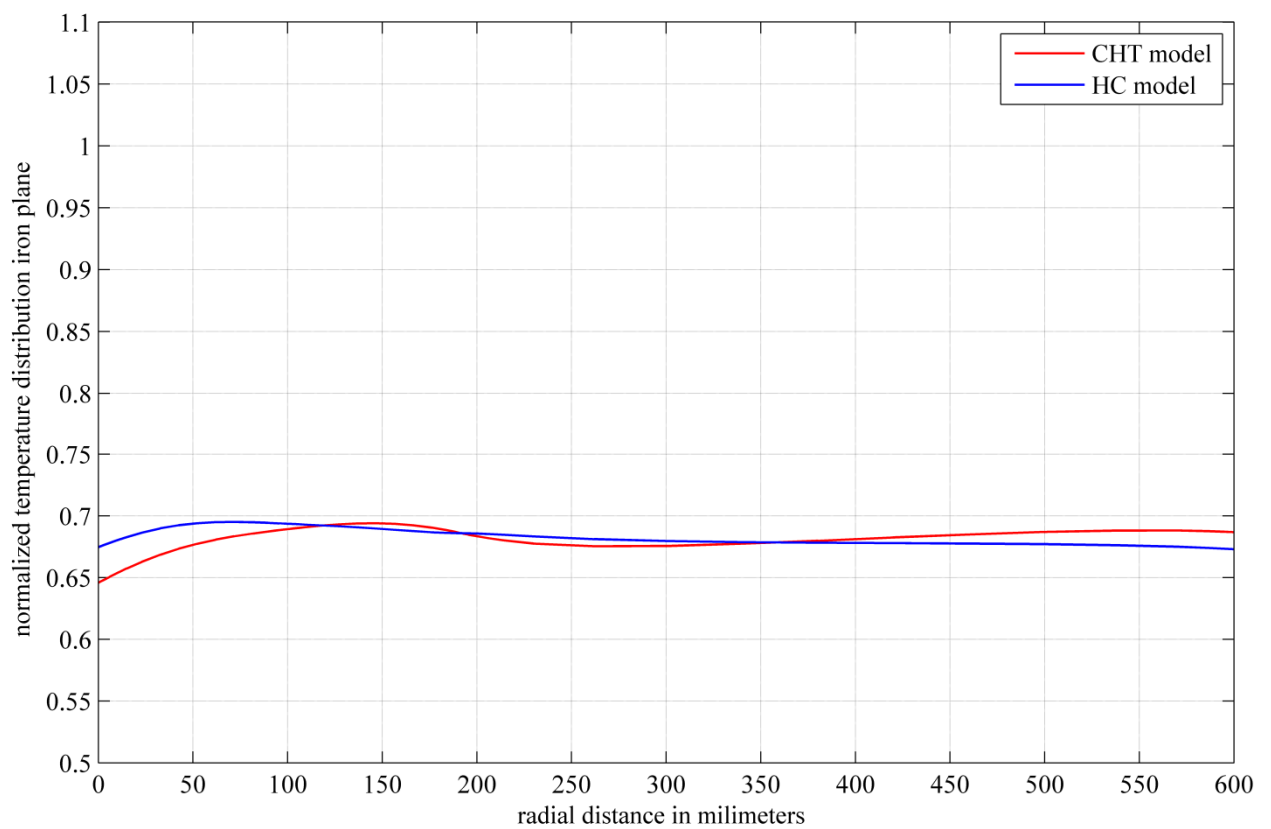


Fig. 78 Normalized temperature distribution in the mean iron plane computed for the 20th ventilation duct of the CHT model and the HC model with the approximated WHTC obtained by the neural network

7 Conclusion

The computation of the fluid and thermal field of electrical machines has been an issue without satisfactory solution for a long time. However, nowadays, the necessary resources in the manufacturing process of electrical machines can be efficiently reduced by a comprehensive understanding of the utilization of each single component. This demands the development of computational methods to provide effective thermal designs.

The review of literature in the first chapter has shown that there are several approaches to determine the thermal management in electrical machines by taking the effects of heat transfer into account. The commonly used network method is the state of the art in the design process, including electric, fluid and thermal networks. These sub-networks are as accurate as the used coefficients obtainable by analytical formulas, numerical simulations and measurements. Specific coefficients can be easily measured with the right equipment, but the evaluation of particular parameters, especially within the housing of the electrical device cannot be carried out by measurements. Therefore, numerical computations have moved to the focus of investigations in the last century using the finite element method to compute electro-magnetic field, computational fluid dynamics (CFD) to determine the fluid flow and the related convective heat transfer by solving the 3-D transport equations concerning the fluid domain and the conjugate heat transfer (CHT) method to take the fluid as well as the solid domains into account. This latter method is a powerful tool to investigate the heat conduction, heat convection and radiation, but the numerical effort involved is extremely high. Even today, simulating the whole machine or the coupling of different approaches is not possible. Consequently, other models or approaches have to be found to determine the variables to be used in the standard design tools.

The fundamentals and theoretical background of fluid dynamics and computational fluid dynamics to solve the equation systems has been presented in chapter 2. The turbulence model plays a crucial role by adding further equations to ensure the solution of the given problem by using steady state simulations. Additionally, several wall formulations have been defined in the last years to compute the effects near the wall surface, especially with focus on the heat transfer. The right choice of the large amount of available turbulence models is an important issue for an appropriate solution.

The investigation of the cooling schemes and of the convective heat transfer has been carried out using CFD, as presented in chapter 3. The state of the art Frozen Rotor method for steady state simulations has been compared with another approach to consider the rotor rotation using a Mixing Plane method. The deviation of fluid and thermal variables is less than 11% between these two methods. The main advantage of the Mixing Plane method is that 40% of the elements can be saved and the numerical effort as well as the computation time can be significantly reduced. The difference is in the modeled stator domain, a pole section including 13 slot sections in the Frozen Rotor model, and a single slot section in the Mixing Plane model. On the one hand, these methods enable a more detailed modeling and thus, more reliable results may be obtained. On the other hand, the more detailed the model, the larger are the computational costs. Therefore, a novel technique has been used to generate the inlet conditions from the overall

models and define these as a boundary condition at the inlet of single ducts models. A pole section model has been introduced to define the boundary conditions of the Frozen Rotor model and a slot section model for the definition of variables obtained by the Mixing Plane model. This domain decomposition is a powerful tool to obtain realistic distributions of several parameters in contrast to the definition of constant parameter values as it is commonly used. The mesh requirements can be satisfied for these single duct models, especially for the investigations on the convective wall heat transfer coefficient. Additionally, a sensitivity study has been carried out on both single duct models with different turbulence models. This study has pointed out that the used Shear Stress Transport (SST) turbulence model with automatic wall treatment is mesh dependent, but the deviations between the results obtained by a coarse and a fine mesh concerning the convective heat transfer coefficient, which is the most sensitive parameter, are in an acceptable range. Using the SST turbulence model, the value for the non-dimensional wall distance y^+ , a parameter characterizing the mesh refinement at the walls, should not be in a range of $5 \leq y^+ \leq 30$ to minimize the numerical error. Furthermore a design study has been done to point out the positive and negative effects of different solid domains for the fluid flow and related heat transfer in the stator ventilation duct.

Further on, a novel conjugate heat transfer model has been developed to compute the temperature field in the fluid as well in the solid domains as presented in chapter 4. The CHT model has been validated with measurements obtained from a laboratory model. This model has included three ventilation ducts and five slot sections. The losses have been produced using heating rods in the full copper bars. A volume flow rate has been defined at the ventilation duct inlet to determine the heat convection for five different operating points. The copper and iron temperature has been measured at different measurement points in the solid domains and the fluid inlet and outlet temperature has been measured to verify the heating up of the coolant. The numerical set-up includes the inlet conditions of the fluid obtained from the measurements and the power losses of the heating rods have been defined in the copper bars. In addition, anisotropic fluid properties, anisotropic thermal conductivity of the stator iron and isotropic thermal conductivities of the other solid domains have been taken into account. The advantage of the SST turbulence model with the automatic wall treatment has been also utilized in the following steady state simulations of this problem. Furthermore, three different winding assemblies have been investigated including different mountings of the copper bars in the slot. The results obtained by the two approaches show a good agreement concerning the measured solid and fluid temperatures for each investigated model. The averaged deviation concerning the copper temperature is less than about 2% and, for the iron temperature, it is less than 13%. The computed fluid temperature is even more accurate with an averaged difference of less than about 1%. The numerical simulation of heat conduction and heat convection yields precise results even if compared with the measurements on a laboratory model. The capability of the conjugate heat transfer method to be able to take account of losses defined in the solid domains leads to a simulation of the actual situation in more detail than assuming a constant wall temperature as common in CFD simulations. The high numerical effort is a burden of the CHT method, especially for modeling small air gaps with an extremely fine mesh. The Reynolds number in this area is in the laminar zone and this can cause problems in the numerical solution due to the turbulence model used. Therefore, an additional approach has been chosen to improve the CHT model developed. A thermal resistance on the surface instead of a modeled axial air gap has been used in further investigations. The model with the thermal resistance on the surface, called interface model, has been validated with the CHT method as well as with the measurements. The interface model computes the same results as the CHT model with a deviation of less than 0.2% and the deviations compared with the measurements are therefore the same as with the CHT model. The computation time can be halved using the thermal resistance.

A significant part of the thesis is chapter 5, including two different approaches to approximate the convective wall heat transfer coefficient for large hydro generators. By the use of CFD, a high variety of different large hydro generator designs has been modeled, computed and evaluated as described in chapter 3. The designs differ in the cooling scheme, different machine geometries and operating conditions. The cooling scheme can be a self ventilation or external ventilation realized by axial and radial fans with different fan characteristics concerning volume flow rates and pressure differences. The geometry designs vary in the cross section of the sub ducts and length of the ventilation ducts in the stator, the number of distance bars, the slot wedge design and as well as the end winding and rotor designs influencing the inlet condition at the ventilation ducts. The operating conditions include different rotational speeds and pole numbers on the rotor. It is worth mentioning that the included models cover a wide range of machines and the obtained correlation would work for each large hydro generator designed by the industrial partner in the last two decades. These CFD data have been validated with 1-D fluid and thermal networks and with measurements. Several non dimensional variables have been defined to approximate the Nusselt number using two different numerical approaches. First of all, a formula has been developed to approximate the Nusselt number by using a constrained non linear optimization algorithm to determine the parameters included. These factors and exponents have been determined with a least square technique and the evaluation shows an accuracy of less than 10% for tooth as well as for the yoke region. Additionally, a neural network has been designed with the aim to generate a more accurate approximation of the Nusselt number. The efficiency of the trained, validated and tested neural network yields an accuracy of less than 5% for both regions. After the determination of the Nusselt number, it is possible to compute the convective wall heat transfer with the thermal conductivity and the hydraulic diameter of the investigated region. Both novel approaches have been implemented in a FORTRAN module, which is going to be employed in the standard design tools. The definition of the approximated convective wall heat transfer coefficient can also be easily incorporated in other numerical tools to define the heat convection as a boundary condition and omit the numerical computation of the fluid domain.

Finally, using the approximated WHTC, a heat conduction model has been developed in chapter 6. The numerical model includes the solid domains only and the convective wall heat transfer coefficient has been used to define a boundary condition at the tooth and yoke surfaces. The fluid reference temperature has been included by an additional equation stating the first law of thermodynamics. The electromagnetic losses have been defined in the top and bottom copper bars as well as in the tooth and yoke iron as obtained by electro-magnetic computations. The averaged and maximal arising temperatures in the bottom and top copper bar, the spacer, the tooth and yoke iron have been validated with the established CHT method. The deviations of the novel heat conduction model from the CHT model are less than about 3%. The temperature characteristics plotted from the inner to the outer diameter, evaluated along the slot and iron planes show a maximal deviation of 3% with nearly the same characteristics. The main advantage of the heat conduction model is the fast computation time of 15 minutes in contrast to the computationally expensive CHT method needing 12 hours.

8 References

- [1] G. Müller and B. Ponick, *Grundlagen elektrischer Maschinen*, 9th edition, WILEY-VCH, Weinheim, 2006.
- [2] G. Müller and B. Ponick, *Berechnung elektrischer Maschinen*, 9th edition, WILEY-VCH, Weinheim, 2006.
- [3] W. Schuisky, *Berechnung elektrischer Maschinen*, Springer-Verlag, Wien, 1960.
- [4] R. Richter, *Elektrische Maschinen*, Springer, Berlin, 1967.
- [5] F. Incropera, and D. DeWitt, *Introduction to heat transfer*, 3rd edition, John Wiley & Sons, New Jersey, 1996.
- [6] A. Bejan and A. D. Kraus, *Heat transfer handbook*, John Wiley & Sons Inc., New Jersey, 2003.
- [7] J. P. Holman, *Heat Transfer*, New York: McGraw-Hill, 1997.
- [8] A. F. Mills, *Heat Transfer*, Englewood Cliffs, NJ: Prentice-Hall, 1999.
- [9] J. R. Simonson, *Engineering Heat Transfer*, 2nd ed., New York: MacMillan, 1998.
- [10] W. S. Janna, *Engineering Heat Transfer*, New York: Van Nostrand-Reinhold, 1988.
- [11] A. Boglietti, and A. Cavagnino, "Analysis of the endwinding cooling effects in TEFC induction motors," *IEEE Transactions on Industry Applications*, vol. 43, no.5, pp. 1214-1222, Sept.-Oct. 2007.
- [12] A. Boglietti, A. Cavagnino, and D. A. Staton, "Determination of critical parameters in electrical machine thermal models," *IEEE Transactions on Industry Applications*, vol. 44, no.4, pp. 1150-1159, 2008.
- [13] A. Boglietti, A. Cavagnino, and D. A. Staton, "End space heat transfer coefficient determination for different induction motor enclosure types," *IEEE Transactions on Industry Applications*, vol. 45, no.3, pp. 929-937, 2009.
- [14] D. Staton, A. Boglietti, and A. Cavagnino, "Solving the more difficult aspects of electric motor thermal analysis in small and medium size industrial induction motors," *IEEE Transactions on Energy Conversion*, vol. 20, no.3, pp. 620-628, 2005.
- [15] L. Yiping, Y. Wenhao, C. Pengfei, and L. Weili, "Mechanism research on air mass flow rate distribution in rotor radial ducts of turbo generator with sub-slot ventilation," in *Proceedings of World Automation Congress (WAC)*, 2008.
- [16] K. Hattori, K. Ide, K. Takahashi, K. Kobashi, H. Okabe, and T. Watanabe, "Performance assessment study of a 250 MVA air-cooled turbo.generator," in *Proceedings of International Electric Machines and Drives Conference (IEMDC)*, 2003.

- [17] M. Tari, K. Yoshida, S. Sekito, R. Brutsch, J. Allison, and A. Lutz, "HTC insulation technology drives rapid progress of indirect-cooled turbo generator unit capacity," in *IEEE Power Engineering Society Summer Meeting*, vol. 3, pp. 1427-1432, 2001.
- [18] L. Weili, C. Feng, and Z. Fen, "Study on eddy current loss and heat-transfer character of stator windings in synchronous generator," in *Proceedings of International Conference on Electrical Machines and Systems(ICEMS)*, 2008.
- [19] L. Weili, G. Chunwei, and Z. Ping, "Calculation of a complex 3-D model of a turbogenerator with end region regarding electrical losses, cooling, and heating," *IEEE Transactions on Energy Conversion*, vol. 26, no. 4, pp. 1073-1080, 2011.
- [20] L. Weili, H. Jichao, H. Feiyang, Z. Xingfu, Z. Yihang, and L. Yong, "Influence of the end ventilation structure change on the temperature distribution in the end region of large water-hydrogen-hydrogen cooled turbogenerator," *IEEE Transactions on Energy Conversion*, vol. 28, no. 2, pp. 278-288, 2013.
- [21] N. J. Carew, "Experimental determination of heat transfer co-efficients of salient pole rotors," *IEE Colloquium on Thermal Aspects of Machines*, 1992.
- [22] S. J. Pickering, D. Lampard, and M. Shanel, "Ventilation and heat transfer in a symmetrically ventilated salient pole synchronous machine," in *Proceedings of International Conference on Power Electronics Machines and Drives*, 2002.
- [23] R. Depraz, R. Zickermann, A. Schwery, and F. Avellan, "CFD validation and air cooling design methodology for large hydro generator," in *Proceedings of 17th International Conference on Electrical Machines (ICEM)*, 2006.
- [24] H. Lang, C. Kral, A. Haumer, M. Haigis, and R. Schulz, "Investigation of the thermal behavior of a salient pole synchronous machine," in *Proceedings of 17th International Conference on Electrical Machines (ICEM)*, 2006.
- [25] S. Houde, C. Hudon, and P.B. Vincent, "Simulations strategies of the cooling flow for large hydro generators," *International Journal on Hydropower & Dams*, no. 6, pp. 93-98, 2008.
- [26] K. Toussant, F. Torriano, J.F. Morissette, C. Hudon, and M. Reggio, "CFD analysis of ventilation flow for a scale model hydro-generator," in *Proceedings of ASME Power Conference*, 2011.
- [27] D. B. Hoseason, "The cooling of electrical machines," *Journal of the Institution of Electrical Engineers*, vol.69, no. 409, pp. 121-143, 1931.
- [28] IEC 34-1: *Rotating electrical machines –Part 1: Rating and performance*. (Reference number 2/933/FDIS), International Electrotechnical Commission, 1996.
- [29] R. Poole, "The application of propeller fans to the cooling of electrical machines," *Journal of the Institution of Electrical Engineers*, vol.77, no. 464, pp. 239-304, 1935.
- [30] C. S. Hudson and M. H. Walshaw, "New method of presenting cooling data for aircraft electrical machines," *Proceedings of the Institution of Electrical Engineers*, vol.112, no.1, pp.63-70, 1965
- [31] J. C. H. Bone, "Cooling and cooling circuits for electric motors," *IEE Journals on Electric Power Applications*, vol. 1, no. 2, pp. 37-44, 1978.
- [32] S. Kunckel, G. Klaus and M. Liese, "Calculation of eddy current losses and temperature rises at the stator end portion of hydro generators," *COMPEL: The International Journal*

for Computation and Mathematics in Electrical and Electronic Engineering, vol. 22, no. 4, pp.877-890, 2003.

- [33] J. Schoenauer, E. Schlemmer and F. Mueller, "Finite element modeling of the temperature distribution in the stator of a synchronous generator," *COMPEL: The International Journal for Computation and Mathematics in Electrical and Electronic Engineering*, vol. 22, no. 4, pp. 909-921, 2003.
- [34] S. Zhang, W. Li, J. Li, L. Wang and X. Zhang, "Research on flow rule and thermal dissipation between the rotor poles of a fully air-cooled hydro-generator," *IEEE Transactions on Industrial Electronics*, in press., 2015.
- [35] E. Schmidt, G. Traxler-Samek and A. Schwery, "3D nonlinear transient finite element analysis of eddy currents in the stator clamping system of large hydro generators," *COMPEL: The International Journal for Computation and Mathematics in Electrical and Electronic Engineering*, vol. 25, no.2, pp. 440-451, 2006.
- [36] G. Traxler-Samek, T. Lugand and A. Schwery, "Additiional losses in the damper winding of large hydrogenerators at open-circuit and load conditions," *IEEE Transactions on Industrial Electronics*, vol. 57, no. 1, pp. 154-160, 2010.
- [37] G. Traxler-Samek, R. Zickermann, and A. Schwery, "Cooling airflow, losses and temperatures in large air-cooled synchronous machines," *IEEE Transactions on Industrial Electronics*, vol. 57, no. 1, pp. 172-180, 2010.
- [38] E. Farnleitner, *Computational fluid dynamics analysis for rotating electrical machinery*, PhD Thesis, Mining University Leoben, Austria, 1999.
- [39] E. Farnleitner, and G. Kastner, "Contemporary methods of ventilation design for pumped storage generators," *Elektrotechnik & Informationstechnik*, vol. 127, no. 1-2, pp. 24-29, 2010.
- [40] B. Streibl, "Fluid mechanical optimization of high-power-density traction motors by means of Computational Fluid Dynamics," *Elektrotechnik & Informationstechnik*, vol. 128, no. 3, pp. 95-101, 2011.
- [41] A. Boglietti, A. Cavagnino, D. Staton, M. Shanel, M. Mueller, and C. Mejuto, "Evolution and modern approaches for thermal analysis of electrical machine," *IEEE Transactions on Industrial Electronics*, vol. 56, no. 3, pp. 871-882, 2009.
- [42] L. Alberti and N. Bianchi, "A coupled thermal & electromagnetic analysis for a rapid and accurate prediction of IM performance," *IEEE Transactions on Industrial Electronics*, vol. 55, no.10, pp. 3575-3582, 2008.
- [43] D.G. Dorrell, "Combined thermal and electromagnetic analysis of permanent-magnet and induction machines to aid calculation," *IEEE Transactions on Industrial Electronics*, vol. 55, no.10, pp. 3566-3574, 2008.
- [44] A. Tenconi, F. Profumo, S. E. Bauer, and M. D. Hennen, "Temperatures evaluation in an integrated motor drive for traction applications," *IEEE Transactions on Industrial Electronics*, vol. 55, no.10, pp. 3619-3626, 2008.
- [45] L. Weili, C. Guan, and P. Zheng, "Calculation and Analysis of Heat Transfer Coefficients and Temperature Fields of air-cooled large hydro-generator rotor excitation windings," *IEEE Transactions on Energy Conversion*, vol. 26, no. 3, pp. 946-952, 2011.

- [46] J. F. Trigeol, Y. Bertin, and P. Lagonotte, "Thermal modeling of an induction machine through the association of two numerical approaches", *IEEE Transactions on Energy Conversion*, vol. 21, no. 2, pp. 314-323, 2006.
- [47] C. Kral, T. G. Habetler, R. G. Harley, F. Pirker, G. Pasoli, H. Oberguggenberger and C. J. M. Fenz, "Rotor temperature estimation of squirrel-cage induction motors by means of a combined scheme of parameter estimation and a thermal equivalent model," *IEEE Transactions on Industry Applications*, vol. 40, no. 4, pp. 1049-1057, 2004.
- [48] B. D. J. Maynes, R. J. Kee, C. E. Tindall and R. G. Kenny, "Simulation of airflow and heat transfer in small alternators using CFD," *IEE Proceedings of Electric Power Applications*, vol. 150, no. 2, pp. 146-152, 2003.
- [49] C. Kral, A. Haumer, M. Haigis, H. Lang and H. Kapeller, "Comparison of a CFD analysis and a thermal equivalent circuit model of a TEFC induction machine with measurements," *IEEE Transactions on Energy Conversion*, vol. 24, no. 4, pp. 809-818, 2009.
- [50] M. Hettegger, B. Streibl, O. Biro and H. Neudorfer, "Measurements and simulations of the convective heat transfer coefficients on the end windings of an electrical machine," *IEEE Transactions on Industrial Electronics*, vol. 59, no. 5, pp. 2299-2308, 2012.
- [51] P. H. Connor, S. J. Pickering, C. Gerada, C. N. Eastwick, C. Micallef and C. Tighe, "Computational fluid dynamics modeling of an entire synchronous generator for improved thermal management," *IET Electric Power Applications*, vol. 7., no 3, pp. 231-236, 2013.
- [52] C. Jungreuthmayer, T. Bauml, O. Winter, M. Ganchev, H. Kapeller, A. Haumer, C.Kral, "A detailed heat and fluid flow analysis of an internal permanent synchronous machine by means of computational fluid dynamics," *IEEE Transactions on Industrial Electronics*, vol. 59, no.12, pp. 4568-4578, 2012.
- [53] F. R. Menter, "Two-equation eddy viscosity turbulence models for engineering applications," *AIAA Journal*, vol. 32, no.8, pp. 1598-1605, 1994.
- [54] W. Vieser, T. Esch, and F. Menter, "Heat transfer predictions using advanced two equation turbulence models," *AEA Technology*, Harwell U.K., 2002.
- [55] M. Schrittwieser, A. Marn, E. Farnleitner and G. Kastner, "Numerical analysis of heat transfer and flow of stator duct models," *in Proceedings of 20th International Conference on Electrical Machines (ICEM)*, 2012.
- [56] M. Schrittwieser, A. Marn, E. Farnleitner and G. Kastner, "Numerical analysis of heat transfer and flow of stator duct models," *IEEE Transactions on Industry Applications*, vol. 50, no.1, pp. 226-233, 2014.
- [57] M. Schrittwieser, O. Bíró, E. Farnleitner and G. Kastner, "Validation of measurements with conjugate heat transfer models," *in Proceedings of 15th International IGTE Symposium on Numerical Field Calculation in Electrical Engineering*, 2012.
- [58] M. Schrittwieser, O. Bíró, E. Farnleitner and G. Kastner, "Validation of measurements with conjugate heat transfer models," *COMPEL: The International Journal for Computation and Mathematics in Electrical and Electronic Engineering*, vol. 32, no.50, pp. 1707-1720, 2013.
- [59] M. Schrittwieser, O. Bíró, E. Farnleitner and G. Kastner, "Validation of numerical approaches for simulating the heat transfer in stator ducts with measurements," *in*

Proceedings of 19th International Conference on the Computation of Electromagnetic Fields (COMPUMAG), 2013.

- [60] M. Schrittwieser, O. Bíró, E. Farnleitner and G. Kastner, “Validation of numerical approaches for simulating the heat transfer in stator ducts with measurements,” *IEEE Transactions on Magnetics*, vol. 50, no.2, pp. 1-4, 2014.
- [61] M. Schrittwieser, O. Bíró, E. Farnleitner and G. Kastner, “Analysis of temperature distribution in the stator of large synchronous machines considering heat conduction and heat convection,” *in Proceedings of 16th Biennial IEEE Conference on Electromagnetic Field Computation*, 2014.
- [62] M. Schrittwieser, O. Bíró, E. Farnleitner and G. Kastner, “Analysis of temperature distribution in the stator of large synchronous machines considering heat conduction and heat convection,” *IEEE Transactions on Magnetics*, vol. 51, no.3, pp. 1-4, in press.
- [63] M. Schrittwieser, O. Bíró, E. Farnleitner and G. Kastner, “Characterizing the convective heat transfer on stator ventilation ducts for large hydro generators with a neural network,” *in Proceedings of 16th International IGTE Symposium on Numerical Field Calculation in Electrical Engineering*, 2014.
- [64] M. Schrittwieser, O. Bíró, E. Farnleitner and G. Kastner, “Characterizing the convective heat transfer on stator ventilation ducts for large hydro generators with a neural network,” *COMPEL: The International Journal for Computation and Mathematics in Electrical and Electronic Engineering*, in review process.
- [65] Andritz Hydro GmbH, *Facts and Figures*, brochure, 2013.
- [66] IEC60034-1. *Rotating electrical machines – part 1: Rating and performance*, 2004.
- [67] M. W. Zemansky, *Heat and Thermodynamics*, McGraw-Hill, New York, 1943.
- [68] S. K. Pal, “Heat Transfer in Electrical Machines - A Critical Review,” *Electrical Research Association Report*, 1971.
- [69] H. D. Baehr and K. Stephan, *Wärme- und Stoffübertragung*, 6th edition, Springer Heidelberg London New York, 2008.
- [70] F. Kreith and M. S. Bohn, *Principles of heat transfer*, 6th edition, Thomson, 2001.
- [71] L. Prandtl, *Essentials of fluid dynamics*, Hafner Publications, New York, 1952.
- [72] G. Brenn, *Strömungslehre und Wärmeübertragung I*, Graz University of Technology, Austria, 2004.
- [73] H. D. Beahr and S. Kabelac, *Thermodynamik– Grundlagen und technische Anwendungen*, 14th edition, Springer, Berlin Heidelberg, 2009.
- [74] H. K. Versteeg and W. Malalasekera, *An introduction to computational fluid dynamics– The finite volume method*, 2nd edition, Pearson Education Limited, 2007
- [75] W. Prager, *Einführung in die Kontinuumsmechanik*, Birkhäuser-Verlag, Basel/Stuttgart, 1961.
- [76] J. D. Anderson, *Computational fluid dynamics – The basics with applications*, McGraw-Hill, New York, 1995.
- [77] J. M. Honig, *Thermodynamics – Principles Characterizing Physical and Chemical Processes*, Fourth Edition, Academic Press, Oxford, 2014.
- [78] H. Schlichting, *Boundary-layer theory*, 7th edition, McGraw-Hill, New York, 1979.

- [79] J. F. Wendt, *Computational fluid dynamics: An introduction*, third edition, Springer-Verlag Berlin Heidelberg, 2009
- [80] J. Spurk and N. Aksel, *Strömungslehre Einführung in die Theorie der Strömungen*, 8th edition, Springer, Berlin, Heidelberg, 2010.
- [81] H. Herwig, *Strömungsmechanik-Eine Einführung in die Physik und die mathematische Modellierung von Strömungen*, 2nd edition, Springer, Berlin, Heidelberg, 2006.
- [82] H. Sigloch, *Technische Fluidmechanik*, Springer, Berlin Heidelberg, 2012.
- [83] ANSYS, *ANSYS FLUENT 12.0 User's Guide*, ANSYS Inc., Southpoint 275 Technology Drive Canonsburg, PA 15317, 2009.
- [84] ANSYS, *ANSYS CFX-Solver Modeling Guide Release 14.0*, ANSYS Inc., Southpoint 275 Technology Drive Canonsburg, PA 15317, 2011.
- [85] K. A. Hoffmann and S. T. Chiang, *Computational Fluid dynamics volume III*, 4th edition, Engineering Education System, Wichita, Kansas, USA, 2000.
- [86] J. Blazek, *Computational fluid dynamics: Principles and applications*, Elsevier Science Ltd, Oxford, 2001
- [87] J. H. Ferziger and M. Peric, *Computational methods for fluid dynamic*, Springer, Berlin Heidelberg, 2008.
- [88] B. Launder, and D. Spalding, *Mathematical models of Turbulence*. London, U.K.: Academic Press, 1972.
- [89] ANSYS, *ANSYS CFX-Solver Theory Guide Release 14.0*, ANSYS Inc., Southpointe 275 Technology Drive Canonsburg, PA 15317, 2011.
- [90] D. C. Wilcox, *Turbulence modeling for CFD: Solutions Manual*, La Canada, CA: DCW Industries, 1994.
- [91] F. R. Menter, "Two-equation eddy-viscosity turbulence models for engineering applications", *AIAA Journal*, vol. 32, no. 8, pp. 1598-1605. 1994
- [92] F. R. Menter, M. Kuntz and R. Langstry, "Ten years of industrial experience with the SST turbulence model", *Turbulence, Heat and Mass Transfer*, vol. 4, Begell House Inc, 2003.
- [93] W. Vieser, T. Esch and F. Menter, *CFX Validation Report: Heat transfer predictions using advanced two-equation turbulence model*, ANSYS Germany, Otterfing, 2008.
- [94] B. A. Kader, "Temperature and concentration profiles in fully turbulent boundary layers," *International Journal of Heat and Mass Transfer*, vol. 24, no. 9, pp. 1541-1544, 1981.
- [95] ANSYS, *ANSYS ICEM CFD Manual*, ANSYS Inc., Southpointe 275 Technology Drive Canonsburg, PA 15317, 2014.
- [96] ANSYS, *Release 13.0 Documentation for ANSYS Workbench*, ANSYS Inc., Southpointe 275 Technology Drive Canonsburg, PA 15317, 2014.
- [97] M. Sridhar, S. Sunnam, S. Goswami and J. Liu, "CFD aerodynamic performance validation of a two-stage high pressure turbine," *in Proceedings of ASME Turbo Expo*, Vancouver, Canada, 2011.
- [98] M. Mansour, J. Gunaraj and P. Goswami, "Validation of steady averaged-passage and mixing plane CFD approaches for the performance prediction of a gas turbine multistage axial compressor," *in Proceedings of ASME Turbo Expo*, Berlin, Germany, 2008.

- [99] VDI-Gesellschaft Verfahrenstechnik und Chemieingenieurwesen, *VDI Heat Atlas*, 10th edition, Berlin, Germany, Springer Verlag, 2006.
- [100] ANDRITZ Hydro GmbH, *Technical Report: Measurements on stator laboratory model*, Weiz, Austria, 2000.
- [101] REISSMANN Sensortechnik GmbH, *Data sheet: Measuring resistor with the Pt100-sensor referring to DIN EN 60751*, Germany, 2010.
- [102] O. Ida and Y. Nagano, “The relaminarization mechanism of turbulent channel flow at low Reynolds numbers,” *Flow, Turbulence Combustion*, vol. 60, no. 2, pp. 193-213, 1998.
- [103] Mathworks, *Matlab Optimization Toolbox – User’s Guide R2014b*, The MathWorks, Inc., Natick, MA, USA, 2014.
- [104] M. H. Hassoun, *Fundamentals of artificial neural networks*, Prentice Hall India, 1995.
- [105] D. E. Rumelhart, G. E. Hinton, and R. J. Williams, “Learning Representations by Back-Propagating Errors,” *Nature*, vol. 323, pp. 533-536, 1986.
- [106] B. G. Kermani, S. S. Schiffman, and H. T. Nagle, “Performance of the Levenberg-Marquardt neural network training method in electronic nose applications,” *Sensors and Actuators B: Chemical*, vol. 110, no. 1, pp. 13-22, 2005
- [107] K. Levenberg, “A method for the solution of certain problems in least squares,” *Quart. Appl. Math.*, vol. 2, pp. 164-168, 1944.
- [108] D. Marquardt, “An algorithm for least squares estimation of non-linear parameters,” *Journal Ind. Appl. Math.*, vol. 11, no. 2, pp. 431-441, 1963.
- [109] D. Nguyen and B. Widrow, “Improving the learning speed of 2-layer neural networks by choosing initial values of the adaptive weights,” *International Joint Conference Neural Networks*, vol. 3, pp. 21–26, 1990.
- [110] M. H. Beale, M. T. Hagan and H. B. Demuth, *Matlab Neural Network Toolbox – User’s Guide R2014b*, The MathWorks, Inc., Natick, MA, USA, 2014.